SAPIENZA
UNIVERSITÀ DI ROMA

PhD course in Electrical, Materials and Nanotechnology Engineering

XXXVII Cycle

Aluminide coatings modified via electroless platinum plating for high temperature applications

Candidate:

Giulia Pedrizzetti

Supervisor:

prof. Francesco Marra

Academic year 2024-2025

Index

Abstract

The performance and durability of gas turbine engine components operating in high-temperature environments critically depend on the effectiveness of protective coatings. Among these, platinum-modified aluminide coatings are widely employed as bond coats in thermal barrier coating (TBC) systems applied to Ni-based superalloys. Pt-aluminide coatings protect the underlying layers from oxidation through the formation of a stable and adherent α-Al_2O_3 scale during high-temperature exposure. Platinum modification is achieved by depositing a Pt layer on the base superalloy prior to aluminizing, and electroplating is currently the only industrial method used for this purpose. However, this technique has several limitations, primarily related to the edge effect of the electric field: the formation of coating with non-uniform thickness on complex geometries, the complexity of the required apparatus and the need for custom-designed anodes for each component to be coated. Difficulties in controlling the Pt deposition process often lead to microstructural non-uniformities in the resulting aluminide, with formation of brittle phases where excess platinum accumulates, and hindered control over degradation phenomena related to thermodynamic imbalance and diffusion processes.

This thesis addresses the above issues by developing and optimizing a Pt deposition method based on electroless plating, and by exploring the potential of innovative microstructural modifications aimed at improving the performance of Pt-aluminide coatings. The work is divided into five main research phases: (i) the design of a new electroless Pt deposition process and (ii) its validation for the production of platinum-modified aluminides, (iii) the optimization of an aluminizing procedure via slurry aluminizing, (iv) the microstructural tailoring via the introduction of an electroless Ni interlayer, and (v) the preliminary development of nanocomposite Pt-aluminide coatings reinforced with α-Al_2O_3 nanoparticles.

Extensive coating characterization was carried out throughout the study, using scanning electron microscopy (SEM), energy-dispersive X-ray spectroscopy (EDS), X-ray diffraction (XRD), quantitative image analysis, grain size measurement, and oxidation kinetics modeling. Oxidation behavior was assessed through mass gain measurements and interpreted using the Monceau parabolic rate model, which provided insights into oxide growth kinetics. Structural parameters such as grain size and nanoparticle distribution were correlated with performance to establish structure–property relationships.

The first part of the thesis focuses on the formulation and validation of a new electroless Pt plating solution, specifically developed for the production of aluminide coatings for high-temperature applications. A completely novel bath formulation was designed and optimized for stability,

deposition rate, and Pt film quality. The process showed excellent flexibility for deposition on Ni-based superalloys with varying chemical compositions, ensuring uniform Pt layers even on complex geometries, and overcoming typical current-density-related issues found in electrolytic processes. The resulting coatings exhibited high purity, controlled thickness, and a nanocrystalline structure suitable for subsequent diffusion treatments. Moreover, the bath formulation ensured high deposition repeatability, platinum consumption comparable to commercial electrolytic solutions, supported bath regeneration via metal turnover, and, most importantly, eliminated the need for an anode, thereby simplifying equipment and increasing industrial flexibility.

In the second phase, coatings obtained via electroless deposition were compared to those produced through conventional electroplating, both in the as-deposited state and after aluminizing. The Pt layers obtained by electroless and electrolytic techniques exhibited comparable morphology, composition, and microstructure; however, the electroless coatings showed significantly better thickness uniformity. After aluminizing, the coatings showed similar phase composition, primarily ζ-$PtAl_2$ and β-(Ni,Pt)Al, but electroless coatings demonstrated greater microstructural uniformity, lower porosity, and slightly superior oxidation resistance. These results confirmed electroless deposition as a valid industrial alternative to electroplating, offering both performance benefits and process simplification.

The third phase involved systematic optimization of the aluminizing step, aimed at controlling aluminum distribution along coating thickness and improving microstructural control. By varying slurry thickness and concentration, aluminum availability during diffusion was modulated, resulting in coatings composed entirely of the β-NiAl phase throughout the thickness. The optimized process was also validated for the production of Pt-aluminides, confirming its versatility for both standard and modified coatings. The effect of the initial Pt layer thickness, ranging from 4.5 to 12 μm, was also studied. Thicker Pt layers favored the formation of an outer ζ-$PtAl_2$ phase and led to increased total coating thickness. Although thicker Pt layers provided improved oxidation resistance, a 7 μm Pt thickness was identified as the best compromise between performance and Pt consumption, supporting the design of more cost-effective and efficient coatings.

In the fourth part, an electroless Ni interlayer was introduced after the Pt layer, aiming to modify diffusion dynamics. The microstructural changes and oxidation resistance were studied for Ni layers of 5, 10, 20, and 40 μm thickness. As Ni thickness increased, a progressive suppression of brittle Pt-rich phases in the outer region was observed, along with stabilization of the β-NiAl phase, reduction of the IDZ thickness, and decreased precipitation of TCP phases (topologically close-packed), which are detrimental to mechanical resistance. However, for Ni layers exceeding 10 μm, the reduced availability of Pt near the external interface led to lower oxidation resistance. As such, the 10 μm Ni

interlayer was selected as the optimal configuration, offering the best compromise between microstructural integrity and oxidation performance.

The fifth and final phase involved the preliminary development of Pt-aluminide nanocomposite coatings, fabricated via co-deposition of α-Al_2O_3 nanoparticles within the electroless Pt layer. The best results in terms of maximum particle incorporation and minimal agglomeration were achieved with 0.5 g/L of α-Al_2O_3 in the plating bath. After aluminizing, the nanoparticles remained localized in the outermost coating region, ideally positioned to serve as epitaxial nucleation sites for α-Al_2O_3 scale formation during oxidation. The particles also induced grain size refinement via Zener pinning mechanism. Preliminary oxidation tests at 1100 °C for 500 hours showed slower oxidation kinetics for nanocomposite coatings, with better protection particularly during the transient oxidation stage. This suggests a faster transformation to α-Al_2O_3, enabled by the synergistic action of the epitaxial template effect of the particles and the enhanced Al diffusion in the fine-grained matrix, ultimately confirming improved protective behavior of nanocomposites compared to standard coatings.

In conclusion, this work represents a significant advancement in the practical application of platinum-modified aluminide coatings, proposing a simpler, more controllable, and scalable Pt deposition method, while also offering new pathways for microstructural and compositional improvements. The outcomes of this research may have direct implications for the development of gas turbine and aero-engine components, where coating reliability and oxidation resistance are critical to improve performance and durability.

1. Gas Turbine Systems

Turbomachines are devices that convert the total energy of a working fluid into mechanical energy and vice versa [1]. They are broadly categorized into two types: power-generating devices, such as turbines, and power-consuming devices that alter the total pressure of a working fluid, such as compressors and pumps.

Gas turbine systems are engines that convert the total energy of a working fluid (typically air) into either mechanical energy for power generation or kinetic energy for propulsion. The history of gas turbines dates back to 1791, when John Barber patented an early concept. However, it was not until the early 20th century that the first operational gas turbine capable of producing surplus net power was developed [2].

The components of gas turbine systems endure extreme dynamic and thermomechanical stresses. They must withstand thousands of hours of operation at high temperatures in highly oxidizing and corrosive environments without losing mechanical integrity. Therefore, components in the most demanding areas of the engine require meticulous design to minimize degradation and maximize efficiency.

Global energy demand has been on a consistent upward trajectory, with consumers worldwide spending nearly $10 trillion on energy in 2022, averaging more than $1,200 per person [3]. In parallel, the aviation sector has experienced remarkable growth. According to the International Air Transport Association (IATA), air transport passenger traffic has more than doubled from 2021 to 2025, and forecasts indicate it will exceed 10 billion passengers annually by 2050 [4]. This escalation underscores the imperative to mitigate emissions, with technological innovation playing a pivotal role. The aviation industry has committed to achieving net-zero carbon emissions by 2050, aligning with the Paris Agreement's 1.5ºC goal. This commitment is supported by enhanced efficiency measures, energy transition, and innovation across the sector, in collaboration with governments worldwide.

Turbomachines are central to this technological advancement. Their meticulous design and incorporation of new technologies is essential to improve service life of components, reduce cost and overall environmental impact, aligning with the broader goal of reducing emissions and achieving sustainability in the face of escalating global energy demands.

1.1 Principle of operation and basic thermodynamics

A simple gas turbine engine consists of three main components: the compressor, the combustion chamber, and the turbine. Air is drawn in through a dynamic intake and directed toward the compressor, where it is slowed down and compressed, increasing its pressure. The high-pressure air then enters the combustion chamber, where fuel is injected and ignited, supplying additional energy. The resulting hot gases are then expanded through the turbine, converting thermal energy into mechanical work to drive the compressor and, if applicable, an external load.

Due to the added energy from combustion, the exhaust pressure at the turbine exit remains higher than ambient pressure. In the case of a jet engine, the flow can be accelerated through a nozzle, producing a high-velocity jet stream that generates thrust for propulsion.

The ideal thermodynamic cycle for a simple gas turbine engine is the Joule-Brayton cycle, illustrated in Figure 1.1.

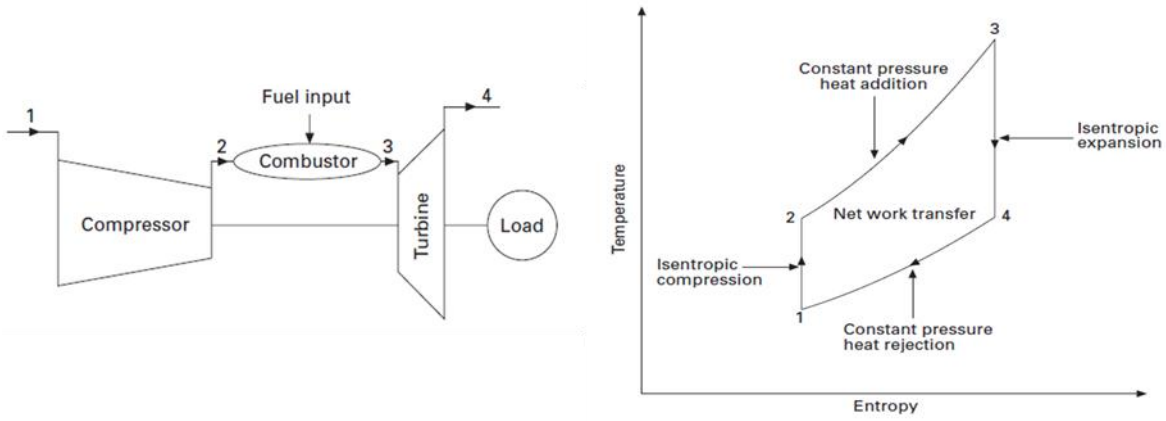

Figure 1.1: Schematic representation of the Joule-Brayton cycle.

To analyze cycle performance, the following idealized assumptions are made:

I. Compression and expansion processes are reversible and adiabatic (i.e., isentropic);
II. Kinetic energy variations between the inlet and outlet of each component are negligible;
III. No pressure losses occur in ducts or the combustion chamber;
IV. The working fluid behaves as a perfect gas with constant specific heats (internal energy and enthalpy depend only on temperature);
V. The fluid composition remains unchanged throughout the cycle, meaning fuel injection and combustion effects on mass flow are negligible:

Based on assumptions (IV) and (V), the combustion chamber can be modeled as a heat exchanger with an external heat source.

Applying the steady-flow energy equation per unit mass:

$$Q = (h_{out} - h_{in}) + \frac{1}{2}(v_{out}^2 - v_{in}^2) + W \quad (1.1)$$

where Q and W are the heat and work transfers per unit mass, respectively, and v_{in} and v_{out} are inlet and outlet velocities. Neglecting kinetic energy changes per assumption (II), the work and heat transfer equations for each component (with subscripts referring to Figure 1.1) become:

$$W_{12} = -(h_2 - h_1) = -c_p(T_2 - T_1) \quad (1.2)$$

$$Q_{23} = (h_3 - h_2) = c_p(T_3 - T_2) \quad (1.3)$$

$$W_{32} = (h_3 - h_4) = c_p(T_3 - T_4) \quad (1.4)$$

where c_p is the specific heat at constant pressure. The thermal efficiency η_{th} is defined as the ratio of net work output to the heat supplied by fuel:

$$\eta_{th} = \frac{W_{net}}{Q_{23}} = \frac{c_p(T_3 - T_4) - c_p(T_2 - T_1)}{c_p(T_3 - T_2)} \quad (1.5)$$

Using the isentropic temperature-pressure relations:

$$T_2 = T_1 \left(\frac{p_2}{p_1}\right)^{\frac{\gamma-1}{\gamma}} \quad (1.6)$$

$$T_4 = T_3 \left(\frac{p_4}{p_3}\right)^{\frac{\gamma-1}{\gamma}} \quad (1.7)$$

Where γ is the isentropic index, defined as c_p/c_v, which equals 1.4 for air. Since heat addition occurs at constant pressure (processes 2-3 and 4-1), the pressure ratio β remains constant:

$$\beta = \frac{p_2}{p_1} = \frac{p_4}{p_3} \quad (1.8)$$

Substituting these relations into equation (1.5), the thermal efficiency can be expressed as:

$$\eta_{th} = 1 - \frac{T_1}{T_2} = 1 - \beta^{\left(\frac{\gamma}{\gamma-1}\right)} \quad (1.9)$$

This shows that efficiency depends only on the pressure ratio and the properties of the working gas. However, the specific work output W_{net}, which determines propulsion performance, is influenced by the maximum cycle temperature T_3 (often referred as the turbine inlet temperature, TIT). Indeed, Figure 1.2 shows the effect of compression ratio and turbine inlet temperature on thermal efficiency.

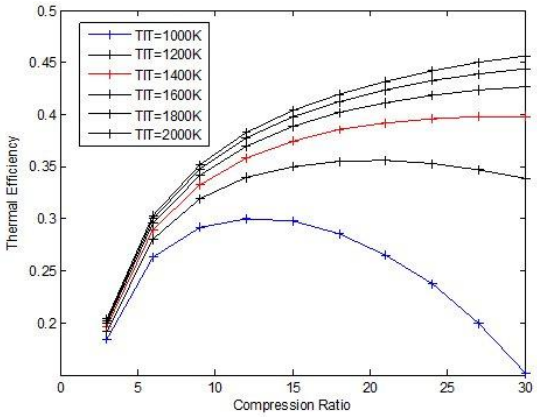

Figure 1.2: Effect of compression ratio and turbine inlet temperature on thermal efficiency [5].

Although increasing fuel input theoretically improves overall efficiency, there is a limit to fuel addition for a given air mass flow. The maximum fuel-to-air ratio is constrained by the thermal limits of turbine blades, as excessive temperatures can lead to material degradation due to creep and oxidation.

The gas turbine cycle described above is termed a simple cycle. However, more advanced complex cycles incorporate additional components to improve efficiency and performance: intercoolers reduce compression power requirements; reheaters enhance turbine work output; heat exchangers lower heat input by utilizing exhaust heat recovery. Although these enhancements were explored early in gas turbine development, modern aviation primarily relies on simple cycles due to the significant efficiency improvements achieved in compressors, turbines, and combustion systems.

1.2 Turbine blades

Gas turbine engines must operate reliably under extreme conditions, where temperature and pressure fluctuate significantly across different engine sections. Figure 1.3 illustrates the temperature rise and pressure distribution throughout the engine. Both curves peak as the gas exits the combustion chamber, where temperatures can reach 1400–1500 °Cand pressures approach 40 atm [6]. Turbine blades, placed just outside the combustion chamber and rotating at high speeds under intense thermomechanical loads, are directly exposed to this hot, high-pressure jet. As a result, they experience multiple degradation mechanisms, making them among the most critical components of the engine.

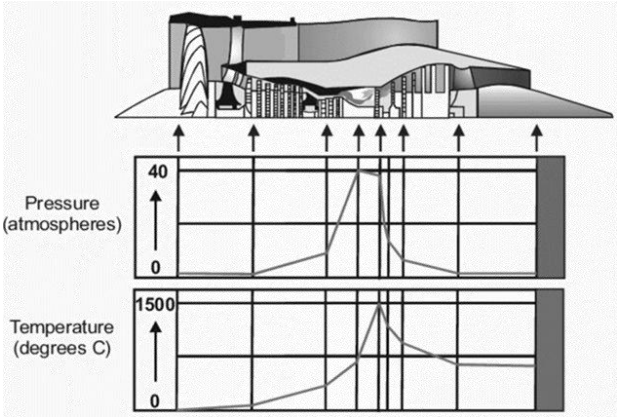

Figure 1.3: Temperature and pressure distribution across the turbofan engine [7].

The most extreme operating conditions occur at the inlet of the high-pressure turbine (HPT), where high-temperature, high-pressure, and high-energy gases exiting the combustion chamber are directed toward the first-stage HPT blades. These blades endure not only intense thermal and mechanical loads but also turbulent flow, dynamic stresses from centrifugal forces, and rapid thermal transients during loading/unloading or flight cycles [8].

The efficiency and overall performance of a jet engine depend heavily on the HPT inlet temperature, making the temperature resistance of turbine blades a crucial factor. Consequently, HPT blades are considered the most critical components of the engine. Their material selection is dictated by the need for high mechanical strength and thermal resistance to enable higher operational temperatures and increased thrust.

Turbine blades are subjected to multiple degradation mechanisms, including low-cycle fatigue (LCF), high-cycle fatigue (HCF), thermal fatigue, and creep damage due to prolonged exposure to extreme conditions. Additionally, they are subjected to high temperature oxidation and face severe environmental attacks as the hot combustion gases contain contaminants such as sulfates and chlorides, leading to hot corrosion. Erosive particles present in both the combustion gases and atmospheric air (especially during takeoff and landing) further accelerate material deterioration.

Notably, failures tend to occur in the blade regions experiencing the highest temperatures, usually at the leading edge. Figure 1.3.3 illustrates the typical temperature distribution in a first-stage HPT blade (with a cooling system) at a turbine inlet temperature of 1211 °C [9]. Given that gas temperatures impacting the blade can exceed this value, the temperature distribution profile may exhibit even higher peaks, although the general trend remains consistent.

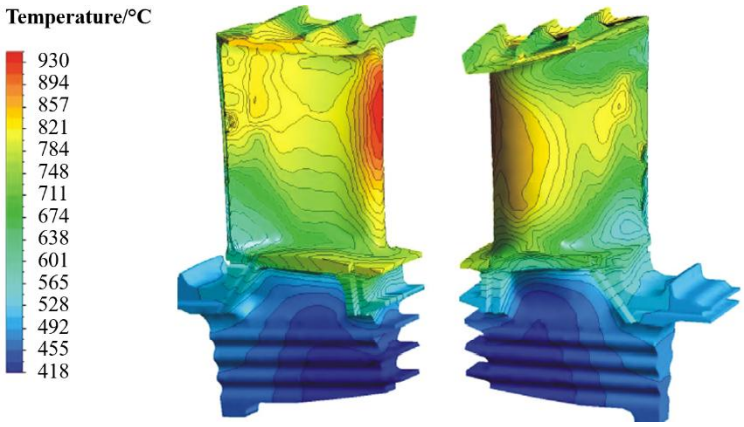

Figure 1.4: Temperature distribution for a high-pressure turbine blade with a turbine inlet temperature of 1211 °C (adapted from *[9]*).

The extreme conditions in which turbine blades operate, combined with the increasing demand for more powerful and efficient engines, necessitate materials that possess:

- High service temperature and creep resistance to endure prolonged exposure to extreme heat;
- Low thermal expansion coefficient to minimize strain and thermal stresses;
- High fracture toughness to resist crack initiation and propagation;
- Low density to reduce both engine weight and power losses in driving the compressor;
- High fatigue strength (both mechanical and thermal) to withstand repeated loading cycles;
- High Young's modulus and yield strength to endure tensile and bending stresses;
- High natural frequency to avoid resonance under high rotational speeds and centrifugal forces;
- Resistance to oxidation, hot corrosion, and erosion to enhance durability.

In reality, no single material can simultaneously fulfill all these requirements. Thus, turbine blades rely on advanced material systems, where a strong substrate works in synergy with a protective surface coating. This combined approach ensures thermo-mechanical integrity, enhances engine efficiency, and prolongs component lifespan under extreme conditions.

1.3 Substrate material – Nickel-based superalloys

Gas turbine applications demand structural materials that can withstand extreme temperatures, high mechanical stresses, rapid thermal transients, and multiple degradation phenomena, as outlined in previous sections. To meet these stringent requirements, nickel-based and cobalt-based superalloys are the most widely used materials in the hottest sections of gas turbine engines.

Nickel-based superalloys are characterized by exceptional strength, creep resistance, and oxidation resistance across the operational temperature range. Their superior mechanical and thermal properties make them more effective than iron or titanium-based superalloys in sustaining performance under harsh conditions [10].

Nickel-based superalloys possess a fully austenitic face-centered cubic (FCC) structure (γ phase), which provides excellent tensile strength, creep resistance, and high-temperature durability. However, pure nickel alone does not meet the required standards for thermo-mechanical strength and oxidation resistance. To enhance its performance, modern nickel-based superalloys have evolved into complex multi-element systems, where various alloying elements contribute to an optimized microstructure tailored for prolonged service life under extreme conditions. These alloys are carefully engineered to contain specific phases that enhance material properties. For instance, the addition of aluminum and/or titanium leads to the formation of the γ' (gamma prime) phase, a key strengthening phase that is coherent with the matrix (with lattice that only differs by 0.5% from γ phase). In this structure, nickel atoms occupy face-centered positions, while aluminum atoms are positioned at the corners of the unit cell, as shown in Figure 1.5. This ordered arrangement significantly improves high-temperature strength and creep resistance, making it a crucial feature of high-performance turbine materials [11].

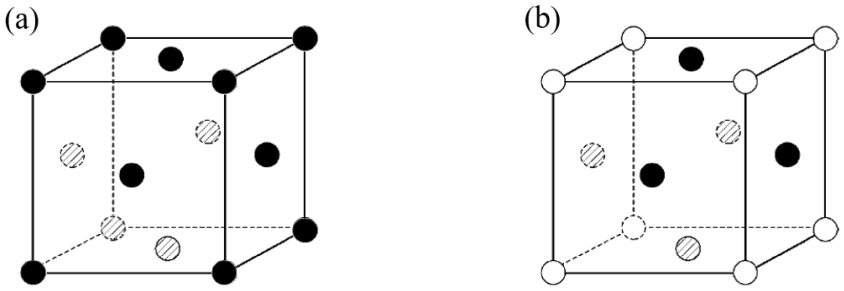

Figure 1.5: (a) FCC nickel crystal structure; (b) ordered FCC crystal structure of γ' phase (●: Nickel atoms shared with the adjacent cell; ○: Aluminum atoms shared with eight cubes at each corner).

In more detail, superalloys primarily consist of an austenitic face-centered cubic (FCC) matrix phase (γ), along with various secondary phases (typically based on intermetallic compounds) that significantly enhance material performance. These secondary phases play a crucial role in strengthening the alloy and improving its resistance to high-temperature degradation. The most valuable secondary phases affecting superalloy properties include carbides, γ' (gamma prime), and γ'' (gamma double prime) [11–13]:

- Carbides (e.g., MC, M_6C, $M_{23}C_6$, with M_7C_3 being rare): these stable compounds contribute to matrix strengthening by impeding grain boundary sliding and dislocation movement. The primary MC-forming elements are titanium, tantalum, niobium, and hafnium, while molybdenum and tungsten can also participate. In alloys with high chromium content, $Cr_{23}C_6$ carbide formation further enhances grain boundary strength, while also contributing to the formation of a protective Cr_2O_3 oxide scale for oxidation resistance;
- γ' (gamma prime) phase, $Ni_3(Al,Ti)$: The dominant precipitation-strengthening phase in nickel-based superalloys. Its nominal composition is Ni_3Al, but up to 65% of aluminum can

be substituted by titanium, leading to the general formula $Ni_3(Al,Ti)$. Additionally, niobium and tantalum can partially replace aluminum, forming metastable γ' variants. Titanium enhances mechanical strength and hot corrosion resistance, while aluminum improves oxidation resistance by promoting the formation of a stable Al_2O_3 protective layer at high temperatures.

- γ'' (gamma double prime) phase, Ni_3Nb: A body-centered tetragonal (BCT) ordered structure that precipitates as small coherent platelets in alloys containing more than 4% niobium, significantly contributing to precipitation hardening.

The development of cobalt-rich or cobalt-based superalloys has recently garnered significant interest due to cobalt's influence on the solubility of alloying elements in the γ matrix. This leads to an increased γ' volume fraction, as well as the stabilization of MC-type carbides and the sigma phase. These alloys are primarily designed to enhance high-temperature strength through solid-solution strengthening and carbide reinforcement. Additionally, their formulation focuses on improving both oxidation resistance and hot corrosion resistance in extreme operating environments.

Figure 1.6 provides an overview of the key alloying elements in nickel-based superalloys, highlighting their primary strengthening functions, along with potentially detrimental tramp elements. The height of the element blocks represents the relative amounts that may be present.

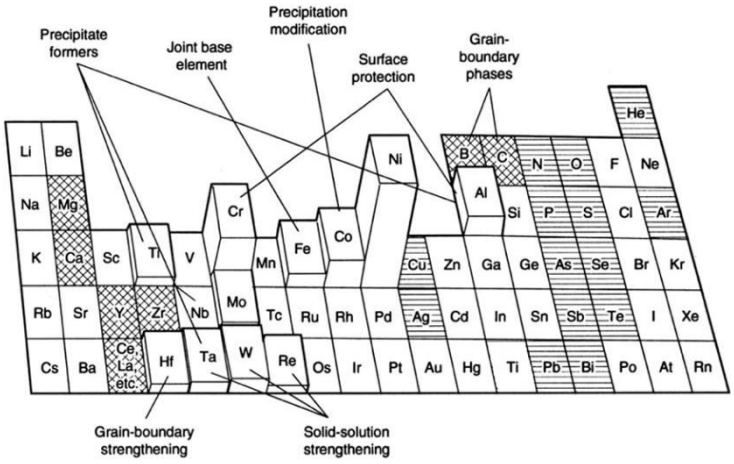

Figure 1.6: Alloying elements used in Ni-base superalloys. Beneficial minor elements are marked with crosshatch, while detrimental tramp elements are marked with horizontal line hatch.

The incorporation of rhenium (Re) and other refractory elements, such as tungsten (W) and molybdenum (Mo), has significantly contributed to the advancement of multiple generations of superalloys by enhancing solid solution strengthening, thereby improving high-temperature performance [14,15]. However, these additions can also lead to the formation of topologically close-packed (TCP) phases, which can degrade mechanical properties when exposed to extreme thermal conditions. To address this issue, the addition of platinum group metals (PGMs), particularly

ruthenium (Ru), has become crucial in the development of next-generation superalloys. Ruthenium plays a key role in further improving phase stability, helping to mitigate the formation of detrimental TCP phases while maintaining the material's high-temperature strength and durability [16,17].

The microstructure and properties of superalloys are influenced not only by their chemical composition, but also by the processing methods used in their manufacturing. Three key microstructural factors, which are grain size, shape, and orientation, play a crucial role in determining the mechanical and physical properties of these alloys. Enhancing the high-temperature performance of superalloys requires minimizing grain boundary weaknesses, particularly by eliminating boundaries that are oriented perpendicular to the applied stress. Directionally solidified alloys, whether in the form of columnar grains (CGDS) or single crystals (SCDS), exhibit superior thermal fatigue resistance and creep behavior compared to conventionally cast polycrystalline (PC) materials [11]. Specifically, columnar and single-crystal structures significantly delay the onset of tertiary creep due to the alignment or complete removal of grain boundaries. Additionally, controlling the solidification direction to align with lower Young's modulus axes effectively reduces thermal stresses within the component, further enhancing its fatigue resistance. A representative comparison of high temperature properties of superalloys as a function of their microstructure (PC, CGDS or SCDS) is reported in Figure 1.7.

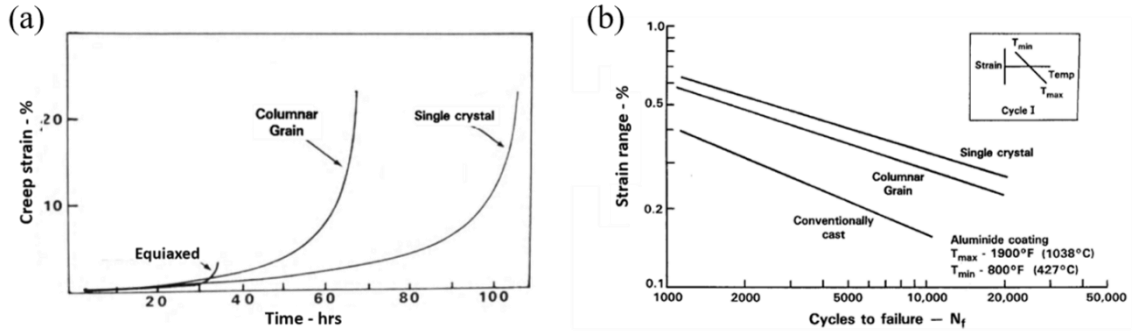

Figure 1.7: Comparison of high temperature properties for PC, CGDS and SCDS cast nickel-based superalloys: (a) creep behavior; (b) thermal fatigue resistance.

2. Degradation phenomena

The high temperatures and harsh operating conditions experienced by turbine blades lead to various degradation phenomena that significantly impact the durability, efficiency, and reliability of the entire propulsion system [18]. Among these, the most detrimental mechanisms include creep (particularly affecting the early turbine stages) along with high-temperature oxidation, hot corrosion and erosion [19]. Each of these degradation processes can severely compromise the structural integrity and operational performance of turbine components, posing major challenges to material selection and service life of the entire system.

2.1 The mechanism of creep and its stages

Creep is a time-dependent plastic deformation mechanism that occurs when a material is subjected to prolonged exposure to high stress levels that remain below its yield strength. This deformation progresses over time under a constant load and becomes more pronounced as materials are exposed to elevated temperatures for extended periods. The tendency for creep increases as the material's temperature approaches its melting point (T_m), typically becoming significant at approximately $0.4T_m$ [20].

As illustrated in Figure 2.1, creep is generally evaluated by measuring deformation as a function of time under a constant load at high temperatures (according to ASTM E139-11 [21]). The creep curve is characterized by three distinct stages, each corresponding to a change in the strain rate over time.

At the onset of creep, the applied load induces an almost instantaneous elastic deformation. This elastic strain is typically greater than what would be observed at room temperature due to the reduction in the material's Young's modulus at high temperatures. However, the elastic response is usually disregarded when analyzing creep behavior.

The first creep stage exhibits a relatively high strain rate that gradually decreases over time due to a process analogous to work hardening at lower temperatures. As deformation continues, the strain rate reaches a minimum and remains nearly constant in the second (or steady-state) stage, where a balance between work hardening and recovery effects occurs. This phase is often the longest and is critical in determining the material's long-term creep resistance. In the third stage, the strain rate rapidly increases due to microstructural instabilities, including the formation of defects such as cavities, grain

boundary separations, and cracks. These defects lead to localized stress concentrations and a reduction in the material's load-bearing capacity. As damage accumulates, fracture eventually occurs

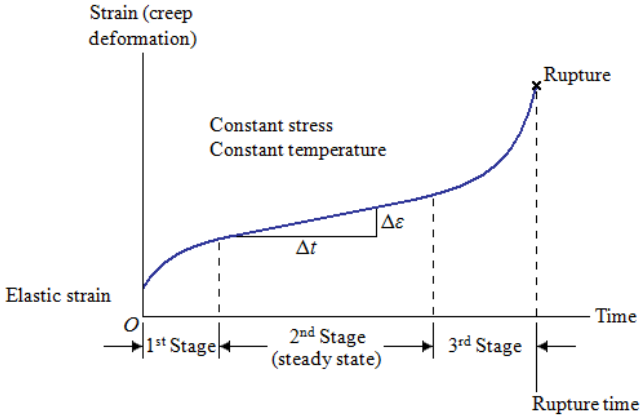

Figure 2.1: Typical creep curve showing the three stages of creep in a constant load test (adapted from [20]).

The creep strain rate is typically described using the following empirical equation [22]:

$$\dot{\varepsilon} = \frac{C\sigma^m}{d^b} e^{-\frac{Q}{kT}} \tag{2.1}$$

Where $\dot{\varepsilon}$ is the strain rate, C is a material-dependent constant related to the specific creep mechanism, σ is the applied stress, m and b are exponents associated with the creep mechanism, Q is the activation energy for creep, d is the average grain size, k is Boltzmann's constant (8.31696 $J \cdot mol^{-1} \cdot K^{-1}$) and T is the absolute temperature. This equation highlights that creep is a thermally activated process, strongly influenced by temperature and microstructural characteristics.

Creep behavior varies depending on temperature and stress conditions, leading to different underlying microstructural mechanisms. Diffusion creep is dominated by atomic diffusion processes, while dislocation creep (or power-law creep) is governed by dislocation movement. Dislocation glide occurs when dislocations move through the crystal lattice but are hindered by obstacles such as precipitates. Grain boundary sliding involves the relative motion of adjacent grains, which is particularly significant in fine-grained materials. Understanding these creep mechanisms is crucial for predicting material performance and designing high-temperature components with enhanced durability [23–26].

Diffusion creep is the dominant deformation mechanism under high-temperature and low-stress conditions. In this process, strain occurs through atomic diffusion, with grain boundaries acting as sources and sinks for vacancies [26]. When a crystal experiences tensile stress, atoms along grain boundaries perpendicular to the stress direction are pulled apart, whereas those along grain boundaries parallel to the stress direction experience compression due to the Poisson effect, bringing them closer together. This difference in atomic spacing generates a driving force for atomic diffusion from grain boundaries aligned parallel to the stress direction toward those perpendicular to it, while vacancies migrate in the opposite direction [27].

Under applied stress, the variation in atomic volume alters the activation energy required for vacancy formation by $\pm\sigma\Omega$, where Ω represents the atomic volume (positive in compressive regions and negative in tensile regions) [28]. The fractional vacancy concentration follows an exponential dependence, given by $\exp\left(\frac{Q_f \pm \sigma\Omega}{kT}\right)$ where Q_f is the vacancy formation energy. As a result, vacancy concentrations are higher in tensile regions than in compressive regions, leading to a net vacancy flux from tension to compression. This vacancy migration corresponds to atomic diffusion in the opposite direction, driving creep deformation as grains elongate in the tensile axis and contract in the compressive regime [29].

There are two primary mechanisms of diffusion creep, classified based on the role of grain size and diffusion pathway. The first is Nabarro-Herring creep, in which diffusion occurs through the bulk of the grains. This mechanism exhibits a weak dependence on stress and a moderate grain size influence, with creep exponents m = 1 and b = 2 in equation (2.1). Under low stress, Nabarro-Herring creep follows the relationship [30,31]

$$\dot{\varepsilon} = C\frac{\sigma\Omega}{d^2}\frac{D_{sd}}{kT} \tag{2.2}$$

where D_s is the self-diffusion coefficient, which is strongly temperature-dependent.

The second mechanism is Coble creep, where diffusion primarily occurs along grain boundaries. This mechanism exhibits a stronger grain size dependence, with exponents m = 1 and b = 3 in equation (2.1). It is particularly significant in fine-grained materials and follows the equation [32]:

$$\dot{\varepsilon} = C\frac{\sigma\Omega}{d^3}\frac{\delta D_{gb}}{kT} \tag{2.3}$$

where D_{gb} represents the grain boundary diffusion coefficient, and δ is the grain boundary thickness. Since grain boundary diffusion requires lower activation energy than bulk self-diffusion, Coble creep is more active at lower temperatures compared to Nabarro-Herring creep [33].

As diffusion creep progresses, grain shape evolves in response to applied stress. To maintain structural coherence and prevent void formation, deformation must be accommodated through grain boundary sliding [34]. If this mechanism is inhibited, such as during tertiary creep when strain rates increase significantly, differential grain boundary sliding can lead to micro-void formation, particularly at triple junctions between grains. These voids serve as nucleation sites for creep fracture, reducing the material's service life [35].

Dislocation creep, also known as power-law creep, dominates at high stress levels and is governed by the movement of dislocations through glide and climb mechanisms. Dislocation glide facilitates deformation, while dislocation climb, enabled by atomic diffusion, controls the overall rate of creep [36]. The activation energy for this process is associated with self-diffusion, and the creep exponents

typically range from m=4 to m=6, while the grain size dependence is negligible (b=0) [33]. Given its strong stress dependence, dislocation creep follows a power-law relationship and can be expressed as [34]:

$$\dot{\varepsilon} = C\sigma^m e^{-\frac{Q}{kT}} \tag{2.4}$$

where Q is the activation energy for self-diffusion, k is Boltzmann's constant, and T is the absolute temperature. At even higher stress levels, where the applied stress approaches the material's yield strength, dislocation glide becomes the primary mechanism, and the role of climb becomes negligible [37]. In this regime, strain rate increases sharply, leading to a transition from steady-state creep to a more rapid deformation process, which can ultimately contribute to material failure.

The last creep mechanism is grain boundary sliding, which actually occurs together with all the previously introduced mechanisms in order to prevent failure. This phenomenon occurs when grain boundaries slide past each other, allowing for deformation without significant internal stress buildup [38]. In metallic materials, grain boundary sliding helps maintain structural coherence during creep deformation by preventing grain boundary separation, which could otherwise lead to premature failure.

The Weertman-Ashby maps play a crucial role in the design of materials for high-temperature creep applications, offering a comprehensive visualization of the dominant creep mechanisms as a function of normalized stress and homologous temperature [39,40]. These maps are particularly valuable as they allow for the incorporation of grain size as a key variable, given its significant influence on the prevailing creep mechanism. By analyzing these maps, engineers can identify regions where dislocation creep, diffusional creep, or grain boundary sliding dominate under specific temperature-stress conditions and grain size distributions. Since each material has a unique Weertman-Ashby map, these diagrams provide essential guidance for optimizing material performances.

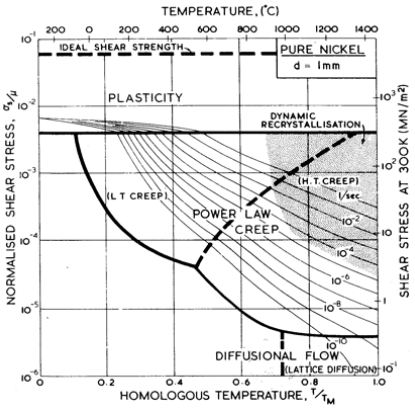

Figure 2.2: Weertman-Ashby map for nickel.

Nickel-based superalloys in single-crystal form lack grain boundaries, which enhances their mechanical properties at elevated temperatures. With a high volume fraction of γ'-strengthened

phases, these alloys exhibit exceptional creep resistance and durability under extreme conditions. As a result, they are widely utilized in the manufacturing of advanced turbine blades for gas turbine engines [41]. These alloys consist of γ and γ' phases, which undergo coarsening during prolonged high-temperature exposure and creep deformation. This process leads to the formation of a dislocation network at the γ'/γ interface [42], which helps to mitigate mismatch stress at the phase boundary [43]. Additionally, this dislocation network acts as an obstacle to dislocation movement, effectively reducing the creep rate and enhancing creep life [44]. Given these superior characteristics, this study will employ single-crystal nickel-based superalloys as the substrate material.

2.2 High temperature oxidation

High-temperature oxidation refers to the chemical reaction between a metal or alloy and oxygen at temperatures typically exceeding 500 °C [45]. This process is particularly significant in environments like turbines, reactors, and industrial furnaces, where materials are exposed to extreme conditions. The components of an alloy have varying affinities for oxygen and different diffusion rates in both the oxide and the base alloy. This can lead to deviations from simple kinetic behavior, especially when secondary elements diffuse into the oxide scale, altering its defect structure, or accumulate beneath the scale as metals or oxides. Additionally, less noble metals may undergo internal oxidation due to the diffusion of atomic oxygen into the alloy.

To better understand and predict oxidation behavior, Ellingham diagrams are commonly used. These diagrams provide a thermodynamic analysis of oxidation reactions, illustrating the change in Gibbs free energy (ΔG) associated with the formation of oxides. The Gibbs free energy change is calculated using the equation:

$$\Delta G = \Delta H - T\Delta S \tag{2.5}$$

Where ΔH is the enthalpy change, T is the temperature in Kelvin, and ΔS is the entropy change. For a reaction to be spontaneous, ΔG must be negative. If ΔG equals zero, the system is at equilibrium, and if ΔG is positive, the reaction is not thermodynamically favorable.

The change in Gibbs free energy for a generic chemical reaction of the form $aA + bB \rightarrow cC + dD$ can be expressed as:

$$\Delta G = \Delta G^0 + RT\ln\left(\frac{\alpha_C^c \alpha_D^d}{\alpha_A^a \alpha_B^b}\right) \tag{2.6}$$

Where ΔG^0 is the standard Gibbs free energy change, R is the gas constant, T is the temperature, and α represents the activity of each species. For oxidation reactions, where a metal (M) reacts with oxygen (O_2) to form a metal oxide (M_xO_γ), the change in Gibbs free energy simplifies to:

$$\Delta G = \Delta G^0 + RT\ln(p_{O_2}) \tag{2.7}$$

Where pO_2 is the partial pressure of oxygen. At equilibrium, ΔG equals zero, and this equation helps predict the stability of metal oxides under various oxygen partial pressures.

Ellingham diagrams graphically represent this relationship, showing how ΔG changes with temperature, allowing for the prediction of which reactions are more likely to occur [46]. Figure 2.3 presents an example of such a diagram.

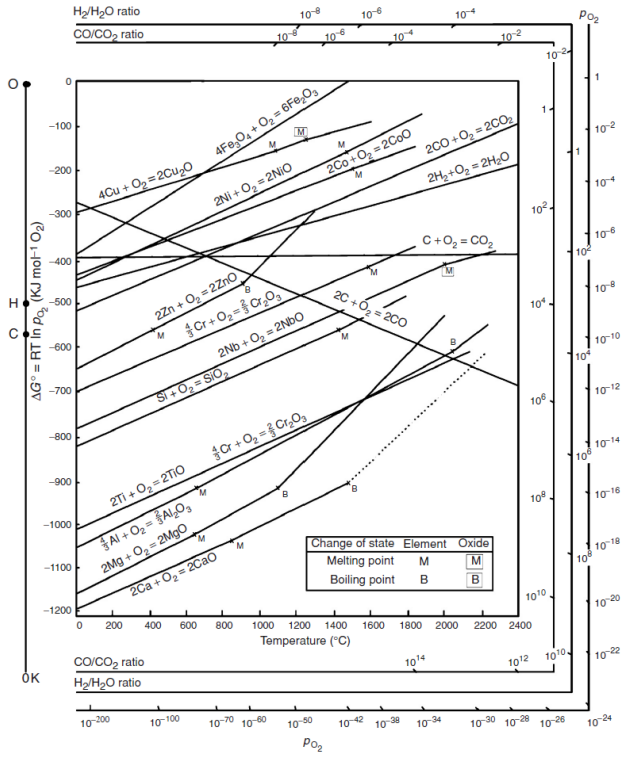

Figure 2.3: Ellingham diagram for the formation of oxides.

When an alloy oxidizes, the oxides of its components may either form a single-phase oxide solid solution, or they may be immiscible, leading to a multiphase oxide scale. The oxidation behavior of binary alloys typically depends on the composition. In alloys with a high concentration of one element (A), oxidation primarily produces the oxide of that element (AO), which dominates the external oxide scale. In alloys with higher concentrations of a less noble element (B), the oxide BO predominates. In intermediate compositions, both AO and BO oxides can form, resulting in a more complex oxidation behavior with the coexistence of both phases.

In some cases, the dominant oxide phase may dissolve small amounts of the other metal, modifying the oxide's defect structure and affecting the oxide growth rate. This is particularly noticeable in alloys where both components are oxidized. The reactions can be classified into two categories: Class I, where only one component is predominantly oxidized, and Class II, where both components are oxidized, forming more complex oxide structures.

In Class I, if the minor element (B) oxidizes, it may occur internally, forming BO particles within the more noble metal A, or externally, forming a BO oxide layer on the surface while depleting the

underlying alloy of B. If the major element (B) oxidizes, the oxidation can result in the formation of a dispersed metal A phase within the BO oxide scale, or an enrichment of metal A beneath the oxide layer, as seen in Ni-Pt or Fe-Cr alloys, where Cr remains enriched below the oxide scale.

This analysis is crucial for understanding the stability and growth of oxide scales on alloys exposed to high-temperature environments and provides valuable insight into the material's performance in these extreme conditions.

In Class II oxidation, when both elements of an alloy oxidize, several outcomes can occur. One possibility is the formation of compound oxides. In this case, the oxides AO and BO may react to create a solid solution in the form of internal (A, B)O regions that are richer in B compared to the surface oxide layer. Alternatively, a double oxide structure may form, typically with a spinel structure, either as a complete surface layer with varying composition or as discrete particles dispersed within an AO matrix.

Another outcome is the insolubility of the oxides. If the less noble metal (B) is present in a smaller proportion, BO may form internally beneath a mixed surface layer of AO and BO. However, when the less noble metal is more dominant, internal oxidation may be suppressed, and the AO oxide will predominantly form the outer scale. Over time, internal oxide particles may merge, eventually creating a continuous BO layer at the base of the oxide scale.

These oxidation behaviors depend on the relative concentrations of the alloy components and the environmental conditions, which influence the stability and structure of the oxide scale.

2.2.1 Kinetics of oxide scale growth

To assess the growth and stability of oxide scales, cyclic or isothermal tests are commonly used, where the material’s mass change is monitored over time. Thermogravimetric analysis (TGA) is a widely employed technique that records in situ mass changes during isothermal exposure, providing valuable insights into oxide growth kinetics. However, discontinuities in TGA curves introduce complexities in determining growth behavior. For example, oxidation of pure chromium, reported in Figure 2.4, often exhibits sudden mass gains, known as mass gain discontinuities, resulting from localized oxide scale failures due to the release of growth stresses [47].

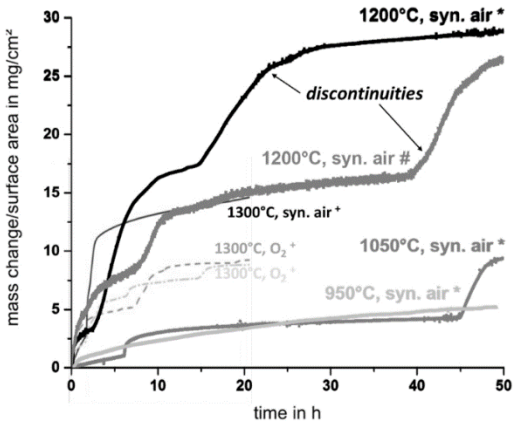

Figure 2.4: Oxidation curves of pure chromium highlighting mass gain discontinuities originating from localized oxide scale failure [47].

The kinetics of oxide scale formation can be described by a four-stage model. Initially, oxygen is absorbed at the metal surface, leading to the formation of the first oxide layer. The efficiency of this process depends on factors such as surface area, temperature, and oxygen partial pressure. As oxidation continues, small clusters of oxide, or nuclei, form, serving as the foundation for further growth. Lateral growth then occurs as these nuclei expand and merge, increasing the overall oxide coverage. Finally, the oxide scale continues to thicken, forming a compact and protective layer whose growth follows different kinetic laws based on environmental conditions [48,49].

Three primary kinetic models describe the relationship between oxide layer thickness and time: linear, logarithmic, and parabolic (Figure 2.5) [50].

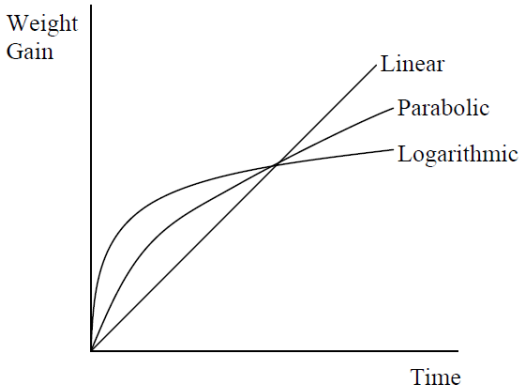

Figure 2.5: Common kinetic laws for the rate of growth of an oxide layer [50].

In linear growth kinetics, the oxide thickness increases at a constant rate, represented by the equation:

$$d = k_L t \tag{2.8}$$

where d is the oxide thickness, k_L is the linear rate constant, and t is time. This behavior is typically observed when the diffusion of metal ions or oxygen remains steady and unimpeded.

Logarithmic growth kinetics describe cases where the oxide layer initially grows quickly but slows down over time as it becomes more protective. This process follows the equation:

$$d = k_{log} \log(t + t_0) + A \quad (2.9)$$

where k_{log} and A are constants at constant temperature. In this regime, the oxide layer initially grows quickly but the rate of growth slows as time progresses. Logarithmic growth is often associated with initial rapid oxidation, followed by a stabilization phase where the growth rate reduces. This behavior can be due to changes in the oxide's structure or changes in the diffusion rates of ions as the oxide becomes more protective over time.

Parabolic growth kinetics occur when the oxidation rate decreases as the oxide thickens, characteristic of metals forming dense, protective oxide films that limit further oxidation. This behavior follows the equation:

$$d^2 = 2k_P t \quad (2.10)$$

where k_p is the parabolic rate constant. This kinetic model is typical for metals that develop stable oxide layers, preventing continued oxidation. The driving force to the transport of matter through the scale is diffusion.

Despite the protective nature of oxide scales, they may fail due to mechanical and thermal stresses. Detachment can occur when gaps form between the oxide layer and metal substrate due to differences in thermal expansion. Internal or external stresses may lead to cracking, allowing corrosive agents to penetrate and accelerate degradation. In some cases, excessive scale thickness or accumulated stress results in spallation, where large portions of the oxide layer break away. Even after cracking or spallation, oxidation may persist within damaged areas, producing more complex oxide structures with reduced protective properties. If large-scale spallation exposes fresh metal surfaces, renewed oxidation may initiate another growth cycle. Understanding these mechanisms is crucial for designing oxidation-resistant materials with long-term stability in extreme environments.

2.2.2 Cabrera-Mott's theory

The growth of oxide films is primarily governed by the movement of ions and electrons, driven by concentration gradients and an electric potential. One of the most widely recognized models describing this process is the Cabrera-Mott model [51]. According to this model, oxygen adsorption on the oxide surface leads to the formation of surface states situated above the oxide valence band and below the metal Fermi level. Electrons tunnel from the metal to these vacant surface states, generating charges at the oxide interfaces and shifting the energy of these states up to the Fermi level. This mechanism establishes a uniform electric field within the oxide film, which is mathematically expressed as:

$$\varepsilon = \frac{V}{L} \quad (2.11)$$

where L represents the oxide film thickness and $V$is the voltage across the film.

The oxide layer's growth is constrained by the activated jumps of metal ions at defect sites along the metal-oxide interface. The rate of oxide film growth is given by:

$$\frac{dL}{dt} = aPk_0 \exp\left(\frac{qb_0V}{k_bTL}\right) \tag{2.12}$$

where a is the distance between adjacent metal layers, and P is the fraction of metal atoms occupying defect sites. For practical applications, this equation is often simplified to:

$$\frac{dL}{dt} = u \exp\left(\frac{A}{L}\right) \tag{2.13}$$

This formulation provides a more convenient approach to modeling oxide growth, particularly in cases where experimental validation is required.

2.2.3 Wagner's diffusion theory

Wagner's diffusion theory provides a fundamental model for understanding the oxidation of metals, particularly for thicker oxide layers where diffusion under a concentration gradient is the primary transport mechanism [52]. This theory operates under key assumptions: the oxide layer is compact and perfectly adherent, and the rate-controlling step is the migration of ions or electrons across the scale. The flux of species (J) through the oxide layer follows Fick's first law for steady-state diffusion:

$$J = D\frac{\partial C}{\partial x} \tag{2.14}$$

where D is the diffusion coefficient, and $\partial C/\partial x$ represents the concentration gradient of the diffusing species across the oxide thickness. Given that thermodynamic equilibrium exists at each interface, the concentration difference between the oxide-gas interface and the oxide-metal interface (ΔC) remains constant. This allows the flux equation to be rewritten as:

$$J = \frac{1}{V_{ox}}\frac{dx}{dt} = D\frac{\Delta C}{x} \tag{2.15}$$

where V_{ox} is the molar volume of the oxide. By consolidating the constant quantities into the parabolic rate constant (k_p), the oxidation rate equation simplifies to:

$$\frac{dx}{dt} = k_P\frac{1}{x} \tag{2.16}$$

Integration of this equation leads to the well-known parabolic growth law, describing how oxide thickness increases over time.

While Wagner's model effectively describes oxidation in pure metals, alloy oxidation introduces greater complexity due to variations in the oxygen affinities of different alloying elements. This difference is reflected in the varying free energies of oxide formation, as depicted in the Ellingham

diagram. The oxidation of multi-phase alloys can result in the formation of ternary and higher-order oxides, altering solubility, diffusivity, and ion mobility within the oxide scale. Additionally, competitive oxidation between alloying elements influences the composition and growth kinetics of the oxide layer.

Despite these complexities, alloy oxidation behavior can be manipulated to enhance oxidation resistance. The formation of a protective passivation layer by certain alloying elements, such as chromium or aluminum, can significantly improve oxidation resistance. Furthermore, the introduction of intermediate compounds can reduce the free energy of oxide formation, stabilizing the protective oxide scale and further slowing oxidation rates. Understanding these principles allows for the strategic design of oxidation-resistant alloys for high-temperature applications.

2.2.4 Monceau's theory

Monceau's theory of oxidation enhances the accuracy of thermogravimetric data analysis by fitting weight gain measurements to a parabolic curve, ensuring a more reliable determination of oxidation kinetics [53]. By applying this approach over short time intervals and extending it throughout the test duration, an instantaneous parabolic rate constant can be obtained, minimizing the influence of transient phases. Oxidation kinetics are generally parabolic, as they are governed by the diffusion of reactive species through the oxide layer or the base metal. However, deviations from ideal parabolic behavior can arise due to factors such as varying diffusion coefficients, heating modes, and surface preparation. In alloy oxidation, a transient period typically precedes the establishment of steady-state oxide growth. According to the Pilling-Bedworth model, oxidation kinetics follow the equation:

$$\Delta m^2 = 2k_p \cdot t \tag{2.17}$$

where Δm represents the weight gain per unit area, and k_p is the parabolic rate constant. Wagner's theory further clarifies that parabolic oxidation kinetics are primarily governed by lattice or volumetric diffusion, meaning k_p is directly related to the self-diffusion coefficients of cations or anions within the oxide scale.

A key challenge arises when integrating the above equation, as the initial condition Δm=0 at t=0 leads to:

$$\frac{dm}{dt} = k_p \cdot \frac{1}{2\Delta m} \tag{2.18}$$

However, this assumption is unrealistic because oxidation may begin during the heating phase before the target temperature is reached, leading to systematic errors. A more accurate approach considers

that oxidation starts at an earlier time t_i with an initial weight change Δm_i. Consequently, the equation is modified to:

$$\frac{dm}{dt} = k_p \cdot \frac{1}{2(\Delta m - \Delta m_i)} \tag{2.19}$$

where Δm_i accounts for the pre-existing oxide layer, which is often more protective than the newly formed scale.

Beyond diffusion, surface reaction rates also play a role in oxidation kinetics. Therefore, oxidation models must incorporate two rate equations, one for diffusion and another for surface reactions, each with distinct rate constants. These equations allow for a more comprehensive analysis, particularly when transient oxidation phases affect the overall kinetics.

Weight gain data over time can be fitted to a parabolic equation:

$$t = A + B\Delta m + C\Delta m^2 \tag{2.20}$$

where the quadratic coefficient C corresponds to the inverse of the true parabolic rate constant (k_p). This ensures an accurate determination of k_p, independent of the oxidation mechanism or transient phases. The coefficients B and A provide additional insight into linear oxidation kinetics (k_l) and transient phase characteristics.

The data fitting procedure can be applied to the entire test duration or to selected time intervals, allowing for real-time observation of kinetic variations. Over short periods, the least squares method is used to fit weight gain data to the parabolic model, and this process is repeated at regular intervals to track changes over time.

2.3 Other degradation phenomena

Other degradation phenomena like hot corrosion, erosion and foreign object damage are very common in gas turbine system environment. For completeness, these will be briefly described in the following paragraphs even though they will not be directly discussed within the thesis work.

2.3.1 Hot corrosion

In many high-temperature applications of metals and alloys, the operating environment can be significantly more corrosive than exposure to oxygen in air alone. Atmospheric or surface contamination can accelerate material degradation, sometimes leading to catastrophic failure.

Gas turbines operate in particularly harsh conditions where combustion products from fossil fuels can cause severe oxidation and corrosion. A particularly aggressive form of attack, known as hot corrosion, occurs when a salt deposit, typically sodium sulfate, forms on the metal or oxide surface.

When contaminants such as sulfates, chlorides, or vanadates are present in the environment, they become incorporated into the sodium sulfate matrix at temperatures between 700 °C and 900 °C, forming a thin film of molten salt. This film disrupts the protective oxide scale on the metal surface, preventing its regeneration. As a result, a porous and non-protective oxide layer develops, allowing aggressive species to penetrate the base metal, leading to accelerated material degradation [54].

In gas turbines, sulfur from fuel reacts with alkali metal chlorides, vanadium, or lead (introduced from ingested air) at high temperatures to form sulfates. These sulfates then deposit on critical hot-section components, such as first-stage turbine blades and nozzle guide vanes, intensifying corrosion. Experimental studies have identified several corrosion mechanisms, influenced by factors such as the amount of salt present, temperature, gas composition, and the base material properties. It has also been observed that cyclic thermal exposure reduces the time required for hot corrosion to initiate, further increasing the damage [54].

Hot corrosion occurs under two primary conditions [55,56]:

- High-Temperature Hot Corrosion (HTHC) or Type I – When the salt deposit is in a molten state from the beginning, meaning corrosion occurs above the melting point of the salts;
- Low-Temperature Hot Corrosion (LTHC) or Type II – When a solid deposit transforms into liquid during exposure, even if the temperature is below the salt's melting point (due to eutectic formation).

As shown in Figure 2.6, Type I hot corrosion occurs within the 815–980 °C range, while Type II hot corrosion occurs between 560–815 °C. At even higher temperatures, oxidation becomes the predominant degradation mechanism.

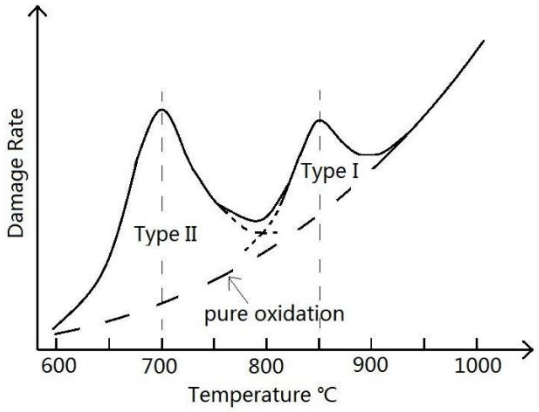

Figure 2.6: Hot corrosion diagram [57].

High-Temperature Hot Corrosion (HTHC, Type I) begins with the condensation of molten alkali metal salts on the surface of components. This initiates a cycle of chemical reactions that first degrade the protective oxide layer and subsequently deplete the substrate of its reactive elements, such as chromium or aluminum. As these elements are consumed, the material loses its ability to form a

protective scale, accelerating oxidation and leading to the development of a porous, non-protective oxide layer. One of the primary contributors to HTHC is sodium sulfate (Na_2SO_4), which readily forms during combustion in the presence of even trace amounts of sulfur. Na_2SO_4 is thermodynamically stable in hot corrosion environments, making it a key facilitator of attack. It can also react with other impurities found in fuel or the atmosphere (such as chlorides, vanadium, lead, and magnesium sulfate) to form eutectic mixtures. These mixtures lower the melting point of the deposit, expand the affected area, and further accelerate corrosion rates. As oxidation progresses deeper into the substrate, the mechanical integrity of the component is compromised due to the loss of structural material. If unchecked, the damage becomes catastrophic, inevitably leading to component failure. Macroscopically, HTHC is often identified by severe metal peeling and distinctive color changes. For instance, Figure 2.3.2 (a) depicts a first-stage turbine blade exhibiting a greenish discoloration on both the pressure and suction sides, resulting from the formation of nickel oxide (NiO) in the highly corroded regions. Microscopically, Type I hot corrosion is characterized by a sulfidation and depletion zone beneath the porous, non-protective scale [58]. The reaction products often contain oxide precipitates dispersed within the salt film, further indicating the severity of the degradation process.

Low-Temperature Hot Corrosion (LTHC, or Type II) typically occurs below the melting point of sodium sulfate (Na_2SO_4), meaning the deposit remains solid under normal conditions. However, liquid phases can still form due to the reaction of base metal sulfates (e.g., $NiSO_4$, $CoSO_4$, and $MgSO_4$) with alkali metal sulfates, creating low-melting eutectic mixtures. These eutectics significantly lower the melting point of the deposit, leading to localized hot corrosion even at moderate temperatures. The formation of base metal sulfates requires a sufficiently high SO_3 partial pressure, which increases with temperature. However, as the temperature continues to rise and enters the HTHC range, the conditions for Type II corrosion become less favorable, and the attack diminishes. In addition to metal sulfates, Na_2SO_4 also readily forms low-melting eutectics with vanadium pentoxide (V_2O_5), a common combustion byproduct in gas turbines. Vanadium, frequently present as an impurity in fuels, reacts with oxygen during combustion, forming V_2O_5, which further contributes to the accelerated degradation of turbine components [54].

Unlike HTHC (Type I), which typically results in widespread degradation, Type II hot corrosion is highly localized, manifesting as pitting corrosion in specific areas where the necessary compositional conditions exist. Additionally, microscopic sulfide formation and chromium depletion, characteristic of HTHC, are not typically observed in LTHC [59].

Hot corrosion generally progresses through two distinct stages: the initiation stage and the propagation stage [60].

The initiation stage is the early phase of hot corrosion, during which the mechanical integrity of the component remains largely unaffected. During this stage, the salt deposit reacts with reducing agents, such as incomplete combustion products (R_1) or metals (M) within the alloy (R_2), in oxidation reactions that lower the local oxygen partial pressure and release sulfur, which can subsequently contribute to the formation of sulfides:

$$NaSO_4 + R_1 \rightarrow Na_2O + 3CO + S \quad (2.21)$$

$$NaSO_4 + R_2 \rightarrow Na_2O + 3MO + S \quad (2.22)$$

The reaction products initially act as a temporary protective barrier, shielding the alloy from direct exposure to the corrosive salt deposit as long as they remain stable. However, simultaneous degradation mechanisms are also at play, including: (i) depletion of protective elements (e.g., chromium or aluminum) from the alloy; (ii) incorporation of sulfur and other contaminants into the substrate; (iii) dissolution of oxides into the salt layer; (iv) formation of cracks and channels in the oxide scale. These processes gradually destabilize the protective barrier, eventually transitioning the system into the propagation stage, where corrosion accelerates.

In the propagation stage, sulfides begin to form at the substrate-deposit interface and undergo further oxidation:

$$Na_2SO_4 + MS \rightarrow MO + Na_2O + 2S \quad (2.23)$$

Since sulfur is a strong oxidizing agent, its continuous oxidation generates more free sulfur, which further reacts to form additional sulfides, creating a self-sustaining (autocatalytic) reaction.

However, reaction (2.23) is not the only possible pathway. In some cases, the sulfate deposit may not react directly with the alloy surface but instead interact with pre-existing native oxide scales, further complicating the corrosion process.

Hot corrosion is a highly complex process influenced by multiple factors. As the initiation stage ends, the liquid deposit begins to penetrate the protective oxide scale, reaching areas with low oxygen activity and an alloy substrate depleted of its protective elements. At this point, the corrosion rate increases significantly, often to a level where continued operation is no longer viable, making it necessary to remove the component from service to prevent catastrophic failure.

2.3.2 Erosion and erosion-corrosion at high temperature

In many industrial applications, metallic components are exposed to high-temperature gas streams that often contain solid particles. Completely eliminating these particles is nearly impossible in real-world systems. Examples such as gas turbines, oil refining units, reformers, and power plants commonly involve gas flows with entrained solids [61].

At room temperature, ductile metals erode through plastic deformation, cutting, plowing, and fatigue. Some of these mechanisms, like cutting, can result from a single particle impact, while others, such as fatigue, require repeated impacts. Brittle materials, by contrast, erode through the formation and propagation of interconnected cracks. At elevated temperatures, most metals remain ductile, while the oxide scales they develop may be ductile (e.g., wüstite, nickel oxide) or brittle (e.g., alumina, chromia). Depending on the oxide's properties and the conditions, the scale may deform plastically or fracture and spall under particle impact [62].

The erosion behavior of ductile and brittle materials also differs with respect to the impact angle of incoming particles. Brittle materials exhibit maximum erosion rates at normal incidence (90°), as shown in Figure 2.7(a). Ductile materials, on the other hand, experience peak erosion at oblique angles (25–30°), with reduced erosion at higher angles (Figure 2.7(b)). This behavior is attributed to work hardening and material removal mechanisms like fatigue at normal impact, and plowing at low angles. Notably, even brittle materials may exhibit ductility under specific conditions, such as impact by very fine particles; this can be relevant for high-temperature oxides that sometimes display ductile characteristics during erosion.

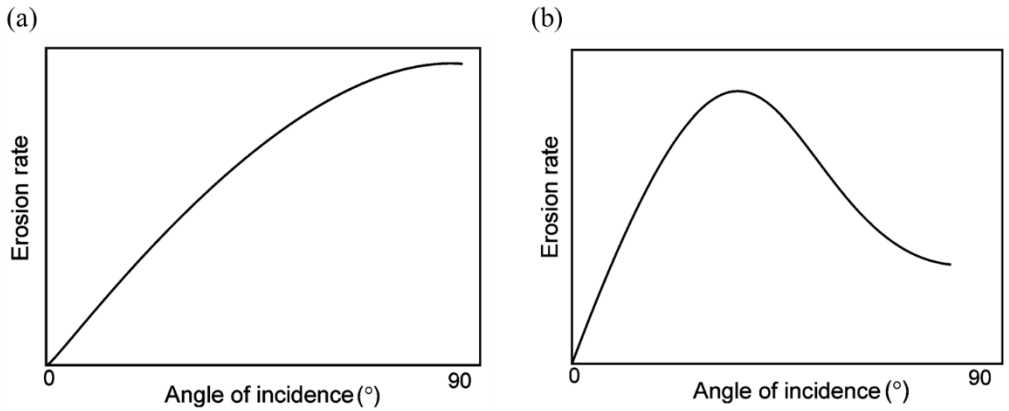

Figure 2.7: Schematic representation of the erosion rate as a function of the angle of incident for ductile (a) and brittle (b) materials [61].

While erosion alone can reduce the lifespan of components, the combined effects of erosion and oxidation in oxidizing atmospheres are significantly more damaging due to their strong synergistic interaction.

In the case of pure metals, hot erosion–corrosion can be seen as the interplay of two opposing processes: oxidation, which forms a protective surface film that slows further reaction, and erosion, which strips away this film and the underlying material. When both occur simultaneously, erosion hinders or prevents the buildup of a protective oxide, allowing oxidation to proceed rapidly. As erosion continues to remove the oxide film, oxidation accelerates, leading to a self-sustaining cycle of rapid degradation. The severity of this process depends on the oxide type and growth rate: faster-

growing scales require more intense erosion to be fully removed. If oxidation is suppressed (for example, by testing in an inert atmosphere or at room temperature) the degradation rate drops sharply. The interaction between erosion and oxidation is typically categorized into two regimes:

- Regime 1: Erosion-enhanced oxidation: in this regime, erosion is relatively mild and only thins the oxide layer without reaching the metal substrate. This occurs when oxide growth is fast enough to replace the eroded scale. The surface remains mostly flat with features from particle cutting. A steady-state scale thickness may be reached when the growth and removal rates balance. The thinner scale enhances oxidation by offering less resistance to diffusion.

- Regime 2: Dominant erosion: erosion is more aggressive, and oxide growth is relatively slow. The protective scale is continuously removed, and particle impacts deform the metal substrate, creating ripples, valleys, and peaks depending on the impact angle. This regime exposes the substrate to continuous oxidation and mechanical damage. For a given material, increasing erosion intensity or switching to a slower-scaling metal can shift the system from Regime 1 to Regime 2.

The temperature dependence of erosion–corrosion typically follows a bell-shaped curve, as shown in Figure 2.8. At low temperatures, oxidation is sluggish, and degradation is erosion-dominated. As temperature rises, oxidation becomes more significant, increasing the overall degradation rate. The peak occurs when oxide growth becomes fast enough that erosion can no longer completely remove the scale, marking the transition from Regime 2 to Regime 1. At higher temperatures, the oxide scale thickens, and both the metal and oxide may become more ductile, absorbing more impact energy through deformation. This reduces material loss from erosion and increases weight gain from oxidation, causing the degradation rate to decline. Additionally, increasing erosive intensity shifts the bell curve to higher temperatures and can push the system back into Regime 2 at temperatures where it would otherwise remain in Regime 1.

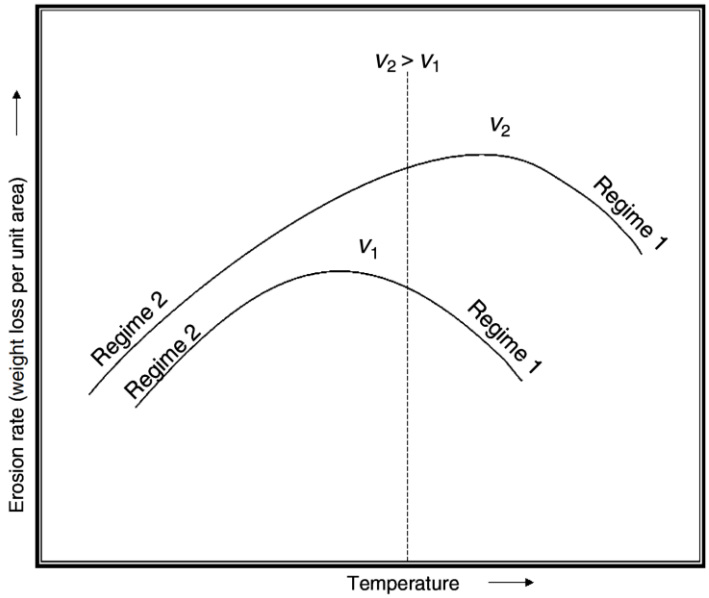

Figure 2.8: Temperature dependence of erosion-corrosion for different erosion intensities (v) [61].

Erosion–corrosion of alloys is generally similar to that of pure metals but presents additional complexities: (i) multiple oxides may form; (ii) initially formed oxides might be removed, leading to the formation of different oxides; (iii) concentration gradients can develop within the alloy; (iv) alloys are typically stronger than pure metals, potentially leading to smaller deformation zones and less energy absorption.

In summary, erosion–corrosion at high temperatures is a complex, synergistic phenomenon driven by the interaction between mechanical and chemical degradation. Understanding how factors like temperature, impact angle, oxide properties, and erosion intensity influence this process is critical for predicting material performance and designing components that can withstand harsh, particle-laden, high-temperature environments.

3. Protective coatings – Thermal Barrier Coatings (TBCs)

The ongoing pursuit of higher performance in gas turbine engines has driven the evolution of systems capable of operating under increasingly extreme conditions. Enhancing overall efficiency is often directly associated with raising the turbine inlet temperature. As a result, there is a critical need for materials that can endure prolonged exposure to severe thermomechanical and dynamic stresses in highly oxidizing and corrosive environments [63,64].

The development of advanced single crystal superalloys has significantly improved the mechanical performance of first-stage turbine blades [11]. However, meeting the extreme demands of high-temperature gas turbine environments requires more than the inherent properties of a single structural material. Since the late 1980s, extensive research has highlighted the necessity of applying protective surface coatings to base superalloys to guarantee resistance against degradation mechanisms such as oxidation, hot corrosion, and erosion [65,66].

One of the most effective and widely employed solutions is the use of Thermal Barrier Coatings (TBCs), which are multi-layer systems designed to thermally insulate and protect the underlying substrate. When combined with modern cooling technologies, TBCs enable operating temperatures that exceed the melting point of the superalloy by 150–300 °C [67]. TBCs are nowadays one of most employed systems to protect turbine blades for both aviation and land-based gas turbine engines [68,69].

TBC systems are primarily composed of two key layers: a ceramic top coat with low thermal conductivity, which reduces the temperature experienced by the metallic underlying layers improving their durability, and a metallic bond coat enriched with aluminum [70].

The top coat in a typical TBC system is commonly composed of yttria-partially stabilized zirconia (Y-PSZ or YSZ). This material is very popular due to its combination of desirable properties, including low thermal conductivity, high chemical stability, a relatively high coefficient of thermal expansion (CTE), and excellent resistance to thermal cycling. Its superior fracture toughness also contributes to its ability to withstand thermal shock conditions [71,72]. The application of the YSZ top coat is generally performed using electron beam physical vapor deposition (EB-PVD), air plasma spraying (APS) or suspension plasma spray (SPS), each offering distinct microstructural characteristics and performance advantages.

The bond coat is applied between the substrate and the ceramic top coat to protect the superalloy substrate from oxidation and corrosion. Bond coats are generally classified into two main categories: diffusion aluminides and MCrAlY overlays, where "M" represents nickel, cobalt, or a combination of both. Diffusion aluminide coatings are typically produced by exposing the nickel-based superalloy

to an aluminum-rich source, either in solid or gaseous form, at elevated temperatures. This can be achieved through methods such as pack cementation or slurry aluminizing. During the process, aluminum atoms diffuse into the surface of the substrate and form an intermetallic layer primarily composed of the β-NiAl phase, which offers effective resistance to oxidation and corrosion [73].

In contrast, MCrAlY coatings are generated using pre-alloyed powders containing approximately 18–22% chromium, 8–12% aluminum, and a small addition of yttrium (typically 0.2–0.5%). These powders are applied to the substrate through thermal spray techniques, such as plasma spraying or high-velocity oxygen fuel (HVOF) spraying [74,75]. MCrAlY coatings consist of a β-NiAl phase in a γ-Ni matrix and are enriched with additional elements to provide superior oxidation and corrosion resistance while maintaining good mechanical properties [76]. Despite their different application methods and microstructures, both types of coatings are rich in aluminum. This high aluminum content enables the formation of a stable and slow-growing α-alumina (α-Al_2O_3) scale, often referred to as the thermally grown oxide (TGO), which serves as a diffusion barrier against further oxidative degradation. Under mildly severe conditions, bond coats can also be applied alone without the necessity of the ceramic top coat. While overlay coatings offer enhanced resistance to oxidation due to their compositional flexibility, the chemistry of diffusion-based aluminide coatings is governed by thermodynamic constraints, making their properties less tunable. Moreover, surface roughness of thermally sprayed overlays can be adjusted to guarantee optimal adhesion to the ceramic top coat, whether its manufacturing technique, while aluminides, characterized by a relatively flat morphology, are applied preferentially under EB-PVD top coats [77]. Nonetheless, aluminide coatings are the most widely adopted in industrial settings due to their relatively low cost and straightforward application through pack cementation or slurry aluminizing processes.

3.1 Aluminide diffusion coatings

Aluminide coatings are extensively employed as bond coats in both the energy production and aerospace sectors, to protect nickel-based superalloy components operating in the high-temperature sections of gas turbine engines. These coatings provide effective protection against oxidation and hot corrosion. At elevated temperatures, β-NiAl-based aluminide coatings promote the selective oxidation of aluminum, resulting in the formation of a dense, adherent layer of α-alumina (α-Al_2O_3). This protective oxide scale acts as a barrier to diffusion, significantly reducing further oxidation of the underlying material.

NiAl-based aluminide coatings can be produced through a variety of techniques, including chemical vapor deposition (CVD), pack cementation, hot dipping, and slurry aluminizing [78]. In both CVD

and pack cementation methods, aluminum is transported in gaseous form from a metallic source, and the coating forms through solid-state diffusion processes [79]. Depending on the aluminum activity during deposition, these coatings are typically classified into two categories according to the process temperature and chemical activity of the species involved in the process. High-activity processes promote inward diffusion of aluminum, which initially leads to the formation of brittle, aluminum-rich intermetallics; the obtainment of the desired β-NiAl phase is then achieved through subsequent high-temperature annealing. Conversely, low-activity processes facilitate outward diffusion of nickel from the substrate, allowing for the direct formation of a near-stoichiometric NiAl phase during the coating process itself [80].

3.1.1 Microstructure of coatings

As previously mentioned, a classification for diffusion aluminide coatings on nickel-based superalloys, based on the predominant diffusion mechanism involved in their growth, was proposed by Goward and Boone [80]. in their foundational study. Indeed, the specific mechanism of coating growth activated during the manufacturing process is primarily influenced by the chemical activity of the aluminum source.

High-activity aluminide coatings are typically formed using a powder pack that contains pure aluminum, which exhibits unit thermodynamic activity. The process is conducted at relatively low temperatures, generally ranging from 700 °C to 900 °C [81]. In this setting, aluminum atoms diffuse inward toward the substrate, leading to the formation of an aluminum-rich Ni_2Al_3 matrix. The coating also contains dispersed precipitates of alloying elements, such as Ti, Co, Cr, Mo, Hf, W, and Nb, that have diffused out from the superalloy substrate. In deeper regions of the coating, β-NiAl phases may also form. Following this, an interdiffusion heat treatment at higher temperatures (1000–1100 °C) is typically applied. This treatment facilitates the outward diffusion of nickel and further inward diffusion of aluminum, thereby transforming the Ni_2Al_3 phase into a hyperstoichiometric, aluminum-rich β-NiAl. This process also induces the formation of an interdiffusion zone (IDZ), characterized by precipitates formed from the interaction of diffusing elements that cannot be fully incorporated into the NiAl matrix. The typical microstructure of an inward grown aluminide, as documented in [80], is presented in Figure 3.1.

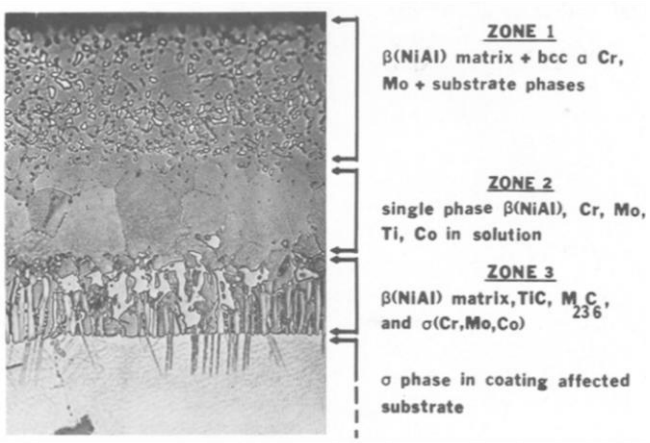

Figure 3.1: Typical microstructure of an inward grown diffusion aluminide after aluminizing and annealing at 1080 °C for 4h, presented in [80].

In contrast, the low-activity aluminizing process utilizes an aluminum sources of reduced chemical potential, typically binary Al-based alloys (e.g. alloying Al with Cr [82–84], Fe [85] or Ni [80]. Due to the lower vapor pressure of aluminum halides generated in this system, higher processing temperatures (usually between 1000 °C and 1150 °C) are required to sustain effective coating formation. In this process, nickel from the substrate is the dominant diffusing species. As it diffuses outward and reacts with aluminum at the surface, a coating layer composed of hypostoichiometric (nickel-rich) β-NiAl forms. Alloying elements also migrate outward during the process and may either remain in solid solution or precipitate within the β-NiAl matrix. The depletion of nickel just below the surface gives rise to an IDZ, like in high activity process, although formed through different kinetics and elemental pathways. Although inward diffusion of aluminum also occurs during HTLA processing, its contribution is significantly less than that of nickel. The disparity in fluxes of Ni and Al generates an imbalance in vacancy movement, which may lead to the formation of Kirkendall voids. While such voids could potentially impair coating adhesion, they are typically minimized in Ni-based superalloys due to interface-based vacancy annihilation mechanisms [81]. The typical microstructure of an outward grown aluminide, prepared by [80] through a low activity process, is shown in Figure 3.2.

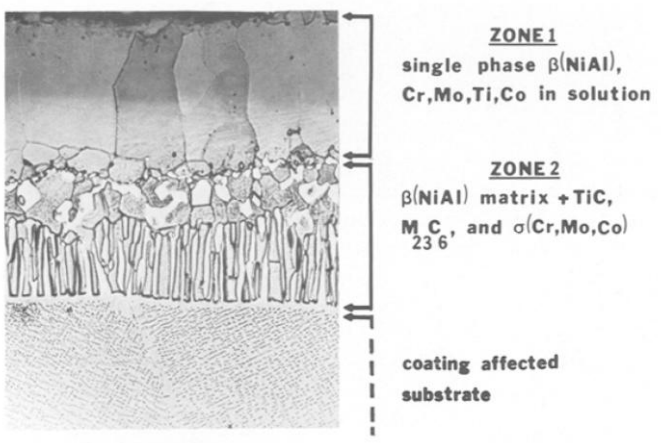

Figure 3.2: Typical microstructure of an outward grown diffusion aluminide, presented in [80].

3.1.2 Deposition techniques – Pack Cementation

Pack cementation is a widely adopted technique for applying aluminide coatings to nickel-based superalloy components, especially in the energy and aerospace sectors. It can be considered as a CVD process carried out in a reactor with the aid of a powder mixture (pack), in or near which the substrate is immersed or suspended. The pack contains a source of the element to be deposited, a halide salt that works as activator (e.g, AlF_3, NaF, NH_4F, $AlCl_3$, NaCl, NH_4Cl.), used to facilitate the diffusion of aluminum or other reactive elements onto the surface of the substrate, and an inert filler powder (such as Al_2O_3, SiO_2 or SiC) [86].

Typically, the substrate is embedded in the powder mixture inside a sealed ceramic crucible, commonly alumina. The assembly is then heated in a furnace (800–1100 °C) under an inert gas flow, such as argon, to prevent unwanted oxidation [87].

There are two principal variants of this technique: standard pack cementation and above-the-pack (or out-of-pack) cementation [88]. In the conventional approach, the component is fully buried in the reactive powder mixture. During heat treatment, the halide salts react with the aluminum source to form volatile aluminum halides, which diffuse through the inert medium to the substrate surface. These vapors decompose or react at the substrate interface, depositing aluminum. In contrast, above-the-pack cementation involves suspending the substrate above the powder bed, relying on the vapor-phase diffusion of the aluminum halides to reach the surface without direct contact with the mixture. In the latter, purity of the coating is controlled by diffusion of the reaction products outside the reactor, and the risks of embedding particles inside the coating is avoided. Above the pack process is, therefore, cleaner and more homogeneous. Both configurations are illustrated in Figure 3.3.

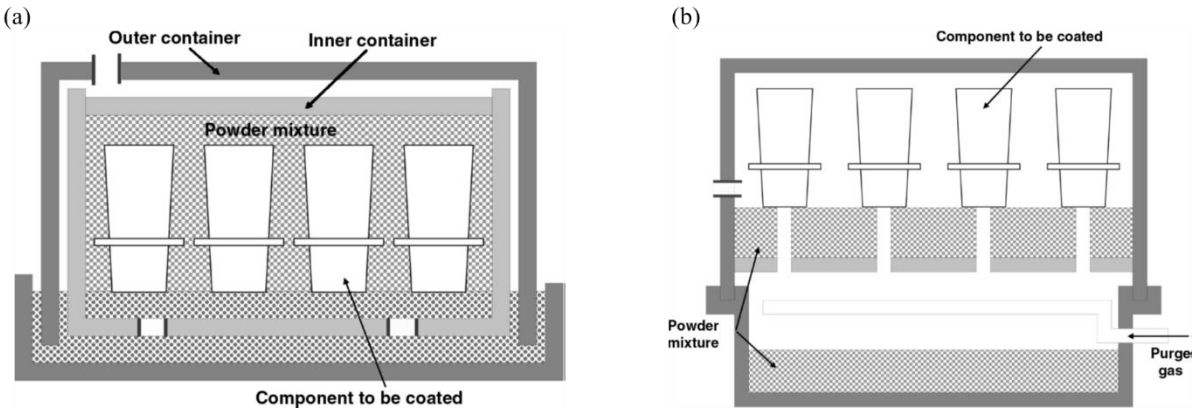

Figure 3.3: Schematic representation of the apparatus used for pack cementation. Conventional (a) and above the pack (b) configurations [87].

Standard pack formulations often consist of 2–3% activator, about 25% aluminum source, with the balance being the inert constituent. The filler helps maintain powder separation, ensures uniform gas diffusion, and prevents sintering of the mixture during high-temperature exposure.

Before processing, both the substrate and pack materials are thoroughly ground and blended. When the mixture is heated, the activator reacts to produce an atmosphere of source element halide, which diffuses in the pack and transfers the source element to the substrate on which the coating is formed [89].

The process is governed by a series of chemical reactions, beginning with the formation of volatile aluminum halides through interactions between the activator and the aluminum source. This reaction can be summarized as:

$$Al + nBX_n \rightarrow AlX_n + nB \quad (3.1)$$

Here, B and X represent the metal cation and halogen anion, respectively. Depending on conditions, different aluminum halide species (AlX, AlX_2, AlX_3) can form. The aluminum partial pressure, influenced by source activity and temperature, drives vapor-phase transport toward the substrate. Upon reaching the surface, aluminum is deposited through one of several reactions, including direct reduction (3.2), disproportionation (3.3)(3.2), reaction with substrate (3.4) or hydrogen reduction, if hydrogen is present (3.5) [87]:

$$AlX_3 \rightarrow Al + 3/2\ X_2 \quad (3.2)$$

$$2AlX \rightarrow Al + X_2 \quad (3.3)$$

$$AlX_2 + Ni \rightarrow Al + NiX_2 \quad (3.4)$$

$$AlX_3 + 3/2\ H_2 \rightarrow Al + 3HX \quad (3.5)$$

Once aluminum is deposited, it diffuses into the nickel-based alloy to form a β-NiAl intermetallic layer. This layer plays a critical role in long-term protection, as it supports the formation of a stable α-Al_2O_3 (alumina) scale at high temperatures. This oxide layer acts as a barrier against oxidation and corrosion, significantly improving the durability of the coated component.

Pack cementation is a low cost and highly reproducible process, which guarantees the manufacturing of highly uniform coatings with generally high deposition rates. The main limitation of the process is given by the necessity of a relatively complicated apparatus and its poor flexibility.

3.1.3 Deposition techniques – Slurry aluminizing

Slurry aluminizing shares similarities with the pack cementation technique, but instead of using loose powders, the metal source and halide activators are combined with an organic binder to create a slurry. This slurry can be locally applied to components, offering benefits in terms of reduced processing cost and simplified application. The method generally operates under high aluminum activity [90–92]; however, using Al alloys (typically CrAl alloys) as the aluminum source can lower the activity level [93]. Despite leading to the requirement of a post-aluminizing annealing step, resulting in longer processing times, this adjustment allows chromium to diffuse into the coating during the manufacturing process, which can enhance high-temperature resistance and overall performance [94]. The slurry aluminizing process comprises several key stages: (i) aluminum-containing vapors are generated through the reaction between activator salts and the metallic aluminum source; (ii) these vapors are transported to the surface of the Ni-based superalloy; (iii) aluminum reacts at the surface to form nickel–aluminum intermetallic compounds; and (iv) solid-state diffusion proceeds, ultimately yielding the desired NiAl phase.

Figure 3.2.3 illustrates the key steps involved in the slurry aluminizing process. The procedure begins with the preparation of a slurry, which is a suspension of aluminum powder dispersed in an organic binder. Common components of the binder include isoamyl acetate, diethyl oxalate, and nitrocellulose. This slurry is uniformly applied, typically by spraying, onto a thoroughly cleaned and polished surface of the component. Once the slurry has cured, the coated part is subjected to a high-temperature heat treatment. This thermal process is usually carried out in an inert argon atmosphere to prevent unwanted oxidation. The primary objective of this step is to promote the diffusion of aluminum into the substrate, enabling the formation of a protective aluminide layer.

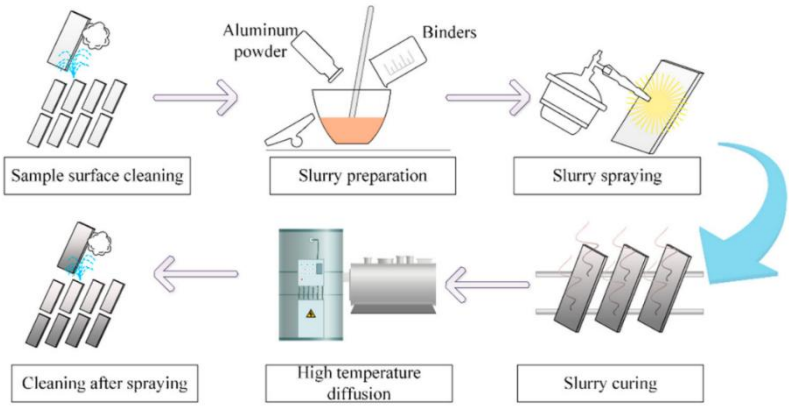

Figure 3.4: Main stages of the slurry aluminizing process [95].

The quality and performance of the resulting aluminide coating are influenced by several key factors:

- Slurry composition: the proportion of aluminum powder and binder within the slurry directly affects the coating's final characteristics, including its thickness, homogeneity, and adhesion to the substrate.
- Slurry layer thickness: the actual thickness of the applied slurry can significantly influence coating morphology, as it determines the initial amount of aluminum available for diffusion.
- Heat treatment parameters: the temperature and duration of the heat treatment are critical for ensuring sufficient aluminum diffusion into the substrate and for achieving the desired intermetallic phases and coating integrity.

Even when slurry composition and heat treatment parameters are held constant, the microstructure of aluminide coatings can vary significantly depending on the aluminum vapor concentration in the reactor chamber and the initial slurry layer thickness. These variables influence the amount of aluminum that reacts with the superalloy during the early stages of the process, thereby affecting the resulting phase composition of the coating and, consequently, its oxidation resistance.

Given the simplicity of the process, with no special equipment required, and the flexibility of the process, slurry aluminizing can be considered one of the most promising techniques for applying protective coatings to components operating in high-temperature environments. Moreover, its ease of application make slurry aluminizing particularly useful for the restoration of locally damaged parts of the coating.

3.2 Thermally Grown Oxide (TGO)

The performance and service life of advanced thermal barrier coating (TBC) systems are strongly influenced by the oxidation characteristics of the bond coat. Ideally, the bond coat should support the formation of a dense, adherent, and slow-growing α-Al_2O_3 oxide scale, which acts as a barrier against further oxidation and degradation.

To successfully develop an α-Al_2O_3 protective scale, the bond coat must contain a sufficient aluminum concentration. This critical threshold is determined not only by the presence of other alloying elements but also by the environmental and operational conditions, particularly temperature and oxygen partial pressure [96]. During initial exposure to elevated temperatures, particularly below ~1100 °C, a series of transient alumina phases may form prior to the stabilization of α-Al_2O_3. At early oxidation stages (700–900 °C), γ-Al_2O_3 typically forms, which may transform into θ-Al_2O_3 through intermediate δ-phase formation. With increasing temperature, these metastable oxides gradually

convert to the thermodynamically stable α-phase [97]. While α-Al_2O_3 becomes dominant rapidly above 1200 °C, metastable forms may persist for extended durations in the 800–1100 °C range.

The growth mechanisms of these alumina phases also vary. Metastable oxides such as γ and θ are believed to grow primarily through outward diffusion of Al^{3+} ions, or a combined flux of aluminum and oxygen species. In contrast, α-Al_2O_3 tends to grow by inward diffusion of oxygen, typically along grain boundaries. Unfortunately, metastable alumina forms tend to grow faster, are more porous, and exhibit poor adherence. Their transformation into the α-phase also induces volumetric and morphological changes, introducing residual stresses and promoting cracking, factors that jeopardize the coating's integrity.

To mitigate these problems, pre-oxidation treatments of the bond coat have been shown to significantly enhance TBC durability. Thermally growing a thin, stable α-Al_2O_3 scale prior to top coat deposition, typically via heat treatment between 1100 °C and 1200 °C, helps prevent the formation of metastable phases and limits stress accumulation during subsequent service exposure. Alternatively, physical vapor deposition (PVD) may be employed to form an oxide layer without consuming aluminum from the bond coat.

Despite its stability, α-Al_2O_3 is still susceptible to spallation under thermal cycling. Tolpygo et al. [98,99] demonstrated that the presence of metastable phases within the thermally grown oxide (TGO) can lead to the incorporation of impurities and dopants like zirconium and yttrium during top coat deposition. Upon transformation to α-phase, these elements segregate at grain boundaries due to their limited solubility, thereby increasing grain boundary diffusion and reducing resistance to cyclic oxidation. In contrast, pre-oxidation stabilizes α-Al_2O_3 and significantly improves coating longevity.

Several other factors also affect the adhesion and stability of the TGO layer. These include thermal stresses induced by mismatches in the coefficient of thermal expansion (CTE) between the TGO and the substrate, the formation of voids and cracks at the interface, and the increased risk of spallation as the oxide layer thickens.

During isothermal oxidation, the growth of the TGO typically proceeds through three stages: an initial transient phase, a steady-state phase representing the effective service life, and a final breakaway phase. The latter is acceptable as long as it occurs beyond the intended lifetime of the system. Nevertheless, it is essential to account for ongoing structural and compositional evolution due to interdiffusion between the bond coat and the substrate. Such diffusion depletes the aluminum content, weakens the ability to form a continuous α-Al_2O_3 layer, and leads to the segregation of unwanted elements that encourage localized failure and scale detachment.

3.3 Failure mechanisms and Pt modification

During service in gas turbine engines, protective coatings are exposed to extreme environments characterized by high temperatures and corrosive conditions. The performance and longevity of these coatings largely depend on the stability and regeneration of the alumina (Al_2O_3) scale that forms on their surface. Under thermal cycling, common in turbine operations, the alumina layer may spall off due to thermal stresses. To maintain protection, aluminum from within the coating must diffuse to the surface to regenerate the oxide scale.

However, aluminide coatings have a limited thickness and contain only a finite aluminum reservoir. Moreover, there is a significant aluminum concentration gradient between the coating and the underlying superalloy substrate. While stoichiometric β-NiAl contains approximately 31.5 wt.% Al, typical Ni-based superalloys have only around 6 wt.% Al. This discrepancy drives interdiffusion at service temperatures above ~1000 °C, further depleting the coating of aluminum.

As both oxidation and interdiffusion processes consume aluminum, the coating gradually loses its protective capacity. Aluminum depletion leads to the formation of the γ' (Ni_3Al) phase at β-NiAl grain boundaries, and prolonged exposure reduces the β phase content within the coating. This transformation compromises high-temperature resistance, and if depletion continues, the γ' phase can eventually transform into the γ matrix phase, further undermining the protective function of the coating.

It should also be mentioned that during high-temperature exposure interdiffusion occurs between the coating and the superalloy substrate. This can lead to the enlargement of the IDZ, which is generally brittle, and to the depletion of beneficial elements from the substrate, potentially affecting the mechanical properties of the component [100]. In addition, interdiffusion with the substrate can lead to the precipitation of detrimental topologically close-packed phases (TCP) in the superalloy matrix, generally below IDZ, which can also degrade mechanical properties and dramatically decrease creep resistance [101,102].

These degradation mechanisms limit the operating temperatures of standard aluminide coatings to around 870-980 °C [103].

To further improve the protective capabilities of aluminide coatings, Pt-modified aluminides have been developed [104,105]. The presence of Pt significantly improves coating performance, but the mechanisms responsible for this improved behavior are not well understood yet: many models have been proposed, but there is no direct evidence that Pt really behaves accordingly to one or more of those.

The fabrication of platinum-aluminide coatings typically involves electroplating a thin platinum layer, approximately 6 μm thick, onto the surface of the superalloy substrate. This is followed by a

thermal treatment that promotes diffusion of platinum into the substrate. The resulting microstructure depends on the extent of this diffusion: if platinum penetrates deeply during the pre-aluminizing annealing stage, a single-phase (Ni,Pt)Al coating forms. Conversely, limited diffusion leads to the development of a dual-phase structure, consisting of an outer $PtAl_2$ layer over a (Ni,Pt)Al phase. In this configuration, the $PtAl_2$ layer serves as an aluminum reservoir [106]. Experimental data has shown that single-phase platinum-modified coatings exhibit superior oxidation resistance compared to their two-phase counterparts [107].

3.4 Pt-modified aluminides

Platinum-modified aluminide bond coats are extensively employed to enhance oxidation resistance in Ni-based superalloy components used in advanced gas turbine engines. The addition of Pt significantly improves high-temperature oxidation performance, which has spurred decades of research into the microstructure and oxidation behavior of these coatings [108].

The fabrication of Pt-aluminide coatings typically involves the following steps [108,109]:

1. Pt deposition: a Pt layer is deposited onto the superalloy substrate, usually via electroplating;
2. Pre-Aluminizing Diffusion Treatment: the Pt-coated substrate undergoes a heat treatment in vacuum. The time and temperature schedule controls interdiffusion between Pt and the substrate, thus influencing the Pt concentration profile and, therefore, coating microstructure;
3. Aluminizing: The substrate is aluminized under either high- or low-activity conditions. Al activity, which is regulated by temperature, time and activity of the Al source, determines the Al content in the coating.
4. Post-Aluminizing Heat Treatment: a final diffusion heat treatment is usually applied to complete coating formation and stabilize the desired phases.

The final microstructure is influenced by several factors, particularly the time-temperature schedule of the prior-aluminizing diffusion treatment. It significantly influences the Pt concentration profile and the subsequent aluminizing kinetics, thus playing a key role in the final coating microstructure: longer or higher-temperature diffusion treatments can lead to a more uniform distribution of Pt within the initial diffusion layer, affecting the phases formed during aluminizing. Simultaneously, the Al content, controlled by the aluminizing process parameters, dictates the relative amounts of different phases in the coating. Higher Al activity generally promotes the formation of Al-rich phases like $PtAl_2$.

Depending on the growth mechanism during aluminizing, Pt-modified bond coats are classified as inward-grown (high activity) or outward-grown (low activity) [110].

Inward grown (high activity) coatings typically have a three-layer structure: a Pt-rich outer layer, an intermediate layer, and an inner IDZ. The Pt-rich outer layer can have a single-phase ζ-$PtAl_2$, a two-phase ζ-$PtAl_2$ + β-(Ni,Pt)Al or a single-phase β-(Ni,Pt)Al structure depending on the Pt and Al concentrations. Indeed, the deposition of a thick initial Pt layer (10 μm or higher) with an high-activity aluminizing process can lead the formation of a continuous $PtAl_2$ outer layer, whereas a thinner Pt layer (1-2 μm) might result in all Pt remaining in solid solution within the NiAl matrix. Conversely, the intermediate layer typically presents a single phase β-(Ni,Pt)Al.

Outward grown (low activity) coatings typically have a two-layer structure: a single-phase β-(Ni,Pt)Al outer layer and an inner IDZ. These coatings generally have lower Al content. Pack cementation processes (high temperature low activity, HTLA) often produce single-phase β-(Ni,Pt)Al coatings [111]. The concentration of Pt in pack cementation coatings can be lower near the surface and higher near the diffusion zone [110].

The addition of Pt enhances oxidation resistance in both isothermal and cyclic environments. However, this benefit depends heavily on Pt content. While a minimum Pt threshold is necessary, beneficial effects do not increase indefinitely with increasing Pt amounts and excess Pt can result in the formation of brittle, Pt-rich phases and high-temperature transformations that might deteriorate coating resistance [112,113]. Studies show optimal performance when the initial Pt layer is 5–7 μm thick [112,114,115]. Lower Pt levels reduce resistance, whereas higher levels may increase rumpling and degrade mechanical integrity [116].

Under isothermal oxidation, introduction of Pt is known to enhance the formation of a continuous and adherent α-Al_2O_3 scale [111,117], and to promote the selective oxidation of Al [100,118]. It was also suggested that Pt presence can inhibit void formation at the oxide scale/coating interface or fill existing voids, thus improving scale adhesion [108,118–120]. It has also been proposed that Pt can reduce stresses in the growing oxide scale, improving the transformation from transient θ-Al_2O_3 to protective α-Al_2O_3, reducing the stresses related to phase change and contributing to better adhesion [108,112,120,121]. Pt also significantly enhances the resistance to spallation of the Al_2O_3 scale during thermal cycling. Indeed, the improved scale adhesion, attributed to Pt, is considered a primary factor affecting cyclic oxidation resistance. Eventually, Pt modification generally also improves hot corrosion resistance compared to plain aluminide coatings [117,122–125]. Pt is also known to impede the outward diffusion of detrimental substrate elements, preserving the scale's protective properties [117].

The exact mechanisms leading to the beneficial effect of Pt addition are still under investigation. Several mechanisms have been proposed, but none of them is univocally accepted yet:

- Enhanced Al_2O_3 scale adhesion: Pt is believed to reduce stresses in the scale, promote the formation of Al_2O_3 pegs that improve scale adhesion by mechanical interlocking, and enhance the contact area between the scale and the metallic coating by reducing interfacial voids [108,118,120];
- Promotion of selective Al oxidation: Pt can enhance the diffusion and selective oxidation of Al, ensuring the formation a protective Al_2O_3 layer even after scale damage or partial spallation [100,105,108,113,126];
- Stabilization of the coating microstructure: Pt can retard the degradation of the β-(Ni,Pt)Al phase and the formation of detrimental phases [120];
- Barrier to diffusion of detrimental elements: Pt can inhibit the diffusion of elements like Cr, Mo, W, and Ti from the superalloy substrate into the coating, preventing their incorporation into the oxide scale, with detrimental effects on its protective properties [127,128];
- Improved mechanical properties: Pt can increase the modulus of elasticity and creep resistance of β-NiAl, which can indirectly enhance oxidation resistance by improving the coating's resistance to cracking and rumpling [126,129–131].

Despite their superior properties compared to standard aluminides, Pt-modified aluminide coatings are susceptible to several degradation phenomena during high-temperature exposure. One major issue is surface rumpling under cyclic thermal conditions, particularly above 1100 °C [114,132,133]. Rumpling, or surface roughening, is influenced by TGO growth, coating swelling due to phase transformations and oxidation, and interdiffusion between the coating and the substrate. It can initiate cracks within the oxide scale and lead to adhesion spallation, ultimately causing TBC failure [134]. Excessive Pt can worsen rumpling due to reduced hardness and Young's modulus of the coating [116]; nonetheless, Yang et al. [122] demonstrated that dual-phase $PtAl_2$-dispersed (Ni,Pt)Al coatings show lighter rumpling compared to single-phase (Ni,Pt)Al coatings due to smaller volume changes during phase transformations and superior creep resistance of ζ-$PtAl_2$.

Extensive research has been conducted to develop modifications that can enhance the durability and extend the service life of Pt-modified aluminide coatings. Incorporation of reactive elements (RE) such as Y, Ce, Hf, and Zr has been demonstrated to improve scale adhesion by promoting the formation of oxide pegs that anchor the scale to the substrate and by reducing the formation of interfacial voids [108,135]. In particular, the modification with Zr increases the oxidation resistance of Pt-modified aluminides by retarding θ-to-α-Al_2O_3 phase transformation and reducing tendencies to rumpling [136]. Noble metals like Pd and Ru have also explored as alternatives or complements to Pt: Hong et al. showed that Pt/Pd-aluminides formed a thicker single-phase β-NiAl layer with reduced tendency to rumpling [137]; addition of Ru demonstrated the potential to suppress TCP formation

[138]. However, Matsuoka et al. [139] indicated that Ru-modified aluminide coatings offer less favorable oxidation resistance and oxide adherence than Pt-modified aluminide coatings; accordingly, Tao et al. [132] have shown that Ru presence aggravates surface rumpling and destroys integrity of the Al_2O_3 oxide scale, leading to accelerated Al depletion.

Ultimately, coating microstructure is key in determining its high temperature resistance and its control is crucial to guarantee the best protective capabilities. Both Pt and Al concentrations must be carefully controlled to optimize the Pt/Al ratio throughout the coating thickness. Indeed, the optimum Pt content is required to fully realize its beneficial effects; in turn, while increasing Al content generally improves oxidation resistance, very high Al concentrations can lead to increased diffusive loss of Al to the substrate and to the formation of brittle Al-rich phases [129].

Despite the importance of control over Pt amount, the most widespread method for Pt deposition is electroplating. However, electrodeposition is sensitive to electrode geometry and electric field distribution. It results is considerable difficulties in controlling coating uniformity on samples with complex-shaped geometries such as turbine blades. This results in over-deposition at edges and under-deposition on convex surfaces, ultimately producing a non-uniform Pt distribution and uneven aluminide microstructure.

3.5 Nanoparticles modified aluminides

Although conventional and Pt-modified aluminide coatings are highly effective, they still present limitations. Among these are the formation of less protective metastable alumina phases during the early stages of high-temperature oxidation, as well as issues with oxide scale adhesion and integrity over time. The protective capabilities of aluminide coatings at elevated temperatures are primarily determined by the formation and stability of the protective Al_2O_3 scale. At temperatures below approximately 1100 °C, the initially formed alumina is often in metastable forms, such as γ and θ phases [140]. These metastable oxides typically grow faster than the stable α-Al_2O_3 and their phase transformation to α involves volume shrinkage (around 10% from θ to α [141,142]), which can induce microcracks in the oxide scale and cavities at the scale/coating interface [140,143]. These defects reduce the protective effectiveness of the scale, accelerating coating degradation and possibly leading to failure.

Reinforcing aluminide coatings with nanoparticles has shown considerable potential in enhancing high-temperature oxidation resistance [73,144]. These improvements are often attributed to nanoparticles' influence on the kinetics of alumina phase transformation and the stability of the oxide/coating interface. A major advantage is their ability to accelerate the transformation of metastable alumina (particularly θ) to the more stable and protective α-Al_2O_3 phase [145,146]. Indeed,

certain nanoparticles, like Cr_2O_3, Fe_2O_3, La_2O_3 and α-Al_2O_3 itself, may promote this transformation by acting as epitaxial templates due to their crystallographic similarity to α-Al_2O_3 [147]. The α-Al_2O_3 scale is more compact, has a significantly slower growth rate (about two orders of magnitude lower than θ-Al_2O_3 [146]), and is more stable than θ-Al_2O_3. Therefore, accelerating its formation leads to a lower overall oxidation rate.

Beyond phase transformation, nanoparticles can enhance the adhesion of the oxide scale to the underlying coating. Some nanoparticles or their reactive elements suppress vacancy condensation at the interface, form mechanical interlocks (pegs), or reduce internal stresses in the oxide layer [146,148,149].

Various types of nanoparticles have been explored, each potentially offering distinct mechanisms for improving oxidation resistance:

- Al_2O_3 nanoparticles, when dispersed in the outer layer of the aluminide coating, can act as nucleation sites for α-Al_2O_3, accelerating the θ-to-α transformation [144,147]. They also may retard grain growth during processing, improving aluminum diffusion and aiding the development of a continuous alumina scale. In the context of MCrAlY coatings, Bai et al. [144]showed that α-Al_2O_3 particles in MCrAlY coatings promoted outward diffusion of Al and suppressed Ni and Cr grain boundary diffusion, resulting in purer Al_2O_3 scales.
- Cr_2O_3 nanoparticles reduce oxidation rates by enhancing the θ-to-α transformation, serving as crystallographic templates for α-Al_2O_3 [140,145]. Khan et al. [145] also observed that the faster θ-to-α transformation promoted by Cr_2O_3 helps prevent the formation of cavities at the alumina/coating interface.
- ZrO_2 nanoparticles exhibit similar behavior, promoting α-Al_2O_3 formation and mitigating interfacial cavities and cracks [146,148]. Qian et al. [150]added ZrO_2 to Pt-modified aluminides, showing minor effect on TGO growth but reduced tendency to rumpling.
- CeO_2 nanoparticles can improve both cyclic and isothermal oxidation resistance by facilitating the θ-to-α transition and serving as diffusion barriers between the aluminide and substrate [151,152].
- Y_2O_3 nanoparticles can enhance hot corrosion resistance of aluminides [153]; however, it was also shown that Y_2O_3 dispersions can suppress or delay the θ-to-α phase transformation [154].

In summary, reinforcing aluminide coatings with specific nanoparticles positioned effectively, can significantly improve high-temperature oxidation resistance. These improvements are primarily achieved by promoting the rapid transformation of metastable alumina phases to the more protective α-Al_2O_3, reducing aluminum diffusion, enhancing oxide scale adhesion, and mitigating defects at the scale/coating interface.

One of the easiest and most common methods to disperse nanoparticles within the aluminide coating is by electrodepositing an additional metallic layer (typically Ni) containing nanoparticles onto the substrate before the aluminizing process [145,147]. In the case of Pt-modified coatings, nanoparticles can be added directly to the electrodeposited Pt layer [150]. However, this process is strongly affected by current density non-uniformities, especially on the complex-shaped components typical of high temperature applications, and homogeneous layers are very difficult to obtain.

4. Platinum plating techniques

Currently, the only method used at an industrial scale for platinum deposition on superalloys is electroplating. While this technique is well-established and capable of producing thin metallic coatings through electrolysis of a solution containing platinum ions or their complexes, it presents significant drawbacks. In particular, electroplating requires highly careful and customized anode design, tailored specifically for each individual component to be coated. This necessity greatly limits flexibility, especially when dealing with components of varying shapes and sizes. Moreover, due to the edge effects of the electric field, achieving uniform coatings on complex geometries, such as turbine blades and nozzle components, becomes extremely challenging, with sharp edges and intricate features often receiving excessive or insufficient plating.

As an alternative, electroless plating has attracted attention. In this process, the electrons required for metal ion reduction are supplied by a chemical reducing agent added to the bath, rather than by an external power source. This fundamental difference eliminates issues related to electric field distribution, enabling the deposition of more uniform and homogeneous coatings even on components with complex shapes. However, despite its promise, electroless deposition of pure platinum remains an area of active research and has not yet achieved a reliable, industrially viable method for producing sufficiently thick Pt films, which is essential requirement for high-temperature applications like gas turbines.

A summary comparing the main differences between electroplating and electroless plating is provided in Table 4.1 [155]

Property	**Electrodeposition**	**Electroless deposition**
Driving force	External power supply	Reducing agent (RA) and autocatalytic properties
Cathode reaction	$M^{n+} + ne^- \rightarrow M$	$M^{n+} + RA \rightarrow M$
Anodic reaction	$M - ne^- \rightarrow M^{n+}$	$RA - ne^- \rightarrow RA_{oxidized}$
Overall Reaction	$M_{anode} \rightarrow M_{cathode}$	$M^{n+} + RA \rightarrow M + RA_{oxidized}$
Anodic Site	Anode itself	Workpiece
Cathodic site	Workpiece	Workpiece

Table 4.1: Comparison between electrochemical and electroless deposition.

4.1 Electroplating

Electrodeposition, commonly referred to as electroplating, is a film growth process in which a metallic coating is deposited onto a base material through the electrochemical reduction of metal ions from an electrolyte solution [156]. The technique takes place within an electrolytic cell (Figure 4.1),

where an external voltage or current is applied across two electrodes. The component to be coated, connected to the negative terminal of the power supply, serves as the cathode, while the anode, connected to the positive terminal, completes the circuit. Both electrodes are immersed in an electrolyte: a solution containing either free metal ions or complexes of metal ions with ligands.

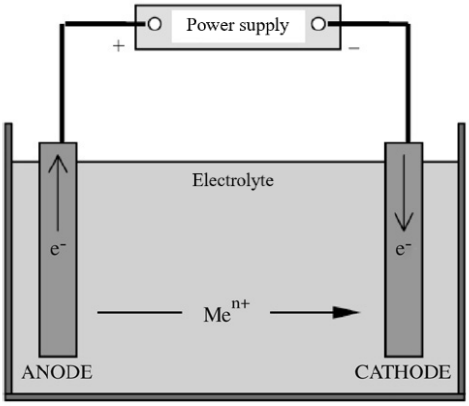

Figure 4.1: Cell setup for electroplating.

The fundamental electrochemical reaction governing electrodeposition can be written as:

$$\left(M_xL_y\right)^z + nxe^- \rightarrow xM + yL \tag{4.1}$$

where L represents a ligand bound to the metal M to form the complex $(M_xL_y)^z$ and n is the number of electrons involved per metal atom deposited. In the simplest case, where hydrated metal ions are directly reduced, the reaction simplifies to:

$$M^{z+} \cdot xH_2O + ze^- \rightarrow M + xH_2O \tag{4.2}$$

Each metal atom requires the transfer of n electrons. Accordingly, the total charge Q necessary to deposit one mole of atoms can be calculated using Avogadro's number (N_A=6.022×10^{23} mol^{-1}) and the Faraday constant (F=96485 C·mol^{-1}), with the relationship:

$$N_A ne^- = nF \tag{4.3}$$

The mass m of metal deposited is directly proportional to the charge Q passed through the system, as described by Faraday's Law:

$$m = \frac{QA}{nF} \tag{4.4}$$

where A is the molar mass of the metal, and n is its valence. If the current I is constant during deposition, the charge is simply:

$$Q = I\tau \tag{4.5}$$

where τ is the electrolysis time. For variable currents, the charge is given by the integral:

$$Q = \int I d\tau \tag{4.6}$$

leading to the generalized form of Faraday's Law:

$$m = \frac{\int I d\tau \, A}{Fn} \tag{4.7}$$

These equations can also be expressed in terms of the thickness t of the deposit, given by $t=m/\rho S$, where ρ is the density and S the surface area being coated.

It is important to note that Faraday's Law predicts an ideal mass gain, assuming all the current contributes exclusively to metal deposition. In practice, however, side reactions (such as hydrogen evolution, the reduction of surface oxides, or co-deposition of undesired metals) consume part of the current, reducing the current efficiency of the process. This efficiency, η, is defined as:

$$\eta = \frac{m_{actual}}{m_{Faraday}} \tag{4.8}$$

where m_{actual} is the real mass of the deposited metal, and m_{Faraday} is the theoretical mass predicted by Faraday's Law.

4.1.1 Electrode potential

The electrodeposition process fundamentally occurs at the interface between the metallic surface and the electrolyte solution. When a metal electrode is immersed into the electrolyte, a charge separation arises at this interface, due to the distinct nature of the mobile charge carriers: electrons in the metal and ions in the solution. As a result of Coulombic interactions, an electrical double layer forms, creating a potential drop across the interface between the bulk metal and the adjacent solution. This inherent potential difference, known as the electrode potential (E_0), reflects the material's tendency to undergo oxidation (i.e., to lose electrons and form ions).

However, the absolute value of the electrode potential cannot be measured directly without introducing a second metal-electrolyte interface. To address this, all electrode potentials are measured relative to the Standard Hydrogen Electrode (SHE), whose potential is conventionally set to zero. By comparing metals according to their electrode potentials, it is possible to establish an electromotive force series (emf series) or galvanic series (Figure 4.2), ranking metals by their ease of oxidation: the lower the electrode potential, the more readily a metal releases electrons. In the design of an electrochemical cell, the material with the higher electrode potential acts as the cathode (where reduction and deposition occur), while the material with the lower electrode potential serves as the anode (where oxidation and dissolution into the electrolyte take place) [157].

Electrode Reaction	Standard Electrode Potential, E^0 (V)	Electrode Reaction	Standard Electrode Potential, E^0 (V)
$Au^{3+} + 3e^- \longrightarrow Au$	+1.420	$Ni^{2+} + 2e^- \longrightarrow Ni$	−0.250
$O_2 + 4H^+ + 4e^- \longrightarrow 2H_2O$	+1.229	$Co^{2+} + 2e^- \longrightarrow Co$	−0.277
$Pt^{2+} + 2e^- \longrightarrow Pt$	~+1.2	$Cd^{2+} + 2e^- \longrightarrow Cd$	−0.403
$Ag^+ + e^- \longrightarrow Ag$	+0.800	$Fe^{2+} + 2e^- \longrightarrow Fe$	−0.440
$Fe^{3+} + e^- \longrightarrow Fe^{2+}$	+0.771	$Cr^{3+} + 3e^- \longrightarrow Cr$	−0.744
$O_2 + 2H_2O + 4e^- \longrightarrow 4(OH^-)$	+0.401	$Zn^{2+} + 2e^- \longrightarrow Zn$	−0.763
$Cu^{2+} + 2e^- \longrightarrow Cu$	+0.340	$Al^{3+} + 3e^- \longrightarrow Al$	−1.662
$2H^+ + 2e^- \longrightarrow H_2$	0.000	$Mg^{2+} + 2e^- \longrightarrow Mg$	−2.363
$Pb^{2+} + 2e^- \longrightarrow Pb$	−0.126	$Na^+ + e^- \longrightarrow Na$	−2.714
$Sn^{2+} + 2e^- \longrightarrow Sn$	−0.136	$K^+ + e^- \longrightarrow K$	−2.924

Figure 4.2: Standard emf series (or galvanic series).

At thermodynamic equilibrium, the electrode potential for a given redox process can be described by the Nernst equation:

$$E_{M^{z+}/M} = E^0_{M^{z+}/M} + \frac{RT}{zF} \ln \frac{\alpha_{M^{z+}}}{\alpha_M} \tag{4.9}$$

Where R=8.3145 J/(mol·K) is the universal gas constant, T is the absolute temperature in Kelvin, F is the Faraday constant, and α represents the activity of the relevant species in the solution.

To achieve a practical deposition rate during electrodeposition, the electrode potential must be shifted in the cathodic direction relative to its equilibrium value. This deviation from equilibrium is referred to as the overvoltage. In electroplating operations, the required overvoltage is generated by the application of an external current, enabling sustained metal ion reduction and continuous film growth.

4.1.2 Electroplating of Pt

In principle, metal deposition can be achieved from simple solutions containing a soluble salt or other compound with the metal in the form of cation, anion, or complex. However, platinum, being a highly noble metal, presents particular challenges: its ions are readily reduced, making it difficult to prepare a stable simple salt solution suitable for a plating bath [158]. Consequently, coordination chemistry plays a crucial role in platinum electrodeposition, and the electrolyte composition largely determines the characteristics and physical properties of the resulting coating.

For an effective platinum source in electroplating baths, three key requirements must be met: (i) Stability against hydrolysis or other decomposition processes; (ii) the ability to reduce Pt(II)/Pt(IV) species readily, even on freshly deposited platinum surfaces; (iii) maintenance of bath composition without irreversible chemical changes during deposition.

Achieving stability often conflicts with the ease of reduction, as strong complexation stabilizes the salt but simultaneously shifts the platinum reduction potential in the negative direction [159].

Over time, several platinum electroplating baths have been developed to meet industrial demands for coatings exhibiting good electrical properties, ductility, fine grain structure, good diffusion behavior, and uniform thickness [155,160].

- Chloride-based baths utilizing Pt(IV) complexes such as H_2PtCl_6 allow for high current densities (2.5–3.4 A/dm²) but suffer from low current efficiencies. When $(NH_4)_2PtCl_6$ is used with a sodium citrate–ammonium chloride supporting electrolyte, current efficiency improves (~70%) at lower current densities. However, high chloride concentrations pose significant corrosion risks, limiting the practical application of these baths. Operating temperatures range between 45–90 °C, and platinum replenishment occurs through dissolution of the Pt anode in the acidic medium.
- Hydroxide-based baths employ $Pt(OH)_6^{2-}$ complexes with sodium or potassium counterions. These systems show efficiencies between 80–100% at 65–90 °C, but their poor stability, despite simple preparation, is a major drawback.

- "P" salt-based baths $[(NH_3)_2Pt(NO_2)_2]$ allow for exceptionally high current densities (up to 5 A/dm²) using supporting electrolytes like ammonium nitrate and sodium nitrate. Nitrite stabilizes the platinum complex by preventing transition to higher-coordinated amines and itself decomposes favorably to assist platinum reduction. Ammonia ensures solubility and stabilizes the system while acting as a pH buffer. Despite the advantages, these baths have low current efficiencies (even at elevated temperatures near boiling) and suffer from evaporation losses, requiring frequent bath replenishment. Health and safety concerns arise due to ammonia vapor release. Replacing ammonia with NaOH increases current efficiency but decreases bath lifetime. Recent developments in carbonate-based "P" salt baths without ammonia improve process stability, reaching efficiencies up to 40%, depending on the electrolyte used.
- "Q" salt-based baths $[(NH_3)_4Pt(HPO_4)]$, developed by Johnson Matthey [161], represent a significant improvement over "P" salt systems. These baths, which avoid sulfur and chlorine contaminants (critical for high-temperature applications), enable the high-rate deposition of thick, high-quality platinum layers, making them ideal for coating turbine blades. A phosphate buffer improves pH control, with typical operating conditions of pH 10.3 (adjusted with NaOH) and 95 °C.

In "Q" salt baths, platinum deposition likely proceeds through a stepwise ligand exchange mechanism [159]:

$$Pt(NH_3)_4^{2+} + xH_2O \rightarrow Pt(NH_3)_{4-x}^{2+}(H_2O)_x^{2+} + xNH_3 \quad (4.10)$$

$$Pt(NH_3)_{4-x}^{2+}(H_2O)_x^{2+} + 2e^- \rightarrow Pt + (4-x)NH_3 + xH_2O \quad (4.11)$$

Due to the lability of ammonia ligands, elevated temperatures are essential to drive the substitution and reduction processes effectively. As shown in Figure 4.3, current efficiency drops sharply below 89 °C, as $Pt(NH_3)_4^{2+}$ becomes electrochemically inactive at potentials more positive than hydrogen

evolution. Regular addition of distilled water is necessary to maintain bath volume and composition due to evaporation losses.

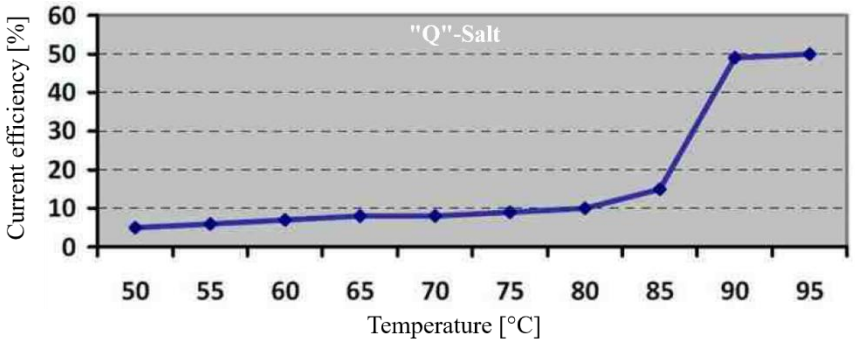

Figure 4.3: Current efficiency as a function of temperature for "Q"-salt electrolyte bath [160].

"Q" salt baths are extensively used for industrial-scale coating of components exposed to aggressive, high-temperature environments. The cyclic voltammogram for a typical "Q" salt solution (Figure 4.4 [162]) reveals a sharp cathodic peak at approximately –740 mV vs. Ag/AgCl during the forward scan, indicating rapid platinum deposition. On the reverse scan, a broader, smaller cathodic peak appears, attributed to the continued platinum reduction on the newly formed platinum surface. At potentials more negative than –850 mV, hydrogen evolution dominates the current response, interfering with platinum deposition [162].

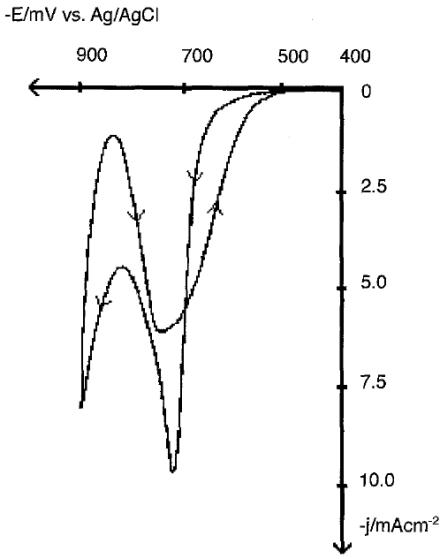

Figure 4.4: Cyclic voltammogram of a typical "Q" salt plating solution at copper disc electrode, recorded at 95 °C [162].

The morphology of the platinum deposits strongly depends on the cathodic deposition potential [159,163]

- At potentials positive to the peak, deposition follows a progressive nucleation and 3D growth model, resulting in bright, highly stressed, and cracked films (Figure 4.5 (a)).

- Slightly more negative potentials yield deposits with finer hemispherical grains and reduced cracking (Figure 4.5 (b)), offering better adhesion but achievable mainly under potential control.
- At significantly negative potentials, angular crystallites form (Figure 4.5 (c)), producing less stressed, matte, and poorly reflective coatings.

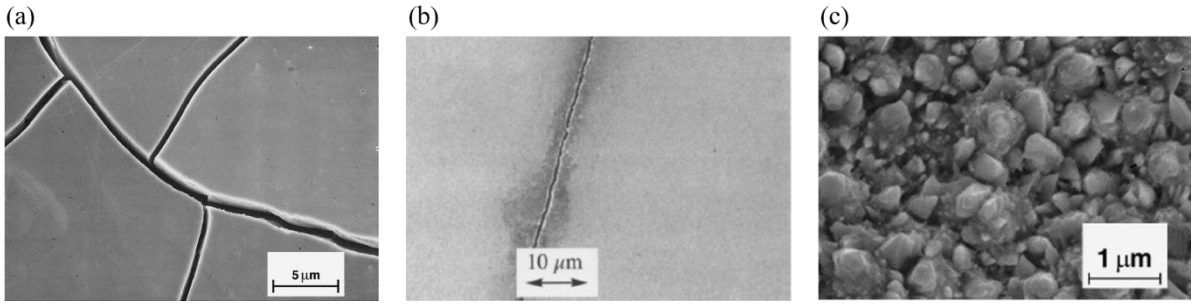

Figure 4.5: Morphology of Pt film obtained at different cathode potentials (vs Ag/AgCl at 95 °C): (a) -620 mV; (b) -750 mV; (c) -850 mV [163].

From a practical standpoint, constant current (galvanostatic) deposition is easier to implement for thickness control but restricts the achievable morphologies to highly cracked or matte coatings due to the peaked nature of the current–potential curve. Moreover, thicker deposits tend to exhibit increased cracking, undermining coating quality. Surface preparation, especially the degree of polishing, critically impacts nucleation behavior and final surface quality.

Beyond these microstructural considerations, one of the main limitations of platinum electrodeposition lies in the difficulty of achieving uniform coating thickness due to the electric field edge effect. Charges accumulate at edges and sharp features (Figure 4.6), leading to locally higher current densities and thicker deposits. This phenomenon occurs at both macroscopic and microscopic scales, making it particularly challenging to coat components with complex or sharp geometries uniformly, such as turbine blades and nozzles.

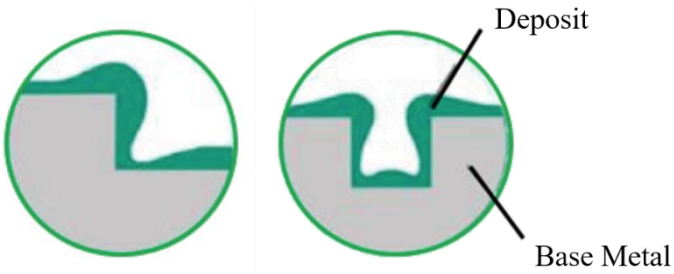

Figure 4.6: Schematic representation of the coating non-uniformity typical of coatings deposited via electroplating.

4.2 Electroless plating

Electroless deposition is an autocatalytic process in which the reduction of metal ions and subsequent film formation occur via the oxidation of a chemical reducing agent present in the plating bath. Unlike electroplating, this technique does not require an external power supply, as the reducing agent serves

as the electron donor. Both anodic and cathodic half-reactions occur on the same surface, which is the substrate to be coated, where electrons are transferred from the reducing agent to the metal ions, which are then reduced and deposited on the substrate surface (Figure 4.7).

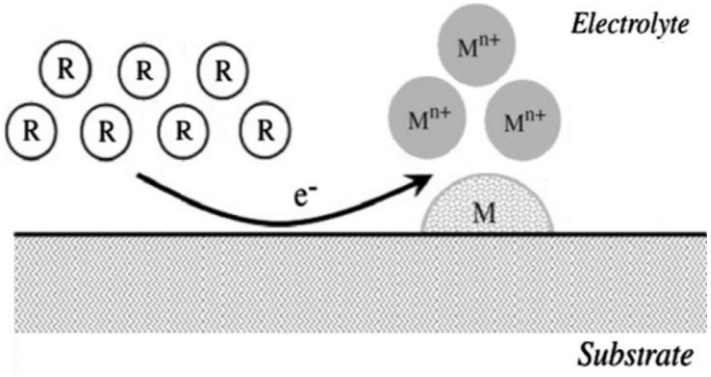

Figure 4.7: Schematic representation of an electroless process, were the reducing agent R is the source of electrons and M represents the metal to be reduced.

The term "electroless" was first introduced by Brenner and Riddell in 1946 [164], who explored the controlled catalytic deposition of Ni–P alloys. Their work laid the foundation for electroless plating as a technique in which metal deposition occurs exclusively on catalytically active surfaces. Since then, extensive research has focused on developing electroless baths for various metals and alloys to produce coatings with unique functional properties [165].

A major advantage of electroless deposition is its ability to produce coatings of uniform thickness, even on complex geometries, as it is not subject to the inhomogeneities of current density seen in electroplating. However, controlling the plating bath can be challenging, particularly in the case of noble metals like platinum, where high redox potentials and side reactions complicate bath stability and deposition control.

Neglecting side reactions, the fundamental electroless deposition mechanism can be represented as follows:

$$Reducing\ agent \xrightarrow{\text{catalityc surface}} Oxidation\ products + ne^- \tag{4.12}$$

$$M^{z+} + ze^- \xrightarrow{\text{catalityc surface}} M \downarrow \tag{4.13}$$

The substrate must be catalytically active to initiate the reaction, although virtually any material can be plated after appropriate surface activation. Nonetheless, unintended deposition may occur on catalytically active sites elsewhere in the bath, such as scratches on container walls or suspended particles, due to their high surface energy.

Electroless deposition should not be confused with galvanic displacement (immersion plating), a non-autocatalytic process in which the more noble metal ions are reduced by the oxidation of a less noble metal substrate. In displacement reactions, deposition halts after forming a monolayer, as the base metal is no longer exposed. In contrast, electroless deposition is self-sustaining, since the deposited

metal layer remains catalytically active, allowing continued growth. Additionally, the redox potential for electroless deposition is generally more positive than that of galvanic displacement. This autocatalytic nature is illustrated in Figure 5.2.2 [166].

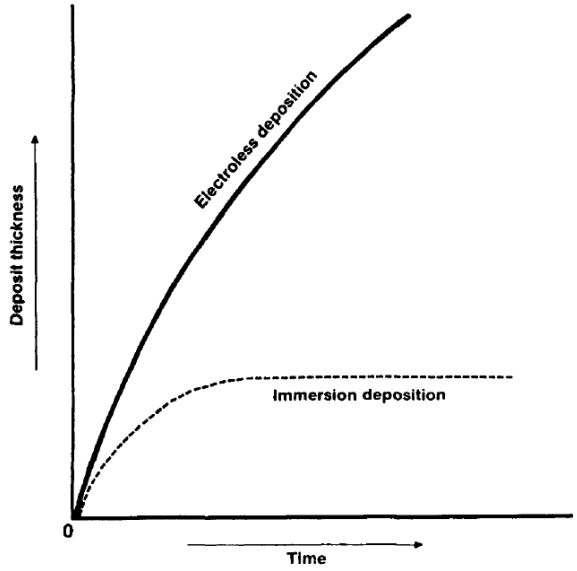

Figure 4.8: Deposition thickness versus time, comparison between immersion deposition and electroless deposition [166].

A typical electroless plating bath contains several essential components, including [167]:

- Metal salts, which provide the metal ions for deposition;
- Reducing agents, which donate electrons to reduce metal ions;
- Complexing agents, typically organic acids or their salts, which bind metal ions to regulate free ion concentrations;
- Stabilizers or inhibitors, which suppress unwanted bath decomposition and minimize spontaneous deposition on non-target surfaces;
- pH regulators, used to set the initial acidity or alkalinity;
- Buffers, which maintain stable pH during operation.

The efficiency and quality of electroless deposition are highly sensitive to bath parameters such as pH, temperature, and the concentrations of all constituents, especially metal ions and reducing agents. Precise control is essential to ensure reproducible deposition and desired coating properties. Despite this complexity, the process itself is relatively straightforward to implement. Uniform and adherent coatings can be achieved simply by immersing properly prepared substrates in the heated plating solution, without the need for external electrical current or complex setup.

4.2.1 Solution composition and deposition mechanisms

Not all reducing agents are suitable for electroless deposition. The most commonly employed reducing agents include sodium hypophosphite, sodium borohydride, amine-boranes, and hydrazine, each with distinct chemical properties and operational requirements, as summarized in Table 4.2.

Reducing agent	Electrons available (#)	Redox potential vs SHE (V)
Sodium hypophosphite	2	-1.40
Sodium borohydride	8	-1.20
Dimethyl amino borane (DMAB)	6	-1.20
Diethyl amino borane (DEAB)	6	-1.10
Hydrazine	4	-1.16

Table 4.2: Most common reducing agents and their characteristics.

The use of phosphorus- and boron-based reducing agents results in the co-deposition of elemental P or B, which can alter the final composition and properties of the coating. Amine-boranes, with the general formula $R_3N–BH_3$, are adducts of amines and boron hydrides. While sodium borohydride is typically restricted to strongly alkaline conditions, amine-boranes are more versatile and can be used in mildly alkaline, neutral, or even mildly acidic media. Hydrazine, on the other hand, is effective in both acidic and alkaline environments, though its reducing power is enhanced in alkaline solutions. It is often used when high-purity deposits (97–99%) are required [155].

To regulate the availability of free metal ions in solution and prevent spontaneous or uncontrolled deposition, complexing agents are added to the bath. These compounds form coordination complexes with metal ions, which are Lewis acids, by donating electron pairs from their ligand groups, typically organic acids, their salts, or amine-containing molecules. By binding to metal ions, complexing agents lower the concentration of free ions, enhancing bath stability and controlling deposition rates. Additionally, complexation generally shifts the metal ion's reduction potential to more negative values, making reduction more selective.

The ability of a ligand (L) to form a stable complex with a metal ion (M^{n+}) is quantified by the formation constant (K_{ml}), expressed by the equilibrium:

$$M^{z+} + L^{n-} \rightarrow (ML)^{(n-z)-} \tag{4.14}$$

$$k_{ML} = \frac{\left[ML^{(n-z)-}\right]}{[M^{z+}][L^{n-}]} \tag{4.15}$$

A higher K_{ml} value indicates stronger binding and a lower concentration of uncomplexed metal ions. However, the effectiveness of complexation is strongly pH-dependent, since it is influenced by the

acid-base dissociation equilibrium of the ligand. If the solution pH is significantly lower than the ligand's pK_a, complex formation will be limited [168].

Even with proper complexation, additional stabilizers are often necessary to suppress unwanted side reactions and prevent deposition on non-target catalytic surfaces. These stabilizers act by adsorbing onto high-energy surfaces, effectively inhibiting uncontrolled nucleation. Common stabilizers include heavy metals from group II [169], thiourea [170,171], and guanidine [172].

In contrast, accelerators may be introduced in small quantities to enhance the deposition rate. Examples include trace amounts (millimolar concentrations or lower) of thiourea, formate, or glycine, which promote faster nucleation and growth by facilitating electron transfer or modifying surface chemistry [168].

While designing an electroless plating bath is relatively complex, requiring careful balance between multiple interdependent parameters, the use of tailored additives (including stabilizers, accelerators, and complexing agents) is often the key to achieving coatings with desirable properties tailored for specific functional or industrial applications.

Understanding and optimizing the electroless deposition process also requires a solid understanding of the electrochemical principles underlying its operation. Building on the previously discussed influence of bath composition and operating parameters, it is important to recognize that electroless plating is fundamentally governed by redox reactions occurring at the substrate surface, and as such, can be effectively modeled using an electrochemical framework [173,174].

According to the mixed potential theory, the overall electroless deposition process results from the combination of two simultaneous half-reactions: the oxidation of the reducing agent and the reduction of metal ions, as described in reactions (4.12) and (4.13). Both reactions take place on the same catalytic surface, each tending to impose its own equilibrium potential. However, rather than each reaching equilibrium independently, the system reaches a steady-state compromise potential, referred to as the mixed potential (E_{mp}).

At this mixed potential, the anodic current from the oxidation of the reducing agent equals the cathodic current from the reduction of the metal ions. This balance establishes a dynamic steady state, even though neither half-reaction is at its true equilibrium. In practical terms, the potential of the reducing agent/oxidation product couple is shifted anodically, while the potential of the metal/metal ion couple is shifted cathodically, enabling continuous deposition.

This behavior can be visualized using current–potential (i–E) curves, as shown in Figure 4.9. The two solid lines represent the anodic and cathodic partial reactions, while the dashed curve represents the net overall reaction. The point where these curves intersect corresponds to E_{mp}, the operational condition under which stable deposition occurs.

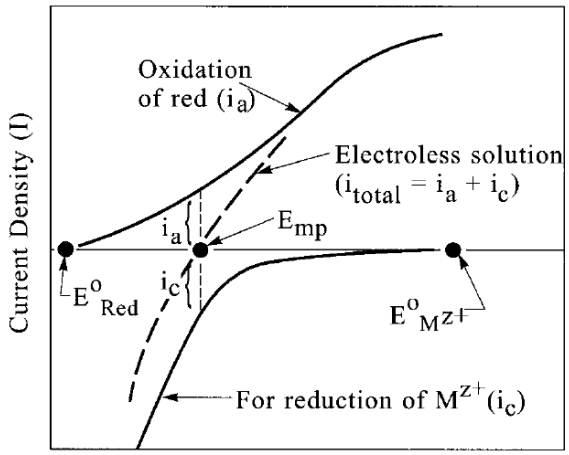

Figure 4.9: Current-potential curves for a generalized electroless deposition reaction. The dashed line represents the curve for the complete electroless solution [168].

This electrochemical perspective complements the chemical understanding of bath formulation by providing a framework to quantitatively evaluate deposition kinetics and predict the effect of changes in bath composition or conditions on the plating rate and film quality.

While the electrochemical framework based on mixed potential theory provides valuable insights into the thermodynamics and kinetics of electroless deposition, a deeper understanding of the process also requires consideration of the catalytic nature of the substrate and the mechanistic pathways underlying reductant oxidation. The ability of a metal or alloy surface to catalyze the oxidation of the reducing agent is a key factor in determining whether electroless deposition can proceed. However, no single metal is universally effective for all reducing agents. Among the known catalysts, palladium exhibits the highest catalytic activity, making it the preferred choice for activating non-catalytic substrates, especially in pre-treatment steps for materials such as plastics or glass.

As discussed previously, only a limited number of reducing agents are practically suitable for electroless deposition, and their performance is highly dependent on a carefully tuned balance of bath composition and operating conditions. To further elucidate the underlying mechanisms, several hypotheses have been proposed over the years [166,168].

One of the earliest and most widely cited is the hydrogen adsorption mechanism, originally proposed by Brenner and Riddell [164,175]. This model suggests that atomic hydrogen, produced by dissociation of the reducing agent and adsorbed onto the catalytic surface, is the true reductant of metal ions. The simultaneous evolution of hydrogen gas, commonly observed during nickel deposition, is attributed to the recombination of adsorbed hydrogen atoms.

Although supported by multiple authors, this mechanism lacks definitive experimental evidence for the direct involvement of adsorbed hydrogen in metal ion reduction. An alternative proposal, the hydride transfer mechanism [176,177], postulates that the reducing agent donates hydride ions (H^-), which directly reduce metal ions, accompanied by hydrogen evolution. However, the limited

experimental confirmation of hydride intermediates in electroless processes has kept this mechanism from widespread acceptance.

A third model, the metal hydroxide mechanism [178,179], suggests that hydrolyzed metal ions complexed with hydroxyl groups serve as the actual reactants. These species adsorb onto the surface and react with the reducing agent, leading to metal deposition. It is important to note that hydroxide coordination, not full precipitation, is assumed; otherwise, insoluble metal hydroxides would inhibit deposition.

Another perspective is the electrochemical mechanism, which frames the process in terms of local galvanic cells forming on the catalytic surface. In this model, electrons supplied by the reducing agent via reaction with water drive cathodic metal ion reduction and hydrogen evolution. However, this simplified approach does not adequately explain the role of catalytic surfaces in sustaining the reaction.

To reconcile these observations, Van Den Meerakken [180] proposed a generalized mechanism for reductant oxidation, integrating catalytic and electrochemical concepts. The model involves initial adsorption of the reducing agent (RH), followed by its dissociation into reactive radical intermediates:

$$RH \rightarrow RH_{ads} \tag{4.16}$$

$$RH_{ads} \rightarrow R^{\cdot}_{ads} + H^{\cdot}_{ads} \tag{4.17}$$

$$R^{\cdot}_{ads} + OH^{-} \rightarrow ROH + e^{-} \tag{4.18}$$

$$H^{\cdot}_{ads} + H^{\cdot}_{ads} \rightarrow H_2 \tag{4.19}$$

This mechanism suggests that pH plays a critical role, as OH^- is directly involved in the anodic step. While not intended as a universal model, it offers a compelling framework for analyzing the behavior of specific metal–reductant systems, particularly where catalysis, surface interactions, and radical intermediates are suspected to play major roles.

4.2.2 Electroless platinum plating: state of the art

Due to its noble character, platinum presents significant challenges in developing stable and efficient electroless plating baths. Its high reduction potential makes spontaneous and uncontrolled deposition likely, especially in the presence of potent reducing agents like hydrazine. Recent research has largely focused on the electroless deposition of platinum nanoparticles for catalytic applications [181–186]. However, well-established methods the production of thick and uniform platinum coatings suitable for industrial applications remain scarce, with only a limited number of studies and patents addressing this need.

The first documented process for depositing pure platinum from an alkaline bath was patented by Rhoda and Vines in 1969 [187]. The bath formulation, listed in Table 4.3, uses platinum(IV)

hydroxide as the metal source, hydrazine as the reducing agent, and a trivalent nitrogen-based stabilizer such as ethylamine, Na_2EDTA, quinoline, or sulfamate ions. Deposition was conducted at 25–35 °C and pH > 8, with reported rates of approximately 12.5 μm/h. However, such a system proved highly stable: bath is very susceptible to decomposition due to the high reducing power of hydrazine and, therefore, it is hardly compatible with any industrial application.

Compound	Concentration (g/L)
$Na_2Pt(OH)_6$	10
NaOH	5
$N_2H_4 \cdot H_2O$	3.7
Ethylamine	10
pH	10
Temperature	35 °C

Table 4.3: Alkaline bath composition proposed by Rhoda and Vines [187].

Subsequently, Steinmetz et al. [188] improved the bath's stability by incorporating ethylenediamine as a complexing agent and adding small amounts of As_2O_5 and imidazole. Though more stable, the bath required high temperatures (~90 °C) and achieved a slower deposition rate (~1.5 μm/h). Uniform coatings were reported on IN100 superalloy substrates.

Leaman [189] later proposed another alkaline bath based on the hydrazine reduction of $(NH_4)_2PtCl_6$, which is formed by neutralizing chloroplatinic acid with ammonium hydroxide:

$$H_2PtCl_6 + 2NH_4OH \rightarrow (NH_4)_2PtCl_6 + 2H_2O \quad (4.20)$$

Stability of the complex in ammoniacal solution increases with increasing alkaline conditions, so deposition was performed at pH in the range 7-13.5. Half reactions taking place during deposition are:

$$N_2H_4 + 4NH_3 \rightarrow 4NH_4^+ + 4e^- + N_2 \quad (4.21)$$

$$(NH_4)_2PtCl_6 + 4e^- \rightarrow 2NH_4Cl + Pt + Cl^- \quad (4.22)$$

According to reaction (4.22), excess chloride ions enhance stability as well. wetting agent may be used to promote coating uniformity, and the bath composition is listed in Table 4.4. A strict control over temperature is required, to avoid the rapid reduction of platinum and bath decomposition. For this reason, the inventor recommends to start deposition at temperatures as low as 20 °C and to gradually increase it as platinum is consumed. According to the patent, the proposed bath formulation is only capable of depositing on metals and metal alloys that are more noble than copper.

Compound	Concentration (mol/L)
$(NH_4)_2PtCl_6$	0.0005 - 0.15
N_2H_4 or its salts	0.005 - 1.50

NH_4OH	0.005 - 13.0
Alkali metal chlorides	0.005 - 1.0
Wetting agents (surfactants)	0 - 0.10

Table 4.4: Alkaline bath composition proposed by Leaman [189].

More recently, Kong et al. [190] patented another hydrazine-based alkaline bath for deposition on copper substrates. The platinum source is H_2PtCl_6 complexed with TMAH (the two reagents are mixed and boiled for several hours to obtain $H_2Pt(OH)_6^-$) and hydrazine is used as the reducing agent. The proposed bath also comprises hydroxylamine to complex hydrazine, sulfamic acid as accelerator and 5-sulfosalicylic acid and EDTA as stabilizers, according to the recipe provided in Table 4.5. Nonetheless, given the specific application for semiconductor processing, the authors only achieved thickness of 100-400 Å after immersing for 0.5-5 min.

Compound	**Concentration**
H_2PtCl_6 + TMAH	2-30 mM
N_2H_4	0.1-1 M
Hydroxylamine	5-50 mM
Sulfamic acid	0-0.5 M
5-sulfosalcylic acid and/or EDTA	2-20 mM
pH	8-12
Temperature	20-85 °C

Table 4.5: Alkaline bath proposed by Kong et al. [190].

Walter and Leaman [191] developed an acidic bath containing chloroplatinic acid and hydrazine, with HCl to maintain pH ~0.6 and sulfosalicylic acid as a wetting (Table 4.6). In this case, the half reactions taking place in the bath are:

$$N_2H_4 \cdot 2HCl \rightarrow 2HCl + H^+ + N_2 + 4e^- \quad (4.23)$$

$$H_2PtCl_6 + 4e^- \rightarrow 2HCl + Pt + 4Cl^- \quad (4.24)$$

This system benefits from increased acidity during deposition, which prevents decomposition. Deposition occurs optimally at 60–70 °C. Of course, acidity of the bath limits application to deposition on very noble metals or substrates that are not susceptible to corrosion.

Compound	**Concentration (mol/L)**
H_2PtCl_6	0.0005 - 0.0625
N_2H_4 or its salts	0.003 -0.25
HCl	0.02 – 5.0
Sulfosalicylic acid	0.0005 - 0.025

Table 4.6: Acidic bath composition proposed by Walter and Laeman [191].

Later, Rao and Pushpavanam [192] extended the work of [191], developing a bath with improved additives to deposit on titanium substrates. They used 1 g/L of platinum source and introduced three types of additives: 1,3,6-naphthalene-trisulfonic acid trisodium salt, benzene-*m*-disulfonic acid and sulfosalicylic acid. However, the introduction of such additives allows the deposition of a stress-free deposit with growth rate only up to of 1 μm/h and the authors specify that the platinum salt/hydrazine ratio should always be maintained constant: if that is not done, the baths get decomposed.

Paul et al. [193] further adapted this bath for use on SiC-Si_3N_4 composites. The recipe is reported in Table 4.7; however, a continuous Pt layer was not produced, but only spherical Pt particles (100-500 nm size) attached to the substrate were obtained.

Compound	Concentration (g/L)
$H_2PtCl_6 \cdot 5H_2O$	1
$C_6H_5O_7Na_3 \cdot 2H_2O$	11
N_2H_4	3.7
HCl	
pH	2
Temperature	66-68 °C

Table 4.7: Acidic bath used by Paul et al. [193].

The main disadvantage of the baths proposed in [189,191,192] is that they are only stable without the addition of the reducing agent, which is added just prior to deposition.

To overcome the stability issues, Strejcek [194] proposed a near-neutral bath based on cis-diammine platinum dinitrite (DNP salt), stabilized with sodium nitrite and accelerated by disodium hydrogen phosphate. Hydrazine monohydrate was employed as the reducing agent: it was added dropwise over 250 minutes to guarantee stability, but the deposition rate was extremely low (~0.15 μm/h) and only substrates like Ni, Pt and Pd are reported to be catalytically active after activation with HNO_3. Complete recipe is reported in Table 4.8.

Compound	Composition for 100 mL solution
$NaNO_2$	10 g
$Pt(NH_3)_2(NO_2)_2$ (DNP salt)	0.124 g
$N_2H_4 \cdot H_2O$	13 mL (added dropwise in 250')
pH	7 - 8
Temperature	60 - 95 °C

Table 4.8: Neutral bath composition proposed by Strejcek [194].

Another bath based on DNP salt and hydrazine monohydrate, capable of depositing on any substrate, was patented by Koslov et al. [195]. Plating occurs in acidic conditions: acetic acid or nitric acid are added to keep pH in the range 2-6. Bath composition for deposition on Inconel X7750 nickel-based superalloy is presented in Table 4.9. Deposition rate is reported to vary in the range 0.1-2 μm/h and the rate increases with increasing temperature and concentration of platinum or hydrazine. However, increasing those parameters leads to a more difficult control over bath stability and coating formation.

Compound	Concentration (g/L)
DNP salt	2
$N_2H_4 \cdot H_2O$	3
CH_3COOH	
pH	3
Temperature	50 °C

Table 4.9: Acidic bath composition proposed by Koslov et al. for deposition on Inconel X750 [195].

Due to the strong reducing power of hydrazine, previously reported electroless platinum plating baths based on this compound often suffer from poor stability. In response, several recent studies have focused on developing baths that utilize milder reducing agents. Additionally, hydrazine is a hazardous substance, so replacing it with safer alternatives is desirable from a health and environmental standpoint.

Kato and Watanabe [196] patented a bath formulation that uses formalin, glucose, formic acid, or formates as reducing agents in combination with any water-soluble Pt(II) or Pt(IV) salt. Organic acids are employed as complexing agents, and the bath pH is maintained between 6.5 and 12 using NaOH or H_2SO_4. At a deposition temperature of 70 °C, a plating rate of approximately 1 μm/h is achieved. However, a key limitation is that autocatalytic deposition only occurs after the substrate is activated by electrodepositing a thin platinum layer.

Another formulation utilizing formic acid or formates was proposed by Sasamura et al. [197]. In this bath, K_2PtCl_4 serves as the platinum source, with EDTA as a complexing agent. Deposition is promoted by the addition of an ion-supplying agent such as KCl. A pH adjuster and buffer are also included. The typical bath composition and conditions are summarized in Table 4.10. However, activation of the substrate with palladium-containing acidic solutions is required regardless of its nature, and the process can only produce platinum films with thicknesses ranging from 0.001 to 0.5 μm. These constraints limit its practicality for industrial applications.

Compound	Concentration (g/L)
K_2PtCl_4	0.5

Potassium formate	10
KCl	50
EDTA	10
KH_2PO_4	10
pH adjuster	
pH	4 - 8
Temperature	50 °C

Table 4.10: Composition of the bath proposed by Sasamura et al. [197].

Alarfaji et al. [198] recently proposed a bath using formaldehyde as the reducing agent for depositing Pt/Pd composite coatings on stainless steel or alumina-coated stainless steel for catalytic applications. However, with the formulation shown in Table 4.11, only deposition of nanoparticles or small clusters of coalesced particles was achieved, not a uniform continuous film.

Compound	**ml in 500 ml H_2O**
H_2PtCl_6 + $PdCl_2$	17 + 0.345 (for 90%Pt 10%Pd in the coating)
Formaldehyde	12
pH	1.8
Temperature	40 °C

Table 4.11: Acidic bath proposed by Alarjafi et al. [198].

A more recent patent by Shibata and Kamimura [199] describes a two-solution system. The first solution contains a water-soluble platinum salt and a hydroxymethyl compound with the structure R′-CH_2-CH_3, where R′ contains an aldehyde or ketone functional group. The second solution includes hydrazine monohydrate as the reducing agent and a complexing agent such as ethylenediamine. The hydroxymethyl compound is intended to enhance selective plating and suppress out-of-pattern deposition. However, the authors report that partial decomposition and unintended deposition on container surfaces occur immediately upon mixing the two solutions. Moreover, the solutions are only stable for long-term storage if the platinum salt and reducing agent are stored separately, which significantly limits their industrial viability.

An alternative approach was proposed by Tamasauskaite-Tamasiunaite et al. [200], using the Co^{3+}/Co^{2+} redox couple as the reducing agent. Using the formulation provided in Table 4.12, the authors achieved platinum deposition up to 0.05 µm thickness at 20 °C on roughed glass sheets (after proper activation with $PdCl_2$). Although the solution exhibits good stability, the deposition rate is too low for practical use in industrial applications in the high temperature sector.

Compound	**Concentration (mol/L)**

H_2PtCl_6	0.004
NH_4OH	0.4
Diethylentriamine	0.16
$CoCl_2$	0.2
HCl	enough for pH=7.5
Temperature	17-20 °C

Table 4.12: Electroless plating bath proposed by Tamasauskaite-Tamasiunaite et al. [200].

Each of the above-described formulations presents notable limitations that hinder their applicability in industrial settings. These challenges emphasize the ongoing need for research into stable and efficient platinum electroless plating solutions. Specifically, such systems should enable the formation of high-quality platinum films with thicknesses of several microns, suitable for applications where modified Pt-aluminides are required.

5. Introduction to the experimental section

The review of the current state of the art reveals that existing electroless platinum deposition processes suffer from several limitations that hinder their practical application. Despite these challenges, electroless plating offers several advantages over conventional electroplating, including:

- Reduced complexity of the equipment required for deposition;
- No need of anode design and improved process flexibility;
- No need of external power supply and no issues related to current density inhomogeneities;
- Uniform coating deposition, even on substrates with complex geometries (see Figure 4.10, where coating in (a) is obtained via electrolytic deposition and coating in (b) is obtained via electroless deposition);
- Ease of deposition and no need of supporting electrolytes that increase the conductivity of the solution, since deposition occurs uniformly wherever the substrate contacts the bath;

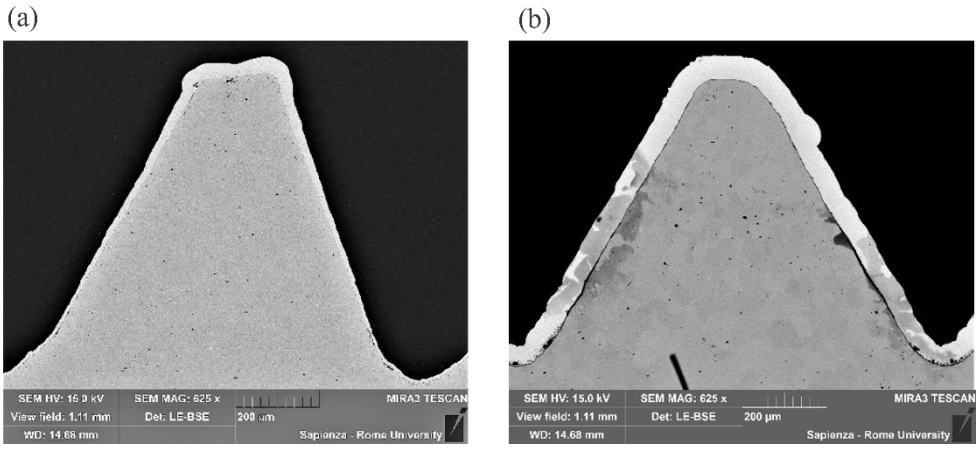

Figure 4.10: Comparison between coating uniformity in electrolytic deposition (a) and electroless deposition (b).

Given these advantages, there is a clear and urgent need to develop a more effective electroless platinum plating bath. Such a solution should be capable of producing coatings with sufficient thickness and performance to meet the demands of high-temperature industrial applications.

The first aim of this work is to study and develop a stable electroless platinum plating bath tailored to industrial requirements. This includes the formulation of the plating solution, investigation of key parameters affecting deposition stability, and evaluation of the resulting film characteristics. The ultimate goal is to obtain high-quality platinum layers suitable for the subsequent formation of aluminide coatings.

Once the optimal electroless platinum plating bath is established, this work will focus on the manufacturing of electroless deposited Pt aluminides by a currently in use industrial process. After each step of the manufacturing process, these will be compared with standard electrodeposited Pt aluminides in terms of morphology, microstructure and phase composition. Eventually, phase

evolution under high temperature exposure and protective properties against high temperature oxidation will be evaluated and compared.

The third phase of the experimental work involves the development of an enhanced slurry aluminizing process capable of improving aluminum distribution and enabling precise control over coating microstructure. This process is further adapted to produce Pt aluminides. The newly developed electroless platinum plating technique ensures excellent uniformity of the initial Pt layer, while the enhanced slurry aluminizing process provides precise microstructural control. Together, these advancements enable a systematic study of the influence of the initial Pt layer thickness on coating behavior. This includes its effect on phase formation, evolution during long-term high temperature exposure, and overall oxidation resistance. As a result, the work identifies the optimal balance between platinum layer thickness, which directly relates to costs, and protective performance, guiding the design of cost-effective, high-performance coatings for high-temperature applications.

Moreover, the unique advantages offered by the electroless deposition technique create new opportunities for further enhancement of aluminide coatings through the introduction of additional functional layers or through the incorporation of second-phase particles, enabling the development of nanocomposite coatings with improved performance.

The fourth part of this thesis focuses on the modification of Pt aluminide coatings by introducing an additional electroless-deposited pure nickel layer, applied after platinum deposition and before the aluminizing step. This intermediate Ni layer is intended to alter concentration gradients and the chemical activity of diffusing species during both the pre-aluminizing heat treatment and the aluminizing process itself. These changes are expected to significantly affect the resulting microstructure of the coating, particularly by enhancing the β-NiAl reservoir and improving the mechanical properties of the outer regions of the Pt aluminide, which are otherwise prone to brittleness.

The fifth and final part of the study explores the preliminary development of nanocomposite Pt aluminide coatings reinforced with Al_2O_3 nanoparticles. Due to the liquid phase nature of electroless deposition, second-phase particles such as Al_2O_3 can be directly suspended in the plating solution and incorporated into the growing coating. When successfully embedded in the outer layers of the Pt aluminide, these nanoparticles can serve as nucleation sites for the epitaxial growth of the thermodynamically stable α-Al_2O_3 oxide scale. Compared to metastable Al_2O_3 phases, α-Al_2O_3 is denser, more adherent, and exhibits a significantly lower growth rate, contributing to enhanced oxidation resistance. This section of the thesis will address the challenges associated with the successful incorporation and uniform distribution of nanoparticles, as well as the preliminary evaluation of their effect on the coating's long-term oxidation behavior.

6. Materials and methods

6.1 Pt plating

Unless otherwise specified, all plating bath studies and experimental tests were conducted using analytical grade chemicals purchased from Alfa-Aesar (Thermo Fisher Scientific, Waltham, MA, USA), used as received without further purification. The main substrate material is Renè N4 single crystal nickel-based superalloy, used for all the experimental activity if not otherwise stated. This alloy is known for its exceptional high-temperature strength and oxidation resistance and it is commonly used as base material for turbine blades [201]. To evaluate coating applicability on substrates of varying compositions, additional experiments were conducted using René 108, GTD-111, and Inconel 625 superalloys. Chemical composition of the substrates is reported in Table 6.1. All substrates had a half-disc shape (2.54 mm in diameter, 2 mm thick) and were supplied by Nuovo Pignone Tecnologie srl (a Baker Hughes company).

	Ni	Cr	Co	Ti	W	Al	Ta	Mo	Fe	Hf
Renè N4	Bal.	8.4	9.5	0.7	9.5	5.5	3.0	0.5	/	1.5
Renè 108	Bal.	10.0	8.0	3.5	6.0	4.2	5.0	2.0	/	0.2
GTD 111	Bal.	13.5	9.5	4.75	3.8	3.3	2.7	1.53	0.23	/
Inconel 625	Bal.	20-23	1.0	0.4	/	0.4	/	8-10	5	/

Table 6.1: Chemical composition of the Ni-based superalloys used as substrate material for Pt plating.

According to the usual industrial procedure, prior to deposition samples were sandblasted with corundum mesh 80 at a pressure of 6.2 bar and a blast distance of 100 mm. Each sample received 10 passes to uniformly increase surface roughness (Ra = 3.877 ± 0.312 μm). Higher surface roughness promotes metal deposition by increasing surface energy [171] and enhances adhesion via mechanical interlocking [202]. After sandblasting, samples were ultrasonically cleaned in acetone using an Elmasonic S 30 (H) bath (37 kHz frequency, 80 W effective power) for 10 minutes, to remove any sandblasting residue. Eventually, they are rinsed with deionized water just before immersion in the plating bath.

The platinum plating bath composition was developed in a prior study by the same author [203], and it is reported in Table 6.2.

Reagent	Function
K_2PtCl_4	Pt source
$Na_2EDTA{\cdot}2H_2O$	Complexing agent
$N_2H_4{\cdot}H_2O$	Reducing agent
HCl (37 vol%)	pH regulator

Table 6.2: Chemical composition of the Ni-based superalloys used as substrate material for Pt plating.

Electroless plating is based on the chemical reduction of metal ions by a reducing agent in aqueous solution, resulting in the deposition of a metallic film onto a catalytic substrate. However, platinum plating is particularly challenging due to the combination of platinum's noble nature and the strong reducing power of the reductants usually employed in electroless processes. Without careful control, spontaneous bath decomposition may occur, leading to the formation of a fine dark grey or black precipitate of platinum nanoparticles, which settle at the bottom of the container. To ensure bath stability and controlled deposition, the use of a milder reducing agent, in combination with metal ion complexation, is essential.

Hydrazine is a widely used reducing agent for electroless deposition of pure metals, effective in both acidic and alkaline media. However, its high reducing power increases the risk of uncontrolled platinum reduction and premature bath decomposition. In this work, hydrazine monohydrate, purchased from Sigma-Aldrich (Merck KGaA, Darmstadt, Germany), was used. Hydrazine follows two principal oxidation pathways::

$$N_2H_4 \rightarrow N_2 + 4H^+ + 4e^- \quad (6.1)$$

$$N_2H_4 \rightarrow N_2 + H_2 + 2H^+ + 2e^- \quad (6.2)$$

Its redox potential is highly sensitive to both pH and temperature, as illustrated in Figure 6.1 [204]. This dependency allows the tuning of process conditions to achieve optimal and controlled deposition behavior:

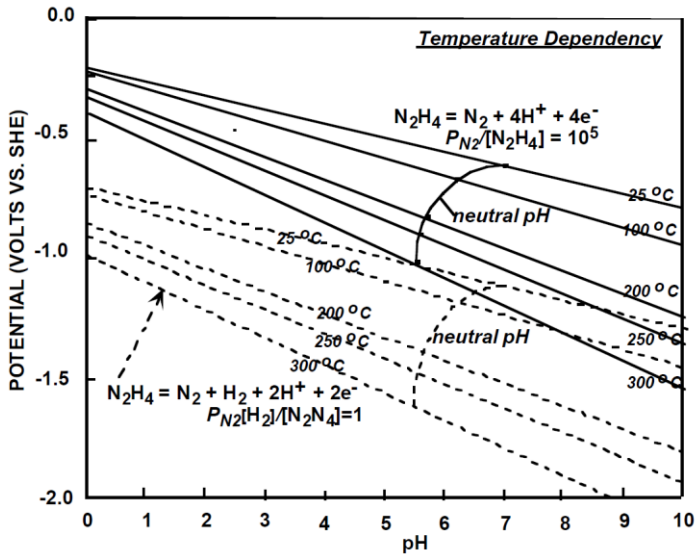

Figure 6.1: pH and temperature dependance for hydrazine redox potential [204].

Potassium tetrachloroplatinate(II) (K_2PtCl_4) was used as the metal ion source in the electroless plating bath. This compound consists of planar $PtCl_4^{2-}$ anionic complexes and potassium cations. The platinum ions are contained within the anionic complex $PtCl_4^{2-}$, which has a reduction potential of +0.73 V, lower than the +1.19 V potential of Pt^{2+} ions. This reduced potential is crucial for achieving

deposition stability, as it narrows the redox gap between the oxidizing and reducing agents, allowing finer control over the electron transfer kinetics and minimizing spontaneous bath decomposition.

The chosen complexing agent was disodium ethylenediaminetetraacetate ($Na_2EDTA \cdot 2H_2O$), selected for its high solubility in water (96 g/L at room temperature), significantly greater than that of free EDTA (around 0.5 g/L) [205]. Complexation plays a crucial role in bath stability and reaction kinetics: when a ligand is present, metal deposition is not obtained by a direct charge transfer, but rather an intermediate step of complex dissociation is required for formation of electroactive species [173].

Despite EDTA complexation, the high reducing power of hydrazine can still trigger uncontrolled reduction of platinum shortly after its addition, leading to bath instability and precipitation of Pt nanoparticles (Figure 6.2)

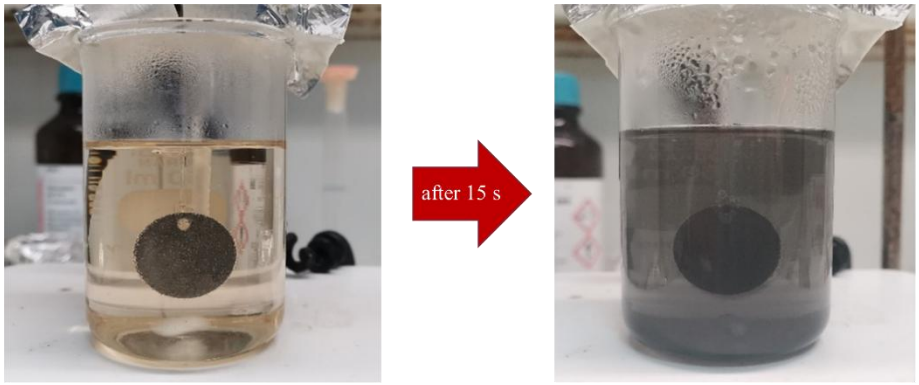

Figure 6.2: Beginning of deposition just after introduction of the reducing agent (left) and bath decomposed after 15 seconds (right).

To mitigate this, pH regulation is critical. Experimental observations showed that a pH below 1 is required to stabilize the plating solution and its precise influence on deposition will be discussed in the next section. Hydrochloric acid (37 vol%), purchased from Sigma-Aldrich (Merck KGaA, Darmstadt, Germany), is used to adjust the pH to the desired value. pH also influences EDTA's solubility and protonation state, as illustrated in Figure 6.3 [206]:

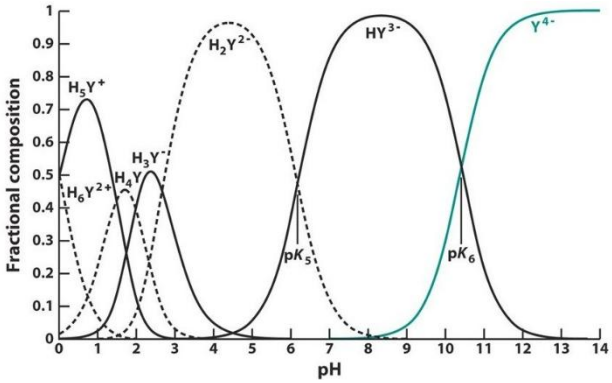

Figure 6.3: Fraction of EDTA species as a function of pH value.

Under highly acidic conditions, EDTA exists in a fully protonated form and exhibits limited complexing ability, predominantly acting as a bidentate ligand. When coordinated to platinum(II),

EDTA can form tetradentate or bidentate complexes by sequentially displacing chloride ligands, first with nitrogen atoms, followed by carboxylate oxygens [207]. However, in the conditions used here, only the nitrogen atoms are likely to participate in bonding, forming a bidentate complex. A possible structure of the Pt-EDTA complex is shown in Figure 6.4.

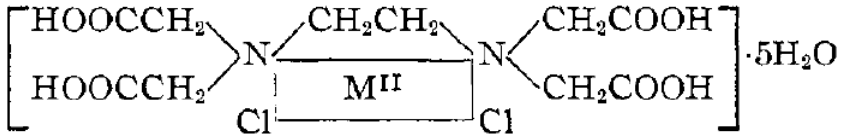

Figure 6.4: Possible chemical structure of the bidentate EDTA complex with platinum(II) (referred as M^{II}) [207].

To avoid bath decomposition, hydrazine must only be added to the plating solution only after the pH has been adjusted and Pt-EDTA complex has formed. For this purpose, the bath constituents were prepared in three separate aqueous solutions:

- Solution A, containing $Na_2EDTA{\cdot}2H_2O$ dissolved in deionized water;
- Solution B, containing K_2PtCl_4 in deionized water, with pH adjusted using HCl;
- Solution C, containing $N_2H_4{\cdot}H_2O$ in deionized water.

The three separate solution, as they were first famulated in [203], for 100 ml deposition solution are given in Table 6.3. Stability in guaranteed by combining the solution in order: solution B into A followed by the addition of C into the A+B mixture.

	Solution A	**Solution B**	**Solution C**	**Dilution**
Deionized water	30 g	30 g	25 g	15 g
$Na_2EDTA{\cdot}2H_2O$	0.5 g	/	/	/
K_2PtCl_4	/	0.1561 g	/	/
$N_2H_4{\cdot}H_2O$	/	/	0.1 g	/
HCl (37 vol%)		6.7 g		

Table 6.3: First formulation of the three solution making up 100 ml of the electroless Pt deposition bath.

Compound weights were measured using a METTLER TOLEDO™ ME54 analytical balance (METTLER TOLEDO International Inc., Columbus, OH, USA), with capacity 52 mg; readability and guaranteed repeatability 0.1 mg. The pH of the plating solution is monitored using a METTLER TOLEDO™ Seven Excellence pH-meter model S400 with an InLab® Viscous Pro-ISM sensor. Before immersion of the substrates, solutions were pre-heated to the desired deposition temperature using an IKA™ C-MAG HS7 digital hot plate (IKA-Werke GmbH & Co. KG, Staufen, Germany) equipped with an ETS-D5 controller and a PT1000 sensor. Depositions were carried out in glass beakers under constant magnetic stirring to prevent temperature and concentration gradients. Deposition temperature was varied between 50 °C, 55 °C and 60 °C, to study its effect of the coating process and on quality of the obtained coatings. Temperatures lower than 50 °C and higher than 60

°C where not explored because of activation and stability issues, respectively. Subsequently, the effect of pH, concentration of reagents (Pt salt, complexing agent and reducing agents) and bath loading (defined as the ratio between volume of solution and surface area to be coated) were investigated. Once an optimal bath formulation was established, the method's versatility was assessed by plating substrates with different chemical composition and its influence of plating rate was explored. Eventually, a bath restoration procedure (commonly referred to as *metal turnover*) was developed to replenish the consumed reactants and extend bath lifespan.

6.2 Manufacturing of Pt-aluminide coatings by industrial method

For the first part of the experimental activity, discussed in Chapter 7, electroless deposited and electrodeposited Pt aluminides where compared and contrasted. To validate electroless method as a reliable alternative to conventional electrodeposition for the preparation of Pt films prior to aluminizing, all subsequent processing steps other than electroless deposition (i.e. electrodeposition of Pt, pre-aluminizing diffusion and aluminizing) where conducted by Nuovo Pignone Tecnologie srl, a Baker Hughes company, using the industrial protocols currently employed. Before Pt deposition, René N4 superalloy substrates are sandblasted with corundum mesh 120 at 4-6 atm pressure with 15-20 cm blast distance. Following sandblasting, the samples underwent sequential cleaning in deionized water, acetone, and an ultrasonic bath at 70 °C for 25 minutes.

Pt electrodeposition was performed using with Johnson Matthey® Q-salt electrolyte solution, depositing 10.7 mg/cm^2 of Pt on each substrate. For comparison, an equivalent Pt loading was achieved via electroless deposition at the Laboratory of Engineering of Materials and Surface Treatments (LIMS) at Sapienza University of Rome. Assuming a bulk Pt density of 21.45 g/cm^3, the deposited mass corresponds to a theoretical film thickness of approximately 5 µm. This value is only indicative, as porosity and structural imperfections reduce the effective density of the deposited layer, making actual thicknesses slightly higher.

After Pt deposition, the pre-aluminizing diffusion heat treatment is performed in vacuum (< 5x10^{-3} mbar) with the following time-temperature schedule:

Intentionally left blank

A graphical representation of the schedule is reported in Figure 6.5.

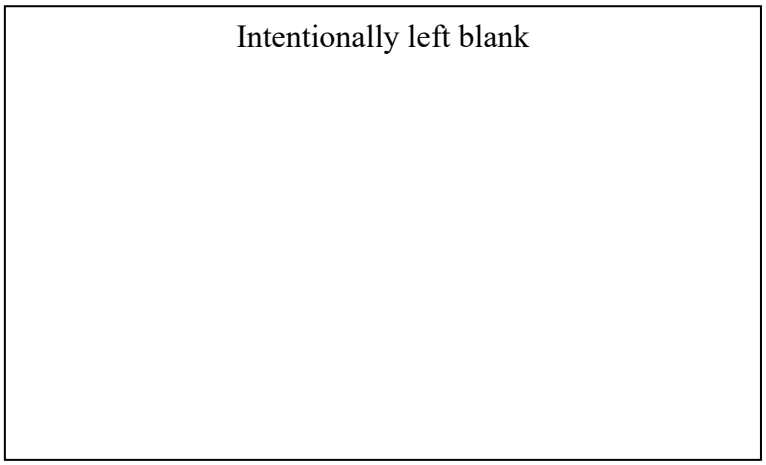

Figure 6.5: Time-temperature schedule of the prior-alumininizing diffusion heat treatment.

This treatment is intended to dilute Pt from the outer layer, to uniform Pt concentration across the resulting aluminide. If no diffusion heat treatment is performed, the top layer of the aluminide would result in single phase $PtAl_2$ [106].

After the diffusion treatment, aluminizing is performed using the slurry method. Main components of the slurry are:

- CrAl powders (with 55 wt% Cr content), with particle size 50-100 μm, are used as aluminum source;
- NH_4Cl and AlF_3 are used as activator salts, to create Al vapor phase and facilitate its diffusion to the substrate;
- Binder (gel), used to mix the CrAl particles and the activator salts. It ensures that particles are evenly distributed and that the slurry has the rheology for spraying.

Composition for 6 kg of slurry are reported in Table 6.4:

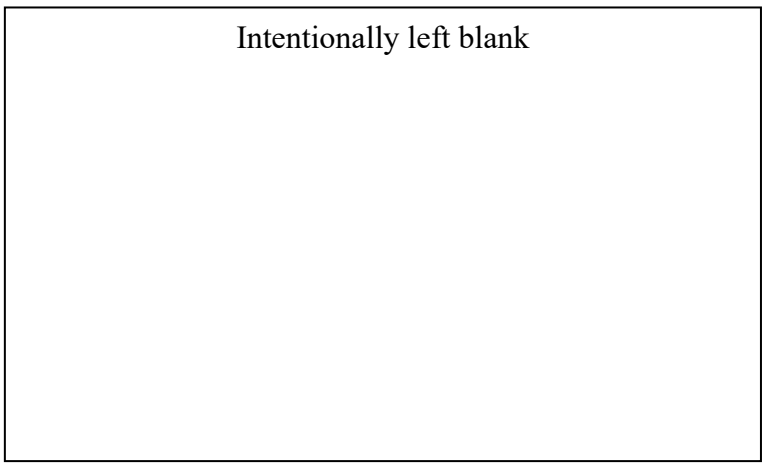

Table 6.4: Formulation for 6 kg of slurry.

Before slurry application, samples were sandblasted using 220 mesh corundum. The slurry was applied using an airbrush at 6.5 atm with a 45° angle and 50 cm standoff. Multiple passes were used

to reach a 400–600 µm slurry thickness, with 1 h drying at 60 °C between passes. After the final coat, samples were heated at 150 °C for 3 h to remove NH_3.

The aluminizing heat treatment is performed under argon atmosphere (1000-1090 mbar) with the following temperature-time schedule:

Intentionally left blank

This schedule is shown in Figure 6.6.

Intentionally left blank

Figure 6.6: Time-temperature schedule of the alumininizing heat treatment.

The first dwell allows aluminizing by Al reaction with the substrate, the second dwell promotes interdiffusion and formation of the desired protective phases. It also serves annealing for the superalloy, to promote the precipitation of secondary phases that increase mechanical strength.

6.3 Optimization of the slurry aluminizing process

The second part of the experimental activity, discussed in Chapter 9, aimed at the development of an optimized slurry aluminizing process, at laboratory scale, with focus on the achievement of a more uniform Al distribution and a precise control over coating microstructure. Renè N4 nickel based

superalloys are used as substrates and the same slurry recipe as the industrial process is adopted. The process for slurry preparation and application, schematized in Figure 6.7, is the following:

1. NH_4Cl was added to the polymeric binder. As soon as the two are mixed, the binder starts to dissolve;
2. CrAl powders and AlF_3 are mixed together manually and added to the NH_4Cl+binder solution, followed by magnetic stirring for at least 30 min (Figure 6.7 (a));
3. The slurry is loaded into an Iwata G3 airbrush (Anest Iwata Corporation, Yokohama, Japan) at room temperature (Figure 6.7 (b)) and sprayed onto the substrate at 0.3 MPa working pressure (Figure 6.7 (c)) and 45° incidence angle.

Between each pass, the samples are dried in an oven at 60 °C for 1h; once the desired slurry amount is deposited, the samples are heated at 150 °C for 3h, to remove residual NH_3.

Prior to slurry deposition, the substrates were sandblasted with corundum mesh 80, to guarantee the same surface finishing and to promote slurry adhesion.

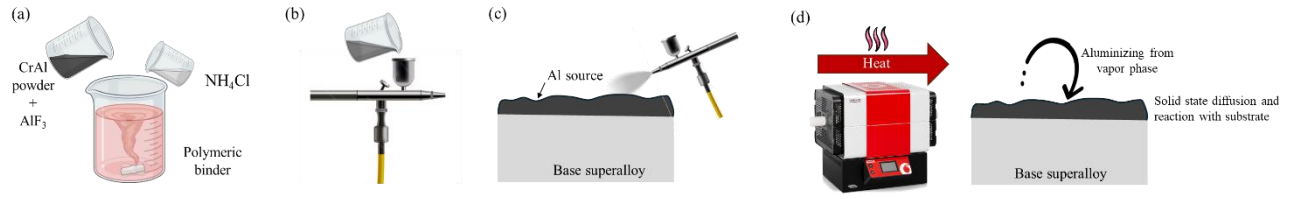

Figure 6.7: Schematic representation of the main step of the slurry aluminizing process: (a) slurry preparation; (b) pouring of the slurry in an airbrush; (c) spraying on the base superalloy; (d) aluminizing heat treatment.

SEM micrograph and XRD analysis of as-received CrAl powder are reported in Figure 6.8 (a) and (b), respectively. All peaks in the XRD spectra can be attributed to the Al_8Cr_5 intermetallic (JCPDS 29-0015), consistently with the 45 wt% Al and 55 wt% Cr nominal composition.

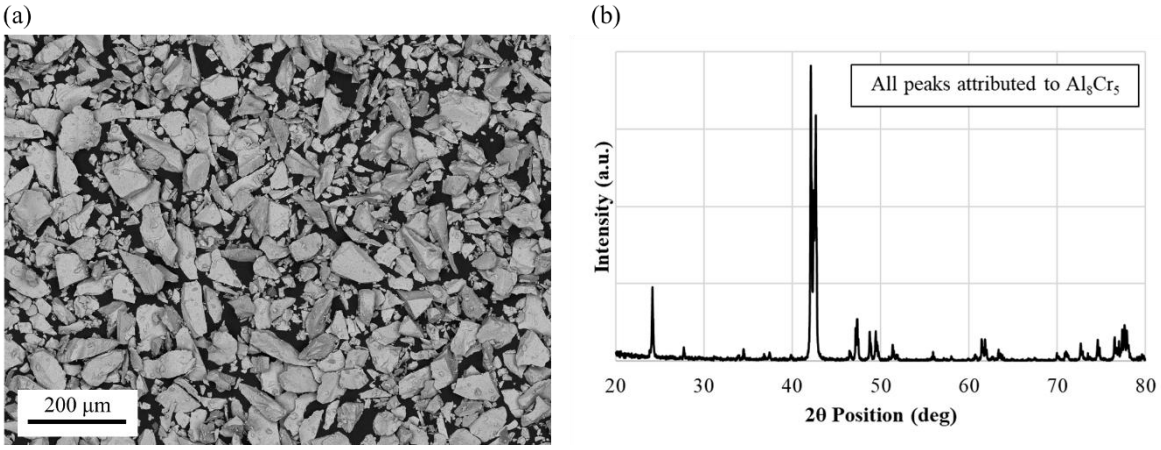

Figure 6.8: SEM-BSE micrograph (a) and XRD spectra (b) of as-received CrAl powders.

Figure 6.9 shows the cross-sectional SEM-BSE micrograph of the slurry layer (120 mg/cm^2) after the drying step at 150°C for 3h, along with the EDS map. The slurry layer appears uniform across the

sample, with homogeneous distribution of CrAl particles. The F signal arises from the fluorine of the AlF_3 activator salt and is present all along sample cross section, though unevenly.

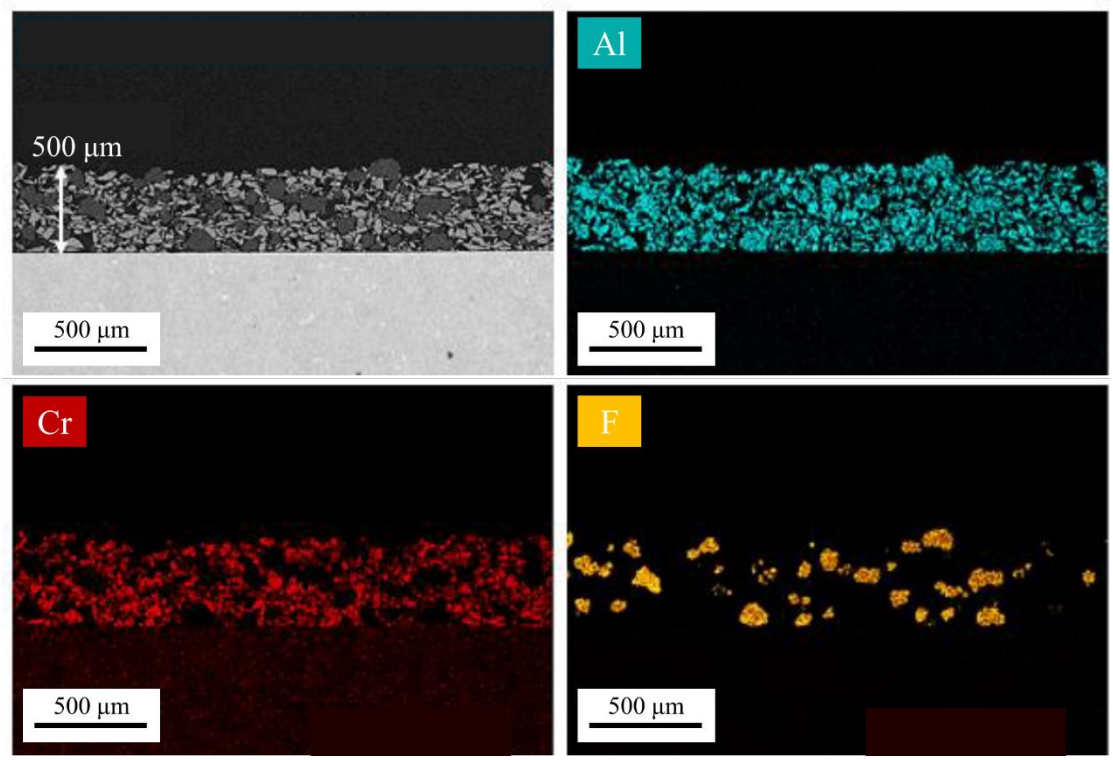

Figure 6.9: SEM-BSE micrograph and EDS map of the slurry layer after drying at 150 °C for 3h.

Eventually, a two-step aluminizing process was performed in a Carbolite-Gero tube furnace (Carbolite-Gero, Sheffield, UK) (Figure 6.7 (d). The first step, which allows aluminizing by Al reaction with the substrate, is performed under argon flux at 0.5 L/min:

1. Heating up to 1100 °C at maximum ramp rate 5 °C/min;
2. Dwell at 1100°C for 4 h;
3. Cooling down to room temperature.

After this, samples are taken out the furnace and excess unreacted slurry is removed. The second step, aiming promote interdiffusion and formation of the desired protective phases, is performed under argon flux at 2.0 L/min:

1. Heating up to 900 °C at maximum ramp rate 5 °C/min;
2. Dwell at 900°C for 6 h;
3. Cooling down to room temperature.

To optimize the process, the effects of the amount of slurry deposited on the substrate (in terms of $mg_{slurry}/cm^2_{\ sample}$) and of the amount of slurry present in the reaction chamber (in terms of $mg_{slurry}/cm^3_{chamber}$) were investigated. First, quantities equal to 80, 100, 120 and 150 $mg_{slurry}/cm^2_{sample}$ were studied, and best results were selected in terms of β-NiAl formation and distribution through the thickness of samples. Once the best amount of deposited slurry was selected, the influence of slurry

load in the reaction chamber was studied varying it between 1.63, 3.25, 6.50 and 13.0 $mg_{slurry}/cm^3_{chamber}$ and the best results were selected in terms of microstructure and β-NiAl distribution. A schematic representation of the investigated parameters is reported **Figure 6.*10*:** Parameters investigated in the slurry optimization activity: (a) coverage effect, investigated by varying the initial slurry layer thickness; (b) Vapor phase concentration effect, investigated by varying the slurry amount in the reaction chamber.Figure 6.10.

For the manufacturing of Pt-modified aluminides, 10.0 mg/cm^2 of Pt were deposited onto the base superalloy by electroless method and a the prior-diffusion heat treatment was performed according to the industrial process at the Baker-Hughes "Nuovo Pignone Tecnologie srl" facility in Florence, before slurry aluminizing.

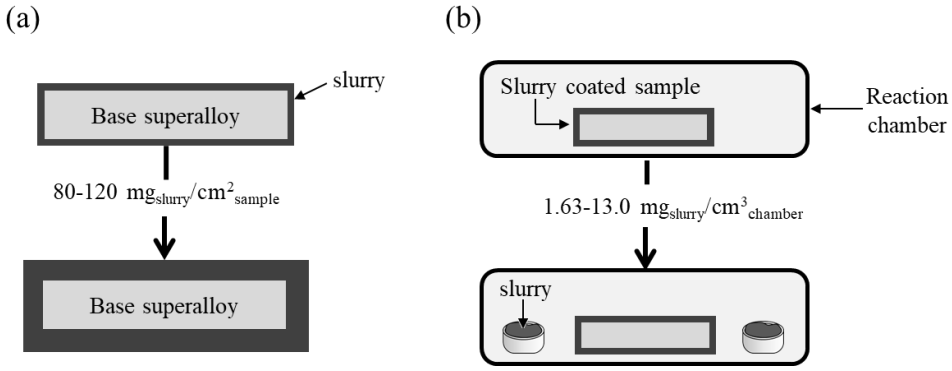

Figure 6.10: Parameters investigated in the slurry optimization activity: (a) coverage effect, investigated by varying the initial slurry layer thickness; (b) Vapor phase concentration effect, investigated by varying the slurry amount in the reaction chamber.

6.4 Coating characterization

Surface morphology, coating thickness and microstructure after all the manufacturing steps were evaluated with a Field Emission Gun–Scanning Electron Microscope (FEG-SEM) Tescan Mira3 (Tescan, Brno, Czech Republic) equipped with an Edax Octane Elect Energy Dispersive X-Ray Spectroscopy (EDS) system (Edax/Ametek Inc., Berwyn, PA, USA). Edax Team v.5 software was used for elementary analysis.

Cross-sectional observation of samples was prepared by mounting in epoxy resin (EpoThin 2, Buehler Ltd., Lake Bluff, IL, USA) and subsequent polishing with SiC papers (P400 grit to P1200 grit) and water-based diamond suspension (up to 1 μm finishing) (Buehler Ltd., Lake Bluff, IL, USA).

The crystalline phases present in the coatings were investigated by X-Ray Diffraction analysis (XRD) with a Philips X'Pert diffractometer (PANalytical BV, Almelo, The Netherlands), operating at 40 KV and 40 mA with CuKα radiation. Minimum scan range of acquisition was 20–80° (2θ), with a feed step of 0.02° and acquisition time of 2 s.

6.5 Manufacturing of electroless-Ni modified Pt-aluminides

The first modification of electroless-deposited Pt-aluminides was done introducing an external nickel layer, after Pt deposition, also deposited by means of electroless method. Purpose of this additional layer is to modify the concentration gradients during the pre-aluminizing diffusion heat treatment, to promote Pt dilution and hinder the formation of brittle $PtAl_2$ phases in the outermost region of the aluminide, aiming to create a single-phase β-(Ni,Pt) al layer. In addition to altering phase formation, the introduction of the pure nickel layer offers other microstructural and potentially oxidation-related benefits. Specifically, it acts as an additional and localized Ni source during the aluminizing process, leading to the formation of a thicker and more uniform β-NiAl bond coat [73]. This not only enhances the reservoir of the protective phase, but also reduces Ni depletion from the underlying superalloy. As a result, two positive effects can be achieved: first, it limits the formation and growth of the initial IDZ, which is typically characterized by chemical gradients and microstructural complexity; second, and more critically, it helps suppress the formation of TCP phases. These form as a result of long-term interdiffusion between the bond coat and the superalloy substrate, especially when elements such as refractory metals (e.g., W, Mo, or Re) segregate due to Ni depletion. TCP phases are brittle and can act as crack initiation sites, significantly compromising the mechanical integrity of the component, particularly under creep conditions [102,208,209]. By mitigating Ni depletion from the substrate, the added Ni layer indirectly limits the driving force for TCP formation, thus contributing to improved long-term structural stability and creep resistance of the coated alloy.

The solution for electroless nickel deposition is prepared according to [210], and bath composition is reported in Table 6.5.

Compound	Concentration (g/L)	Function
$KHCO_3$	45.00	Complexing agent
$N_2H_4{\cdot}H_2O$	31.30	Reducing agent
K_2CO_3	61.90	Complexing agent
$NiCl_6{\cdot}6H_2O$	23.76	Metal ion source
K_2HPO_4	87.00	Buffer
KOH	19.56	pH regulator

Table 6.5: Formulation of the electroless nickel plating bath.

First, a solution comprising $KHCO_3$ and $N_2H_4{\cdot}H_2O$ is prepared in 334 ml of deionized water and kept under magnetic agitation for 4 h, after which K_2CO_3 is added to form hydrazine-carboxylate ($N_2H_3COO^-$), a compound having a lower redox potential that pure hydrazine. Nickel chloride is then dissolved in about 34 ml of deionized water and added to the mixture to form the metal ion complex.

Eventually a solution comprising K_2HPO_4 and KOH in prepared in 166 ml of deionized water and added to the mixture to control its pH.

Pt-plated Renè N4 superalloy is used as substrate. Before immersion in the plating bath, samples are carefully rinsed in deionized water. A fresh plating solution was prepared for each deposition and the substrates were immersed in the solution pre-heated at 80 °C. Deposition was performed under continuous magnetic stirring, and deposition time was varied between 0.5 h and 4h according to the required thickness of the coating: samples with pure Ni coatings of 5, 10, 20 and 40 µm thickness were prepared, to evaluate the effect of thickness on coating microstructure, phase formation and oxidation resistance. Deposition parameters are reported in Table 6.6.

Parameter	Value
Temperature	80 °C
pH	11
Bath loading	55 ml/cm^2
Plating rate	10 µm/h

Table 6.6: Deposition parameters for electroless pure nickel plating.

SEM micrograph of the typical structure of the Pt/Ni bilayer is reported in Figure 6.11 (a). EDS maps are shown in Figure 6.11 (b), (c) and (d), to confirm purity of each layer.

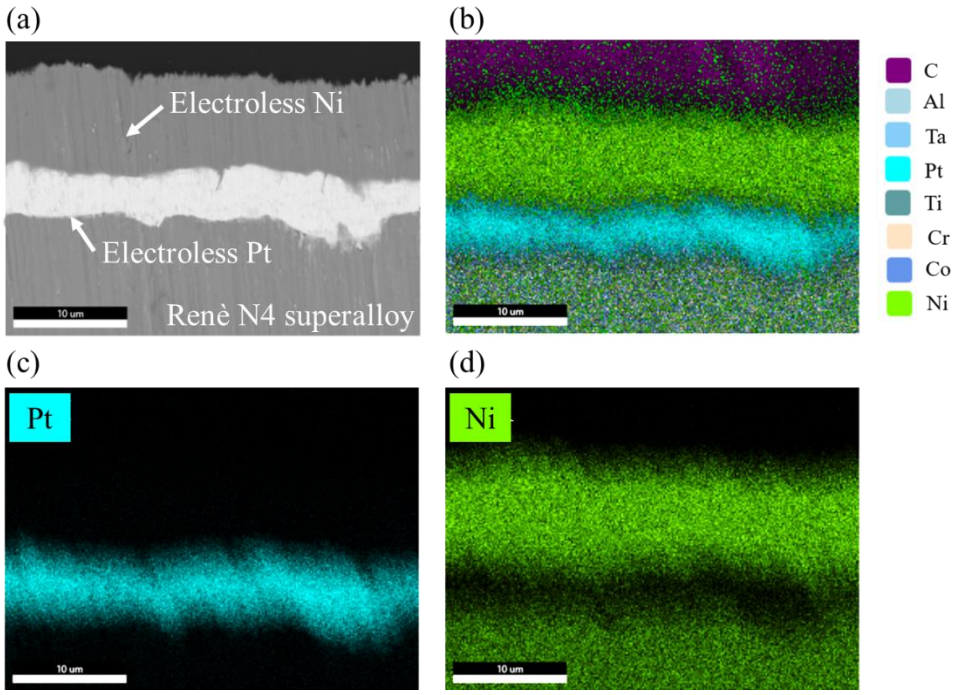

Figure 6.11: SEM-BSE cross sectional micrograph of the electroless Pt/Ni bilayer (a). EDS map showing element signal overaly (a), Pt signal only (b) and Ni signal only (c).

6.6 Manufacturing of Al_2O_3 nanocomposite Pt-aluminides

For the fabrication of Pt-aluminide nanocomposites, commercial α-Al_2O_3 nanoparticles with an average particle sizes of 78 nm were purchased from NanoGrafi (Nanografi, Çankaya/Ankara Turkey). SEM micrographs of the as-purchased nanoparticles are shown in Figure 6.12 (a).The chemical purity of the nanoparticles was confirmed by the EDS analysis reported in Figure 6.12 (b), which revealed only peaks corresponding to aluminum and oxygen.

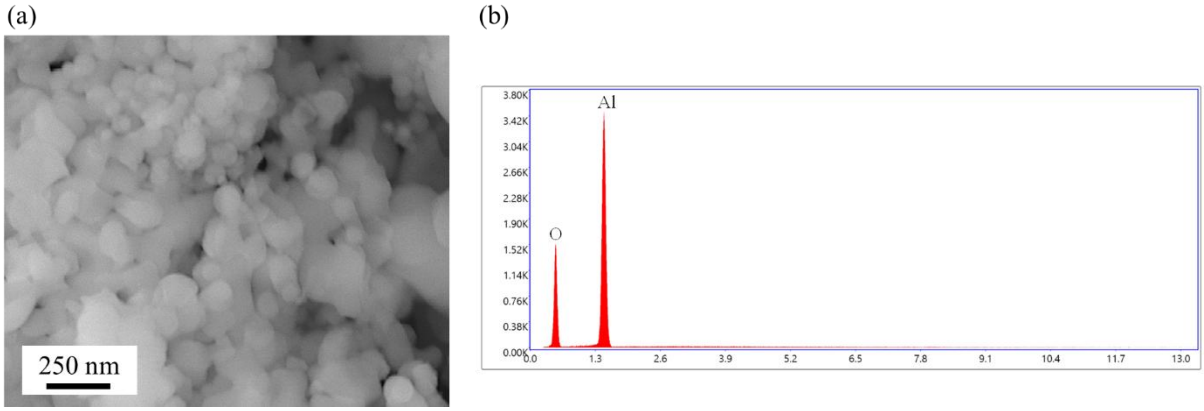

Figure 6.12: SEM micrographs (a) and EDS analysis (b) of as-purchased Al_2O_3 nanoparticles.

The particle size distribution (PSD), derived from over 230 measurements taken from SEM images, is presented in Figure 6.13. The calculated mean size was 79.3 nm.

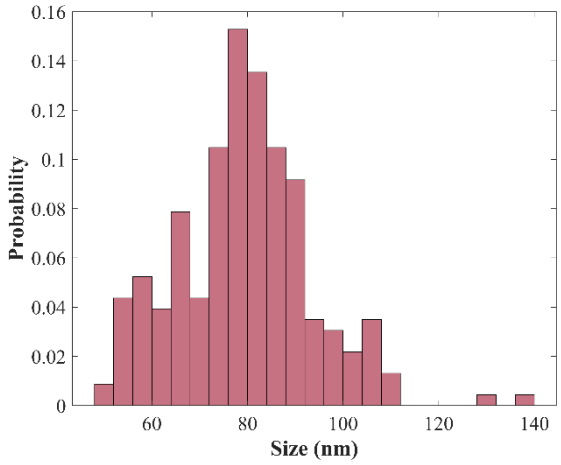

Figure 6.13: PSD of as-purchased Al_2O_3 nanoparticles.

Al_2O_3 nanoparticles were selected for their expected function as nucleation sites for the epitaxial growth of the thermodynamically stable α-Al_2O_3 oxide scale. Additionally, thanks to their high ζ-potential, they are expected to be relatively easily dispersed in the electroless solution, preventing agglomeration into large clusters [211].

Nanoparticles were dispersed in deionized water to create suspensions at concentrations of 0.25 g/L, 0.5 g/L, 1.0 g/L, and 1.5 g/L. Before addition to the plating bath, each suspension was ultrasonicated using a Fisher Scientific 505 tip sonicator at 20% intensity for 10 minutes to break up agglomerates and improve dispersion. For each 100 mL of Pt plating solution, 5 mL of nanoparticle dispersion was

added after 10 minutes of pure Pt deposition. The pH was then adjusted with HCl (37 vol%) to restore optimal plating conditions. With the addition of nanoparticles, the platinum plating solution appears more whitish and opaque, as shown in Figure 6.14.

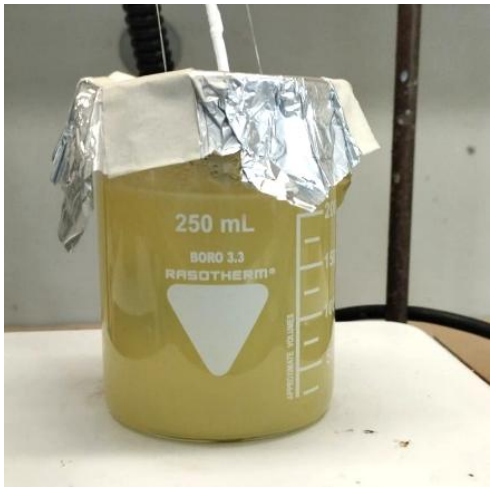

Figure 6.14: Electroless platinum plating solution after the addition of Al_2O_3 nanoparticles.

According to the model proposed by Ger et al. [212], nanoparticle incorporation into the coating proceeds through a three-step mechanism:

1. Transfer of particles from the bulk solution to the substrate via forced convection;
2. Loose adsorption onto the cathode surface;
3. Irreversible entrapment into the growing metal matrix, given adequate residence.

The use of finely dispersed nanoparticles, which can be easily kept in suspension, can aid their adsorption onto the substrate and incorporation within the growing coating. The volume fraction of incorporated particle was measured by an image processing and analysis MATLAB routine (v. R2022b, The MathWorks Inc., Natick, MA, USA) opportunely developed. The image analysis procedure (schematized in Figure 6.15) aims to precisely identify Al_2O_3 nanoparticles in the coating and is based on the compositional contrast between the Ni matrix and Al_2O_3 nanoparticles. Al_2O_3 appears darker in BSE images compared to the metal matrix (Figure 6.15 (a)), therefore, binarizing according to the proper color threshold in the grayscale can enable the precise identification of particles (Figure 6.15 (b)). Figure 6.15 (c) show the process output with red spots corresponding to particles superimposed to the original SEM micrograph, to prove the good matching. Detailed description of the quantitative image analysis procedure is reported in a previous work by the same author [213].

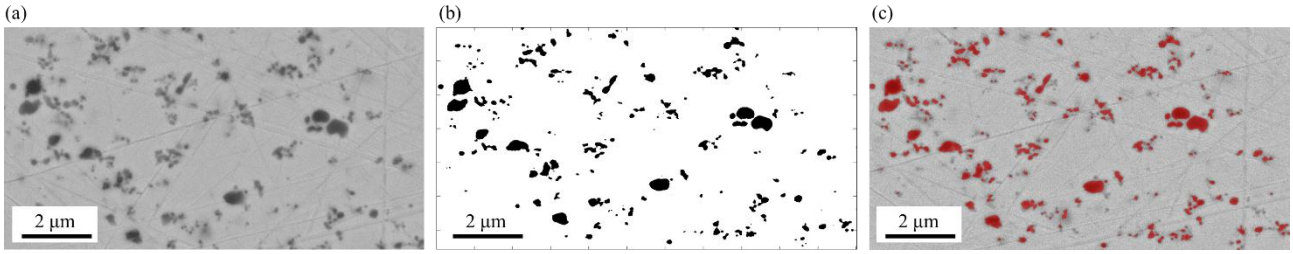

Figure 6.15: Representation of the quantitative image analysis procedure for identification of particles: (a) original SEM-BSE micrograph; binarizing process for particles identification (b); routine output with particles (c) reported in red and superimposed on the original micrograph, to demonstrate the good matching.

Nanoparticles incorporation (i.e., Al_2O_3 content value within the coating) can be quantified and are expressed as area fraction (A%). This parameter is defined as the ratio between the cross-sectional area occupied by nanoparticles and the area of the analyzed cross-section. Area fraction can be considered equal to the volume fraction when spherical-like shapes are considered [214], which is the case Al_2O_3 particles. Agglomeration of particles can also be calculated and expressed in terms of mean number of particles per agglomerate. This parameter is calculated as the ratio between the mean measured size of embedded reinforcement and the mean size of purchased particles (79.3 nm), and will be indicated with Na: the higher Na, the higher is the degree of nanoparticles agglomeration within the coating. The best concentration of particles to be incorporated in the coating is selected as the one that maximizes %A and the minimizes Na.

After deposition of the Pt nanocomposite layer, aluminide coatings are manufacture by the slurry method, with the diffusion and aluminizing schedules described in section 6.2.

6.7 Isothermal oxidation tests

Isothermal oxidation tests were conducted in static air at 1100 °C using a Lenton tube furnace (currently Carbolite-Gero, Sheffield, UK) to evaluate the high-temperature oxidation behavior of the prepared aluminide coatings. The total exposure time was 1000 hours, divided into alternating cycles of 7 and 14 hours for the initial 105 hours. Beyond this period, each cycle lasted 100 hours.

Specimens were introduced into the preheated furnace gradually, with a mean heating rate of 50 °C/min. At the end of each cycle, they were removed and air-cooled to room temperature at a controlled rate of 5 °C/min to minimize thermal shock. After cooling, the samples were stored in a desiccator containing silica gel to prevent moisture absorption.

Mass change due to oxide scale growth and/or spallation was recorded after each cycle using a Mettler Toledo analytical balance with a resolution of ±0.0001 g. For each coating type, at least four samples were tested, and results are presented as mean values with standard deviations.

To compare electroless and electrodeposited Pt-aluminide coatings, cross-sectional SEM observations and X-ray diffraction (XRD) analyses were conducted alternately every 7 and 14 hours

during the first 105 hours, and subsequently every 100 hours until 1000 hours were reached. For modified coatings, SEM and XRD evaluations were performed at 100 hours intervals throughout the entire test duration.

7. Study of the electroless Pt plating solution

Solutions for electroless platinum plating are prepared at room temperature under constant control over pH. Substrates are immersed after reaching the operating temperature and main streps of the plating process are illustrated in Figure 7.1.

Deposition starts immediately upon substrate immersion, evidenced by the formation of small gas bubbles on the surface of the sample (Figure 7.1, left). These bubbles result from the oxidation of hydrazine to nitrogen gas (N_2), indicating the onset of redox reactions. Initially, the bubbles are small and persistent, but as the deposition progresses, a mild effervescence can be observed. In the early stages deposition the coating appears black and non-reflective (Figure 7.1, center), but as it thickens, its appearance transitions to white and bright (Figure 7.1, right).

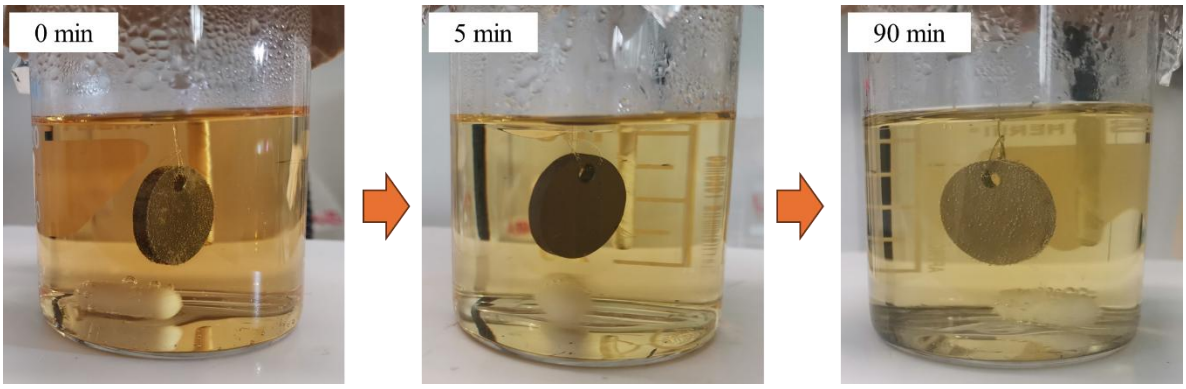

Figure 7.1: Stages of the Pt plating process on Renè N4 nickel based superalloy.

This visual transformation reflects the underlying microstructural evolution of the coating during growth. Initially, deposition occurs preferentially at catalytic high-energy surface sites, where platinum nanoparticles nucleate (Figure 7.2 (a)). These particles subsequently grow and coalesce laterally to form a continuous platinum monolayer (Figure 7.2 (b)) [215]. The initial black color can be attributed to the particular light absorption and scattering behavior of the nanostructured surface. As deposition continues, the platinum nodules enlarge and the surface flattens (Figure 7.2 (c)), leading to a brighter and more reflective (white) appearance.

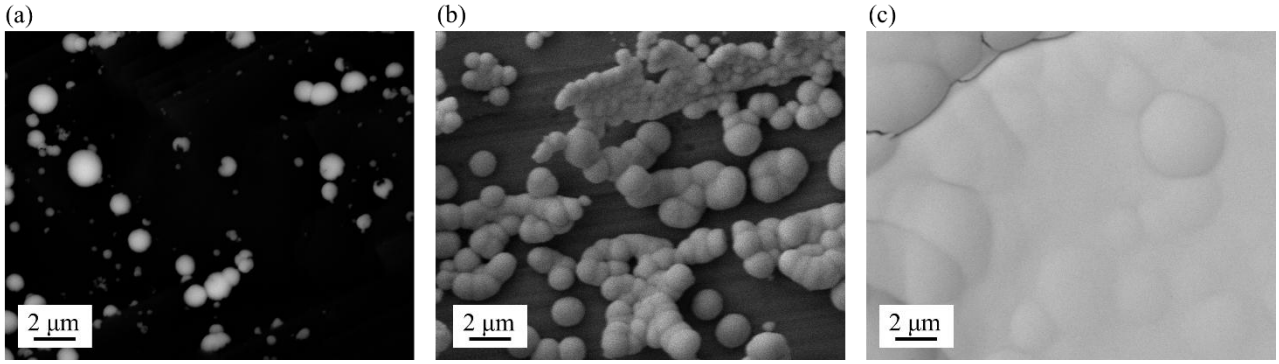

Figure 7.2: Nucleation and growth mechanism of the Pt film: (a) Pt nanoparticles nucleating at catalytic sites; (b) growth and coalescence of Pt particles; (c) morphology of the thick Pt layer.

Given the autocatalytic nature of the process, platinum itself catalyzes further deposition. The reaction proceeds as long as thermal energy is supplied and Pt ions remain available in solution. As the deposition advances, the plating solution gradually becomes lighter in color, as shown in Figure 7.3, reflecting the depletion of Pt ions.

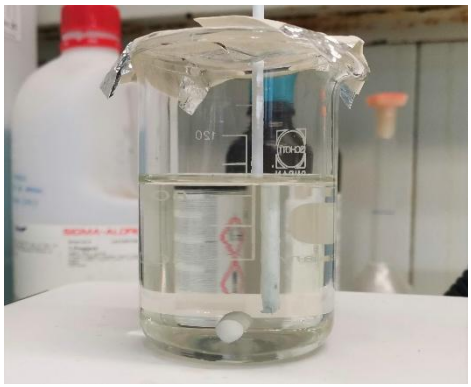

Figure 7.3: Plating solution after deposition, depleted from Pt ions.

7.1 Effect of temperature and pH

Temperature acts as the driving energy source for electroless deposition, influencing both the reactivity of chemical species in solution and the kinetics of the plating process. As such, deposition temperature significantly affects the plating rate, coating microstructure, and surface morphology. In general, higher temperatures accelerate the deposition rate and promote faster film growth. However, excessive reactivity at elevated temperatures can trigger uncontrolled deposition reactions, resulting in non-uniform coatings with poor adhesion. Moreover, deposition may occur on unintended surfaces (e.g. scratches on the beaker) or even lead to premature bath decomposition.

Deposition can initiate at temperatures as low as 40 °C, but at such low temperatures, the plating rate is too slow to meet industrial requirements. Conversely, when the temperature exceeds 60 °C, the process becomes difficult to control, often yielding non-adherent and defective coatings. Therefore, to find a good compromise between deposition rate and coating quality, the effect of temperature was systematically investigated in the range of 50–60 °C. Two platinum salt concentrations were evaluated: 1.5 g/L and 3.0 g/L, both equimolar with the complexing agent to ensure bath stability.

Figure 7.4 (a) presents the plating rate curves for a Pt salt concentration of 1.5 g/L. The curves for 55 °C and 60 °C overlap closely during the first hour of deposition, suggesting similar initial kinetics. However, after this period, the plating rate at 55 °C noticeably slows down. A gradual reduction in plating rate over time is expected due to the consumption of Pt^{2+} ions; however, the change in slope observed at 55 °C suggests that a higher energy input becomes necessary once the Pt^{2+} concentration drops below a critical threshold. In contrast, the curve at 50 °C shows a nearly linear trend, but the deposition rate is significantly lower. This indicates that at 50 °C, the energy input is insufficient to

sustain faster deposition kinetics, and no substantial effect from Pt depletion is observed within the 2-hour timeframe, likely because the ionic concentration remains relatively high throughout.

To further examine the influence of Pt^{2+} depletion on deposition kinetics as a function of temperature, experiments were repeated using a doubled Pt salt concentration of 3.0 g/L. The results, shown in Figure 7.4 (b), confirm that increased Pt availability leads to substantially faster deposition at all temperatures. In this case, the plating rate curves at 55 °C and 60 °C remain nearly identical over the entire 2-hour period, reinforcing the conclusion that Pt^{2+} concentration plays a critical role in sustaining high deposition rates when sufficient thermal energy is provided. The deposition at 50 °C still proceeds at a significantly slower rate, consistent with the results obtained at lower concentration, thereby highlighting the limiting role of temperature in determining plating efficiency when energy intake is too low.

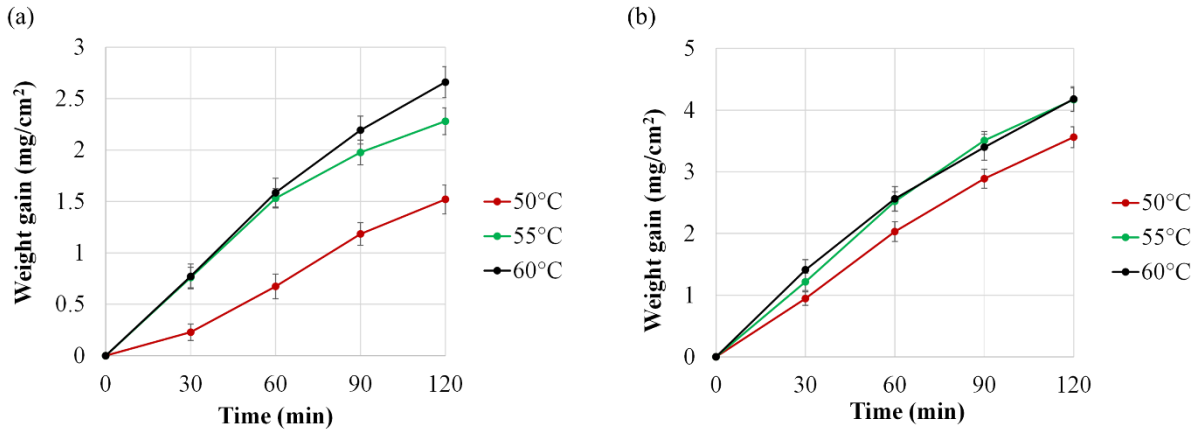

Figure 7.4: Plating rate curves as a function of temperature for Pt salt concentration in the plating solution equal to 1.5 g/l (a) and 3.0 g/l.

To more precisely identify the optimal deposition temperature, the influence of temperature on coating quality was examined for samples deposited at 55 °C and 60 °C, which exhibited similar plating rates. Surface morphology of coating deposited at 60°C is shown in Figure 7.5 (a). The film appears extensively cracked and displays poor adhesion in several areas, with visible regions of spallation where the underlying substrate is exposed. The higher magnification micrographs in Figure 7.5 (b) reveals the presence of Pt nanoparticles on the exposed substrate surface, suggesting that spallation occurred during deposition, followed by renewed nucleation and growth on the newly exposed areas. The rise in the bath temperature increases the reaction rate but at the same time it compromises the bath stability [216]. Although some cracks are also observed in the coating deposited at 55 °C (Figure 7.5 (c) and (d)), the deposition appears uniform, and no regions of delamination or detachment are visible. The formation of tensile stresses during Pt deposition is a well-documented phenomenon, particularly in electrodeposited films [217,218]. These stresses are primarily attributed to the entrapment of gas bubbles (e.g., H_2 or N_2) or other stress-inducing species

during growth. At 60 °C, the increased energy input accelerates the reaction rate, which likely amplifies stress accumulation, ultimately leading to cracking and partial detachment of the Pt layer, thus compromising coating integrity.

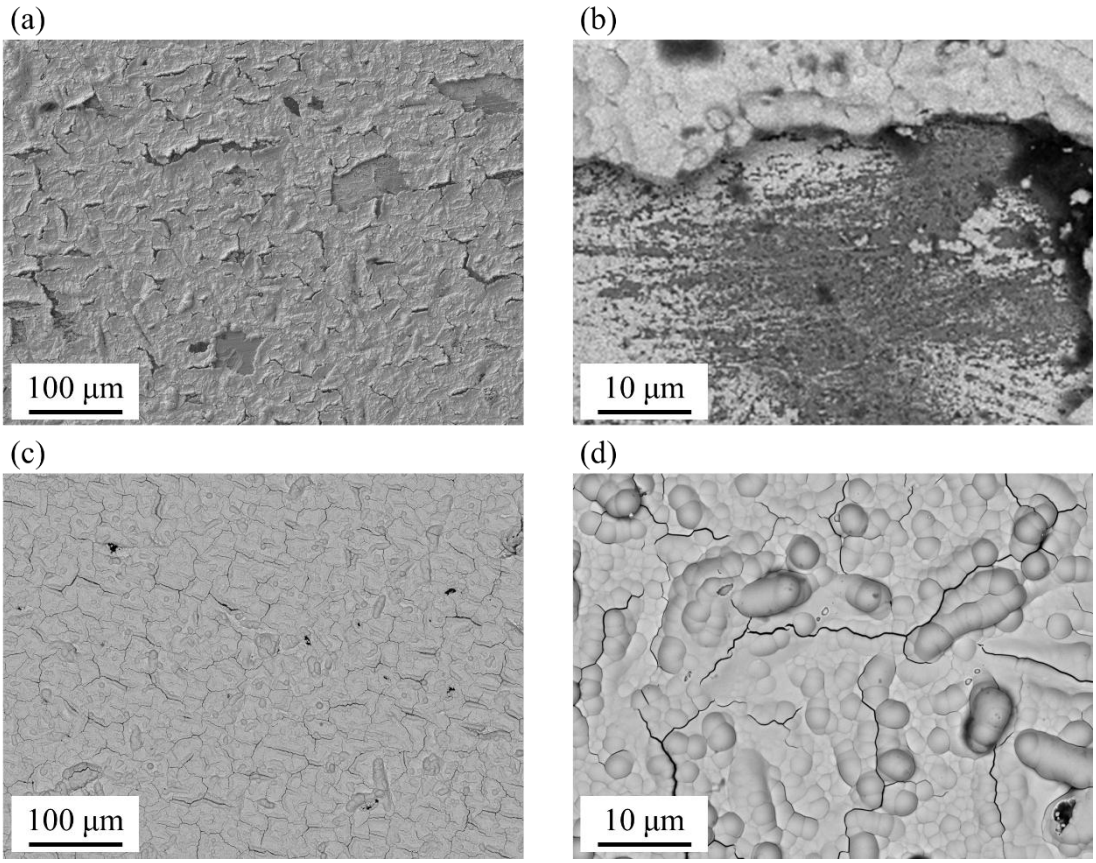

Figure 7.5: SEM-BSE top view micrographs of Pt coatings deposited at 60°C (a, b) and 55°C (c, d).

Cross-sectional SEM micrographs, reported in Figure 7.6, support the above observations. Despite exhibiting similar thicknesses, consistent with the plating rate curves, the coating deposited at 60 °C (Figure 7.6 (a)) is characterized by the presence of through-the-thickness cracks and visible internal interfaces, indicating regions where spallation and subsequent re-deposition occurred. In contrast, the coating deposited at 55 °C (Figure 7.6 (b)) appears dense, continuous, and adherent throughout the cross-section, confirming superior coating quality when deposition is performed at the lower temperature.

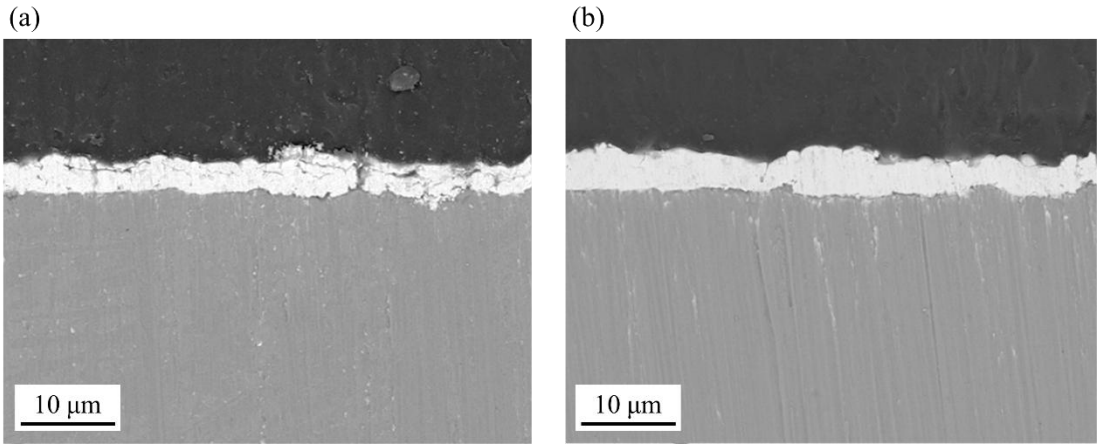

Figure 7.6: SEM-BSE cross sectional micrographs of Pt coatings deposited at 60°C (a) and 55°C (b).

pH is a critical parameter for maintaining the stability of the electroless plating bath, as it significantly affects the reducing power of hydrazine. While it was observed that bath stability is generally ensured at pH values below 1, pH also influences coating growth and plating rate. To investigate this effect, experiments were conducted at 55 °C using a platinum salt concentration of 3.0 g/L (equimolar with the complexing agent). The pH was systematically lowered to a minimum value of 0.5, and the results are presented in Figure 7.7. A clear trend is observed and the plating rate decreases with decreasing pH value. This behavior can be attributed to the reduction in the potential difference between hydrazine and the platinum ions at lower pH values, which diminishes the thermodynamic driving force for metal reduction. However, at pH equal to 0.5, the deposition process becomes unstable, and large sections of the coating delaminate from the substrate. This suggests that pH not only influences reaction kinetics but also plays a role in the development of tensile stresses during film growth. Although the extent of surface cracking does not appear to vary significantly with pH, the severe spallation observed at very low pH indicates a threshold below which stress buildup compromises coating adhesion.

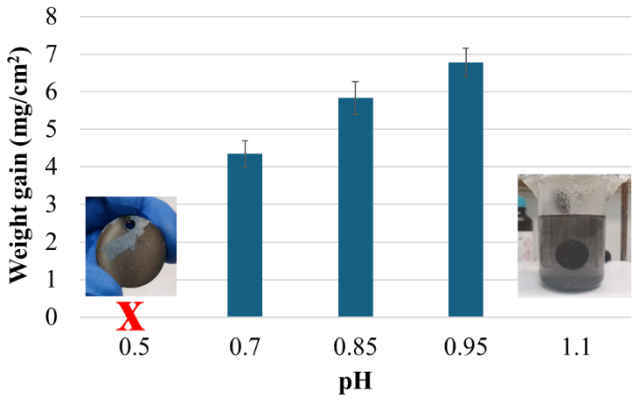

Figure 7.7: Plating rate as a function of pH value of the electroless Pt plating solution.

7.2 Effect of concentration of reagents

The concentration of reagents in the plating solution directly affects their chemical activity and the rate of the deposition reactions. Higher concentrations result in a greater number of reactive species, increasing collision frequency and the likelihood of successful redox reactions. As a result, reagent concentration influences not only the overall coating growth rate but also its morphology.

To evaluate the role of each component in the plating process, the effects of varying the concentrations of the complexing agent, platinum salt, and reducing agent were systematically investigated.

The first parameter studied was the concentration of the complexing agent. To assess how the degree of complexation influences deposition, the concentration of the complexing agent was varied while keeping the platinum salt concentration constant. Three ratios were examined: half-molar, equimolar, and double-molar relative to the platinum salt. Concentrations of complexing agent lower of this threshold increase the probability of uncontrolled reduction of Pt^{2+} to metallic nanoparticles, while higher concentrations approach the solubility limit of EDTA in acidic conditions.

The effect of Na_2EDTA concentration on plating rate is shown in Figure 7.8. The faster plating rate is observed at lower concentrations of the complexing agent; as its concentration increases, the deposition rate gradually decreases. This is consistent with literature findings [171,219], which show that increasing complexation reduces the amount of free metal ions available for reduction and lowers their redox potential, thus slowing down the reaction kinetics. However, while lower degrees of complexation yield faster deposition, they also reduce the control over bath stability, increasing the risk of uncontrolled nanoparticle formation or unwanted deposition on container surfaces.

A mild reduction in plating rate is observed after 60–90 minutes of deposition, likely due to the gradual depletion of Pt^{2+} ions. This effect is more pronounced when the complexing agent concentration is lower, likely due to faster ion consumption in the first half of process. As a result, the total mass gain after 2 hours is similar across all three formulations, despite initial differences in plating rate.

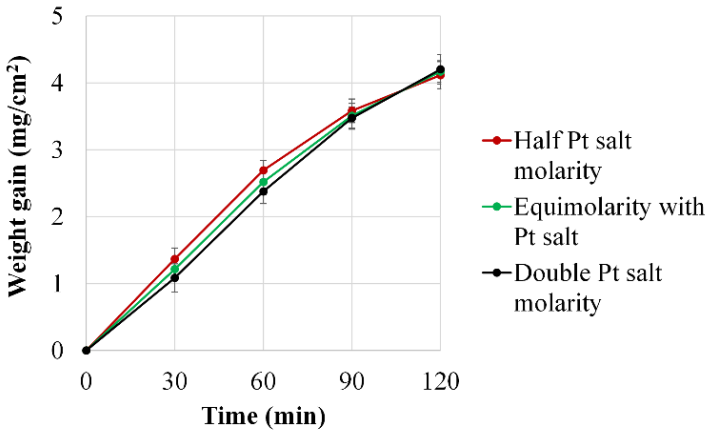

Figure 7.8: Plating rate curves for different Na_2EDTA concentration (expressed as ratio with the Pt salt concentration).

In addition to deposition rate, complexation strongly influences coating morphology. At lower complexing agent concentrations, the surface morphology is dominated by a high density of small Pt nodules, as shown in Figure 7.9 (a). As the concentration of complexing agent increases (Figure 7.9 (b) and (c)), the nodules grow larger and the surface becomes progressively smoother. This trend can be explained by nucleation phenomena: with more free metal ions available at lower complexation, more nucleation sites are activated, resulting in finer nodule structures due to limited lateral growth of each nucleus. Conversely, higher complexation favors slower nucleation but allows more extensive growth and coalescence of fewer nuclei, producing a smoother coating surface [220,221].

These results confirm that the degree of complexation plays a central role not only in controlling deposition kinetics but also in defining the microstructure and surface characteristics of the resulting Pt coatings.

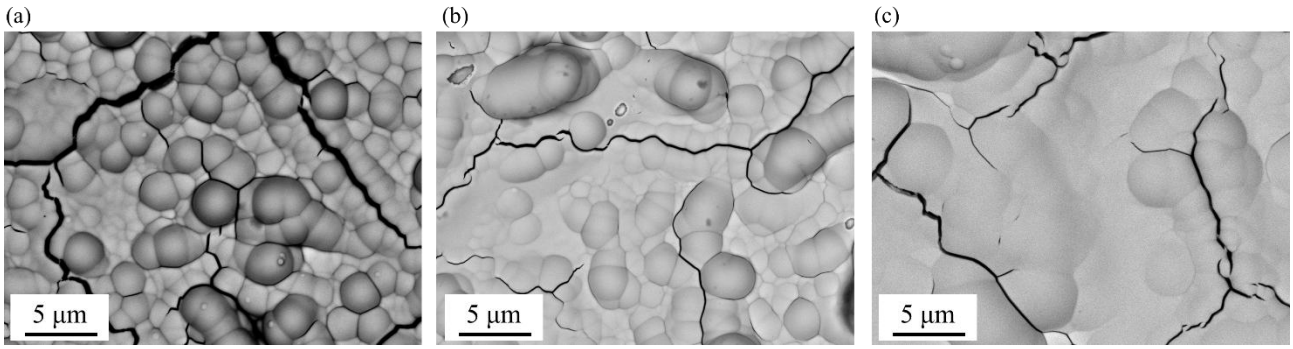

Figure 7.9: SEM-BSE micrographs of morphology of coatings with different complexing agent ratios: (a) half-molar, (b) equimolar, and (c) double-molar relative to the platinum salt.

The concentration of platinum salt in the plating solution plays a critical role in determining both the kinetics and efficiency of the deposition process. Specifically, it governs the availability of Pt^{2+} ions for reduction and influences their electrochemical reduction potential, as described by the Nernst equation [222]. Higher concentrations of platinum salt increase the thermodynamic driving force for reduction, enhancing the plating rate.

In this study, the effect of K_2PtCl_4 concentration was investigated while maintaining equimolarity with the complexing agent (Na_2EDTA), to ensure complete complexation of Pt^{2+} ions and minimize the risk of uncontrolled reduction and nanoparticle precipitation. Four concentrations were tested: 1.5, 3, 4, and 5 g/L. The corresponding plating rate curves are shown in Figure 7.10.

As expected, the plating rate increases with increasing platinum salt concentration. The curves exhibit similar shapes, with higher concentrations resulting in steeper slopes, indicating faster coating growth.

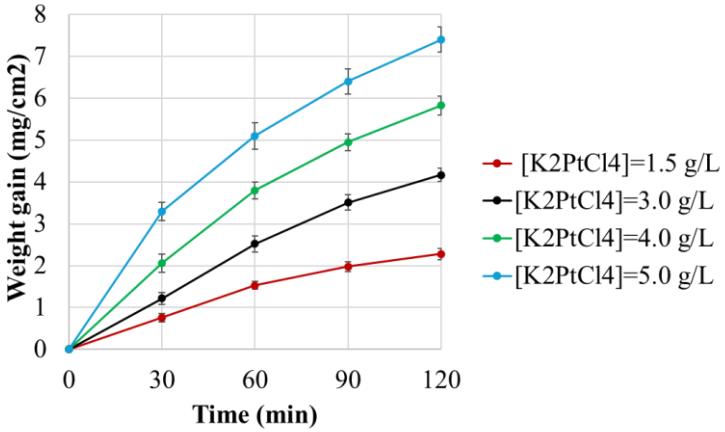

Figure 7.10: Plating rate curves for different K_2PtCl_4 concentration.

The total amount of platinum deposited over a 2-hour deposition period, shown in Figure 7.11, follows an almost linear trend with respect to K_2PtCl_4 concentration. A least-squares linear fit yields a correlation coefficient, R_{corr}, of 0.998 and a slope of 1.47 (y = 1.47x), demonstrating strong correlation between metal ion concentration and deposited mass.

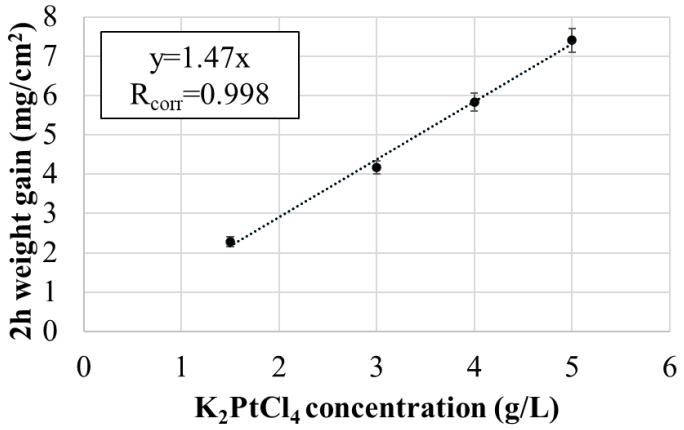

Figure 7.11: Total amount of platinum deposited over a 2-hour deposition period; dashed line represents linear fitting of data.

Despite differences in deposition rate, no significant variations in coating morphology were observed across the different concentrations. This suggests that under equimolar complexation conditions, morphology is primarily governed by the degree of complexation and not by the absolute concentration of Pt^{2+}. As a result, the primary benefit of increasing platinum salt concentration is

achieving greater coating thickness within a shorter time frame. However, while higher concentrations improve deposition rate, they must be balanced against economic and practical considerations. Excessively high Pt concentrations may not be fully utilized, especially in the frame of Pt layers for aluminide coating modification, reducing the overall efficiency of the bath. From an industrial perspective, the optimal concentration should be selected based on the desired coating thickness and process duration, aiming to maximize bath efficiency (i.e., the ratio of Pt deposited to Pt initially available in solution). Additionally, overly concentrated solutions may approach stability limits, further emphasizing the importance of balancing deposition rate with bath stability and cost.

Finally, the effect of hydrazine concentration on the electroless platinum deposition process was investigated. Hydrazine concentrations of 2.0, 2.5, 3.0, and 3.5 g/L were tested, while keeping platinum salt concentration constant at 3.0 g/L and maintaining equimolar Na_2EDTA, to ensure bath stability through full complexation. Although all selected concentrations correspond to an excess of reducing agent relative to Pt^{2+}, it was observed that at concentrations lower than 2 g/L uniform coatings could not be achieved, likely due to insufficient reducing power to drive consistent nucleation and growth. Conversely, when hydrazine concentration exceeded 3.5 g/L, the reaction became too vigorous and uncontrollable, leading to uncontrolled Pt reduction.

Interestingly, plating rate curves showed no significant variation with changing hydrazine concentration across the tested range. This result contrasts with common literature findings for other electroless systems, where plating rate typically increases with the concentration of the reducing agent [223–225]. However, Steinmetz et al. [188] observed a similar trend for the electroless deposition of noble metals, reporting that hydrazine concentration had minimal effect on the growth rate. This can be explained by the fact that, once a certain threshold is reached, further increases in reducing agent concentration do not contribute to faster deposition because the process becomes limited by other factors, such as the rate of Pt^{2+} diffusion or the surface reaction kinetics [221].

Although hydrazine concentration did not influence the plating rate, it had a notable impact on the morphology and integrity of the deposited coatings. Figure 7.12 presents SEM top-view micrographs of coatings obtained using 2.0 (a), 2.5 (b), 3.0 (c), and 3.5 (d) g/L hydrazine. Coatings deposited at the lowest hydrazine concentration exhibit large regions of spallation and poor adhesion. As hydrazine concentration increased, the degree of cracking progressively decreased, reaching a minimum at 3.0 g/L. However, further increasing the concentration to 3.5 g/L led to a renewed increase in cracking and surface damage. This non-monotonic trend suggests that hydrazine concentration affects the internal stress state of the coating during deposition. It can be hypothesized that at lower hydrazine concentrations, the deposition struggles and could possibly proceed non-uniformly, resulting in heterogeneous stress distribution and weak bonding to the substrate. As the

concentration increases to an optimal range (around 3.0 g/L), the reaction proceeds more uniformly, promoting more consistent grain growth and reducing internal tensile stresses. However, at even higher concentrations, the rapid and exothermic nature of the reaction could lead to the entrapment of gas (e.g., nitrogen or hydrogen) within the growing film, thereby increasing internal stresses and leading to cracking. Excessive hydrazine may increase the generation of nanoscale gas bubbles during the reduction of Pt^{2+}, which are embedded in the growing film and can interfere with crystal growth, contributing to microvoids, roughness, or local delamination, all of which can negatively affect coating integrity.

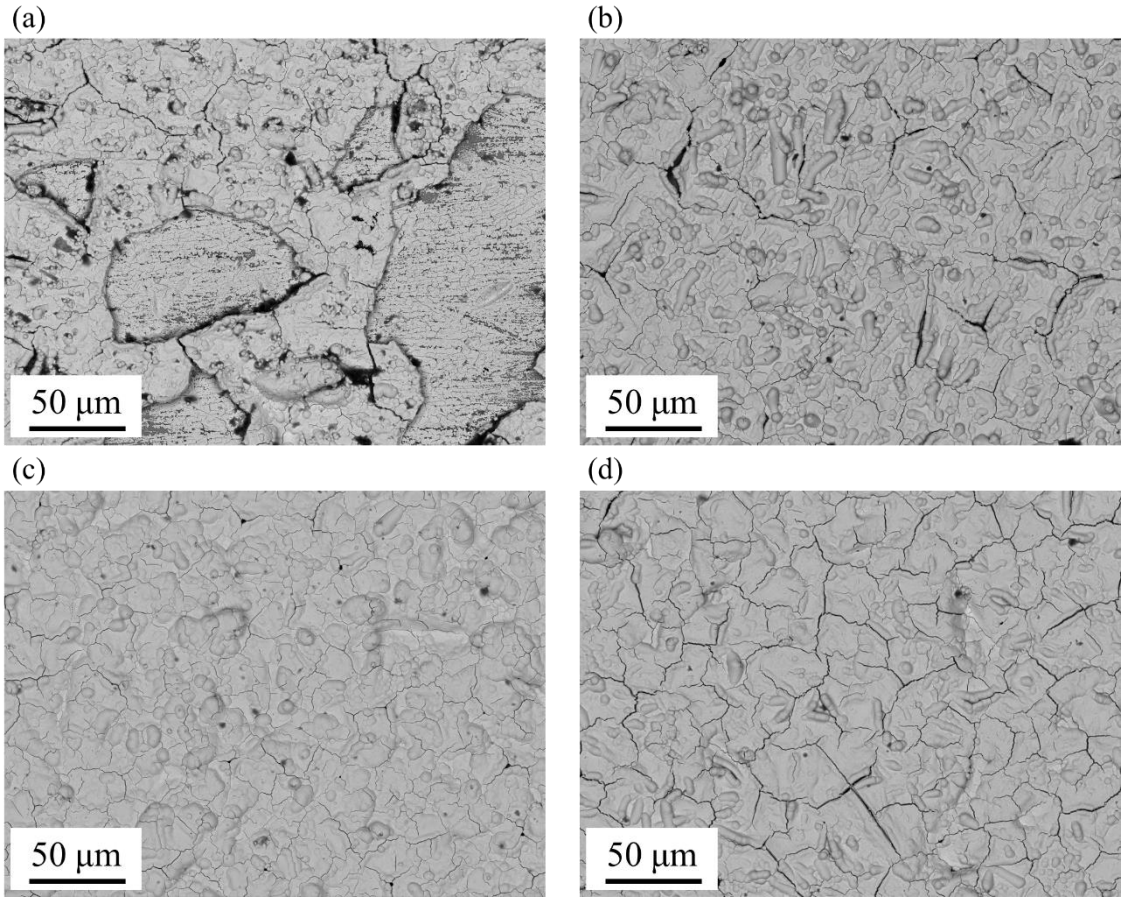

Figure 7.12: Surface morphology of Pt coating deposited with different concentrations of hydrazine: (a) 2.0 g/L, (b) 2.5 g/L, (c) 3.0 g/L and (d) 3.5 g/L.

Based on the above investigations, the best plating parameters, identified to achieve a reliable compromise between plating rate, bath stability, and coating quality, are: 4.0 g/L of K_2PtCl_4, 0.34 g/L of $Na_2EDTA{\cdot}2H_2O$ (equimolar with Pt salt) and 3.0 g/L of $N_2H_4{\cdot}H_2O$, with 55 °C deposition temperature and 0.85 pH. From now on, all deposition are performed with this bath formulation, if not otherwise specified.

7.3 Effect of bath loading

The influence of bath loading, defined as the ratio between the volume of plating solution and the surface area to be coated (expressed in mL/cm²), was investigated to evaluate its impact on the deposition process. Experiments were performed using a sample with a surface area of 9.2 cm², immersed in 75 mL, 100 mL, and 250 mL of plating solution, corresponding to bath loadings of 8.14, 10.87, and 27.17 mL/cm², respectively.

Bath loading directly affects the availability of platinum ions per unit area, which in turn influences both the plating rate and the impact of Pt depletion from the plating solution over time. As shown in Figure 7.13, increasing bath loading results in a higher total mass gain after 360 minutes of deposition. This trend is expected, as a greater volume of solution provides more Pt ions, thereby sustaining the reaction for a longer duration and mitigating the slowdown typically caused by ion depletion.

Interestingly, a different behavior is observed during the initial phase of deposition (first 2 hours). At lower bath loadings, the initial plating rate is higher. This effect can be attributed to the role of catalytic surface area in initiating the redox reaction. A minimal amount of catalytic surface is required to effectively trigger the deposition process. When the surface-to-volume ratio is too low (as in the high-bath-loading condition), the system may struggle to achieve a sufficient activation threshold, leading to a slower onset of the deposition process. In contrast, smaller volumes with the same surface area promote a faster activation of the redox reactions, enhancing the initial growth rate. However, as deposition progresses, Pt ion availability becomes the rate-limiting factor, which is more evident at lower bath loadings. For instance, deposition becomes slower than that of 27.17 ml/cm^2 after approximately 60 minutes at 8.14 mL/cm² and after 120 minutes at 10.87 mL/cm², due to the faster depletion of Pt ions in the more limited solution volumes.

It is also important to point out that plating rate is not expected to increase indefinitely with bath loading. Beyond a certain threshold, the surface becomes saturated with catalytic sites, and the rate of metal ion reduction is limited by the reaction kinetics at the surface, rather than the bulk concentration of ions in the solution [210].

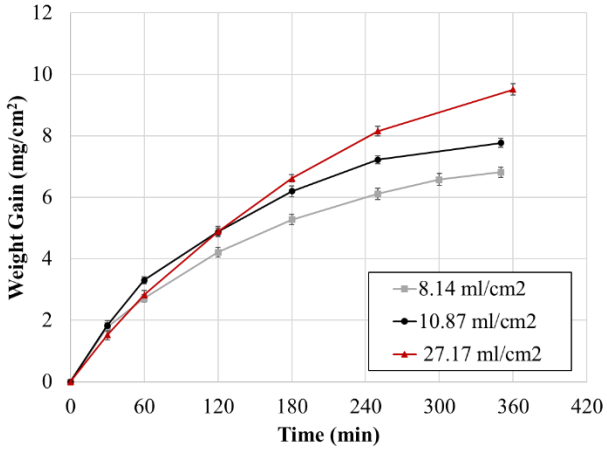

Figure 7.13: Plating rate curves at different bath loading.

7.4 Flexibility over different substrate composition

Electroless deposition processes are highly sensitive to the chemical composition and surface condition of the substrate, which must exhibit catalytic activity to initiate and sustain metal reduction. Surface contaminants, especially non-conductive species or oxides, can significantly inhibit deposition. In conventional Ni-P electroless systems, for instance, steel substrates often require activation treatments, such as acid pickling in HCl, to remove native oxides and ensure a clean, reactive surface [171].In this study, however, no activation step was performed prior to deposition due to the extremely acidic nature of the Pt plating bath, which inherently promotes oxide removal and ensures catalytic surface conditions.

To evaluate substrate effects, electroless Pt deposition was performed on four Ni-based superalloys with varying chemical compositions and microstructures: René 108, René N4, GTD 111, and Inconel 625. These alloys have progressively increasing chromium (Cr) content, equal to 8.4 wt%, 10 wt%, 13.5 wt%, and 20–23 wt%, respectively, which is known to influence passivation behavior. Higher Cr content increases the alloy's tendency to form passive oxide layers that hinder the initiation of deposition [226].

Figure 7.14 presents the plating rate curves for each substrate, while Table 7.1 summarizes the average plating rates over 240 minutes. It can be observed that the plating rate decreases with increasing Cr content, consistent with the greater passivation tendency of Cr-rich surfaces.

However, the deposition dynamics vary significantly among substrates. René 108 exhibits a rapid initial deposition, with fast coating growth within the first 30 minutes. The rate then slows, likely due to Pt ion depletion in the bath. René N4 and GTD 111 exhibit a similar trend, with almost linear deposition over the first hour for the former and for the first 2h hours for the latter. Inconel 625, with

the highest Cr content, displays a nearly linear deposition rate throughout the entire process, suggesting a delayed initiation due to extensive surface passivation.

These differences can be attributed to the formation of chromium-rich passive films on the alloy surfaces. At higher Cr contents, fewer active nucleation sites are initially available, slowing the onset of autocatalytic deposition. However, once a continuous Pt monolayer is established, the deposition becomes autocatalytic and proceeds uniformly, regardless of the original substrate.

These differences in deposition behavior can be primarily attributed to the chromium content in the superalloys. Higher Cr content increases the tendency of the substrate to form a thin, passive oxide layer, which impedes the initial reduction of Pt ions and delays the onset of deposition. Despite this, the high acidity and strong reducing environment of the plating solution enable deposition to initiate at a limited number of active catalytic sites. From these initial sites, the Pt coating gradually expands laterally, eventually forming a continuous autocatalytic monolayer. In alloys with higher Cr content, the density of nucleation sites is lower, meaning that it takes more time to establish the continuous Pt layer. This results in a slower initial deposition rate. However, once the monolayer is complete, deposition proceeds in an autocatalytic manner and becomes largely independent of the substrate's original surface chemistry. Nevertheless, plating rate curves differ across substrates, even after monolayer formation. This is due to the varying rates of Pt ion consumption in the solution. Alloys with faster initial deposition (e.g., René 108) deplete the available Pt ions more quickly, leading to a noticeable slowdown in the later stages of deposition. In contrast, substrates like Inconel 625, with slower initial rates, experience more gradual Pt consumption, allowing a more consistent growth rate throughout the process. This is further illustrated by the intersection of the plating curves for René N4 and GTD 111 after 90 minutes, which aligns with their respective Cr contents: René N4, with lower Cr, initiates deposition more rapidly, whereas GTD 111, with higher Cr, begins more slowly but maintains a more consistent growth rate over time).

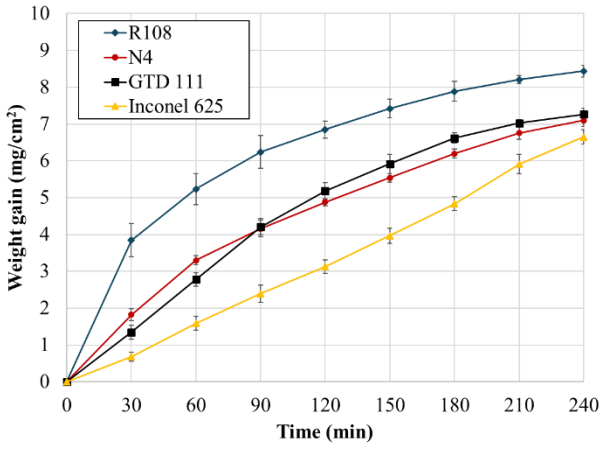

Figure 7.14: Plating rate curves minutes for deposition over different Ni-based superalloys.

Substrate	Average plating rate over 240 min (µm/h)
Renè 108	2.10
Renè N4	1.78
GTD 111	1.82
Inconel 625	1.67

Table 7.1: Average plating rates over 240 minutes for deposition over different Ni-based superalloys.

To confirm that deposition becomes uniform once the monolayer is formed, SEM micrographs of coatings on each substrate are shown in Figure 7.15. All coatings exhibit the characteristic cauliflower-like morphology and a similar degree of cracking, suggesting that growth stresses are also comparable across substrates. The only notable difference is that the coating on Renè 108 displays a finer, more refined morphology, with smaller nodules. This supports the hypothesis that higher initial nucleation activity occurs on this substrate: the greater number of active nucleation sites promotes the formation of numerous small nodules and, as a result, nucleation is favored over lateral growth, leading to a more refined nodular structure.

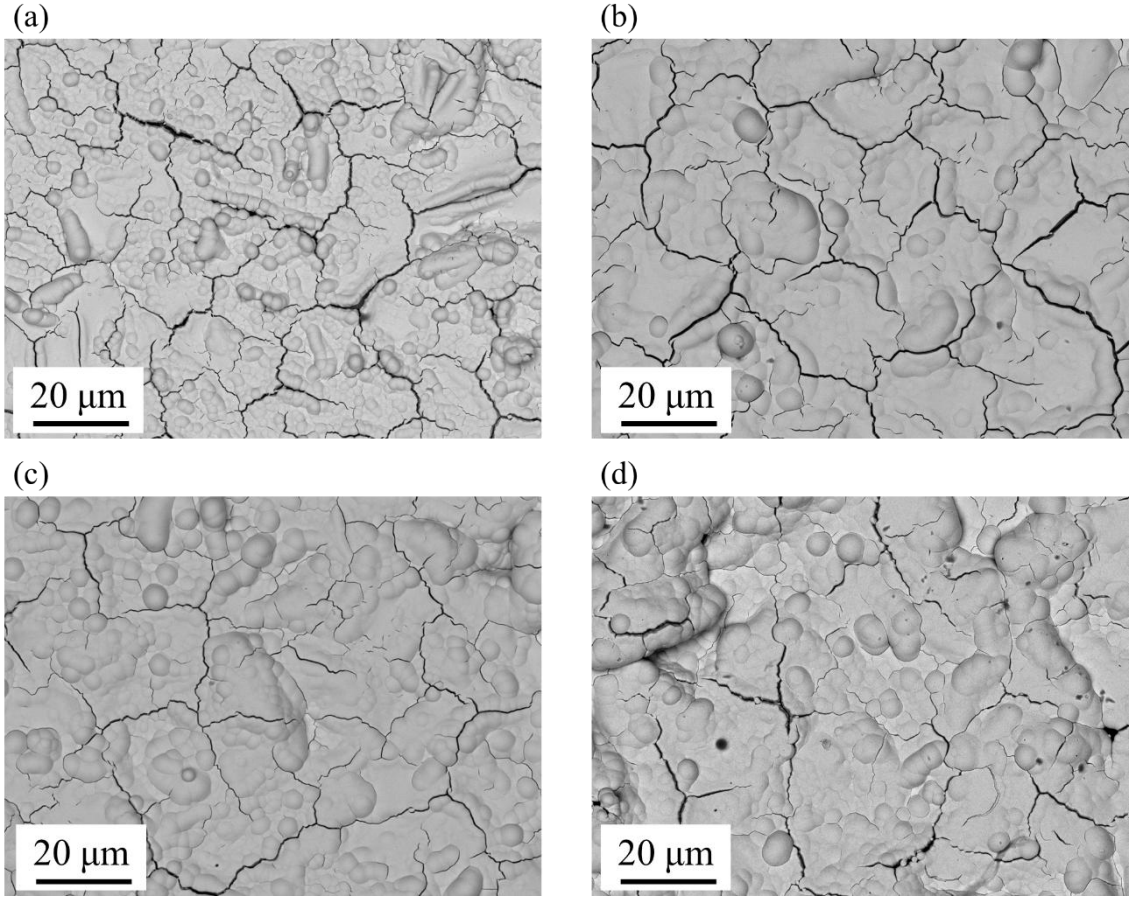

Figure 7.15: SEM top view micrographs showing morphology of Pt coatings deposited onto Renè 108 (a), Renè N4 (b), GTD 111 (c) and Inconel 625 (d).

7.5 MTO

The results discussed above highlight the crucial influence of platinum ion concentration and its gradual depletion on the electroless plating rate. Moreover, a minimum concentration of Pt ions is essential to initiate the autocatalytic deposition process. To develop a process suitable for industrial-scale applications, it is vital to ensure a stable deposition rate, extend bath lifespan, and improve process efficiency (i.e., the yield of deposited Pt relative to the Pt available in solution). For this reason, implementing a metal turnover (MTO) strategy, aimed at replenishing the consumed reagents in the plating bath, is a key step toward improving cost-effectiveness and minimizing waste.

As shown in Figure 7.16, the plating rate curve for electroless Pt deposition on René N4 superalloy exhibits a parabolic trend, with a correlation coefficient of 0.995 (fitting the equation $x = 5.221y^2 - 0.0354y$). This is characteristic of processes governed by Pt ion diffusion from the bulk solution to the substrate surface [227]. In such diffusion-limited systems, the gradual depletion of Pt ions results in a continuous decline in plating rate. To mitigate this effect and ensure a near-constant deposition rate over time, a controlled regeneration procedure is necessary to restore the initial concentration of metal ions and reactants.

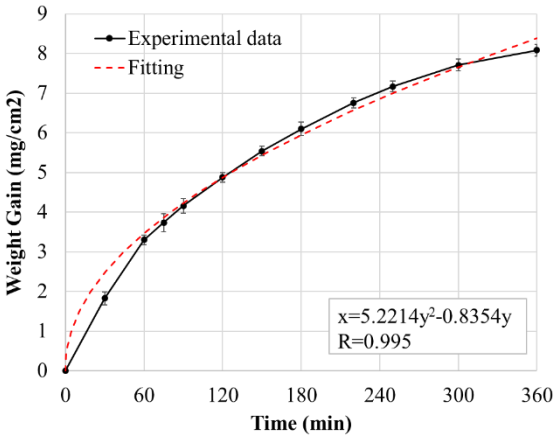

Figure 7.16: Plating rate curve on Renè N4 superalloy substrate and fitting of experimental data to confirm the parabolic rate.

The development of the MTO process focused on four key aspects: (i) identifying appropriate reagents to replenish both the complexed Pt ions and the reducing agent; (ii) integrating a pH adjustment step to maintain solution stability; (iii) defining the timing and method of addition to ensure consistent deposition while preserving operational simplicity; and (iv) verifying the absence of contamination in the coating after regeneration.

Experimentally, under the optimized plating conditions (4.0 g/L K_2PtCl_4, 3.4 g/L $Na_2EDTA{\cdot}2H_2O$, 3.0 g/L $N_2H_4{\cdot}H_2O$ at 55 °C and pH 0.85, with a bath loading of 10.7 mL/cm²), approximately 60 mg of Pt (0.0003075 mol) are deposited over 180 minutes in a 100 mL solution. Based on the overall redox reaction:

$$2PtCl_4^{2-} + N_2H_4 \rightarrow 2Pt + 8Cl^- + 2H_2 + N_2, \quad (7.1)$$

around 1.5377×10^{-4} mol of hydrazine are consumed and must be replenished.

Since Pt ions cannot be safely added to the plating solution in their free ionic form due to the risk of uncontrolled nanoparticle precipitation, they must be pre-complexed with $Na_2EDTA \cdot 2H_2O$ in equimolar ratio. Therefore, the regeneration requires adding:

- 0.1556 g K_2PtCl_4
- 0.1317 g $Na_2EDTA \cdot 2H_2O$
- 0.0094 g $N_2H_4 \cdot H_2O$

These reagents must be dissolved in 20 mL of distilled water before being added to the plating bath. This additional volume increases the total bath volume and slightly dilutes reagent concentrations. To compensate, extra quantities must be added proportionally:

- 0.08 g K_2PtCl_4
- 0.068 g $Na_2EDTA \cdot 2H_2O$
- 0.06 g $N_2H_4 \cdot H_2O$

Thus, the total amount of reagents to be added for full regeneration becomes:

- 0.2357 g K_2PtCl_4
- 0.1997 g $Na_2EDTA \cdot 2H_2O$
- 0.0694 g $N_2H_4 \cdot H_2O$

Maintaining the pH at 0.85 is essential for bath stability. However, the small volumes involved at laboratory scale prevent accurate pH measurement using a probe. Instead, the required HCl volume is calculated: to reach pH 0.85 in a 100 mL solution, 6.7 g of 37% HCl are required; for the 12 mL complexation solution, this translates to 1.34 g of HCl.

As with the original bath preparation, the MTO procedure involves preparing three separate regeneration solutions (detailed in Table 7.2). These can be stored and used as needed. In practice, after 90 minutes of deposition, solutions A_{MTO} and B_{MTO} are premixed and added to the bath, followed by solution C_{MTO}.

	Solution A_{MTO}	**Solution B_{MTO}**	**Solution C_{MTO}**	**Dilution**
Deionized water	6 g	5 g	5 g	4 g
$Na_2EDTA \cdot 2H_2O$	0.1997 g	/	/	/
K_2PtCl_4	/	0.2357 g	/	/
$N_2H_4 \cdot H_2O$	/	/	0.0694 g	/
HCl (37 vol%)		1.34 g		

Table 7.2: Formulation of the three solution for MTO of 100 ml electroless Pt deposition bath.

This regeneration method can be repeated indefinitely, as illustrated in Figure 7.17. The plating rate curve for the MTO-enabled process is shown in Figure 7.18. Linear fitting of the data confirms a constant deposition rate ($y = 2.4834x$, $R_{corr} = 0.999$), validating the effectiveness of the regeneration procedure.

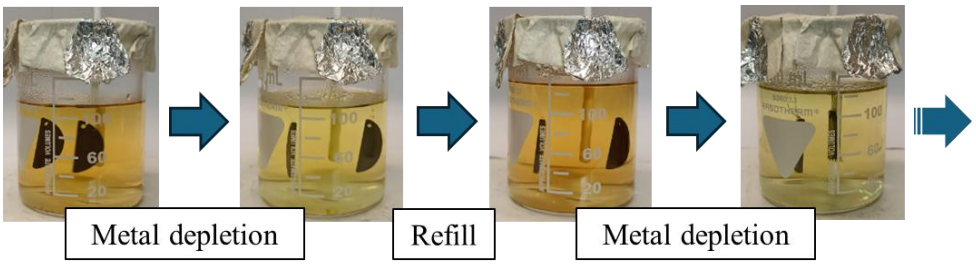

Figure 7.17: MTO procedure.

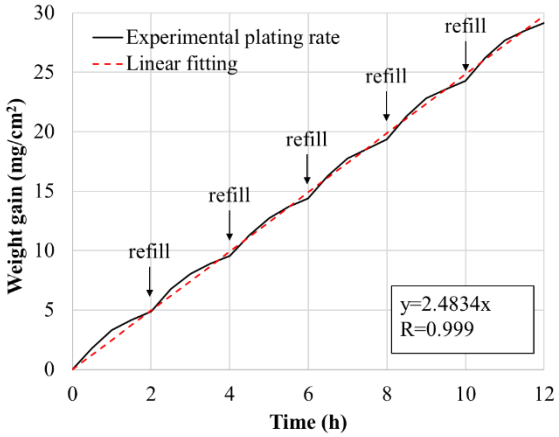

Figure 7.18: Plating rate curve of deposition with MTO procedure and fitting of experimental data to confirm the linear rate.

Crucially, coatings produced with repeated MTO cycles exhibit identical morphology, purity, and microstructure to those obtained from a single-use bath. No contaminants were detected via EDS analysis, even after depositing up to 40 mg/cm² of Pt (a value four times higher than the process target). The deposition bath can be regenerated and reused multiple times without risk of contamination or decomposition, as the only by-products besides metallic Pt are gaseous N_2 or H_2, which are naturally removed through effervescence. Consequently, the primary factor limiting the bath's otherwise virtually indefinite lifetime is the solubility of EDTA, the only reagent that accumulates during successive replenishments. Once repeated MTO cycles bring the bath close to the EDTA solubility threshold, complete bath replacement becomes necessary. The developed MTO strategy, therefore, ensures the best compromise between plating rate, bath stability, and Pt utilization, supporting long-term, scalable, and sustainable operation.

7.6 Conclusions

Based on the comprehensive investigation of the effects of temperature, pH, and the concentrations of the complexing agent, metal salt, and reducing agent, the optimal plating parameters were identified to achieve a reliable compromise between plating rate, bath stability, and coating quality (including morphology, cracking and uniformity). Special consideration was given to ensuring a Pt deposition target of approximately 10 mg/cm².

The results indicate that the best performance is obtained using:

- K_2PtCl_4: 4.0 g/L
- Na_2EDTA: 3.3 g/L (slightly above equimolar, to ensure full complexation while maintaining solution stability)
- Hydrazine monohydrate: 3.0 g/L
- Temperature: 55 °C
- pH: 0.85

These conditions provide a sufficiently high plating rate, maintain bath stability over time, and produce a dense, uniform, and adherent platinum coating with minimal cracking or spallation. The selection of 55 °C ensures controlled reaction kinetics, preventing excessive stress development while supporting efficient film growth. The selected pH supports both bath stability and a favorable reduction potential, while the optimized reagent concentrations avoid unwanted side reactions and decomposition. A bath loading of 10.7 mL/cm² was identified as optimal for maintaining plating rate and coating uniformity while avoiding premature depletion of Pt ions.

The substrate's composition, particularly its Cr content, was found to significantly influence the early stages of deposition. However, once a continuous monolayer is formed, the growth proceeds autocatalytically and identically across different Ni-based superalloy substrates.

To extend bath lifespan and ensure consistent deposition, a MTO procedure was developed to replenish consumed reagents. The regeneration strategy involves separate, pre-prepared solutions containing the appropriate amounts of K_2PtCl_4, $Na_2EDTA \cdot 2H_2O$, and hydrazine, added in a controlled sequence to restore both reagent concentrations and total bath volume. Platinum must be reintroduced in a pre-complexed form with Na_2EDTA to avoid uncontrolled reduction, and pH must be carefully adjusted to maintain bath stability. This approach enables multiple consecutive plating cycles without degradation in coating quality or contamination, with almost linear plating rate.

The developed procedure enables the deposition of high-purity platinum coatings with uniform thickness, independent of the geometry of the substrate. This versatility is demonstrated in Figure 7.19, which shows a homogeneous Pt layer deposited on a threaded screw, along with the corresponding EDS map confirming the uniform elemental distribution across the complex surface.

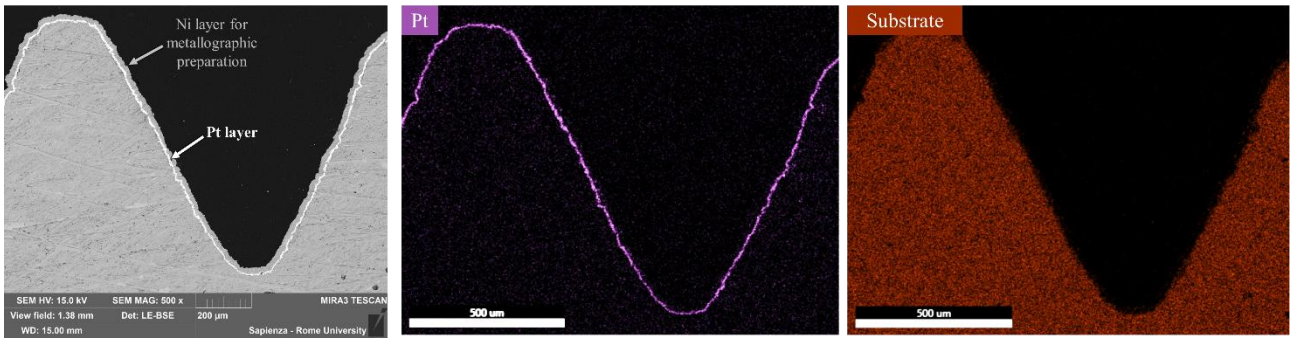

Figure 7.19: SEM-BSE cross-sectional micrograph of the Pt coating deposited on a threaded screw and corresponding EDS maps.

8. Electroless vs electrolytic Pt aluminides

This chapter provides a detailed comparison between electroless and electrodeposited platinum coatings used as precursors for Pt-modified aluminide coatings. The coatings are analyzed in terms of morphology, microstructure, phase composition and elemental distribution in the as-deposited state and after aluminizing.

To assess long-term high-temperature stability, all aluminide coatings are subjected to accelerated oxidation tests at 1100 °C (a temperature that significantly exceeds actual service conditions). These harsh conditions are selected to promote rapid degradation, exposing failure mechanisms and highlighting differences in oxidation kinetics, microstructural evolution, and phase stability, thus providing insights into long-term behavior and coating reliability.

Electrodeposition is currently the most widespread industrially adopted process for platinum plating in in the production of Pt-modified aluminide coatings. However, a major limitation of this technique is the lack of uniformity in the Pt layer, that is particularly problematic for components with complex geometries, such as turbine blades. Achieving deposition over such shapes, though not uniform, requires meticulously engineered anode systems, often custom-designed for each specific component to be coated.

To present the severity of the problem, Figure 8.1 shows an industrial case study of Pt aluminide coating applied to a René N4 turbine blade (Figure 8.1 (a)). Cross-sectional micrographs acquired from three distinct regions, pressure side (b), tip (c), and suction side (d), clearly reveal the microstructural inhomogeneity in the final coating. While both pressure side and suction side regions exhibit a dual-phase outer layer of ζ-$PtAl_2$ and β-(Ni,Pt)Al, the thickness of this layer varies significantly, likely due to uneven initial Pt deposition. At the tip, where the current density is highest during electrodeposition, the dual phase layer is even thicker and an additional outer single-phase $PtAl_2$ layer forms, reflecting excessive local Pt content and incomplete interdiffusion during the pre-aluminizing treatment.

This kind of non-uniformity is to have critical implications over coating performance. Excessive Pt content can lead to greater brittleness of the outer layers, reduced ductility, spallation risk, and rumpling issues during service.

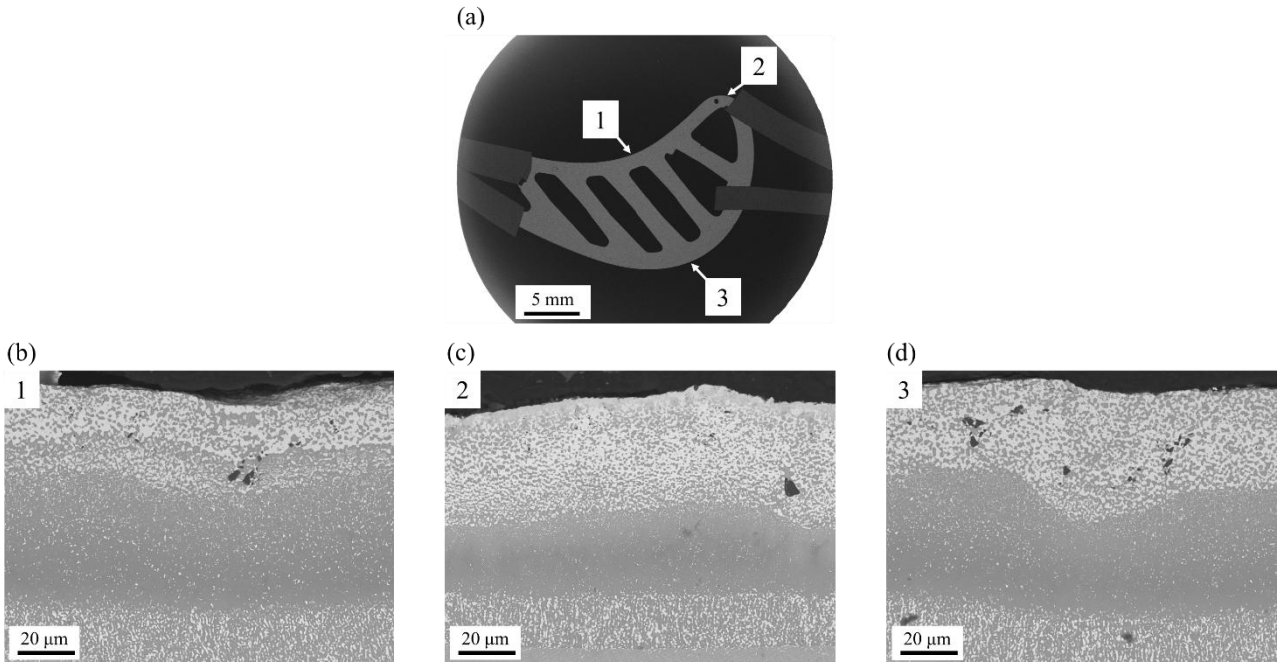

Figure 8.1: Industrial case study of Pt aluminide coating applied to a René N4 turbine blade: cross sectional micrographs of the overall blade (a) and coatings on the pressure side (b), tip (c) and suction side (d).

This non-uniform elemental distribution is further corroborated by EDS analysis shown in Figure 8.2 and Figure 8.3. Only elements with concentrations above 1 wt% are reported for clarity.

At the suction side of the blade (Figure 8.2), EDS confirms high Pt and Al concentrations in the outer layer, characteristic of a ζ + β dual-phase region. Below this, a region of hypostoichiometric β-(Ni,Pt)Al (Al-deficient) is observed. The microstructure is typical of inward-growing aluminides, featuring Cr- and W-rich precipitates, which diffused from the superalloy substrate. At the tip (Figure 8.3), however, the coating includes an additional outer layer with Pt content reaching up to 50 wt%. This is a direct consequence of excessive Pt deposition during electroplating, due to the edge effect of the electric field. The locally too thick Pt layer has not undergone effective diffusion with the substrate during the pre-aluminizing heat treatment, hampering proper diffusion during subsequent aluminizing too and resulting in a microstructure that lacks proper gradation and presents a higher risk of thermal mismatch and mechanical instability.

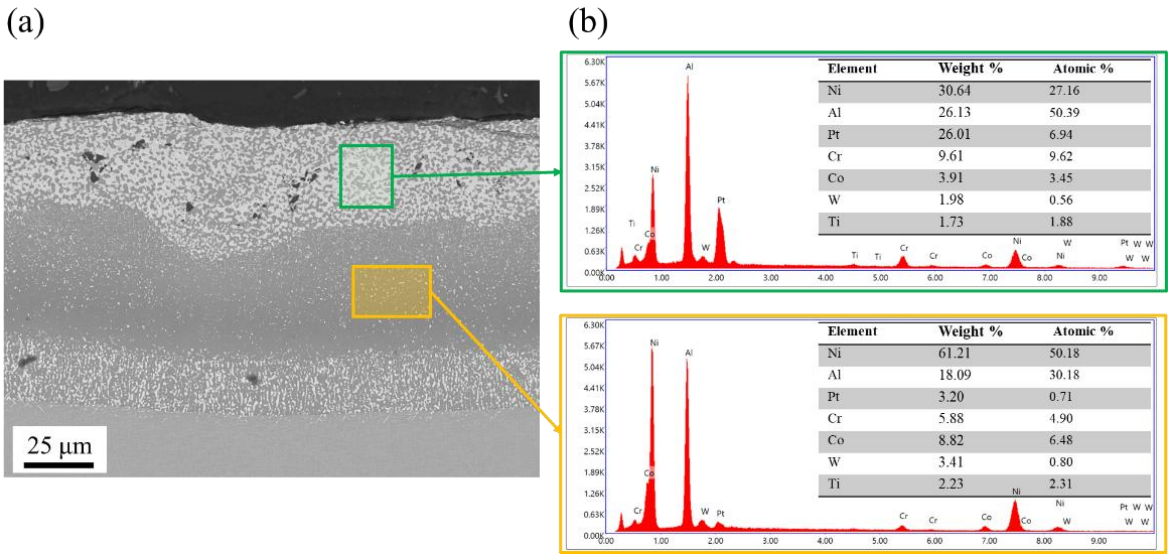

Figure 8.2: SEM-BSE cross sectional micrograph of the coating in correspondence of the suction side (a) and EDS spectra with quantitative analysis (b).

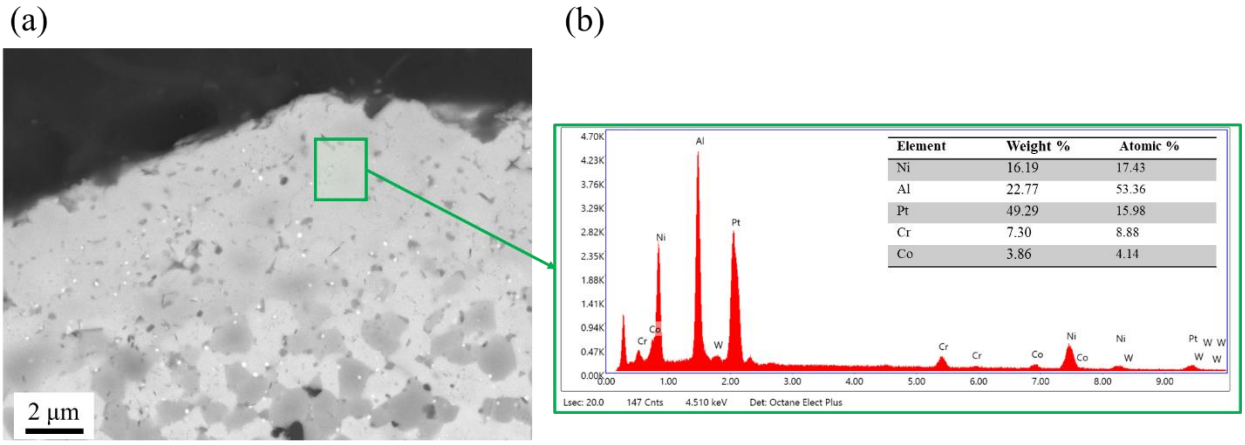

Figure 8.3: SEM-BSE cross sectional micrograph of the outer layer of the coating in correspondence of the tip (a) and EDS spectrum with quantitative analysis (b).

A similar pattern is observed for GTD 111 substrates, illustrated in Figure 8.4. Once again, a dual-phase Pt aluminide forms at both pressure side and suction side surfaces. At the tip, however, a highly irregular microstructure appears. The initial Pt layer was probably so thick that aluminizing was unable to proceed effectively, resulting in a thin aluminide layer composed solely of a Pt-rich phase, with no transitional dual-phase region between the outer layer and the underlying NiAl. This indicates an even more limited diffusion depth of Pt after the pre-aluminizing treatment and demonstrates an ineffective aluminizing when excessive Pt is present.

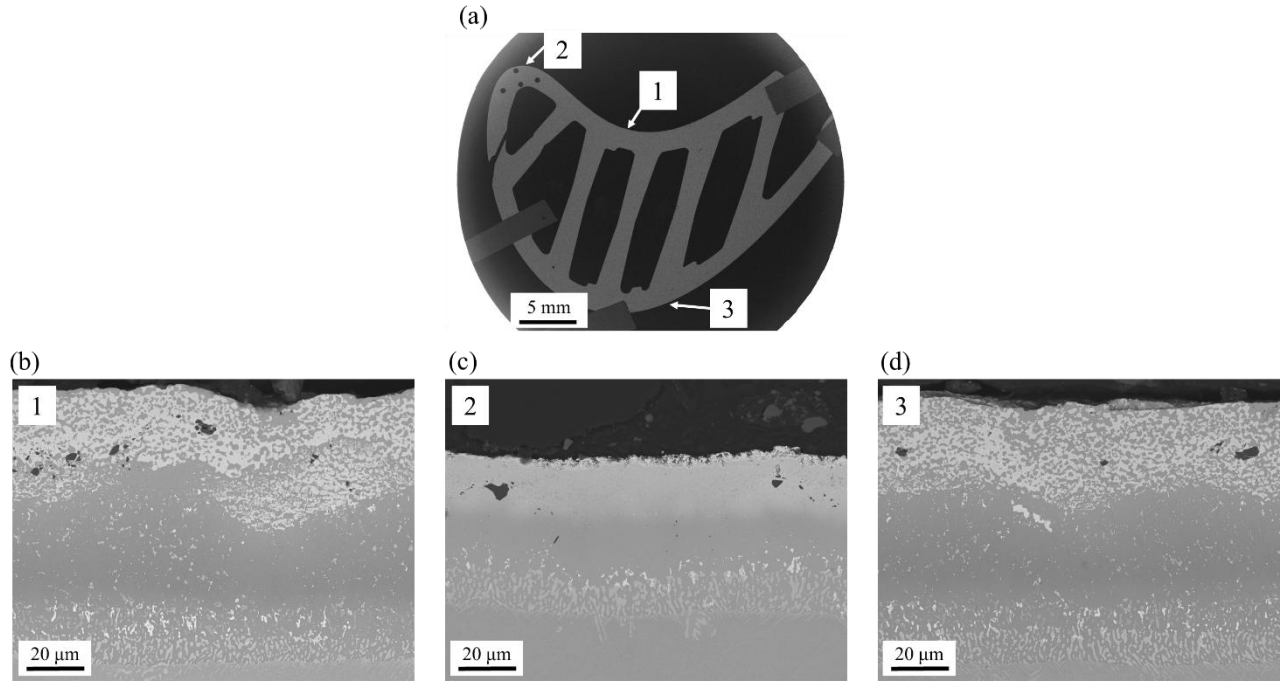

Figure 8.4: Industrial case study of Pt aluminide coating applied to a GTD 111 turbine blade: cross sectional micrographs of the overall blade (a) and coatings on the pressure side (b), tip (c) and suction side (d).

8.1 As deposited Pt coatings

To directly compare electroless and electrodeposited coatings, 10.7 mg/cm² of Pt were applied to René N4 substrates via both methods. Electrodeposition was performed using Johnson Matthey's Platinum Q Salt® electrolyte. The Q Salt bath is supplied as solutions containing 5 g/L of Pt and, at room temperature, has a pH of 10.2–10.8. Before plating, the solution is heated to 91–93 °C, then the pH is adjusted to pH 10.0–10.6 (optimum 10.5) using ammonia. Distilled water must be regularly added to maintain the volume of the bath and platinum concentration must be constantly maintained at 4–6 g/L by adding Platinum Q Salt® Pt 20Q replenishing solution. Strict control of temperature and pH is essential, since cathode current efficiency falls off sharply below 89 °C, and any drift in pH outside the specified window degrades deposit quality.

The main parameters of the two deposition processes are summarized in Table 8.1: although the electroless bath operates at a slower deposition rate, it requires lower Pt concentration and temperature, and relies on a simpler, more cost-effective setup, as no anodes are needed.

	Electroless Pt @Sapienza	**Platinum Q Salt® Johnson Matthey**
Pt salt concentration (g/l)	4	5
Deposition rate (mg/cm²/h)	3.5	8
Temperature (°C)	55	91-93
Pt anode	None	Custom design required

Table 8.1: Comparison between the main plating parameters of electroless Pt deposition and electrodeposition using Johnson Matthey's Platinum Q Salt® electrolyte.

Figure 8.5 (a, b) shows the surface morphology of the electrolytic Pt layer, while Figure 8.5 (c, d) shows the electroless coating. Both exhibit the characteristic cauliflower-like morphology of nucleation-coalescence growth, yet some details differ. Indeed, the electroless film contains numerous fine cracks, indicator of high internal tensile stress during accretion.

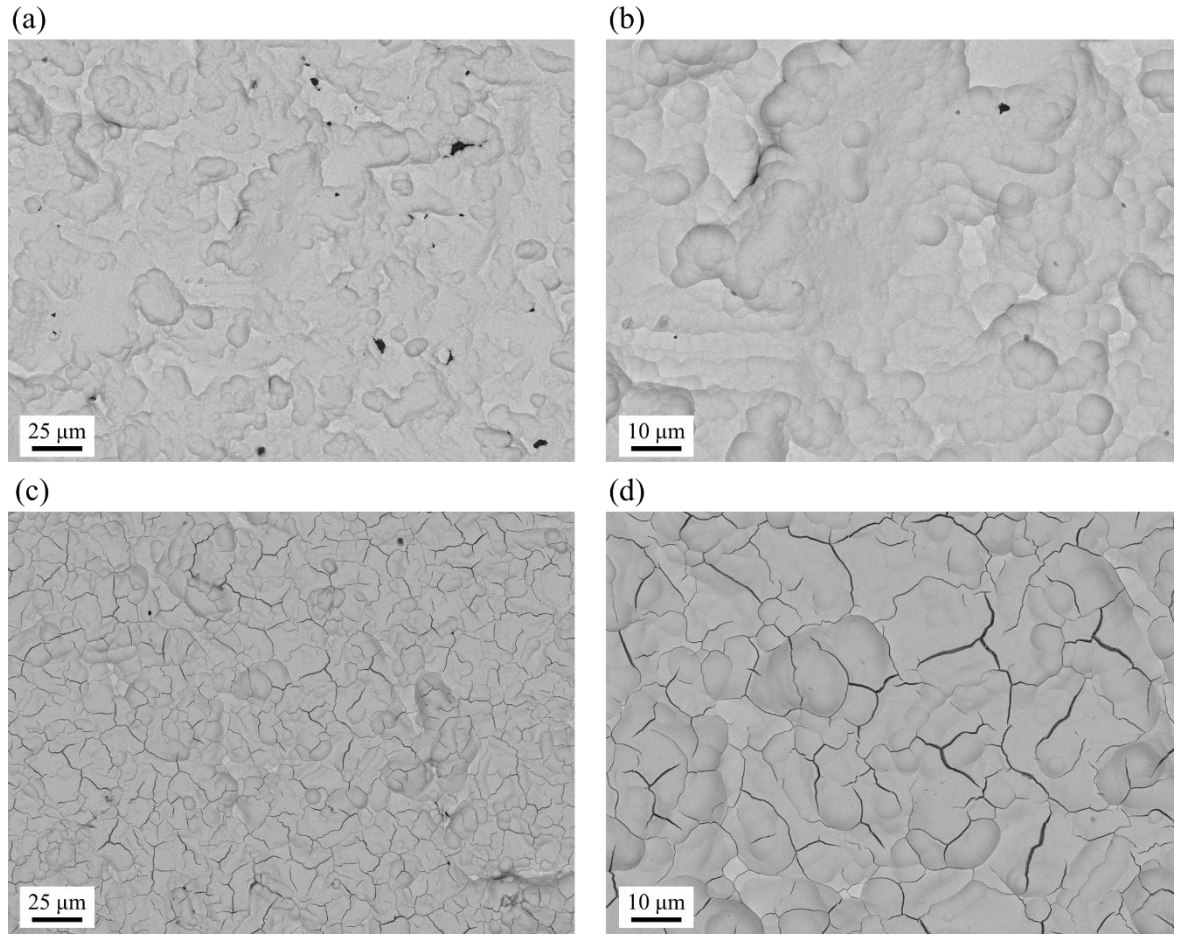

Figure 8.5: Comparison of surface morphologies of platinum coatings obtained by electroplating (a, b) and electroless plating (c, d)**.**

Despite the presence of cracks, the low-magnification SEM-BSE image of the electroless coating presented in Figure 8.6 confirms a fully continuous film with no substrate exposure. Based on EDS analysis, the black spots that are occasionally observed consist entirely of carbon and are attributable to surface dirt.

Figure 8.7 highlights a localized uplift in the electroless coating where internal stresses have caused partial delamination. EDS mapping across this feature shows no substrate exposure: the crack is not through-the-thickness, and a continuous Pt layer remains beneath the raised region.

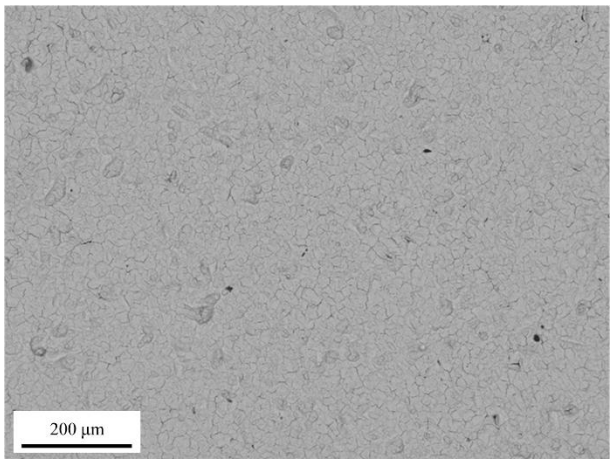

Figure 8.6: SEM-BSE micrograph showing low magnification of the electroless Pt coating surface**.**

Figure 8.7 highlights a localized uplift in the electroless coating where internal stresses have caused partial delamination. EDS analysis on this feature shows no substrate exposure: the crack is not through-the-thickness, and a continuous Pt layer is present beneath the lifted region.

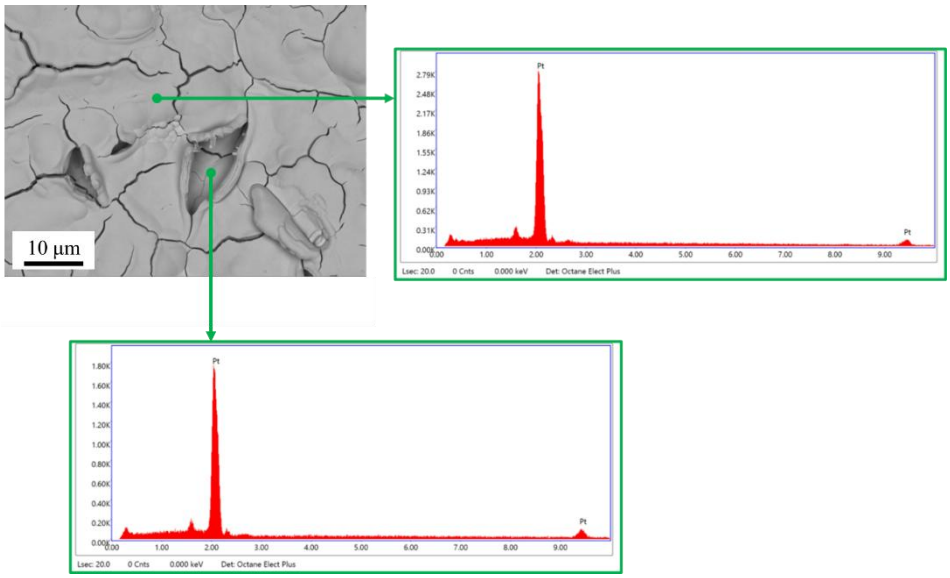

Figure 8.7: SEM and EDS analysis of a region where internal growth stresses in the electroless Pt coating led to partial uplift.

EDS spectra in Figure 8.8 (a) confirms that both coatings are made of pure Pt, with only trace carbon from surface contamination. Crystallographic characterization by XRD (Figure 8.8 (b)) further reveals that both films share the face-centered cubic (fcc) Pt structure. The electroless coating shows broader diffraction peaks, suggesting smaller grain size compared to the electrodeposited layer.

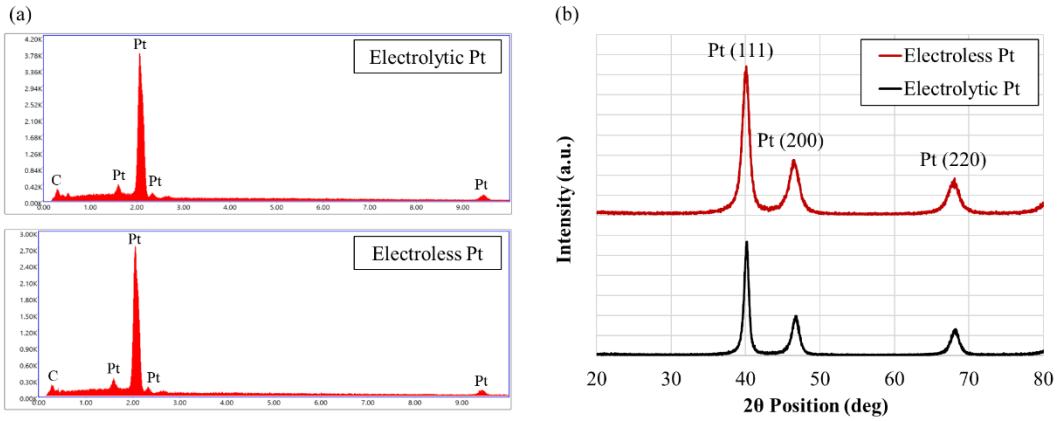

Figure 8.8: EDS (a) and XRD (b) spectra of electroless and electrolytic Pt coatings.

Figure 8.9 presents cross-sectional micrographs of platinum coatings deposited by electroplating (a) and electroless plating (b), with both sections taken at consistent positions spanning from the sample edge (left) to its center (right). Although the geometry of the substrate is simple (a flat disc, the difference in coating uniformity between the two deposition methods is immediately apparent. The electroplated coating displays a pronounced variation in thickness due to the well-known edge effect: the electric field intensifies near the edge of the sample, resulting in increased local current density and consequently a thicker deposit. Specifically, at the outer edge, the coating reaches a thickness of approximately 13 µm, almost double the intended average of 7 µm. This thickness progressively decreases toward the center of the sample, where it drops to a minimum of around 2.5 µm. In sharp contrast, the electroless deposited sample shows a uniform coating thickness across the entire cross-section. No significant variation is observed between edge and center, confirming the inherently conformal nature of this chemical deposition technique.

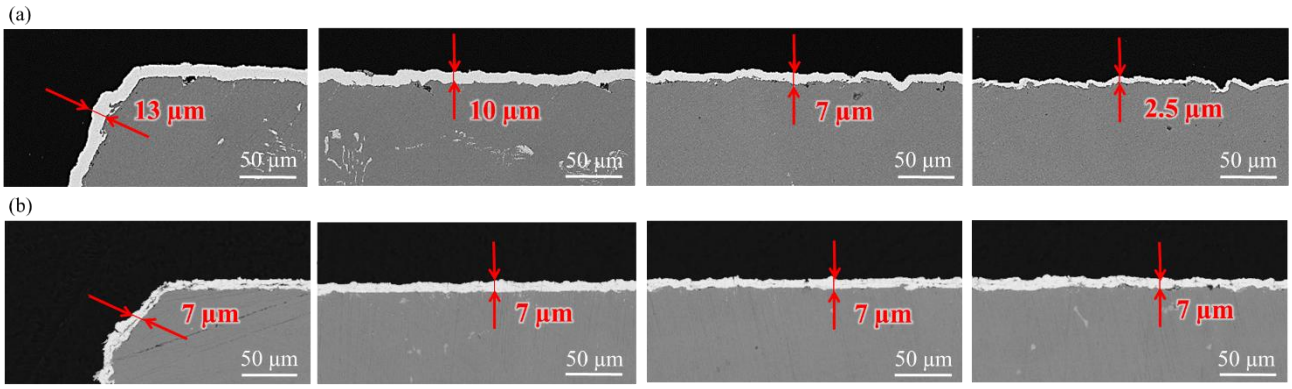

Figure 8.9: cross-sectional micrographs of platinum coatings deposited by electroplating (a) and electroless plating (b) taken at consistent positions spanning from the sample edge (left) to its center (right).

To quantitatively assess the uniformity of the coatings, Figure 8.10 reports the statistical distribution of coating thicknesses obtained via both deposition routes. The histograms show the experimental data, while the dashed curves represent the corresponding Gaussian fits. For the electrolytically plated samples, the data reveal a wide spread, reflecting the deterministic influence of electric field gradients

across the substrate surface. This distribution highlights the difficulty in controlling layer uniformity through electroplating, even on relatively simple geometries. On the other hand, the electroless coating data fit a narrow Gaussian distribution, indicative of a highly controlled and reproducible deposition process. The narrowness of the distribution highlights the process's insensitivity to geometrical features, offering a significant advantage for coating complex components where electroplating would require tailored anode designs and still fail to achieve consistent coverage.

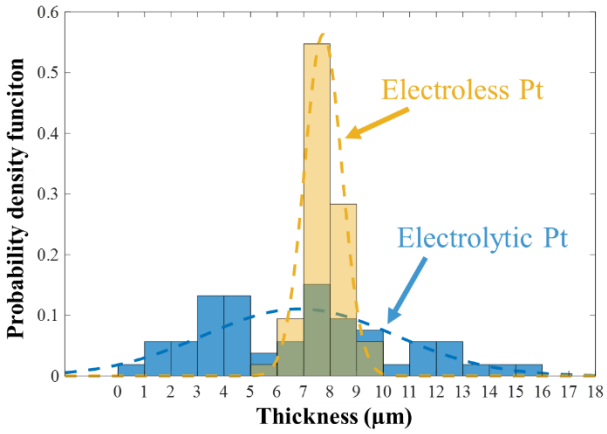

Figure 8.10: Statistical distribution of thickness measurements of electroless platinum (in yellow) and electroplated platinum (in blue) coatings.

8.2 As aluminized Pt-aluminide coatings

The protective performance of platinum-modified aluminide coatings is critically influenced by the amount and uniformity of platinum deposited on the substrate prior to aluminizing. he aluminide obtained by electrolytic deposition of Pt has a final average thickness of approximately 60 µm, including about 16 µm of IDZ. However, microstructural variations within the coating directly reflect the non-uniform distribution of the initial Pt layer. Figure 8.11 presents SEM cross-sectional micrographs acquired from three distinct positions across the sample, progressing from edge to center. Below each micrograph the EDS concentration profiles of Ni, Pt, and Al as a function of coating depth is presented, and the initial Pt layer thickness for each region is highlighted in the red box above each micrograph. Despite the overall appearance of a single-phase microstructure in all regions, possibly with very fine $PtAl_2$ precipitates, the thickness and characteristics of the outermost Pt-rich layer vary significantly, clearly correlating with the initial Pt distribution. Near the sample edge, where the original Pt layer was thickest, the resulting aluminide coating shows a relatively constant Pt concentration throughout its thickness. Although a slight drop in Pt content is observed at the boundary with the IDZ, the concentration does not reach zero until the substrate itself is approached. This uniformity in Pt distribution corresponds with a relatively low Ni content throughout the coating, indicating the predominance of Pt-Al intermetallics in the outer region. Interestingly, the total coating

thickness in this region is lower compared to the others, suggesting that interdiffusion during aluminizing may have been limited due to the higher Pt content, which acts as a diffusion barrier for Ni.

As the analysis moves toward the center of the sample, where the initial Pt thickness was lower, the microstructure changes significantly. The Pt-rich outer layer becomes progressively thinner, and the depth at which Pt concentration drops to undetectable levels moves closer to the external surface. The EDS curves in these regions show a more gradual decline in Pt content and a more pronounced increase in Ni concentration through the coating thickness. This microstructure is consistent with enhanced interdiffusion between the substrate and the Pt layer during the pre-aluminizing diffusion heat treatment. The reduced initial Pt thickness in these regions facilitates more effective dilution of Pt into the superalloy matrix, leading to interdiffusion to deeper depths and formation of a thicker β-(Ni,Pt)Al aluminide.

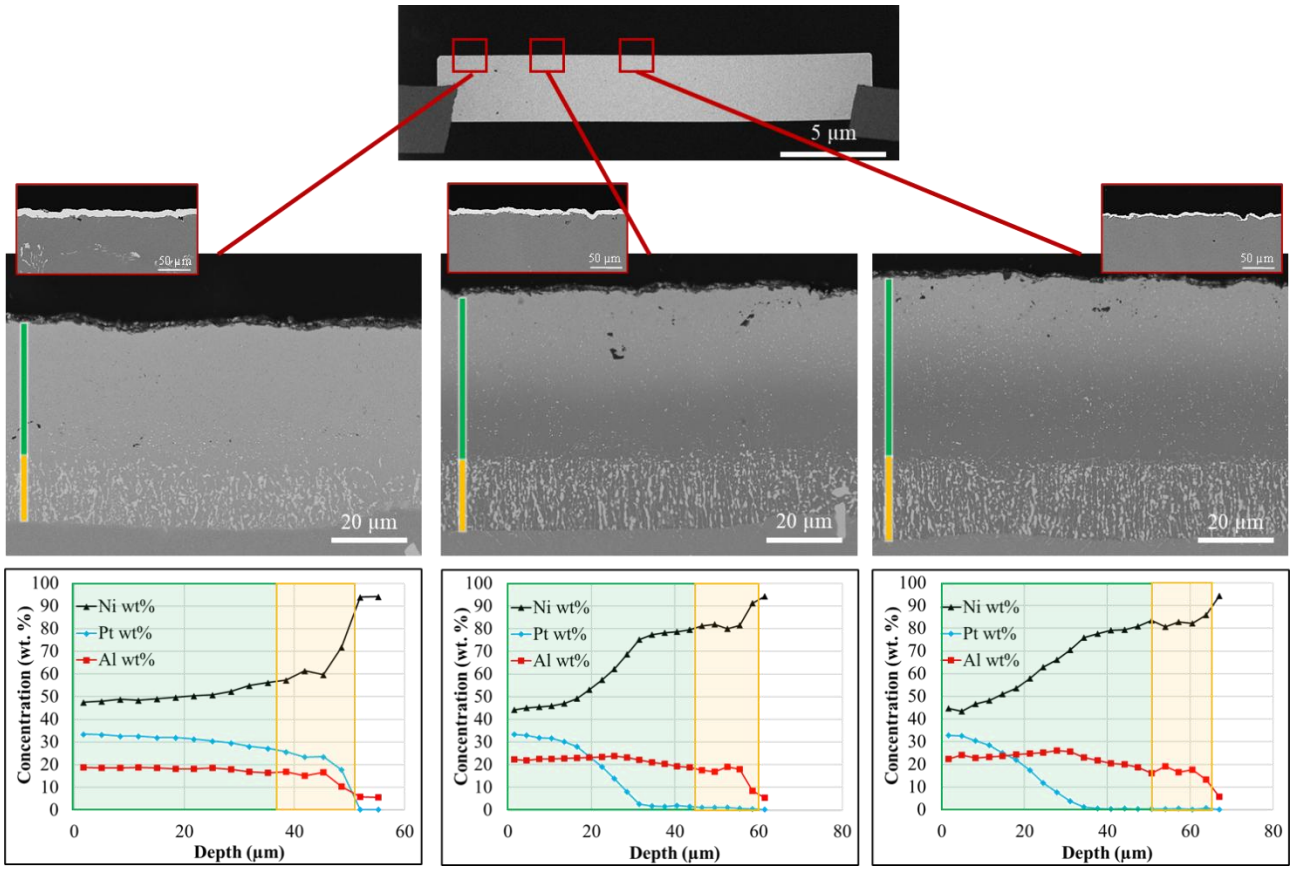

Figure 8.11: SEM cross-sectional micrographs acquired from three distinct positions across the electrodeposited Pt-aluminide sample, progressing from edge (left) to center (right) and corresponding EDS concentration curves (initial Pt layer thickness for each region is highlighted in the red box above each micrograph).

To further support the observations discussed above, EDS elemental maps presented in Figure 8.12 illustrate the distinct distribution of Ni, Al and Pt in two regions of the electrolytic Pt-aluminide coating: one near the sample edge (a) and the other at the center (b). Near the edge, platinum is distributed throughout the entire coating thickness, reaching the lower limit of the IDZ. In contrast,

at the center of the sample, platinum is confined to the outermost region of the coating. At the edge, the Ni signal is consistently low, indicating minimal Ni diffusion into the Pt-rich outer layer, while at the center, a distinct Ni-poor external region aligns with the higher Pt content, followed by a gradual increase in Ni signal closer to the IDZ. This gradient reflects the effectiveness of Pt dilution into the substrate during the pre-aluminizing diffusion heat treatment, which is more pronounced where the initial Pt layer was thinner.

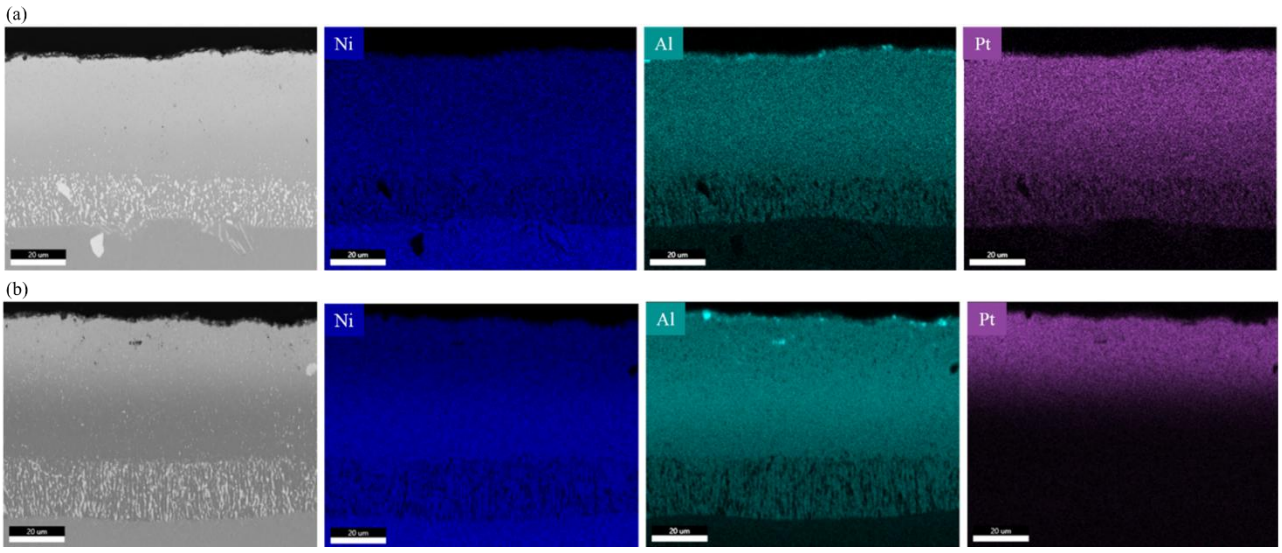

Figure 8.12: EDS maps of the electrolytic Pt-aluminide zone near the edge (a) and in the central zone (b).

Figure 8.13 shows the Pt-aluminide coating obtained using the electroless method, examined in three analogous zones of the sample, from edge to center. At microstructural level, the bond coat produced by the electroless process is fully comparable to the one obtained by standard electrolytic deposition: it presents a total thickness of approximately 60 µm and a uniform monophasic Pt-rich outer region. However, unlike the electrolytic coating, the electroless bond coat exhibits excellent microstructural homogeneity across the entire sample surface, reflecting the highly uniform platinum layer achieved prior to aluminizing. This uniformity is further validated by the EDS concentration profiles reported beneath each micrograph, which reveal consistent elemental distributions of Pt, Ni, and Al across all examined regions. The slight variation in bond coat thickness (thinner at the sample edge) and the slightly elevated Pt content in that area are likely due to localized inefficiencies in the aluminizing process, possibly caused by non-ideal slurry spraying in that specific region. This interpretation also applies to the electrolytic Pt-aluminide samples; however, the limited variation observed here is not sufficient to account for the significant disparities in Pt concentration and thickness recorded in the coatings produced by galvanic deposition.

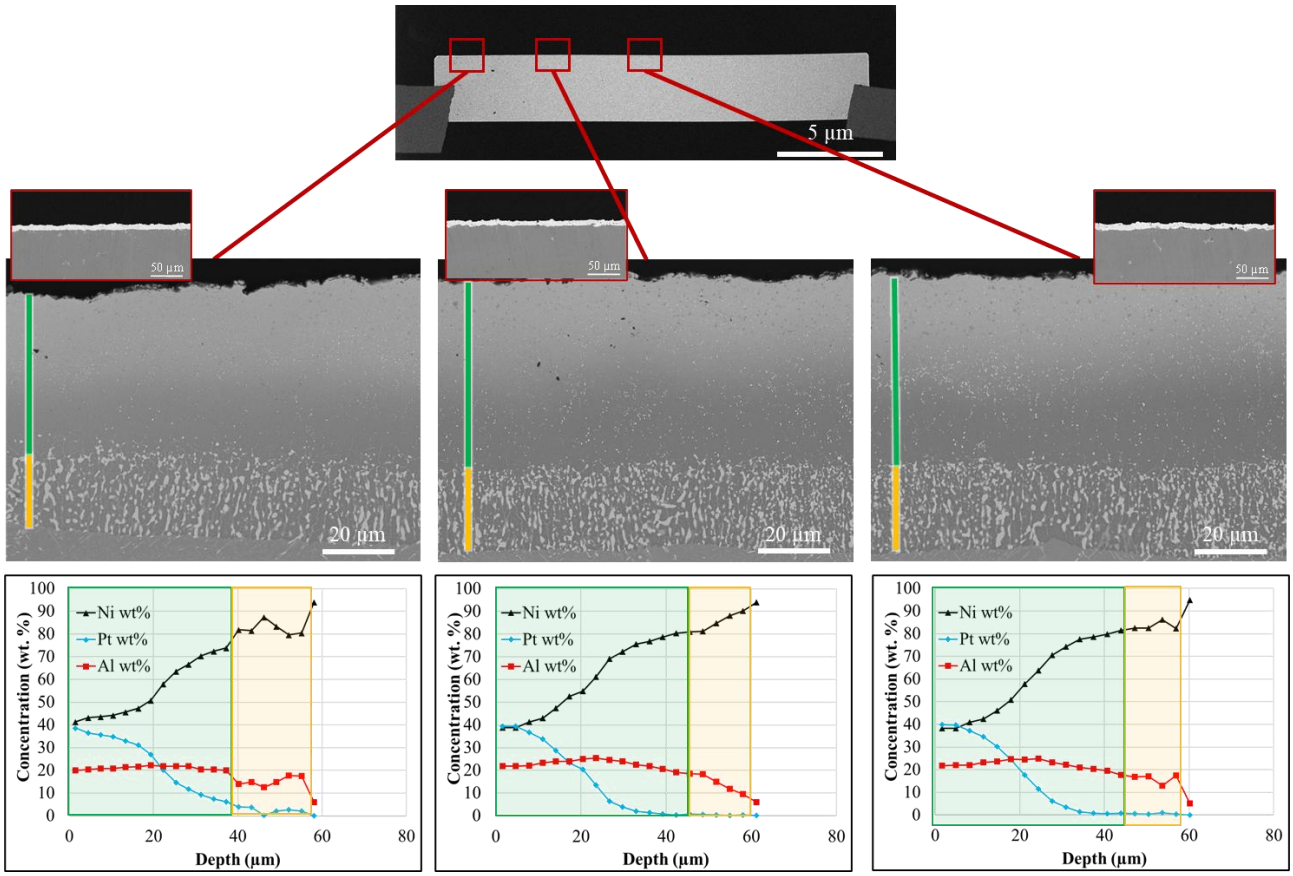

Figure 8.13: SEM cross-sectional micrographs acquired from three distinct positions across the electroless Pt-aluminide sample, progressing from edge (left) to center (right) and corresponding EDS concentration curves (initial Pt layer thickness for each region is highlighted in the red box above each micrograph).

The uniform distribution of Pt, Al, and Ni in the electroless Pt-aluminide coating is in excellent agreement with literature data for monophasic Pt-aluminide coatings produced by galvanic methods, where similar initial Pt amounts and comparable thermal treatments for diffusion and aluminizing were employed [106]. This confirms the reliability and reproducibility of the electroless approach in achieving homogeneous coating microstructures, even over larger surface areas.

To further investigate and compare platinum distribution in coatings produced by galvanic and electroless methods, Figure 8.14 presents the Pt concentration profiles recorded at positions A, B, and C on the samples. The curves corresponding to the electrolytic Pt-aluminide coating are clearly separated, reflecting significant variability in platinum distribution across different regions of the sample. This variability is in stark contrast to the electroless Pt-aluminide coating, where the three profiles are nearly superimposable, indicating a highly uniform platinum distribution throughout the sample. Notably, the Pt concentration profile of the electroless Pt-aluminide closely matches that of the galvanic Pt-aluminide in region B, where the initial platinum layer thickness was also approximately 7 µm. This agreement further confirms the ability of the electroless process to produce coatings with consistent composition, comparable to those obtained using controlled galvanic deposition techniques.

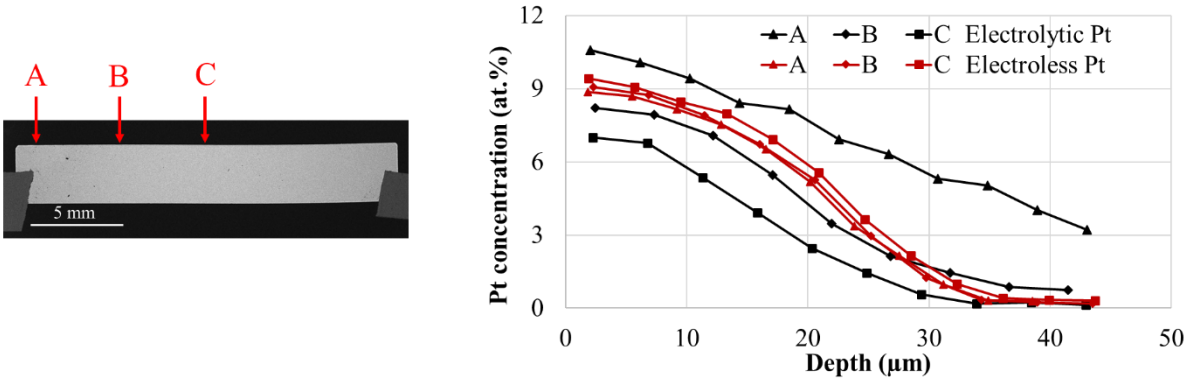

Figure 8.14: Pt concentration profiles recorded at positions A, B, and C on the samples for electrolytic and electroless Pt-aluminides.

For completeness, the composition of the coatings in terms mutual concentrations of nickel and aluminum (in at%) across the thickness, from the outer surface to the interface with the IDZ, is reported in Figure 8.15. The concentration profiles were acquired at position B of the sample (as indicated in Figure 8.14), and the green band represents the compositional stability range of the β-NiAl phase. It can be observed that stoichiometric NiAl composition is only present in the outermost region of the coating. Moving inward toward the IDZ, the aluminum content progressively decreases, leading to sub-stoichiometric compositions. This compositional gradient is evident in both electrolytic and electroless Pt-aluminide coatings, suggesting that it originates from the slurry aluminizing process rather than the Pt deposition method. Such Al depletion in the inner regions of the coating should be carefully considered when evaluating the overall oxidation resistance and long-term stability of the coatings.

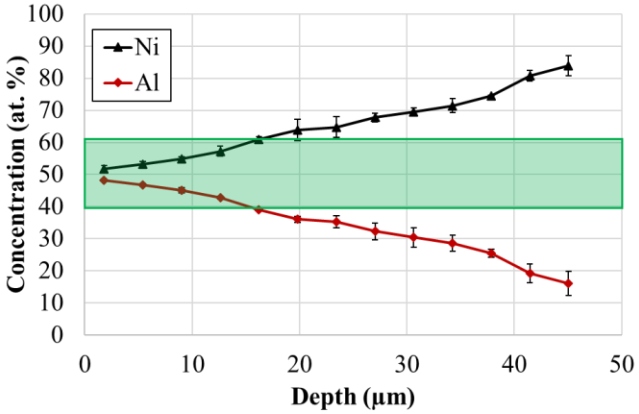

Figure 8.15: EDS compositional profiles of Ni and Al mutual at.% across coating thickness.

To complete the comparison, XRD analysis of the two coatings is shown in Figure 8.16. The diffraction patterns are nearly identical, indicating that no substantial difference exists in phase composition between the coatings. All observed peaks correspond to the β-NiAl phase (JCPDS 20-0019). However, the incorporation of platinum into the β-NiAl lattice results in a distinct shift of the diffraction peaks to lower 2θ angles compared to those of pure β-NiAl (2θ = 44.3678°), consistent with previous findings [106,228]. This shift is attributed to the distortion of lattice parameters caused

by the substitutional incorporation of Pt atoms at Ni sites within the NiAl crystal structure. It is a well-established phenomenon that the incorporation of foreign atoms into a crystal lattice induces local strains and stresses, the magnitude of which depends on the atomic size difference between the original and the incorporated species. In this case, the atomic radii of Ni and Pt are 124.0 pm and 138.5 pm, respectively [229]. This considerable size mismatch leads to a distortion of the lattice, introducing strain fields and internal stresses that manifest as a measurable peak shift in the XRD spectrum. These findings further validate the substitutional nature of Pt incorporation and provide indirect confirmation of its homogeneous integration into the β-NiAl matrix in both coatings.

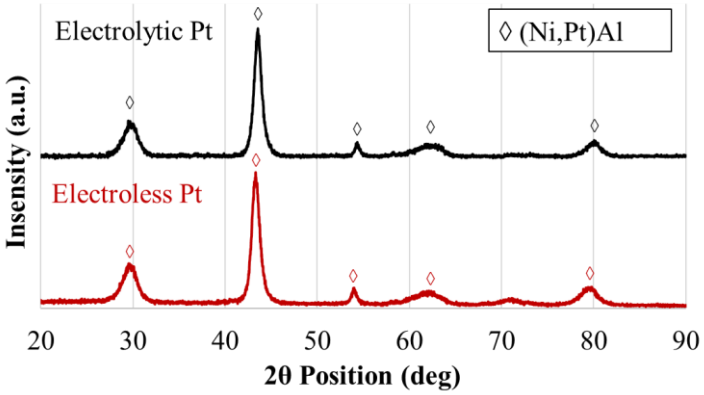

Figure 8.16: XRD spectra of electrolytic Pt-aluminide (black line) and electroless Pt-aluminide (red line).

8.3 Isothermal oxidation tests

Samples were subjected to isothermal oxidation tests at 1100 °C to evaluate their protective capabilities and to compare the performance of electroless Pt-aluminide coatings with that of electrolytic Pt-aluminides. The goal is to assess the viability of the electroless process as a reliable alternative to galvanic deposition for producing Pt-modified aluminide coatings.

Figure 8.17 shows the microstructural evolution of the coatings up to 1000 hours of oxidation for both the electrolytic Pt-aluminide (a) and the electroless Pt-aluminide (b). No significant differences in oxidation behavior are observed between the two coating types. At 21 h, both coatings develop a thin Al_2O_3 scale, which exhibits localized whisker-like morphology, characteristic of θ-Al_2O_3 [230]. This indicates that, at this early stage, the full transformation to stable, protective α-Al_2O_3 has not yet occurred, and transient alumina phases are still present, consistently with previous literature [231]. As oxidation progresses and a continuous oxide scale forms, the oxygen partial pressure at the oxide–metal interface decreases. Consequently, only the most thermodynamically stable oxide, α-Al_2O_3, remains, while the transient phases are gradually replaced. By 28 h, both coatings exhibit a fully developed, adherent, and continuous α-Al_2O_3 scale with no visible traces of transient alumina phases, confirming that the transient oxidation phase concludes within this timeframe for both systems.

At 500 h, the oxide scale thickens to approximately 2.8 ± 0.2 µm for the electroless coating and 3.4 ± 0.4 µm for the electrolytic coating. Despite the increased thickness, the oxide layer remains protective and well-adhered. Concurrently, the initial formation of γ'-Ni_3Al is observed in both coatings (indicated by white arrows), as a result of aluminum depletion due to oxide growth. High-magnification micrographs in Figure 8.18, acquired at 500 h, also reveals the development of peg structures at the oxide/metal interface (white arrows), which are characteristic of Pt-aluminides and are known to enhance oxide scale adherence [108]. Red arrows mark γ'-Ni_3Al precipitation at grain boundaries.

By 1000 h, the oxide scale thickness has increased significantly, and spallation of large portions of the Al_2O_3 layer is evident. Additionally, large tantalum precipitates are clearly visible throughout the oxide scale. This is expected, as the coating at this stage is almost entirely depleted of the protective β-phase, and the remaining region beneath the oxide consists mostly of γ'-Ni_3Al, a consequence of continued aluminum loss both from oxidation and diffusion into the substrate due to concentration gradients.

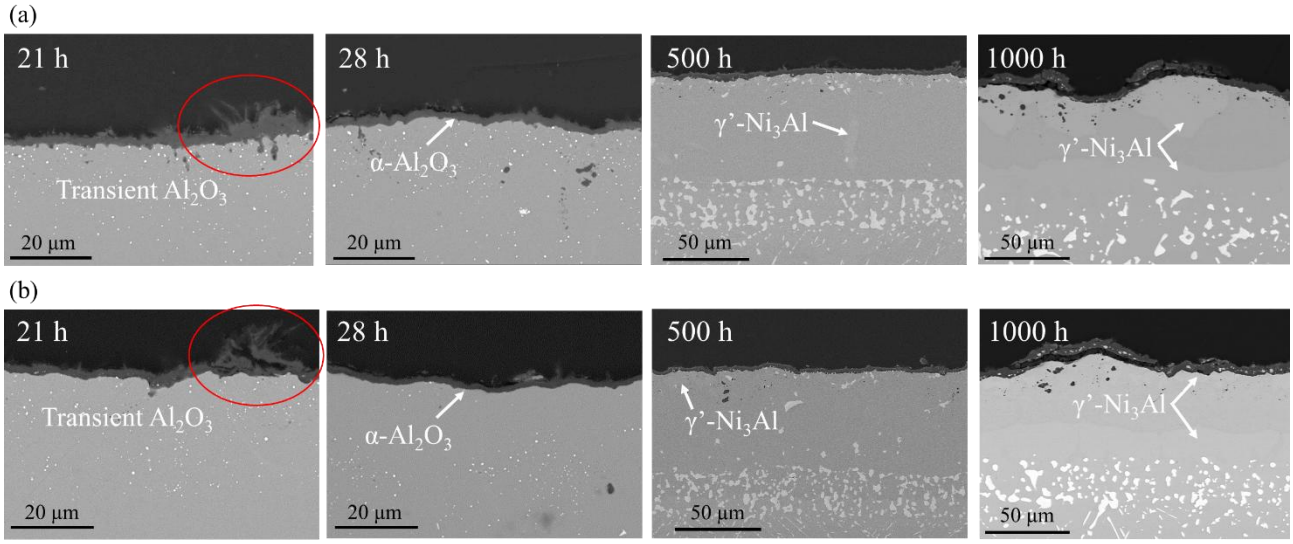

Figure 8.17: Microstructural evolution of the coatings up to 1000 hours of oxidation at 1100°C for the electrolytic Pt-aluminide (a) and the electroless Pt-aluminide (b)

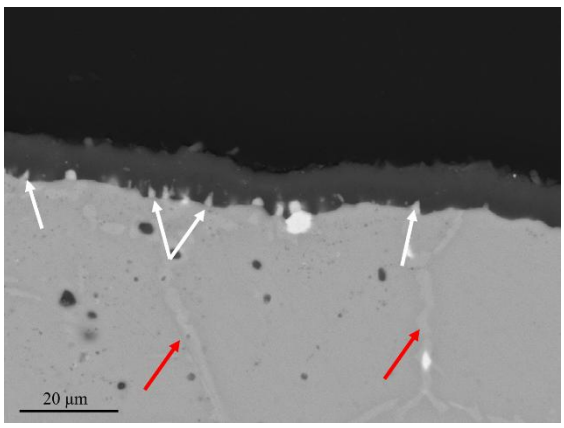

Figure 8.18: High-magnification micrographs of the oxide scale developed at 500h of oxidation at 1100 °C (electroless Pt-aluminide).

White arrows point at pegs at the oxide/metal interface, red arrow point at Ni_3Al formation at grain boundaries.

Oxidation kinetics for both coatings are plotted in Figure 8.19. The electrolytic Pt-aluminide exhibits a faster oxide scale growth during the first 100 h. However, both coatings follow a similar parabolic growth trend up to 600 h. Beyond this period, both coatings show a sharp increase in oxide thickness, followed by a decrease and then another increase, indicative of partial oxide scale spallation and subsequent regrowth. Interestingly, this behavior is common to both coating types, suggesting that it is independent of the Pt deposition method and can be addressed to the relatively low amount of Al initially present in both coatings. Fitting the experimental data to Monceau's parabolic oxidation model [53] up to 600 h (dashed lines in Figure 8.19) yields parabolic rate constants (k_p) and correlation coefficients reported in Table 8.2. The results confirm comparable oxidation kinetics, with the electroless Pt-aluminide even showing slightly better performance. The high correlation values ($R_{corr} > 0.99$ for both cases) confirm the good fitting.

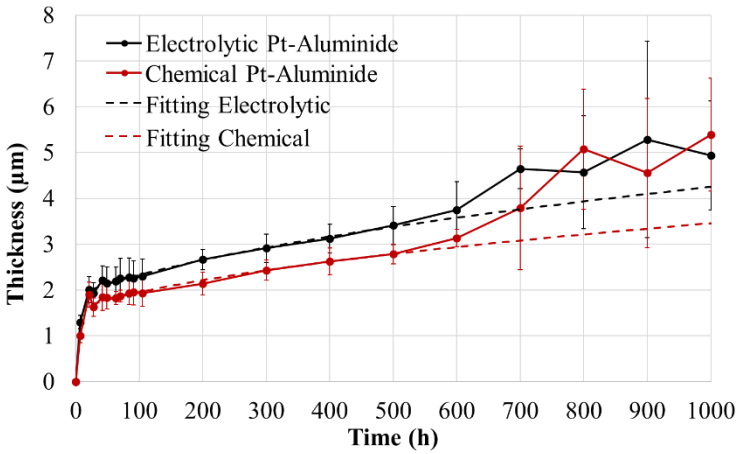

Figure 8.19: Oxidation kinetics curves for electrolytic Pt-aluminide (black line) and electroless Pt-aluminide. Fitting according to Monceau's model is reported as dashed lines.

	k_p (µm²/s)	R_{corr}
Electrolytic Pt-aluminide	0.0098	0.996
Electroless Pt-aluminide	0.0057	0.996

Table 8.2: Parabolic constants calculated according to Monceau's model for the electrolytic Pt-aluminide and electroless Pt-aluminide and correlation coefficient of data fitting.

Figure 8.20 displays concentration profiles of Ni, Al, and Pt as a function of oxidation time for the first 105 h, along with corresponding SEM micrographs. Profiles and images for the electrolytic Pt-aluminide are shown in (a) and (b), while those for the electroless Pt-aluminide are presented in (c) and (d), respectively. The initially higher Al content in the electrolytic coating leads to a more rapid depletion of Al during the transient oxidation stage, especially within the first 7 h. This aligns with the early-stage kinetics and suggests that an excessive Pt concentration in some regions of the electrolytic coating impedes the attainment of phase equilibrium during aluminizing. This imbalance accelerates Al consumption during early high-temperature exposure. Micrographs at 100 h confirm

the thicker Al_2O_3 scale on the electrolytic coating. Nonetheless, both coatings display signs of β-to-γ' transformation at grain boundaries. Moreover, extensive needle-like TCP phase formation is evident beneath the IDZ (in the secondary reaction zone, SRZ) for both systems.

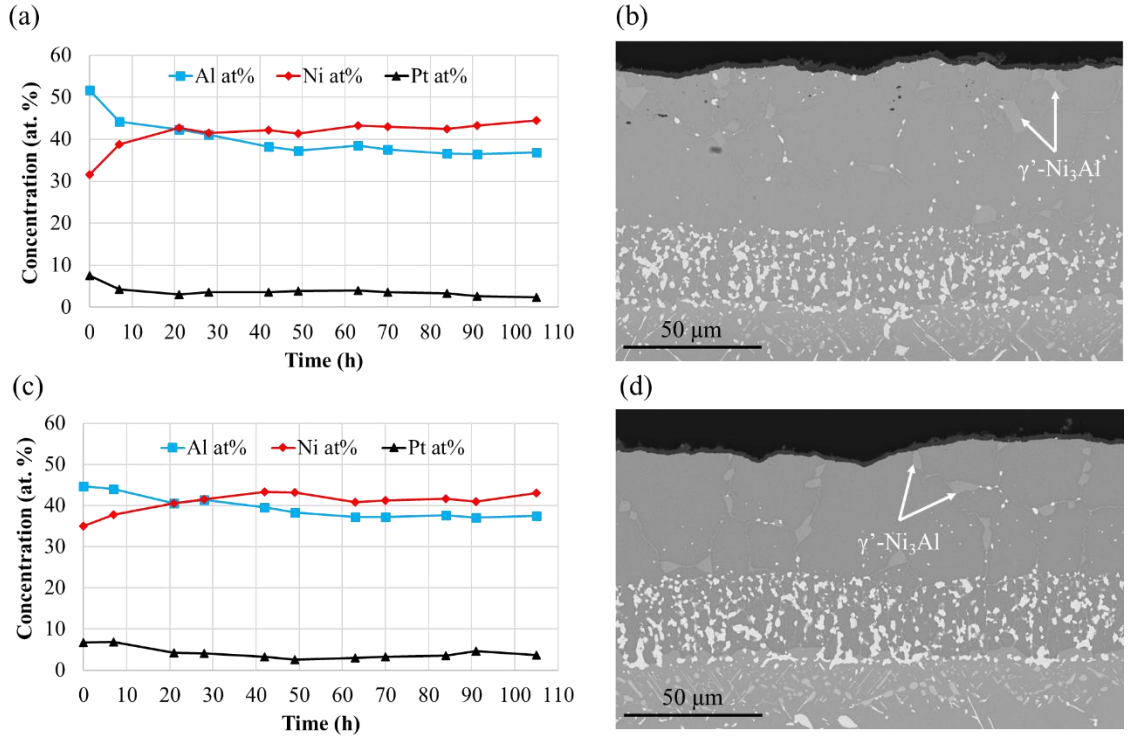

Figure 8.20: Concentration profiles of Ni, Al, and Pt as a function of oxidation time for the first 105 h along with corresponding SEM micrographs for electrolytic Pt-aluminide (a, b) and electroless Pt-aluminide (c, d).

Eventually, XRD analysis at 28 h, 105 h, 500 h and 1000 h of oxidation are presented in Figure 8.17, for electrolytic Pt-aluminide in (a) and electroless Pt-aluminide in (b). Both coatings follow the same general phase evolution pathway. At 28 h, Al_2O_3 peaks are clearly detected (JCPDS 81-1667), along with NiAl peaks and a minor peak corresponding to the Ti_2Al intermetallic (JCPDS 47-1410) [232]. At 105 h, Ta_2O_5 peaks (JCPDS 18-1305) appear in the electrolytic Pt-aluminide spectrum, likely due to the high Ta content in the substrate and its significant oxidation tendency ($\Delta G \approx -620$ kJ [233]). However, these are not detected in the electroless Pt-aluminide and were not observed in SEM images. Furthermore, the Ta_2O_5 peaks disappear from the spectrum at 500 h, indicating that the quantity is too low to be resolved as peak intensity from other phases increases.

The emergence of Ni_3Al peaks (JCPDS 65-0140) at 105 h is observed in both type of coatings, in agreement with the nucleation of this phase observed in SEM micrographs. Intensity of Ni_3Al peaks increases with increasing exposure time and reflects the progressive Al depletion.

At 500 h, TiO_2 peaks (JCPDS 76-0322) are observed in both coatings, suggesting Ti contamination in the Al_2O_3 scale, likely due to progressive Al depletion. At the same time, NiAl peaks move towards higher angles, likely due to the combined effect of the progressive deviation from stoichiometry (transformation to Al-poor NiAl phase) and the continued Pt diffusion towards inner regions.

Initial evidence of $NiAl_2O_4$ spinel formation (JCPDS 71-0965) is seen, which becomes pronounced at 1000 h. This phase formation corresponds with extensive Ni_3Al presence and highlights the coating's loss of ability to sustain a protective, pure Al_2O_3 scale formation. These findings are consistent with the coating degradation trends evident from the oxidation kinetics and microstructural evolution.

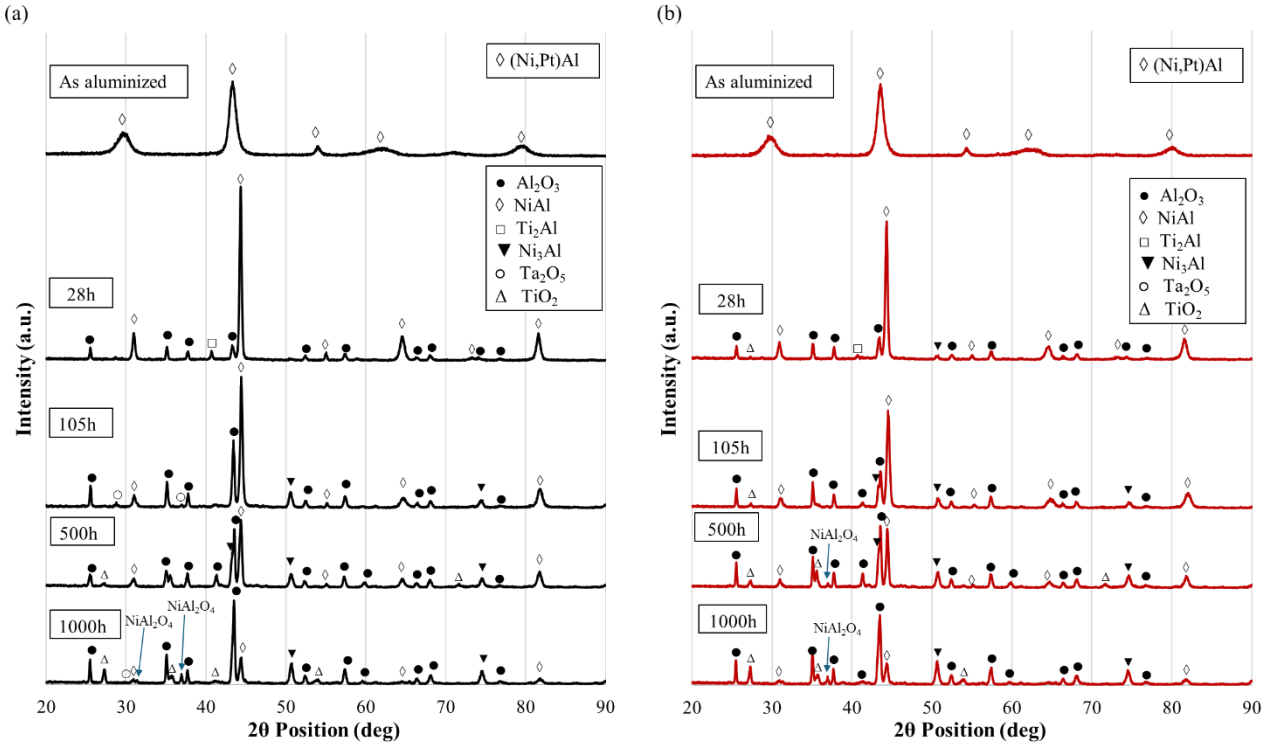

Figure 8.21: XRD spectra at 28 h, 105 h, 500 h and 1000 h of oxidation for electrolytic Pt-aluminide (a) and electroless Pt-aluminide (b).

All the above results highlight the comparable oxidation resistance of electroless and electrolytic Pt-aluminide coatings, with the electroless variant even exhibiting slightly slower oxidation kinetics, thereby confirming electroless deposition as a technically sound and viable alternative to electrodeposition for the production of platinum-modified aluminides.

8.4 Conclusions

This chapter presented a comprehensive comparative study between electroless and electrolytic Pt-aluminide coatings, with the aim of assessing the feasibility of the electroless route as an alternative to traditional electrodeposition for the development of high-performance aluminide bond coats.

The analysis of platinum distribution prior to aluminizing revealed notable differences between the two deposition methods: despite sharing similar morphology and identical purity, electrolytic coatings displayed significant thickness variability across the sample cross-section, while electroless coatings exhibited excellent uniformity. This homogeneity was preserved after the aluminizing step:

consistent Pt, Al, and Ni levels across different regions of the sample were observed in the electroless Pt-aluminide coatings, while electrolytic Pt-aluminide highlighted a variability consistent with the non uniformity of the initial Pt layer. Microstructure of the electroless Pt-aluminide, characterized by a single monophasic layer (richer in Pt in the outer layer), was comparable to that of the electrolytic coatings in the regions of comparable initial Pt amount. XRD analysis further confirmed that both coatings shared the same phase composition, dominated by β-NiAl with Pt substitution.

Isothermal oxidation tests at 1100 °C demonstrated the protective behavior of both coatings over prolonged exposure (up to 1000 h). Both coatings developed a continuous and adherent α-Al_2O_3 scale after the initial transient stage, with similar microstructural evolution and formation of characteristic features, such as interfacial pegs and nucleation of γ'-Ni_3Al zones as high temperature exposure proceeds, due to aluminum depletion. Oxidation kinetics curves demonstrated that the long-term oxidation behavior of both coatings was comparable; importantly, the electroless Pt-aluminide exhibited slightly slower oxidation kinetics, with lower parabolic rate constant.

In conclusion, the electroless deposition method not only ensures excellent control and uniformity of platinum distribution prior to aluminizing but also provides oxidation resistance comparable with, and in some aspects superior to, that of electrolytic Pt-aluminides. These findings validate the electroless process as a robust and viable alternative for the manufacturing of Pt-modified aluminide coatings, with potential advantages in process simplicity, efficiency and cost-effectiveness.

Despite these promising results, it is understandable why electroless platinum deposition has not yet replaced electrolytic methods in industrial practice. Historically, electroless deposition has lacked standardized, robust formulations suitable for large-scale application. Previous attempts were limited either by insufficient bath stability or by the inability to achieve the coating thicknesses required for high-temperature applications. In contrast, electrolytic deposition, despite its well-known limitations, is a mature and deeply established technology. Decades of research and process optimization have enabled the industry to achieve reproducible results using standardized electrolytes and highly engineered apparatus. Transitioning from this established framework to a new electroless process would inevitably require significant capital investment, as well as the development of new know-how, while existing electroplating infrastructure would become obsolete. Furthermore, the industrial implementation of the electroless formulation proposed in this work, though highly promising, is not without challenges. The reliance on hazardous reagents such as hydrochloric acid and hydrazine introduces important health, safety, and environmental considerations. Addressing these concerns will require new handling and disposal protocols, along with modifications to equipment and materials to ensure durability under low-pH operating conditions.

9. Optimization of the slurry method for Pt-aluminides

Following the characterization of industrially produced Pt-aluminide coatings, it became evident that both electrolytic and electroless variants exhibit a progressive depletion of aluminum across the coating thickness, with stoichiometric β-NiAl phase confined only to the outermost regions. Given the critical role of the β-NiAl phase in ensuring long-term oxidation resistance, this compositional gradient, likely introduced during the slurry aluminizing process, represents a limiting factor for coating performance. Therefore, the present chapter focuses on the laboratory-scale optimization of the slurry aluminizing process, with the goal of achieving a more uniform and stoichiometric β-NiAl phase throughout the entire coating thickness. This optimization is expected to enhance the protective behavior and thermal stability of the coatings under high-temperature exposure. In addition, the chapter explores the effect of varying the initial electroless-deposited platinum layer thickness on the microstructure and oxidation behavior of Pt-aluminide coatings, in order to establish more robust processing–structure–property relationships for the design coatings with enhanced protective capabilities.

9.1 Optimization of the slurry method

The optimization of the slurry aluminizing method was first addressed by evaluating the influence of the initial slurry layer thickness. Samples were prepared with slurry loadings of 80, 100, 120 and 150 $mg_{slurry}/cm^2_{sample}$, while keeping the overall slurry concentration in the reaction chamber constant at 3.25 $mg_{slurry}/cm^3_{chamber}$. Cross-sectional micrographs of the resulting coatings are presented in Figure 9.1. For samples with initial slurry layers of 80, 100 and 120 $mg_{slurry}/cm^2_{sample}$, coating thicknesses were nearly identical, measuring approximately 92 ± 3 μm, with an IDZ of 24 ± 2 μm. However, a significant increase in both coating thickness (115 ± 4 μm) and IDZ thickness (32 ± 3 μm) was observed when the slurry layer reached 150 $mg_{slurry}/cm^2_{sample}$. These findings align with observations by Li et al. [95], who suggested that excessively thick slurry layers can accelerate Ni–Al diffusion kinetics, thus producing thicker coatings. Regardless of slurry layer thickness, all coatings exhibited the typical inward-grown aluminide microstructure, characterized by Cr-rich precipitates in the outer region and finely dispersed Ta-rich precipitates throughout the coating thickness, in agreement with previous work by Goward and Boone [80].

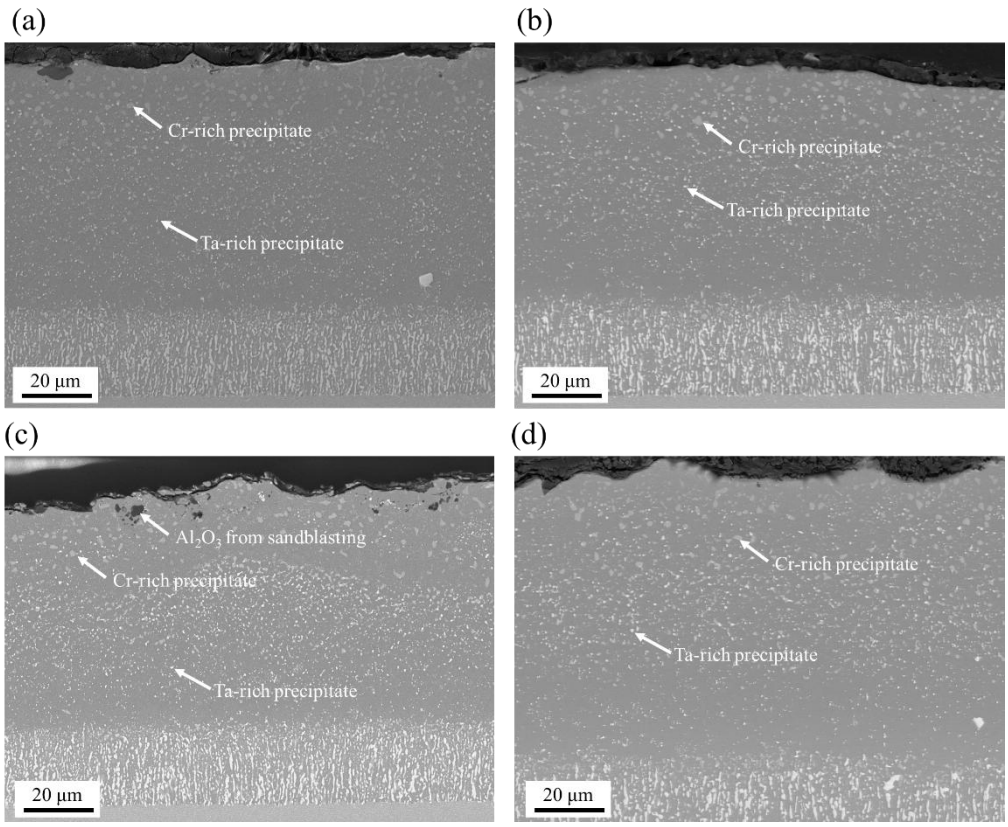

Figure 9.1: Cross sectional micrographs of coatings deposited with 80 $mg_{slurry}/cm^2_{sample}$ (a), 100 $mg_{slurry}/cm^2_{sample}$ (b), 120 $mg_{slurry}/cm^2_{sample}$ (c) and 150 $mg_{slurry}/cm^2_{sample}$ (d).

However, notable differences were observed in the Al/Ni atomic ratio along the coating depth, as determined by EDS analysis (Figure 9.2 (b)), while a representative micrograph is shown in Figure 9.2 (a). This ratio plays a critical role in determining the resulting matrix phase: Al/Ni ratios exceeding 1.2 can lead to the formation of the brittle Ni_2Al_3 intermetallic, while ratios below 0.7 favor the development of Ni_3Al, which compromises oxidation resistance. The amount of deposited slurry influences the concentration gradients that develop during the aluminizing process. If the aluminum content is too high, as in the case of 80 and 120 $mg_{slurry}/cm^2_{sample}$, there may not be enough time during the diffusion heat treatment for NiAl to form uniformly across the coating, leading to aluminum-rich outer layers. Conversely, the sample coated with 150 $mg_{slurry}/cm^2_{sample}$ showed a deficiency in aluminum in the inner region, likely due to ineffective Al transport caused by the excessive slurry thickness. Thus, the optimal initial slurry amount was determined to be 100 $mg_{slurry}/cm^2_{sample}$, as it yielded a uniform Al/Ni ratio compatible with β-NiAl phase formation throughout the coating thickness.

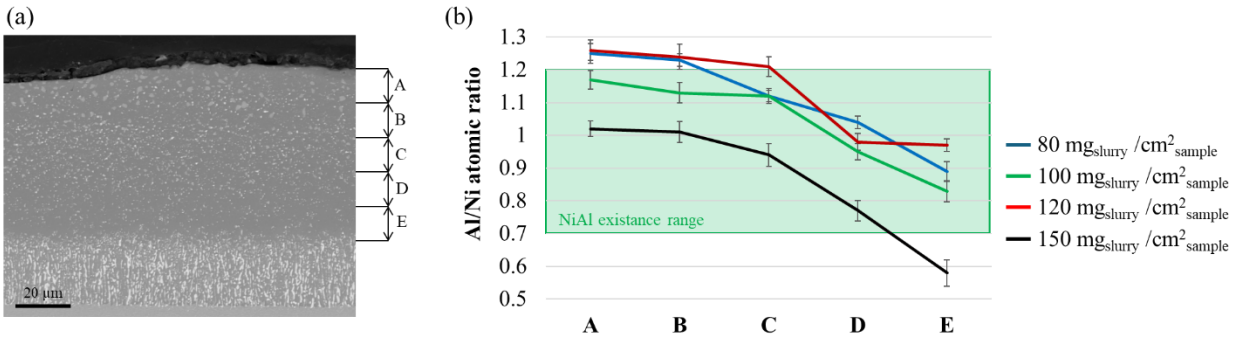

Figure 9.2: (a) Typical cross-sectional micrograph of aluminized samples; (b) Al/Ni atomic ratio as a function of depth for different $mg_{slurry}/cm^2_{sample}$ (letters on x-axis refer to depths from (a)).

Next, the influence of slurry concentration within the reaction chamber was explored while maintaining a constant initial slurry thickness of 100 $mg_{slurry}/cm^2_{sample}$. The Al/Ni atomic ratio profiles across the coating depth for coatings produced with 1.63, 3.25, 6.50, and 13.0 $mg_{slurry}/cm^3_{chamber}$ are shown in Figure 9.3. Optimal results were observed for 3.25 and 6.50 0 $mg_{slurry}/cm^3_{chamber}$. At 1.63 0 $mg_{slurry}/cm^3_{chamber}$, the coatings exhibited an Al/Ni profile consistent with NiAl only near the outer surface, while the matrix gradually transitioned to Ni_3Al toward the IDZ. On the other hand, excessive Al availability at 13.0 0 $mg_{slurry}/cm^3_{chamber}$ led to higher Al/Ni ratios throughout the coating, indicative of the presence of Ni_2Al_3, a brittle and non-protective phase. These observations can be attributed to the increase in Al vapor concentration with increasing slurry content in the chamber, which affects the initial Al accumulation at the substrate surface before solid-state diffusion begins [234], promoting the formation of Al-rich phases during heat treatment.

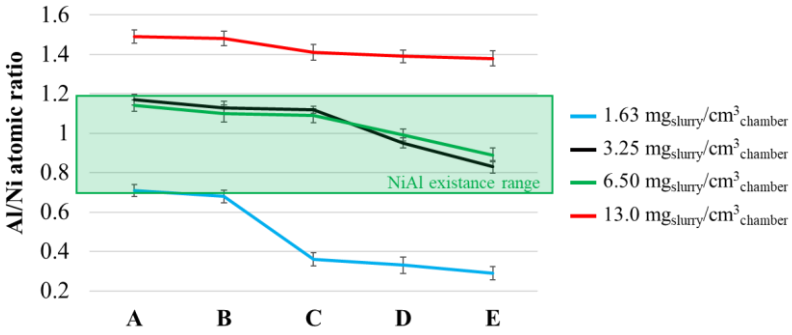

Figure 9.3: Al/Ni atomic ratio as a function of depth for different mgslurry/cm3 chamber (letters on x-axis refer to depths from Figure 9.2 (a)).

The corresponding microstructures are shown in Figure 9.4. Backscattered electron (BSE) imaging reveals that the coating produced with 1.63 $mg_{slurry}/cm^3_{chamber}$ contains light-grey phases, which correspond to Ni_3Al. This phase was not observed in coatings produced with higher slurry content. As slurry concentration increased, a slight thickening of the coatings was noted, along with the development of more pronounced outer zones enriched in Cr_xAl_γ intermetallic compounds, due to the reaction between chromium from the substrate and the abundant aluminum at the superalloy surface [235]. These results further support the conclusion that increased $mg_{slurry}/cm^3_{chamber}$ enhances

aluminum availability at the surface, facilitating the formation of aluminum-rich intermetallics as diffusion progresses.

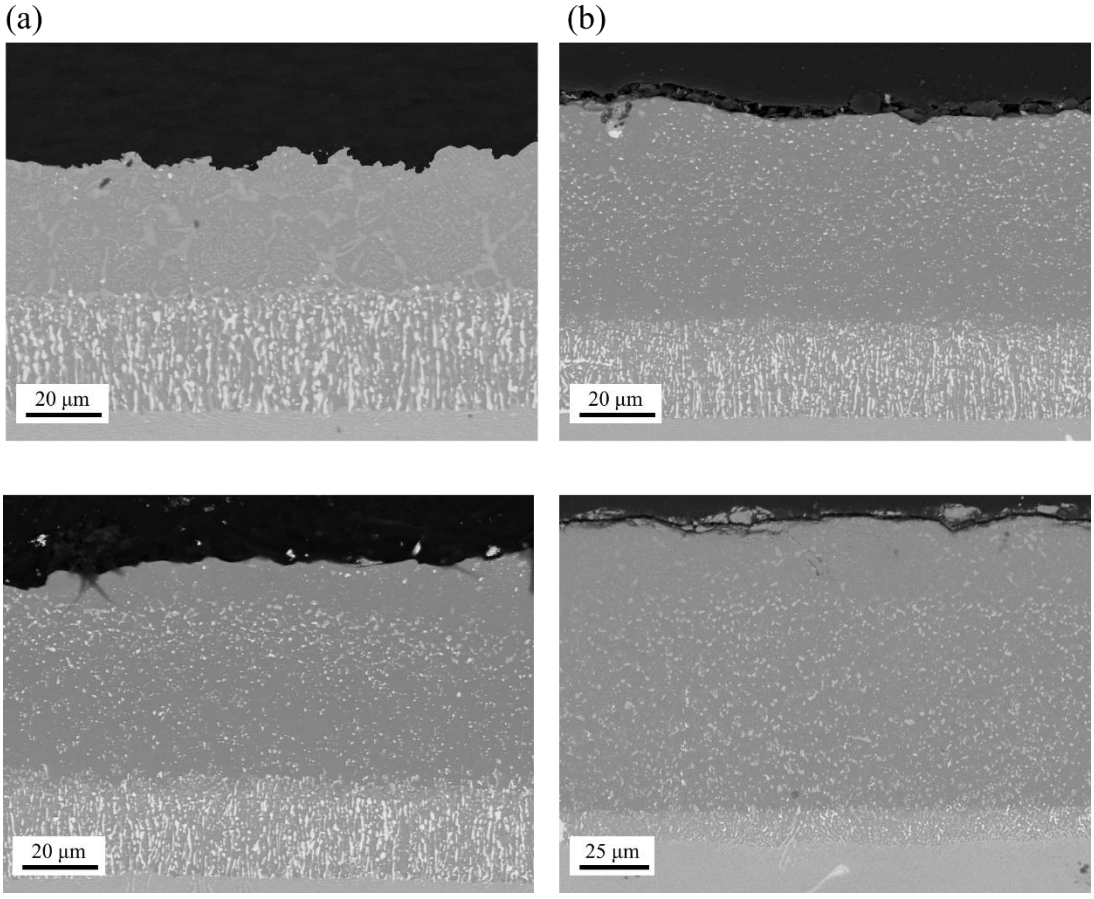

Figure 9.4: SEM-BSE cross sectional micrographs of aluminide coatings obtained with (a) 1.63 $mg_{slurry}/cm^3_{chamber}$, (b) 3.25 $mg_{slurry}/cm^3_{chamber}$, (c) 6.50 $mg_{slurry}/cm^3_{chamber}$, (d) 13.0 $mg_{slurry}/cm^3_{chamber}$.

Based on these findings, 6.50 $mg_{slurry}/cm^3_{chamber}$ was selected as the optimal slurry amount in the reaction chamber. This condition provides a coating with an Al/Ni profile comparable to that obtained with 3.25 $mg_{slurry}/cm^3_{chamber}$, while offering increased coating thickness and the possibility of treating larger surface areas per batch, thereby improving process efficiency.

Phase composition of the coatings was confirmed by XRD analysis. Figure 9.5 (a) displays diffraction spectra for coatings produced with 80, 100, and 150 $mg_{slurry}/cm^2_{sample}$. All samples primarily consist of the NiAl phase, but a distinct Ni_2Al_3 signal is detected in the 80 $mg_{slurry}/cm^2_{sample}$ coating, in line with EDS findings shown in Figure 9.2 (b). Cr_xAl_γ intermetallic peaks, typical of inward-grown coatings, are present in all samples. Additionally, $AlTi_2$ peaks appear, resulting from titanium diffusion from the substrate. Spectra for coatings produced with different slurry chamber concentrations are reported in Figure 9.5 (b). Coatings from 1.63 $mg_{slurry}/cm^3_{chamber}$ exhibited a biphasic structure of NiAl and Ni_3Al, confirming insufficient Al vapor generation for forming a uniform NiAl layer. Conversely, at excessively high slurry content, Ni_2Al_3 and $NiAl_3$ phases were detected, indicating an overabundance of aluminum and the formation of brittle, non-protective

intermetallics. Only NiAl and $AlCr_2$ peaks were observed in the sample processed at 6.50 $mg_{slurry}/cm^3_{chamber}$, confirming its capability to develop a protective α-Al_2O_3 scale under high-temperature conditions.

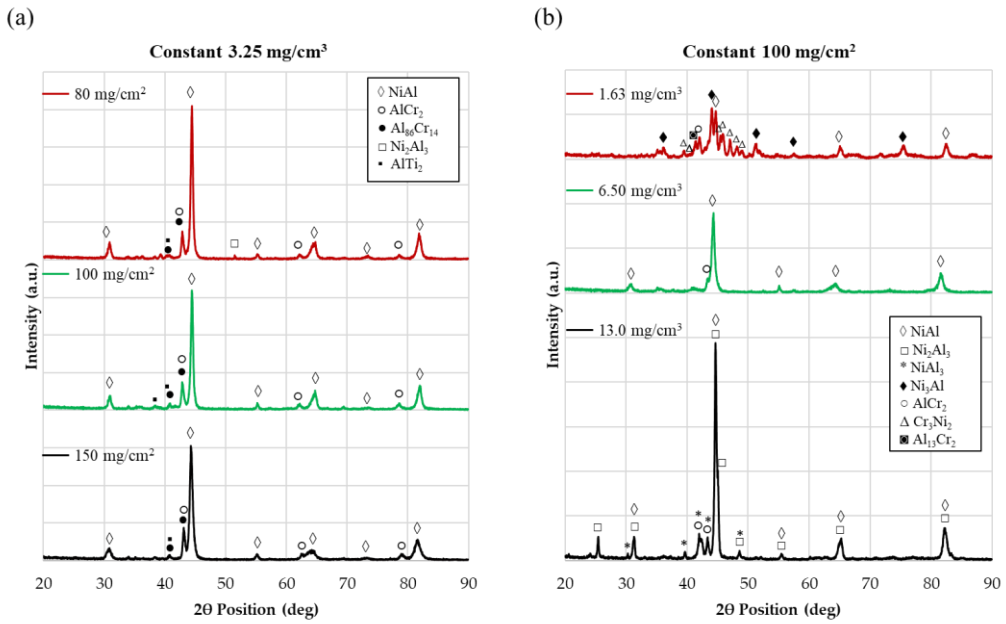

Figure 9.5: XRD spectra of aluminide coatings obtained by varying the $mg_{slurry}/cm^2_{sample}$ (a) and $mg_{slurry}/cm^3_{chamber}$ (b).

To further validate the flexibility and applicability of the optimized slurry aluminizing process for high-demand applications, platinum-modified aluminide coatings were manufactured. A 4.5 µm-thick Pt layer was first deposited onto the superalloy substrate, followed by a pre-aluminizing diffusion heat treatment prior to slurry application. The cross-sectional micrograph of the resulting Pt-aluminide coating is shown in Figure 9.6 (a). The overall coating thickness was measured to be 98 ± 4 µm, comprising an interdiffusion zone (IDZ) of 24 ± 3 µm and an outer biphasic layer of 29 ± 3 µm. A detailed view of the microstructure in the outer biphasic region is provided in Figure 9.6 (b), along with corresponding EDS analysis of the constituent phases. The brighter phase corresponds to ζ-$PtAl_2$, which likely incorporates minor amounts of Cr and Ni, as indicated by the quantitative data in the beside table. Notably, the brightness of individual ζ-phase grains appears to decrease with increasing Ni and Cr content, reflecting local compositional variations. In contrast, the light-grey phase in the outer layer corresponds to β-(Ni,Pt)Al. Small, bright, well-dispersed dot-like precipitates are observed throughout the coating, particularly along grain boundaries. These precipitates are rich in Ta and W and originate from the underlying superalloy, which is rich in these refractory elements. Despite the higher bulk W content in the superalloy, EDS analysis suggests that the precipitates are predominantly composed of Ta. This is attributed to the much higher interdiffusion coefficient of Ta compared to W, about one order of magnitude greater, at typical coating temperatures [236].

The presence of Cr-rich precipitates is also observed in the coating. This may be explained by the limited solubility of Cr in the plain β-NiAl phase [237]. In Pt-modified coatings, high Pt activity can promote the formation of PtCr intermetallic phases, as reported in [238]. Over prolonged high-temperature exposures, these phases may undergo transformation and result in localized Cr enrichment or secondary precipitation.

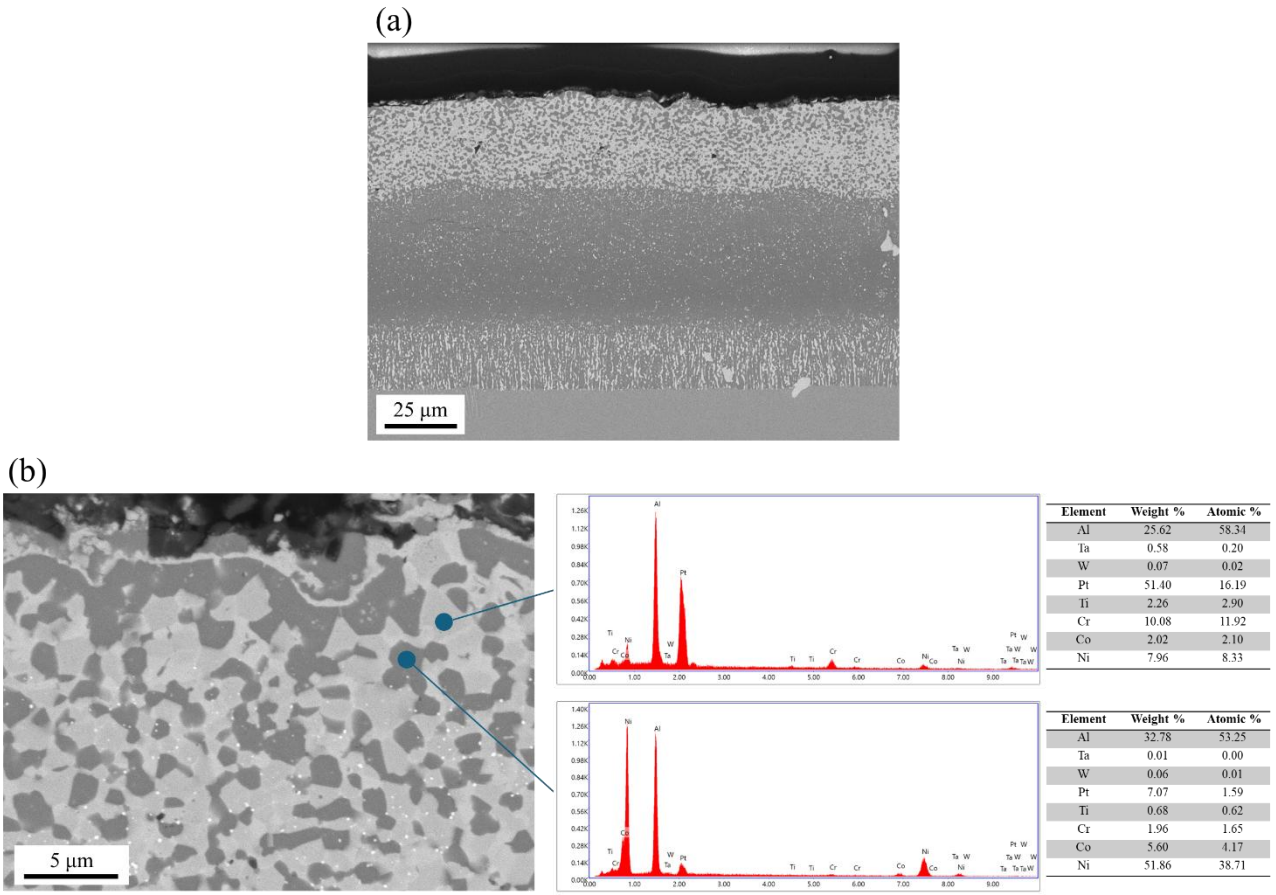

Figure 9.6: (a) Cross-sectional micrograph of the Pt-aluminide coating obtained with the optimized slurry method and (b) high magnification view of the microstructure in the outer biphasic region with EDS analysis.

Elemental concentration profiles of Ni, Al, and Pt across the coating thickness (expressed in atomic percent) are plotted in Figure 9.7. Both Pt and Al concentrations are elevated in the outermost region, consistent with the observed biphasic ζ-$PtAl_2$ and β-(Ni,Pt)Al microstructure. Crucially, the Al concentration does not exhibit a sharp drop before the IDZ. At a depth of 60 µm from the surface, an Al/Ni atomic ratio of approximately 0.8 is still present, indicating that the coating remains within the compositional range of β-NiAl.

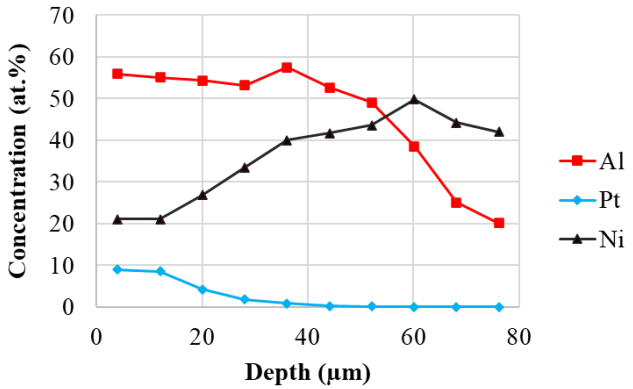

Figure 9.7: Elemental concentration profiles of Ni, Al, and Pt across the coating thickness.

Further confirmation of the phase constitution was obtained via XRD, as shown in Figure 9.8 (a). The diffractogram reveals the presence of both $PtAl_2$ (JCPDS 65-2983) and NiAl peaks, consistently with the biphasic microstructure of the outer coating layer. The incorporation of Pt into the β-NiAl lattice causes a noticeable shift of the NiAl diffraction peaks toward lower angles, consistent with lattice expansion due to Pt substitution [239]. Similarly, the $PtAl_2$ peaks are also shifted relative to those of the stoichiometric phase, likely due to the partial incorporation of Ni and/or Cr, as previously observed in studies such as [106]. Detail of peak shifting in reported in Figure 9.8 (b). A minor peak corresponding to Al_5Cr is also detected and is attributed to residual particles originating from the aluminizing slurry.

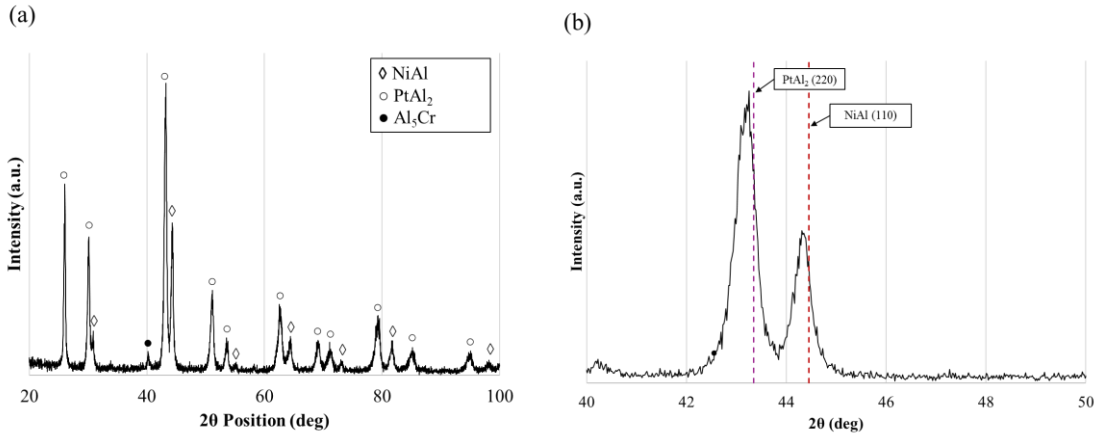

Figure 9.8: (a) XRD diffractogram of the Pt-aluminide coating obtained with the optimized slurry method and (b) detail of NiAl and $PtAl_2$ peak shifting.

This demonstrates that the slurry-based aluminizing process, when combined with the optimized thermal treatment protocol, is capable of delivering sufficient aluminum to form a protective β-NiAl phase throughout the coating thickness even in complex systems such as Pt-aluminides.

The microstructure and phase composition achieved with the present process differ from those obtained using the industrial route described in Chapter 8. In that case, the coatings exhibited a monophasic β-(Ni,Pt)Al structure. The difference can be attributed to the limited availability of

aluminum in the industrial setup, likely due to the much larger reaction chamber volume. Under fixed Ni and Pt concentrations, a higher Al content at elevated temperatures promotes the formation of $PtAl_2$ precipitates [108]. This outcome is beneficial, as the presence of a continuous β-phase through the coating thickness is expected to enhance high-temperature oxidation resistance, while the occurrence of $PtAl_2$ precipitates is known to mitigate rumpling and improve creep resistance [122].

9.2 Microstructure of Pt-aluminides with different initial Pt layer thickness

The newly developed slurry aluminizing process, combined with the innovative electroless platinum plating technique, enables precise investigation of the influence of initial Pt layer thickness on the microstructure and isothermal oxidation behavior of Pt-aluminides. Unlike galvanic methods, which often result in non-uniform Pt deposition due to edge effect, resulting in excessive accumulation on edges and insufficient coverage on convex surfaces, the electroless plating process ensures precise control over the deposited Pt thickness, regardless of the substrate geometry. This uniformity eliminates microstructural variability related to Pt thickness variability, which could affect diffusion profiles and lead to localized oxidation failures, such as oxide scale spallation or reduced adherence in under-plated areas. Using electroless deposition, the produced coatings exhibit a homogeneous and reproducible microstructure, allowing a true assessment of the intrinsic oxidation behavior of the Pt-aluminide system as a function of initial Pt content only, without interference from external deposition variables.

To investigate this systematically, initial Pt layer thicknesses of 4.5 µm, 7 µm, and 12 µm were deposited on René N4 superalloy discs, followed by identical diffusion and slurry aluminizing cycles as described in Paragraph 9.1. The resulting cross-sectional micrographs are shown in Figure 9.9. All three coatings exhibit the typical inward-grown aluminide structure, consisting of an outer dual-phase region of ζ-$PtAl_2$ and β-(Ni,Pt)Al, and an inner single-phase β-(Ni,Pt)Al zone. The coatings are uniform and pore-free across the entire section. Some Al_2O_3 particles, marked by red arrows, are visible at the coating's outermost surface: these originate from the sandblasting step and indicate the original position of the alloy surface prior to treatment. A noteworthy observation is that the overall thickness of the aluminide layer increases slightly with the thickness of the initial Pt layer. This phenomenon is likely due to the faster diffusion of Ni in the NiAl system containing Pt, as reported by [240]. The higher diffusion rate enables more Ni atoms to migrate from the substrate to the coating surface, where they react with Al to form a thicker β-(Ni,Pt)Al layer. Consequently, thicker bond coats are formed as the Pt layer thickness increases. The thickness of the dual-phase region also exhibits a clear dependence on the initial Pt layer thickness: it increases from 30 µm for an initial Pt layer of 4.5 µm, to 45 µm for 7 µm Pt, and up to 63 µm for 12 µm Pt. Moreover, the relative proportion

of the $PtAl_2$ phase in the dual-phase layer also increases with the initial Pt thickness. For the coating with the thickest Pt layer (12 µm), the outermost region is almost entirely composed of $PtAl_2$, with only minor β-(Ni,Pt)Al microprecipitates present. These results align closely with findings from previous studies, such as those by Krishna et al. [112], who noted that the form of the Pt-rich $PtAl_2$ phase in the outer coating layer is strongly influenced by the dilution of the initially pure Pt layer during the diffusion treatment. Therefore, a higher initial Pt content typically leads to a higher proportion of $PtAl_2$, in agreement with the Ni-Pt-Al phase diagram at the process temperature [241]. Since the Pt concentration decreases with depth, the dual-phase structure appears just below the surface in the 12 µm Pt sample, at depths where the Pt content is low enough to allow for the coexistence of β-(Ni,Pt)Al. Some localized two-phase regions may still occur near the surface due to minor fluctuations in Pt diffusion during treatment.

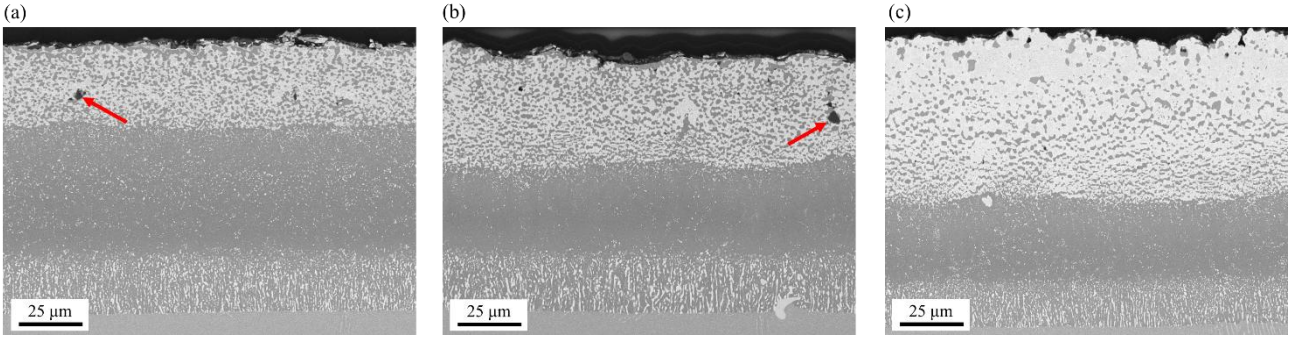

Figure 9.9: Cross-sectional micrographs of Pt aluminide coatings manufactured with different initial Pt layer thickness: (a) 4.5 µm, (b) 7 µm and (c) 12 µm. Red arrows point at alumina particles that are residue of sandblasting.

EDS concentration profiles for Ni, Pt, and Al across the outer, central, and inner regions (above the IDZ) of coatings with initial Pt layer thicknesses of 4.5 µm, 7 µm, and 12 µm are shown in Figure 9.10 (a), (b), and (c), respectively. As expected, Pt concentration in the outermost layer increases with initial Pt thickness. Pt content is highest in the outer layer and decreases toward the inner regions in all coatings. This trend is more pronounced for coatings with thicker initial Pt layers, where Pt remains at higher levels in the central region as well. Al content is comparable in the outer regions of coatings with 4.5 µm and 7 µm Pt layers, but is slightly higher in the 12 µm sample, reflecting the transition from a dual-phase to a near-monophasic $PtAl_2$ structure. Additionally, Al maintains a longer gradient extension toward the IDZ with increasing Pt content, reflecting the growing thickness of the dual-phase region. The Ni concentration trends are also coherent with these results. In the 4.5 µm coating, a sharp increase in Ni content is seen in the central where microstructure transitions to single-phase β-(Ni,Pt)Al. For the 7 µm sample, the gradient is more gradual, consistent with a broader dual-phase region. In the 12 µm sample, Ni rises sharply again, but only near the IDZ, where the single-phase β layer is observed. These differences are attributed to the less effective diffusion heat treatment prior to aluminizing in higher-Pt samples. A thicker Pt layer results in reduced dilution, limiting Ni outward

diffusion and favoring $PtAl_2$ formation at the surface. Notably, Al/Ni ratio in the inner region is equal to 1.1 in all three coatings, irrespective of the initial Pt amount, indicating the presence of the β phase in the entire coating.

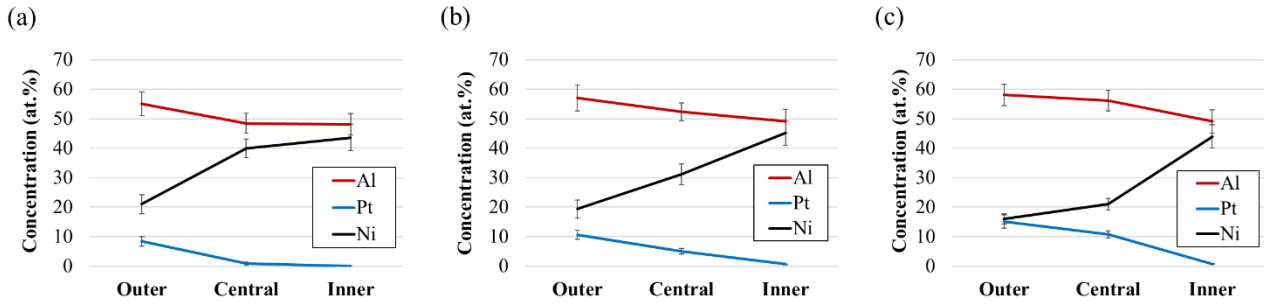

Figure 9.10: EDS concentration profiles across the outer, central, and inner regions (above the IDZ) of coatings with initial Pt layer thicknesses of (a) 4.5 µm, (b) 7 µm and (c) 12 µm

XRD spectra, presented in Figure 9.12, confirm the presence of only $PtAl_2$ and β-NiAl phases in all samples. A minor Al_5Cr peak is also detected and is attributed to residual slurry material. Notably, the intensity of the β-NiAl peak relative to $PtAl_2$ decreases with increasing Pt thickness, reaching a minimum in the 12 µm sample. This confirms the predominance of $PtAl_2$ in the outermost region for thicker Pt layers. In all cases, the β-NiAl phase exists as (Ni,Pt)Al, with diffraction peaks consistently shifted from those of stoichiometric β-NiAl, due to Pt incorporation; similarly, the $PtAl_2$ peaks show shifts from the nominal positions, attributed to solid solution of Ni and Cr (Figure 9.13). However, the extent of these shifts is similar across all three coatings, suggesting that the level of lattice distortion due to substitutional solutes remains similar regardless of initial Pt thickness. These findings are in good agreement with the results reported by Krishna et al. [112], who also observed limited variation in lattice parameters despite differing Pt concentrations. In contrast, Pauletti et al. [242] reported more significant peak shifts as a function of initial Pt thickness. However, it should be noted that in that study, the authors produced single-phase, outward-grown β coatings, which likely involved different diffusion mechanisms and solute distributions. This discrepancy highlights the importance of growth mode and processing conditions when interpreting XRD data in Pt-aluminide systems.

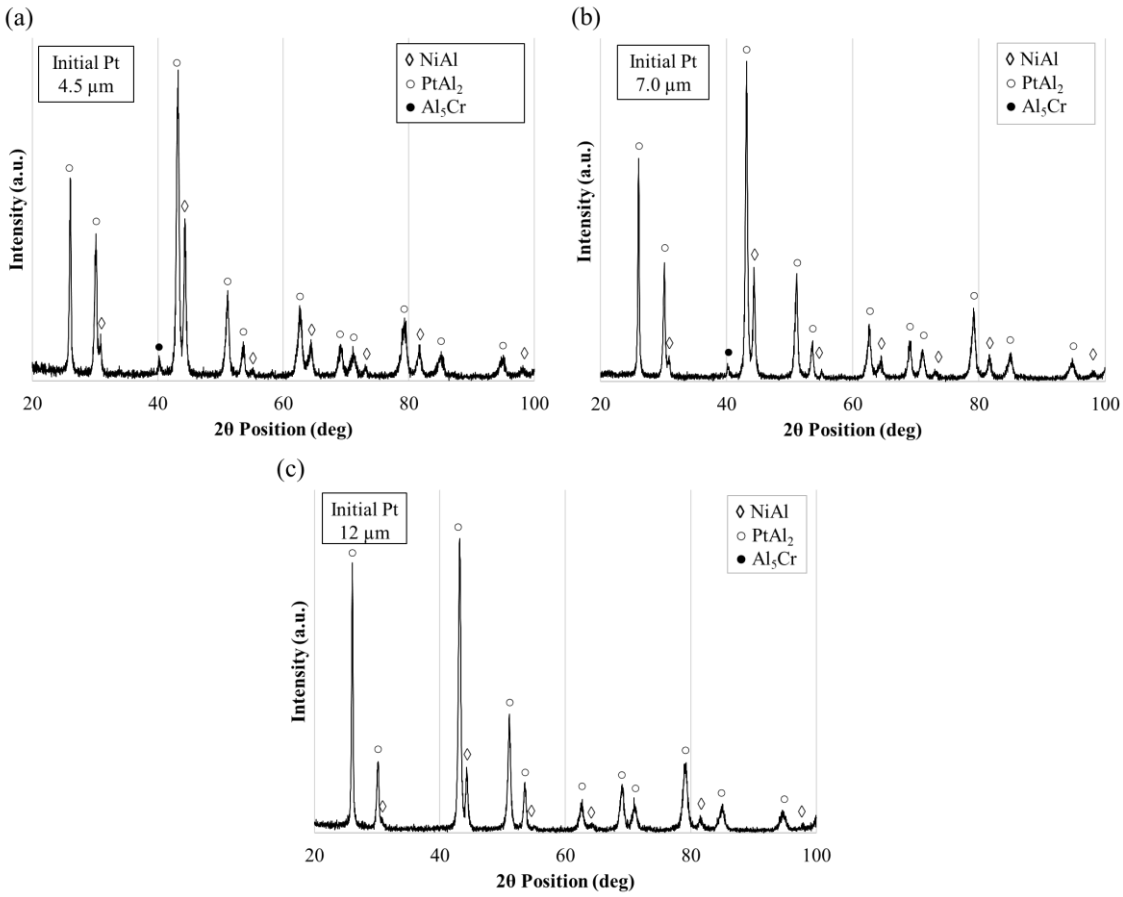

Figure 9.11: XRD spectra of Pt-aluminide coatings obtained with different initial Pt layer thickness: (a) 4.5 µm, (b) 7 µm and (c) 12 µm.

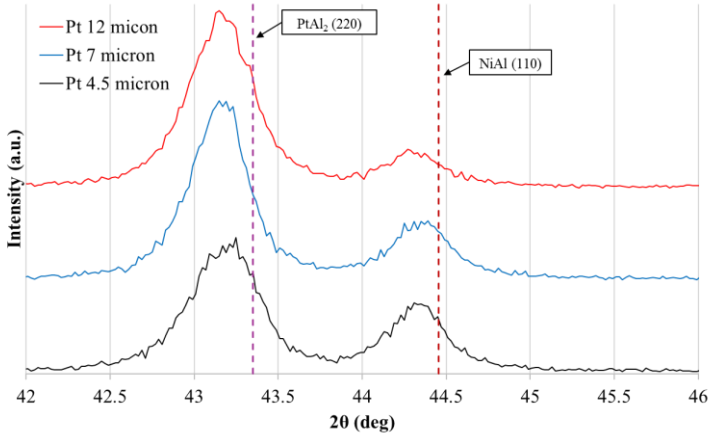

Figure 9.12: Detail of the XRD diffractograms highlighting NiAl and $PtAl_2$ peak shifting.

9.3 Oxidation resistance of Pt-aluminides with different initial Pt layer thickness

Isothermal oxidation resistance of Pt-aluminide coatings with varying initial Pt layer thickness was evaluated by monitoring mass gain during exposure at 1100 °C, as shown in Figure 9.13. During the initial stages of oxidation, up to approximately 40 hours, the oxidation kinetics are similar for all three coatings, indicating that initial Pt thickness does not significantly influence the early growth rate of

the Al_2O_3 oxide film. This is consistent with findings from prior studies conducted at both 1000 °C [242] and 1150 °C [104], where the different Pt content was shown to have a negligible effect on initial oxide scale formation.

However, with continued exposure, significant difference emerge between the behavior of coatings depending on their composition. After 1000 hours, the coating with an initial Pt thickness of 4.5 µm exhibits the highest mass gain, indicating faster oxide scale growth and inferior long-term oxidation resistance. In contrast, the coating with 12 µm of Pt initially shows the highest weight gain within the first 100 hours, but its oxidation rate rapidly decreases thereafter, resulting in the lowest cumulative weight gain after 1000 hours. The 7 µm Pt coating displays intermediate behavior, with the slowest initial oxidation rate, but similar long-term behavior to the coating with 12 µm of Pt.

The quantitative comparison of oxidation behavior is shown by fitting the experimental data using Monceau parabolic model (Figure 9.13, dashed lines) [53] and comparing the parabolic rate constants (k_p), summarized in Table 9.1. The high correlation coefficients (R_{corr}> 0.98 for all samples) confirm the reliability of the model fit. The significantly higher k_p for the 4.5 µm Pt coating highlights its limited protective capability, while the lower constants for 7 µm and 12 µm Pt coatings indicate superior oxidation resistance, characterized by slower oxide growth during prolonged high-temperature exposure, suggesting enhanced stability of the β phase, reduced Al depletion, and limited interdiffusion.

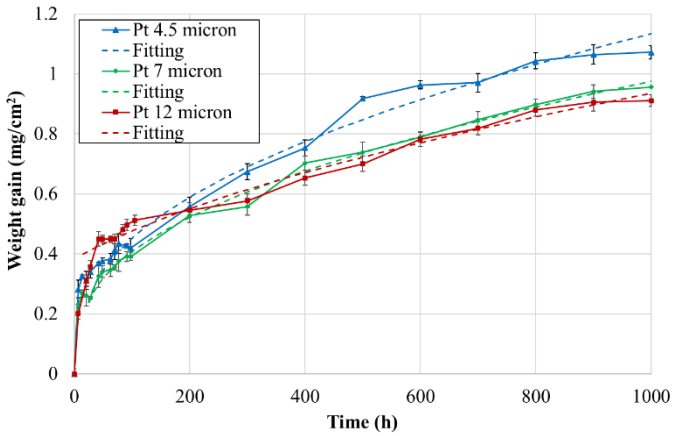

Figure 9.13: Weight gain curves for Pt-aluminides with different thickness of the initial Pt layer during oxidation tests at 1100°C.

	k_p (mg²/cm⁴/h)	R_{corr}
Pt 4.5 µm	$9.27 \cdot 10^{-4}$	0.983
Pt 7 µm	$6.41 \cdot 10^{-4}$	0.998
Pt 12 µm	$6.25 \cdot 10^{-4}$	0.994

Table 9.1: Parabolic constants calculated according to Monceau's model for Pt-aluminides with different initial Pt layer thickness and correlation coefficient of data fitting.

Cross-sectional micrographs after 1000 hours at 1100 °C provide further insight into the degradation mechanisms. In the 4.5 µm Pt coating (Figure 9.14 (a)), the bond coat appears completely depleted from the β phase below the oxide scale, and a large layer of γ′-Ni_3Al has formed. Moreover, the widespread presence of large portions of Ni_3Al across the bond coat confirm the severe Al depletion and local spallation of the oxide scale indicates early stages of failure. Bright Ta precipitates are dispersed throughout the coating. The higher-magnification image in Figure 9.14 (b) reveals that the TGO is no longer composed of pure Al_2O_3. Indeed, an outer layer of Ni- and Ti-rich Al_2O_3 is present, while Ta-rich oxides are visible internally. The formation of mixed oxides is likely the primary cause of the higher mass gain observed in the oxidation curves. The corresponding EDS elemental map in Figure 9.15 confirms the above observations, showing substantial Al depletion, Ti and Ni incorporation in the external oxide, and Cr enrichment in the γ′ phase beneath the TGO.

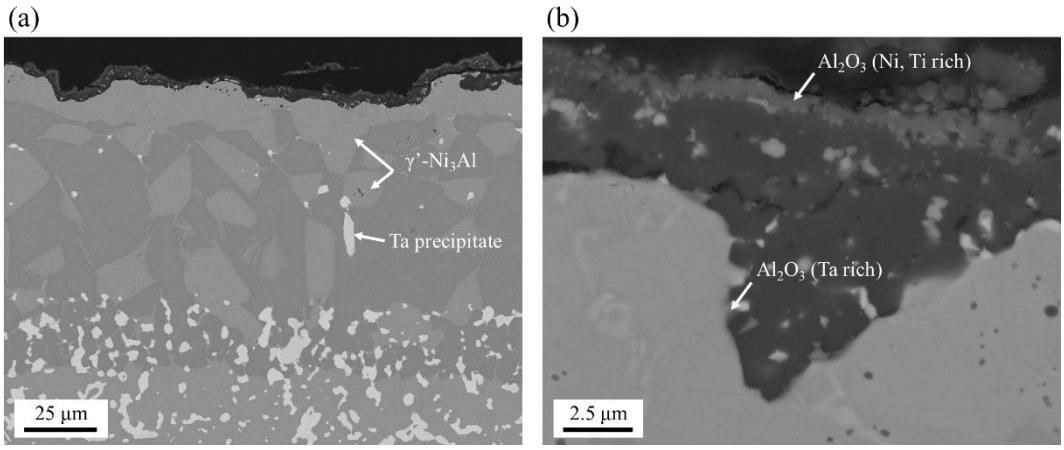

Figure 9.14: Cross-sectional micrographs after 1000 hours at 1100 °C for the 4.5 µm Pt coating: (a) overall coating and (b) higher magnification of the TGO.

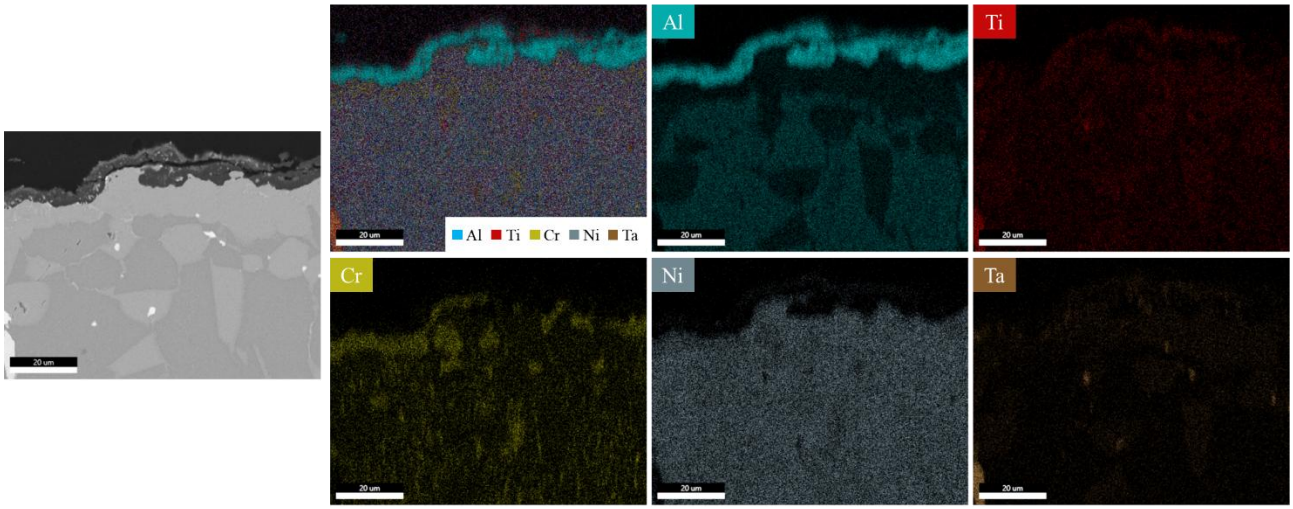

Figure 9.15: EDS elemental map of 4.5 µm Pt coating after 1000h at 1100°C.

In the 7 µm Pt coating, Figure 9.16 (a) shows a less extensive formation of Ni_3Al, suggesting a slower rate of Al depletion compared to the 4.5 µm case. However, β phase degradation is still evident below the oxide, and some regions of oxide spallation are visible, indicating that the coating is nearing the

end of its protective life. A Ni- and Ti-rich outer oxide scale is again present, as shown in Figure 9.16 (b). Despite being thinner and more discontinuous than in the 4.5 Pt coating, it still implies that Al amount in the coating is not sufficient to guarantee the selective oxidation of Al to protective pure and dense Al_2O_3 anymore.

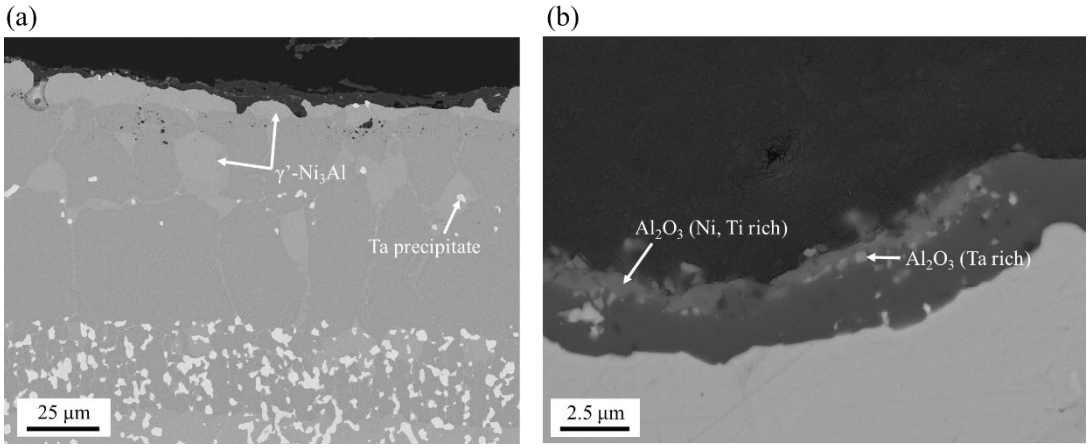

Figure 9.16: Cross-sectional micrographs after 1000 hours at 1100 °C for the 7 µm Pt coating: (a) overall coating and (b) higher magnification of the TGO.

Conversely, the 12 µm Pt coating shows considerably lower formation of Ni_3Al even after 1000 hours. As shown in Figure 9.17 (a) and (b), the coating still exhibits a dense and adherent α-Al_2O_3 scale, demonstrating excellent oxidation resistance. It suggest that a higher Pt content acts as a more effective diffusion barrier, suppressing Ni and Ti outward diffusion and thereby mitigating the formation of non-protective Ni and Ti oxides. This effect also contributes to stronger adherence of the TGO, since formation of fragile mixed oxides is retarded.

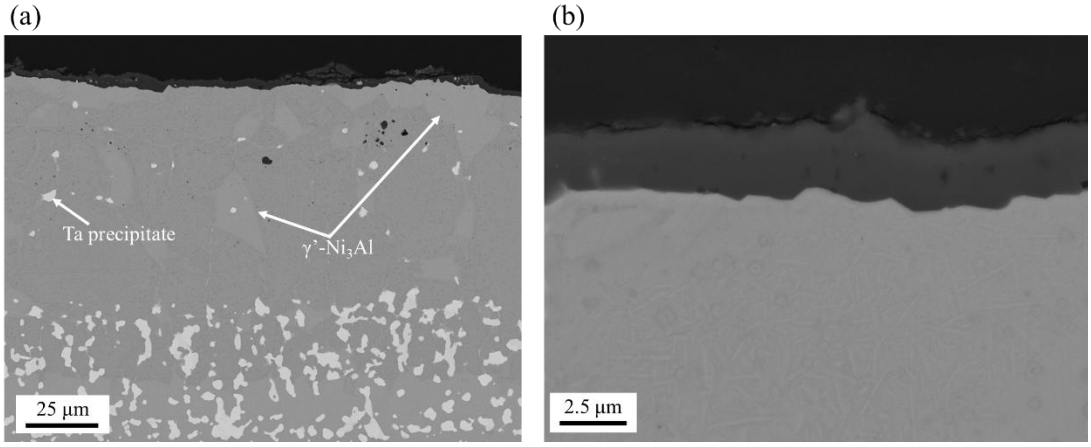

Figure 9.17: Cross-sectional micrographs after 1000 hours at 1100 °C for the 7 µm Pt coating: (a) overall coating and (b) higher magnification of the TGO.

Ta-rich precipitates are present in all three coatings, with no significant variation in distribution or morphology, suggesting that Pt content does not noticeably influence Ta mobility during prolonged oxidation. Additionally, no internal porosity or void formation was observed in any of the coatings

even after 1000 hours, indicating excellent microstructural stability of the bond coats fabricated through the electroless plating and slurry processes.

XRD spectra of the coatings after 1000 hours of oxidation are shown in Figure 9.18. All three coatings exhibit similar phase compositions, with peaks corresponding to Ni_3Al that forms as a result of Al depletion and β phase consumption. However, the relative intensity of the peaks varies, indicating different quantities of these phases. Notably, in the coatings with initial Pt thicknesses of 4.5 µm and 7 µm, the NiAl peaks correspond to an Al-deficient (hypostoichiometric) β phase (JCPDS 44-1185), and peaks of $NiAl_2O_4$ spinel and TiO_2 are clearly present. In contrast, no spinel or other oxide peaks are detected in the 12 µm Pt coating, confirming its reduced Al consumption and enhanced ability to maintain a stable, protective oxide layer throughout high-temperature exposure.

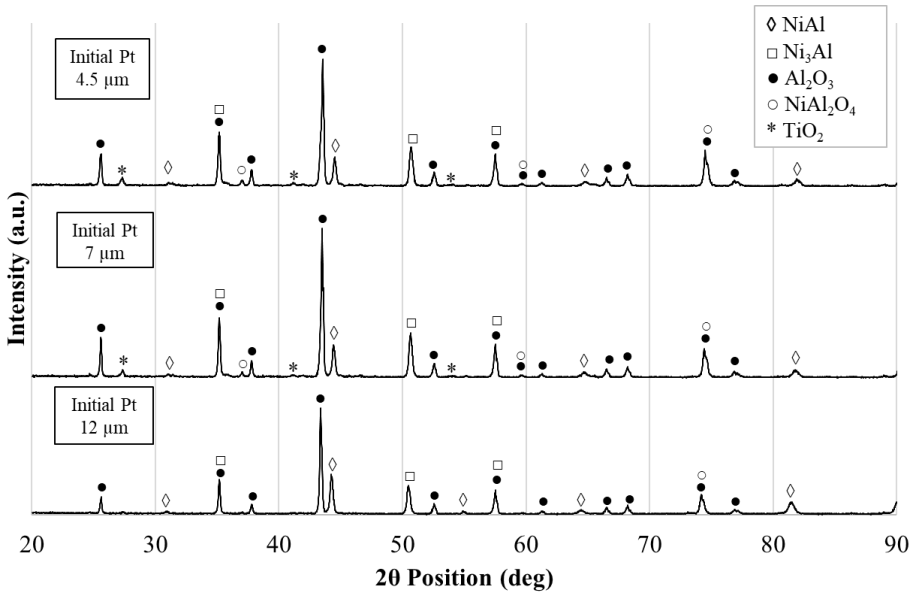

Figure 9.18: XRD spectra of coatings after 1000h of oxidation at 1100 °C.

Taken together, these results demonstrate that increasing Pt content up to at least 12 µm significantly enhances the oxidation resistance of Pt-aluminide coatings during isothermal exposure at 1100 °C. This is in disagreement with prior literature, which has often reported optimal oxidation resistance for coatings with 5–7 µm of initial Pt [112,114,242]. The discrepancy may arise from differences in coating architecture and the uniform Pt distribution enabled by the electroless plating process employed in the current study. It is also noteworthy that all Pt-aluminide coatings produced using the optimized slurry process, whether with comparable, higher, or lower Pt thickness, exhibited superior high-temperature oxidation resistance compared to those fabricated by the industrial method described in Chapter 8. The inferior performance of the industrial coatings can be attributed to their extremely low aluminum content, which led to severe Al depletion and extensive oxide spallation after only ~600 h of exposure. These findings emphasize the need for a synergistic balance among all coating constituents and underscore the critical importance of controlling every step of the

manufacturing process to achieve the desired microstructure. Nonetheless, it is important to point out that the presented results pertain exclusively to isothermal oxidation resistance. Further testing, including cyclic oxidation and thermal fatigue studies, will be required to evaluate the long-term durability and industrial applicability of these coatings under more realistic service conditions.

9.4 Conclusions

This chapter focused on optimizing a slurry-based aluminizing method and assessing the effects of initial platinum layer thickness on the microstructure and oxidation behavior of Pt-aluminide coatings.

The optimal initial slurry loading was determined to be 100 mg/cm², producing coatings with uniform Al/Ni ratios compatible with β-NiAl formation. Thinner or thicker layers led to Al-rich and Al-deficient regions, respectively, due to imbalanced aluminum transport during diffusion. Adjusting the slurry concentration in the reaction chamber identified 6.50 mg/cm³ as optimal, offering increased coating thickness while maintaining favorable phase composition. Lower or higher concentrations resulted in the formation of Ni_3Al or Ni_2Al_3, respectively, both detrimental to coating performance.

The optimized process was successfully applied to fabricate Pt-aluminide coatings. A 5 µm Pt layer followed by aluminizing produced a 98 µm coating with a biphasic outer region of ζ-$PtAl_2$ and β-(Ni,Pt)Al. EDS analysis confirmed the presence of a stable β-phase throughout the coating thickness, also near the IDZ.

Initial Pt thickness had a pronounced effect on coating microstructure. Pt layers of 4.5 µm, 7 µm, and 12 µm were studied. All coatings exhibited a biphasic outer region of ζ-$PtAl_2$ and β-(Ni,Pt)Al, over a single-phase β zone. Thicker Pt layers yielded increased total coating thickness of the coating and thicker dual-phase regions (30 to 63 µm), with higher $PtAl_2$ content near the surface. Nonetheless, the Al/Ni ratio in the β phase remained constant (~1.1) across all samples.

Increasing Pt thickness enhanced oxidation resistance at 1100 °C for up to 1000 h by stabilizing the β-phase and promoting α-Al_2O_3 scale formation. Thinner Pt layers led to faster Al depletion and the appearance of spinels and TiO_2, compromising protection.

In conclusion, the optimized slurry parameters enable the formation of oxidation-resistant coatings with controlled phase composition and diffusion profiles. The Pt layer thickness strongly influences coating architecture and oxidation behavior by modifying phase proportions, diffusion profiles, and growth kinetics, although long-term cyclic testing is recommended for comprehensive evaluation.

10. Electroless Ni-modified Pt-aluminides

Building upon the optimized slurry aluminizing and electroless platinum deposition process developed in Chapter 9, this chapter investigates the advanced modification of Pt-aluminide bond coat architecture through the incorporation of an additional, electroless deposited pure nickel interlayer. Deposited above Pt layer prior to subsequent diffusion and aluminizing steps, this intermediate Ni layer is designed to strategically modify concentration gradients and chemical activity of the diffusing species during both the pre-aluminizing heat treatment and the aluminizing process itself. These changes can significantly affect the resulting microstructure of the coating, with the aim of enhancing the β-NiAl reservoir and mitigating the formation of brittle outer phases, such as ζ-$PtAl_2$. This microstructural refinement is expected to improve the mechanical integrity of the coating, particularly under cyclic and long-term thermal exposures where outer-layer embrittlement is a critical concern.

Moreover, the presence of the Ni layer acts as an external Ni source, thereby reducing the extent of Ni depletion from the underlying superalloy during coating formation and mitigating interdiffusion between the coating and the substrate during high temperature exposure.

Extensive interdiffusion of Al and Ni during high-temperature service can disrupt the coherent γ/γ′ microstructure, facilitating the precipitation of TCP phases. These are typically enriched in refractory elements such as W, Re, Mo, and Cr, which have significantly lower solubility in both the β and γ′ phases compared to the γ matrix. As a result, the refractory species are progressively rejected during exposure and their precipitation becomes inevitable, leading to the formation of a SRZ at the coating/substrate interface (below the IDZ).

The formation of these TCP phases, particularly in needle- or platelet-like morphologies, is widely recognized as detrimental to the high-temperature mechanical performance of superalloys. Their presence reduces the concentration of solid solution strengthening elements and promote intergranular embrittlement, negatively impacting creep resistance and fatigue resistance [101,208];

To address this issue, the Ni interlayer serves a dual purpose: it provides an auxiliary Ni source to support the formation of the β-phase during aluminizing, thereby minimizing Ni depletion from the superalloy substrate, and it acts as a diffusion buffer that retards the extent of coating-substrate interdiffusion, reducing the driving force to TCP precipitation.

Numerous strategies have been previously proposed to limit interdiffusion between metallic coatings and superalloys. These include the addition of reactive elements [101,243–245] and the incorporation of inert second-phases to create diffusion barriers [246–248]. However, relatively few studies have examined the effect of introducing an additional pure Ni layer as a strategy to modify aluminide

coatings [73,249,250], and only one has addressed its application to Pt-aluminides specifically [128]. To the author's knowledge, no systematic study has yet been conducted to explore how the thickness of the pre-deposited Ni interlayer influences the microstructure and oxidation resistance of Pt-aluminide coatings. This chapter addresses this gap by examining the influence of electroless Ni interlayers with initial thicknesses of 5, 10, 20, and 40 µm. Sketch in Figure 10.1 illustrates the procedure for the manufacturing of modified coatings. The study analyzes the resulting microstructure and elemental distribution after both the diffusion heat treatment and the aluminizing process. Furthermore, the high-temperature performance of the coatings is evaluated through isothermal oxidation tests conducted at 1100 °C for durations of up to 1000 hours.

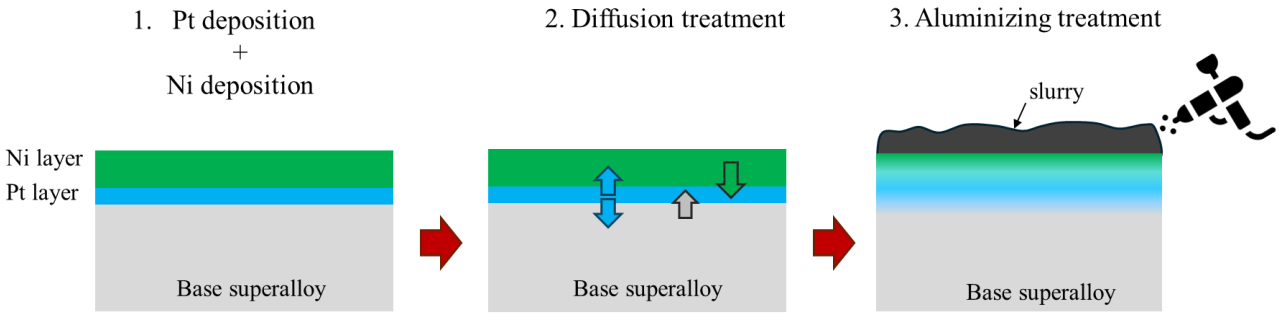

Figure 10.1: Sketch of the procedure for the manufacturing of Ni modified Pt aluminides.

10.1 As deposited and as diffused coatings

A representative cross-sectional micrograph of the as-deposited Pt/Ni multilayer system is shown in Figure 10.2. Both the platinum and nickel coatings appear uniform and well-adherent to the substrate. Although some microcracks are visible within the Pt layer, there are no regions of substrate exposure. In contrast, the Ni layer exhibits a dense, compact, and defect-free structure. Notably, the electroless-deposited Ni layer penetrates into the existing cracks of the Pt layer, ensuring a continuous and fully sealed multilayer structure.

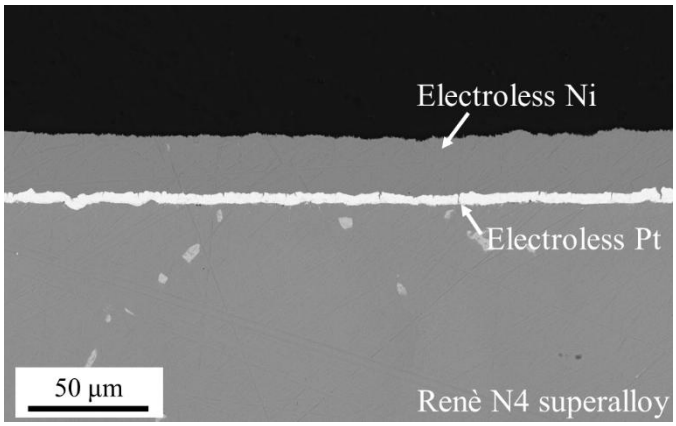

Figure 10.2: SEM-BSE cross-sectional micrograph of the as-deposited Pt/Ni multilayer system.

The surface morphology of the electroless Ni coating is presented in Figure 10.3 (b). In accordance with prior observations [210], the surface displays a hierarchical topography, with nodular features

at the microscale and nanoscale protrusions forming spike-like structures. For comparison, the cauliflower-like morphology of the as-deposited Pt surface is shown in Figure 10.3 (a).

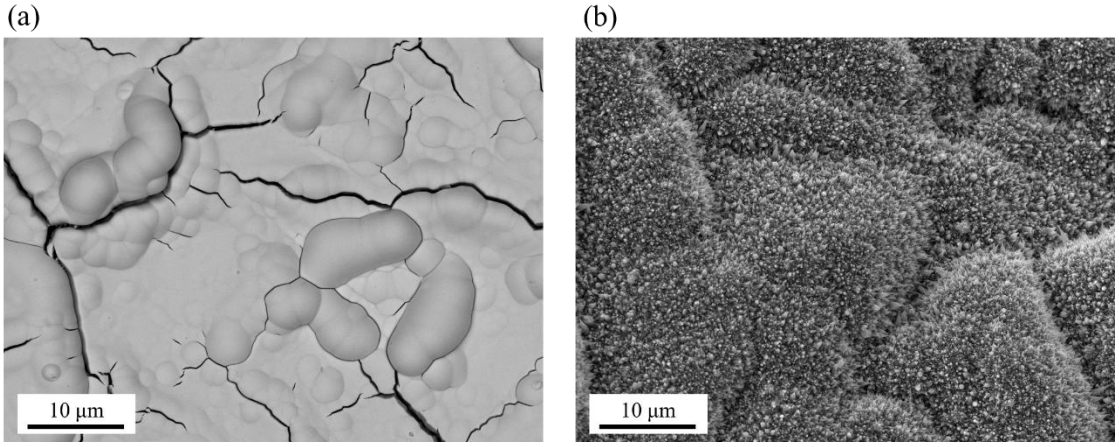

Figure 10.3:. Morphology of the as-deposited Pt layer (a) and Pt/Ni multilayer system (b).

Substantial changes in surface morphology occur after the pre-aluminizing diffusion heat treatment for both the standard and Ni-modified systems, as illustrated in Figure 10.4. The surfaces become similar and evolve toward a more coarsened and granular structure, as reported in [251]. Single grains in the Pt-only surface are considerably smaller, suggesting a lower initial grain size of the Pt structure. Both coatings appear free of surface defects, and the microcracks originally present in the Pt layer are no longer visible, suggesting effective stress interlayer diffusion during the heat treatment.

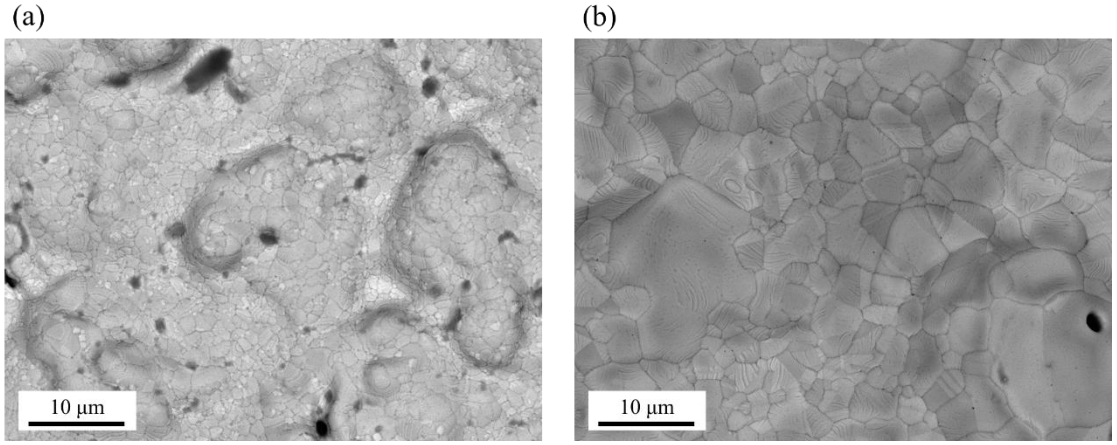

Figure 10.4:. Morphology of the Pt layer (a) and Pt/Ni multilayer system (b) after the pre-aluminizing diffusion heat treatment at 1100°C for 1h.

The cross-sectional microstructure of the diffusion-treated coating without nickel modification is shown in Figure 10.5 (a). It reveals a dual-layer configuration, with an outer region predominantly composed of a Pt-rich γ phase, and an inner interdiffusion zone consisting of both γ and γ′ phases. The primary diffusion front is irregular, and no significant enrichment in refractory elements such as Ta or W is detected, despite their known mobility at temperatures above 1000 °C [236]. EDS analysis indicates 4.2 at.% Al and 12.2 at.% Pt in the outer γ region, while the γ/γ′ interdiffusion zone contains

7.4 at.% Al and 16.4 at.% Pt. The presence of superalloy constituents such as Ni, Cr, and Al near the top surface confirms their upward diffusion during the thermal treatment [238]. Voids are observed at the interface between the interdiffusion zone and the substrate, which are attributed to the Kirkendall effect, as previously documented [106,252,253]. These voids follow the Pt diffusion front and are attributed to vacancy condensation resulting from unequal interdiffusion rates between elements [253]. When a 5 µm electroless Ni layer is introduced prior to the diffusion heat treatment, the microstructure remains dual-layered with an outer Pt-rich γ phase and an inner interdiffusion zone comprising γ and γ′ phases (Figure 10.5 (b)). As expected, the overall diffusion layer becomes thicker, and the external γ region expands. The γ′ phase content in the interdiffusion zone is reduced, suggesting that the additional Ni promotes more uniform Pt dilution during diffusion. Al concentration in the outer region is slightly lower (3.6 at.%), while in the interdiffusion zone it increases significantly to 17.8 at.% in correspondence with Pt-rich γ′ domains. Importantly, no Kirkendall porosity is observed in this case, indicating that the altered diffusion gradients due to the Ni interlayer reduce vacancy supersaturation and suppress void formation.

As the thickness of the Ni interlayer increases to 10 µm (Figure 10.5 (c)), the diffusion layer becomes further extended, and the γ′ phase presence diminishes. In this case, γ′ precipitates are only sporadically found below the initial substrate interface, identifiable by embedded Al_2O_3 particles left from the sandblasting process. An even thicker diffusion layer is observed for coatings with 20 µm Ni and further decreased amount of Pt-rich γ′ phase is present (Figure 10.5 (d)), to eventually become not visible for the 40 µm thick Ni interlayer (Figure 10.5 (e)). In the thicker Ni-modified coatings, small voids begin to form within the diffusion layer above the original interface. These are likely associated with the Kirkendall effect, but now manifest within the multilayer itself rather than at the substrate boundary. The extent of void formation increases with Ni thickness, indicating that an excess Ni supply might locally disrupt balanced diffusion, leading to supersaturation and subsequent void coalescence.

Interestingly, the diffusion layer does not continue to thicken indefinitely with increased Ni interlayer thickness. The coating produced with 40 µm of Ni shows a reduced diffusion depth compared to the 20 µm variant. This behavior can be explained by considering that once a sufficient quantity of Ni is available to fully dilute the Pt during diffusion, further increases in Ni thickness do not significantly alter interdiffusion kinetics. Additionally, the thicker Ni layer could act as a diffusion buffer, slowing down the advancement of reactive species. This may reduce the overall extent of interdiffusion and reaction zone development, limiting the growth of the diffusion layer.

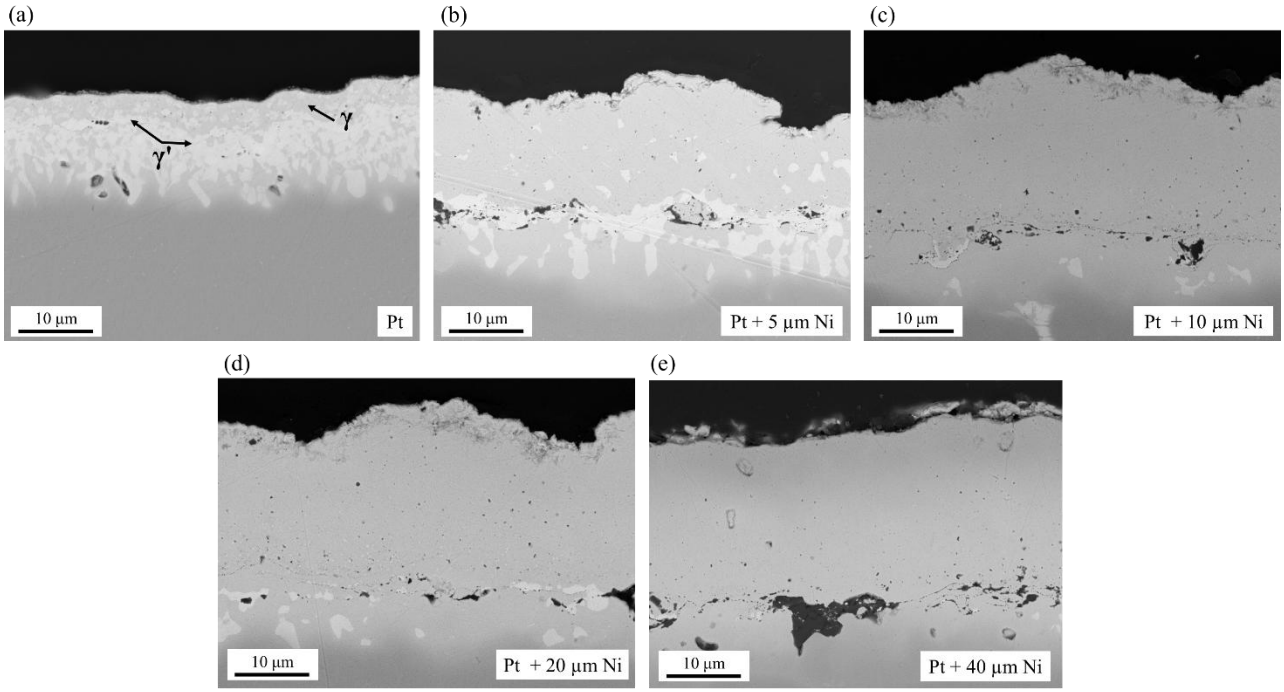

Figure 10.5: SEM-BSE cross sectional micrographs of coatings after diffusion at 1100°C for 1h: (a) Pt-only coatings and coatings modified with (b) 5 µm Ni, (c) 10 µm Ni, (d) 20 µm Ni, (e) 40 µm Ni.

EDS concentration profiles for Al, Pt, and Ni across the coating thickness are presented in Figure 10.6 (a–c). In all samples, aluminum (Figure 10.6 (a)) exhibits a characteristic profile: its concentration is lowest at the surface (γ region), peaks in the interdiffusion zone where γ′ phases are present and eventually decreases after the interdiffusion zone. The peak is most pronounced in the Pt-only and 5 µm Ni coatings, while in thicker Ni-modified samples (10, 20, and 40 µm), the Al profile becomes more gradual and the peak concentration values are reduced.

For Pt (Figure 10.6 (b)), high concentrations are observed near the surface in the Pt-only and 5 µm Ni coatings, with a maximum in the interdiffusion zone corresponding to the γ′ phase. However, for the 10 µm Ni sample, the Pt profile is relatively flat throughout the diffusion zone, dropping only at the substrate interface. In contrast, the 20 and 40 µm Ni coatings show increasing Pt concentration from the surface inward, with a peak near the original interface before rapidly dropping to zero. This trend reflects the enhanced dilution of Pt due to the thicker Ni layer, which promotes a more uniform and deeper penetration of Pt during diffusion. Indeed, the thick Ni interlayer limits Pt accumulation at the surface and allows homogeneous distribution within the diffusion zone.

Nickel concentration profiles (Figure 10.6 (c)) show increasing surface values with increasing Ni layer thickness, followed by gradual decreases toward the substrate for all the modified coatings. The minimum observed in the 5 µm Ni coating coincides with the γ′ region where Pt and Al peak. Conversely, in the Pt-only coating, Ni content increases steadily from surface to substrate, but it stabilizes at the same value as other curves as the substrate is reached.

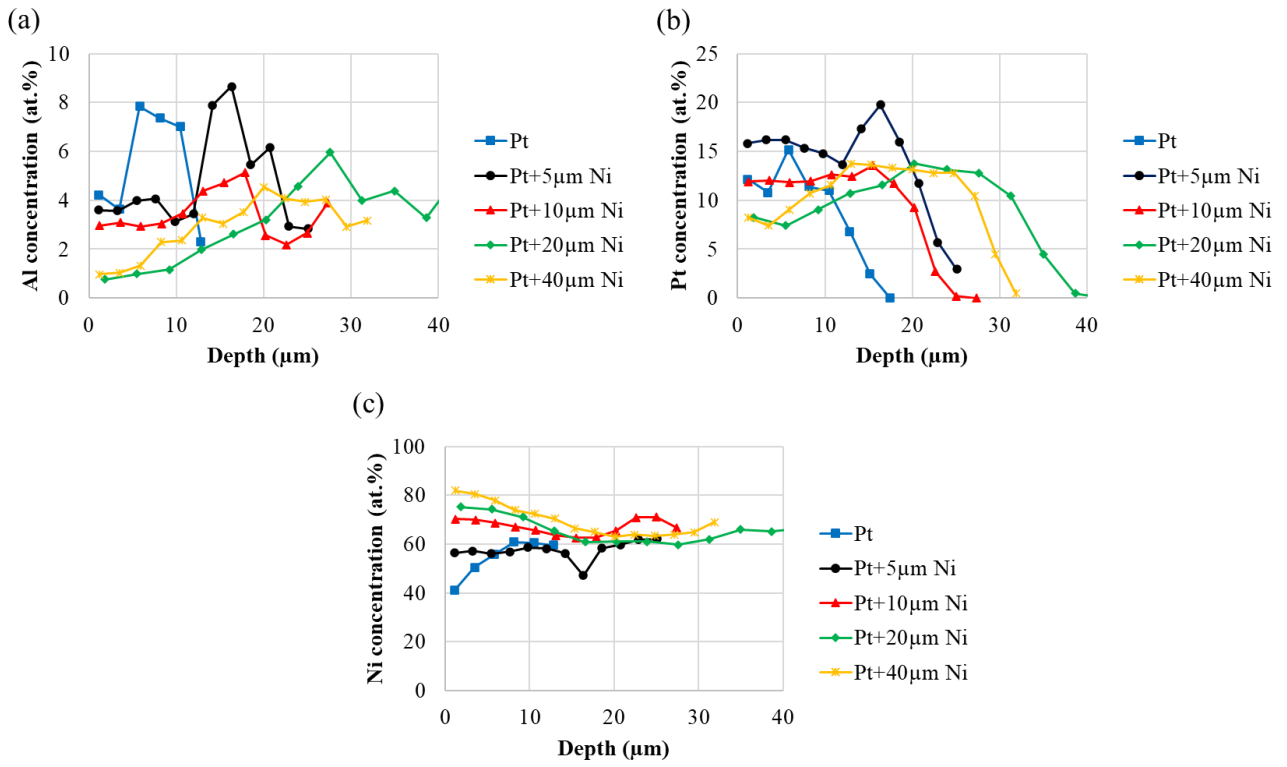

Figure 10.6: EDS concentration profiles for Al (a), Pt (b), and Ni (c) as a function of the distance from the surface (depth).

XRD spectra of standard and Ni-modified coatings following diffusion treatment are shown in Figure 10.7. The Pt-only coating exhibits only γ′-(Ni_3Al) reflections, with a pronounced left-shift of the peaks, indicating substantial Pt incorporation within the Ni_3Al lattice [254]. In coatings modified with 5 and 10 µm of Ni, both γ and γ′ phases are detected, with the intensity of γ peaks increasing with Ni layer thickness. The left-shift in γ′ peaks is progressively reduced, suggesting a decreasing Pt content in the Ni_3Al phase due to improved Ni availability during diffusion. For coatings with 20 and 40 µm Ni layers, only γ-phase peaks are observed due to excess Ni buffering the Pt content, in agreement with the microstructural observations by SEM micrographs.

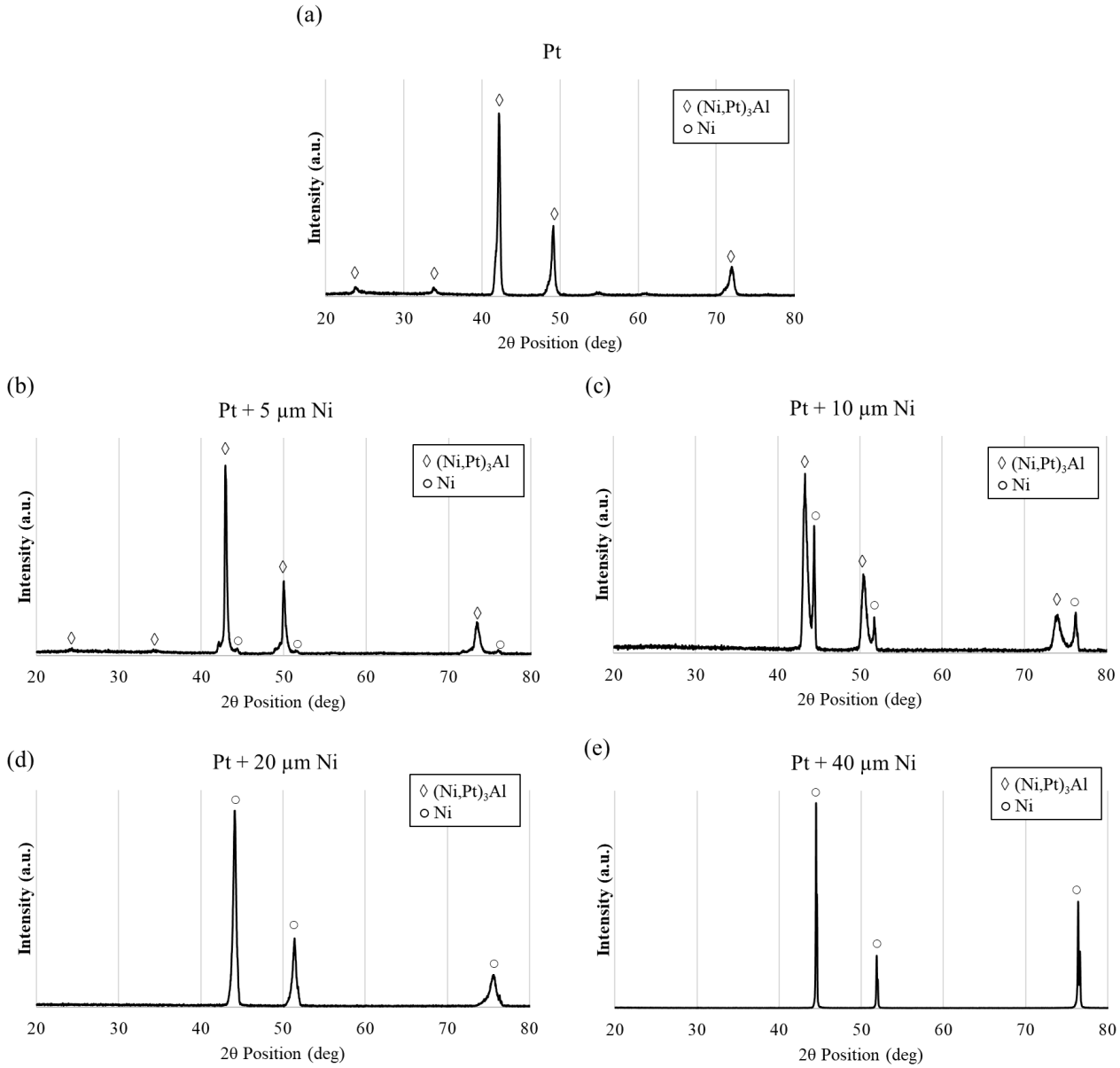

Figure 10.7: XRD diffractograms of coatings after diffusion at 1100°C for 1h: (a) Pt-only coatings, and coatings modified with (b) 5 µm Ni, (c) 10 µm Ni, (d) 20 µm Ni, (e) 40 µm Ni.

10.2 As aluminized coatings

Cross-sectional micrographs of Ni-modified coatings are presented in Figure 10.8, with the micrograph of the standard Pt-aluminide coating shown in Figure 10.8 (a) for reference. All coatings, regardless of the Ni layer thickness, exhibit a comparable bond coat thickness of approximately 75 µm, excluding the IDZ. However, a progressive reduction in the IDZ thickness is observed with increasing thickness of the pre-deposited Ni layer. This behavior is attributed to the role of the Ni layer as a nickel reservoir, supplying Ni for β-NiAl phase formation during aluminizing. As the external Ni thickness increases, more nickel is available to participate in β-phase formation, which reduces Ni diffusion from the substrate, thereby limiting IDZ development. This inverse relationship

between IDZ thickness and Ni layer thickness is quantitatively illustrated in Figure 10.9. Experimental data (35 measurements per Ni thickness and 35 for IDZ) were fitted using the ordinary least squares method, yielding a linear trend with a high correlation coefficient (R_{corr} = 0.9988), in agreement with trends reported for standard aluminides [73]. Despite these changes in IDZ, the overall bond coat thickness (excluding IDZ) remains constant across all samples, indicating that aluminum availability, not nickel, limits the total thickness of the aluminide coating under the given processing conditions.

Significant microstructural evolution is observed with increasing Ni layer thickness. The 5 µm Ni-coated sample, shown in Figure 10.8 (b), exhibits a biphasic outer layer composed of β-(Ni,Pt)Al and ζ-$PtAl_2$, similar to the standard Pt-aluminide. Beneath this, a homogeneous single-phase β-(Ni,Pt)Al layer overlays the IDZ. However, the quantity and size of $PtAl_2$ precipitates in the outer region are reduced compared to the standard coating, indicating partial suppression of the Pt-rich phase.

When the pre-deposited Ni layer is increased to 10 µm (Figure 10.8 (c)), the outer $PtAl_2$ phase is further diminished, and a thin, single-phase β-(Ni,Pt)Al layer is observed at the surface. With a 20 µm Ni layer (Figure 10.8 (d)), this outer β-layer becomes significantly thicker, nearly 40 µm, while only small $PtAl_2$ precipitates persist, mainly at grain boundaries. A biphasic region still appears below this thick β-layer, suggesting that 20 µm of Ni is not sufficient to fully dilute the Pt content and completely eliminate $PtAl_2$ formation. It should also be noted that in the inner single β-phase layer, the quantity of finely dispersed precipitates of alloying elements (mainly Cr and Ta), which diffuse from the superalloy substrate, is significantly reduced as the thickness of the pre-deposited Ni layer increases. The suppression of the fragile $PtAl_2$ phase in the outermost region of the coating with 20 microns Ni is expected to increase mechanical properties, since Pt solid solution strengthening is known to increase tensile strength [255]. Moreover, according to the work by Taylor et. al [256] the fine dispersion of second-phase particles present in the outer region can associate with associated high creep strength. Conversely, two-phase coatings usually exhibit higher hardness and low ductility at low temperatures. Despite a gain in ductility is expected during high temperature exposure due to the progressive dissolution of the two-phase NiAl/$PtAl_2$ structure, much damage is caused in the first high temperature cycles, which lead to a shortening in service life by a factor of 2-3 [228,257,258].

As the Ni layer is increased to 40 µm (Figure 10.8 (e)), the microstructure transitions toward a single-phase β-(Ni,Pt)Al coating, free of $PtAl_2$ and secondary precipitates. In this case, the single phase beta-(Ni,Pt)Al front has climbed towards the outer surface: an external beta layer free of precipitates forms, and the microstructure is similar to that of outward grown (low-activity) aluminides [80]. Similar results are reported in literature for aluminides modified by pre-deposition of Ni or Co prior to pack or slurry aluminizing [73,249,259,260]. It can be hypothesized that in the presence of a thick Ni layer,

the β-phase forms primarily through direct reaction between Ni and Al, with limited Al inward diffusion. As reported by Sarraf et al. [260], high process temperatures and excess Ni favor outward Ni diffusion, while inward Al diffusion becomes rate-limiting. Moreover, since Ni diffuses more rapidly than Al, especially in Al-deficient environments [261], this unbalanced diffusion flux gives rise to Kirkendall-type porosity, which are indeed observed in the 40 µm Ni coating.

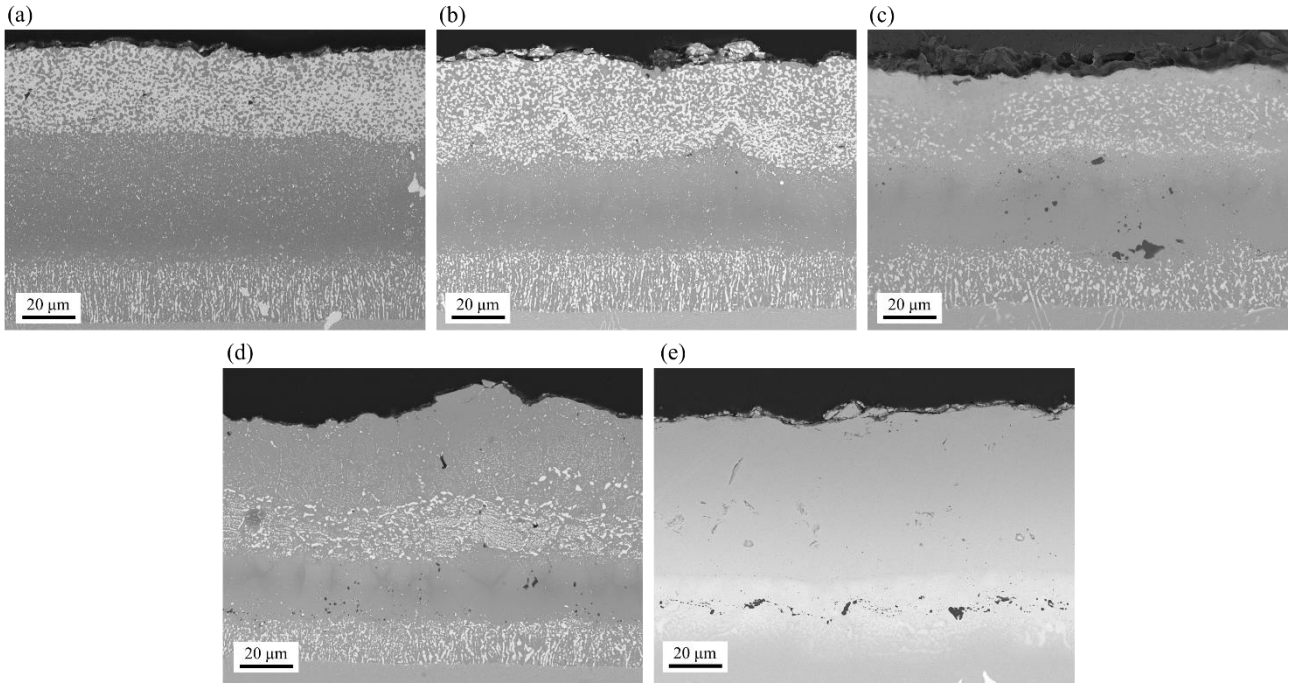

Figure 10.8: SEM-BSE cross sectional micrographs of coatings after aluminizing: (a) Pt-only coatings and coatings modified with (b) 5 µm Ni, (c) 10 µm Ni, (d) 20 µm Ni, (e) 40 µm Ni.

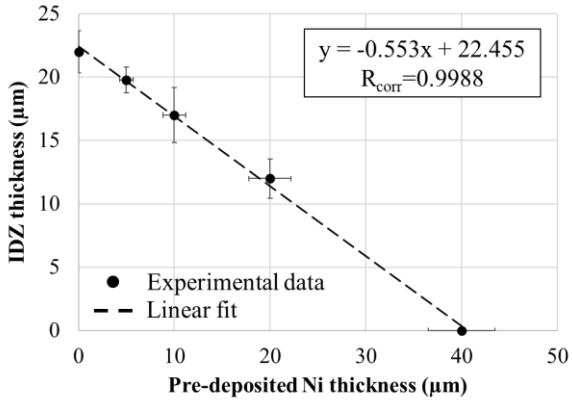

Figure 10.9: Progressive reduction of IDZ as a function of the thickness of the pre-deposited nickel layer. Experimental data were fitted according to ordinary least squares method, to prove the inverse linear trend.

Elemental concentration profiles obtained by EDS for the standard and Ni-modified Pt-aluminides are displayed in Figure 10.10. The gap between Ni and Al concentrations narrows as the Ni layer thickness increases, since the higher Ni availability promotes the formation of a Ni-richer layer. For the Pt-only and 5 µm Ni coatings, the profiles are very similar, except for a slightly higher Ni

concentration in the outer region of the 5 µm Ni sample, which reflects the contribution of the additional Ni layer without significantly altering the overall phase structure.

In contrast, the 10 µm Ni coating shows a different concentration profile, which closely mirrors the corresponding cross-sectional microstructure. In this case, a thin, hyper-stoichiometric NiAl layer forms at the surface, indicating an excess of Ni relative to Al. This is followed by a biphasic region, enriched in both Pt and Al, and a final hypo-stoichiometric β phase in the innermost part of the coating, characterized by reduced Al content. This gradient corresponds well with the microstructural stratification observed in cross-sectional imaging.

In the Pt-only, 5 µm, and 10 µm Ni coatings, a higher Cr content is also detected in the outer region. This can be attributed to the limited solubility of Cr in the β-NiAl phase [262], and the tendency for PtCr intermetallics to form under Pt-saturated conditions, which, during high-temperature exposure, decompose and release Cr back into the matrix [238].

For the 20 µm Ni sample, the Pt concentration increases notably within the biphasic region, while the outermost zone displays a quasi-stoichiometric NiAl composition. Moving inward, the β-phase becomes slightly Al-deficient, with an average Al/Ni atomic ratio of approximately 0.9 in the layer just above the IDZ.

In the 40 µm Ni coating, the entire β-phase region exhibits a consistent hypo-stoichiometric composition, with an average Al/Ni ratio of 0.71. This confirms that Al availability becomes the limiting factor in coating formation when excess Ni is present. This stoichiometry also explains the outward growth mechanism of the coating: Al and Ni diffusivities vary strongly with composition, and Al diffusion becomes increasingly limited in Ni-rich environments [263–265], promoting the formation of outward-growing coatings. A platinum-enriched region is observed in correspondence of the interface between the coating and the substrate, coinciding with the former location of the IDZ.

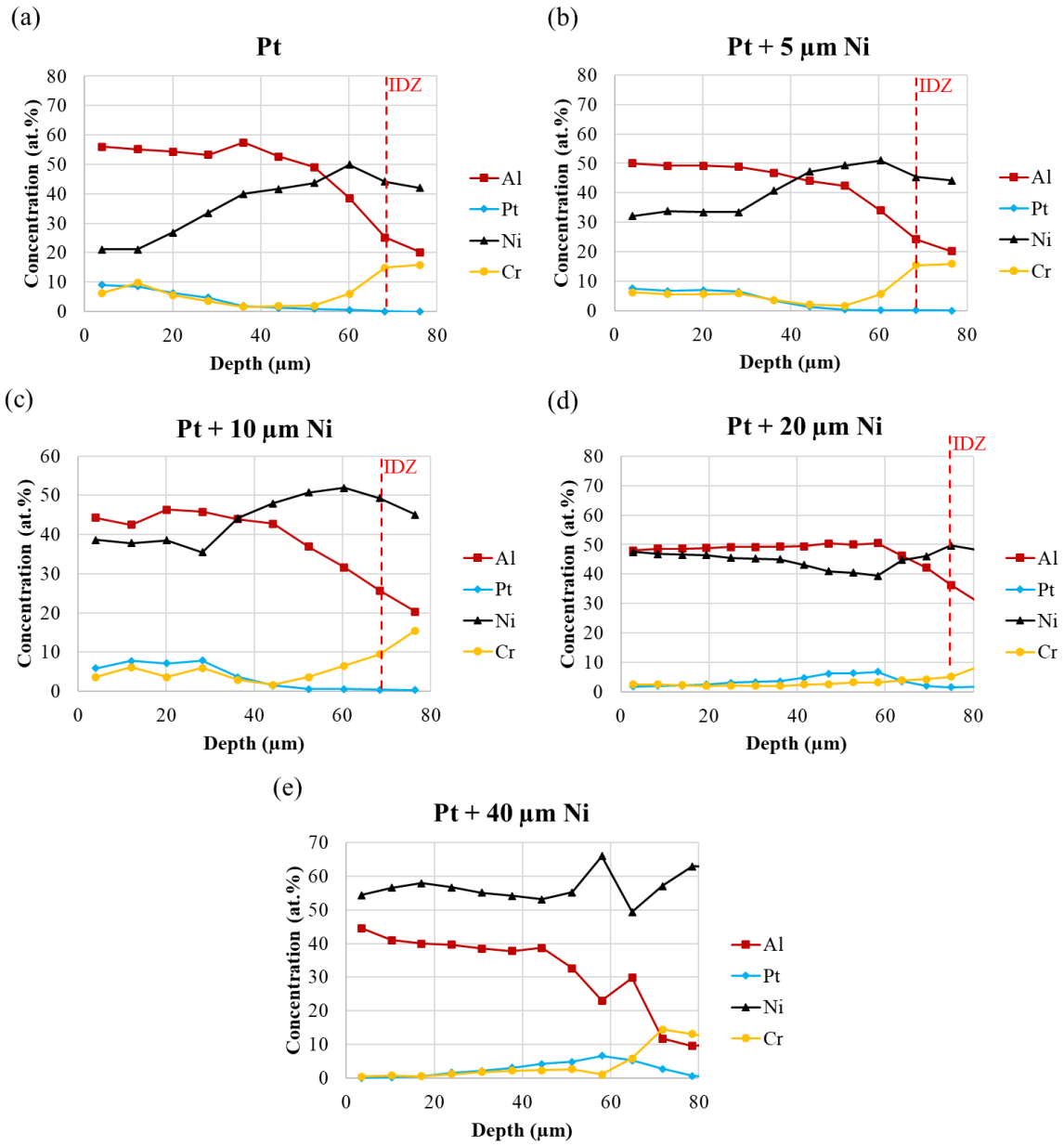

Figure 10.10: EDS concentration profiles as a function of the distance from the surface (depth) for the standard Pt-aluminide (a) and for Pt-aluminides modified with 5 µm Ni (b), 10 µm Ni (c), 20 µm Ni (d) and 40 µm Ni (e).

XRD diffractograms of all coatings are shown in Figure 10.11, and they support the microstructural and compositional observations discussed above. For the standard Pt-aluminide, as well as the 5 µm and 10 µm Ni-modified coatings, both NiAl and $PtAl_2$ diffraction peaks are clearly identified. This is consistent with the presence of a biphasic microstructure observed in cross-sectional analysis, comprising a dominant β-(Ni,Pt)Al matrix with secondary $PtAl_2$ precipitates in the outer region. However, the relative intensity of the $PtAl_2$ peaks progressively decreases with increasing thickness of the pre-deposited Ni layer. This trend indicates a reduction in the volume fraction of $PtAl_2$ in favor of the NiAl phase, as more Ni becomes available during aluminizing, promoting the formation of a more uniform β-NiAl phase and diluting Pt to levels insufficient for $PtAl_2$ precipitation.

In contrast, for the coatings modified with 20 µm and 40 µm Ni, only NiAl peaks are detected. Although a biphasic region is still visible in the cross-section of the 20 µm Ni coating, the absence of $PtAl_2$ peaks in the XRD spectra can be explained by the limited penetration depth of X-rays, which likely prevents the detection of the deeper biphasic region. Additionally, the fine dispersion and low volume fraction of $PtAl_2$ precipitates in the outermost layer may result in a signal too weak to be resolved above the background noise.

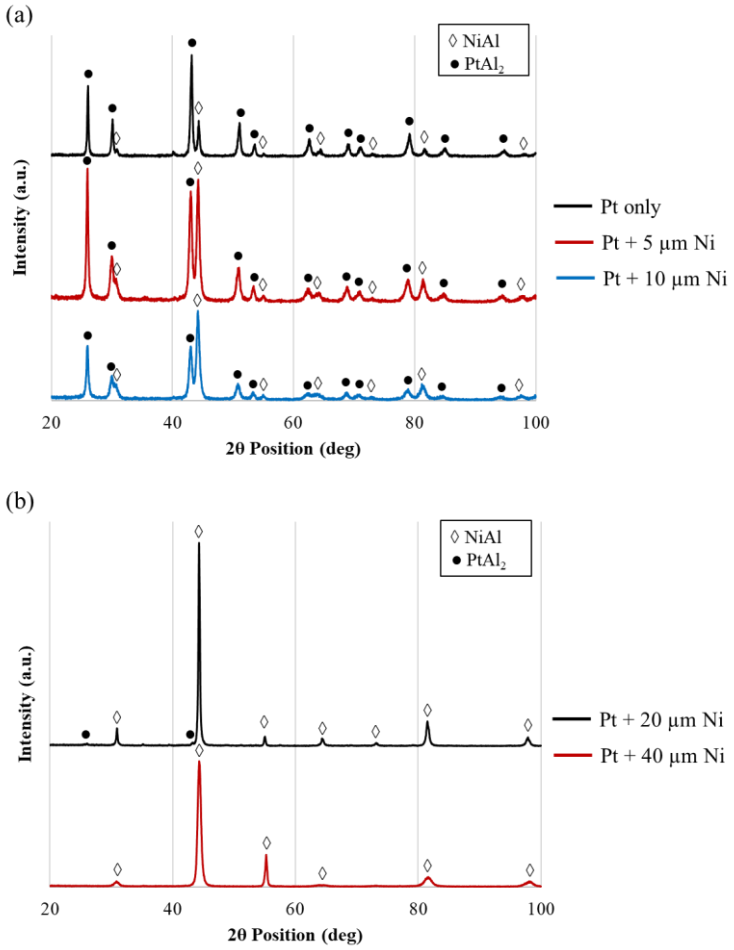

Figure 10.11: XRD diffractograms of coatings after aluminizing: (a) standard Pt-aluminide (upper, black), Pt-aluminide modified with 5 µm Ni (middle, red) and Pt-aluminide modified with 10 µm Ni (lower, blue); (b) Pt-aluminide modified with 20 µm Ni (upper, black) and Pt-aluminide modified with 40 µm Ni (lower, red).

10.3 Oxidation resistance

The isothermal oxidation resistance of Pt-aluminide coatings modified by the introduction of a pre-deposited nickel layer of varying thickness was assessed by monitoring mass gain during exposure at 1100 °C in air. The evolution of weight gain over the first 100 hours of exposure is reported in Figure 10.12. In this early stage of oxidation, coatings modified with Ni consistently exhibit higher weight gain compared to the standard Pt-aluminide, indicating a faster growth of the oxide scale.

This initial behavior can be attributed to the role of platinum in stabilizing the oxide scale. Previous studies [108,120,121] have shown that Pt plays a crucial role in facilitating the transformation of transient θ-Al_2O_3 to the more stable α-Al_2O_3. This transformation is typically accompanied by significant volume changes and the development of internal stresses, which can compromise scale adhesion. Pt reduces these stresses and promotes a faster and more uniform α-phase formation, thereby enhancing oxide scale adherence and reducing spallation. However, in Ni-modified coatings, the introduction of a Ni-rich outer layer results in reduced local Pt concentration near the coating surface, especially in the early stages of exposure. Consequently, this Pt-driven stabilization mechanism is suppressed, and initial oxide scale growth is accelerated.

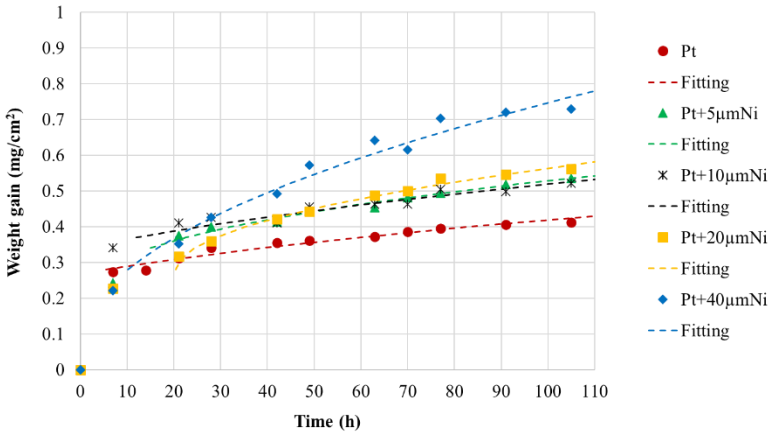

Figure 10.12: Weight gain curves of the first 100 h of oxidation at 1100°C for Pt-aluminides modified with different thickness of the pre-deposited Ni layer.

When the analysis is extended to 1000 hours of exposure (Figure 10.13), a marked change in oxidation behavior is observed. Coatings with 5 µm and 10 µm of pre-deposited Ni show significantly lower total weight gain compared to the standard Pt-aluminide, with the 10 µm Ni-modified sample exhibiting the best long-term performance. The coating with 20 µm of Ni displays a weight gain curve that is comparable to that of the unmodified Pt-aluminide, showing comparable overall weight gain after 1000 h of exposure. The worst performances are exhibited by the coating with 40 µm of Ni, with are characterized by the highest weight gain over the entire timeframe.

These trends are quantitatively supported by fitting the experimental data with Monceau's parabolic oxidation model [53], as shown in Figure 10.13 (dashed lines). The parabolic rate constants (reported in Table 10.1) provide a measure of oxidation kinetics: a lower constant indicates slower oxide scale growth, reduced Al depletion, and more stable β-phase retention during high-temperature exposure. Accordingly, the 10 µm Ni-modified coating exhibits the lowest parabolic constant, confirming its superior long-term oxidation resistance, while the 40 µm Ni-modified coating is characterized by the highest, confirming the worst protective properties likely associated with the lower availability of β-

NiAl in the coating. The high value of the correlation coefficient (R_{corr}>0.97 for all samples) confirms the good fitting.

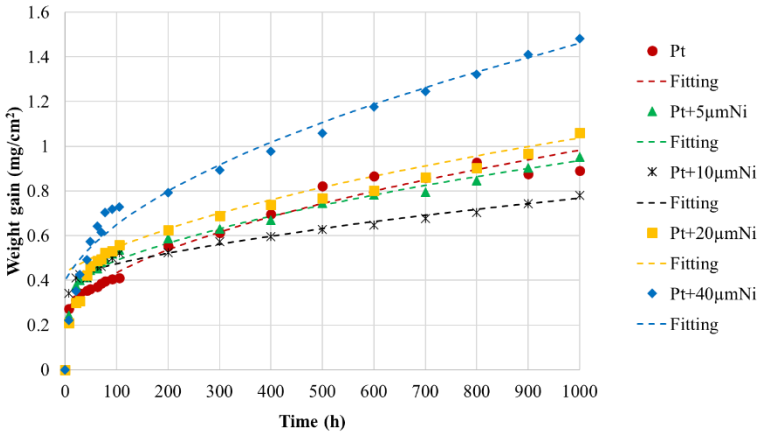

Figure 10.13: Weight gain curves up to 1000 h of oxidation at 1100°C for Pt-aluminides modified with different thickness of the pre-deposited Ni layer.

	k_p (mg²/cm⁴/h)	R_{corr}
Pt	$6.755 \cdot 10^{-4}$	0.973
Pt + 5 µm Ni	$5.058 \cdot 10^{-4}$	0.995
Pt + 10 µm Ni	$2.658 \cdot 10^{-4}$	0.989
Pt + 20 µm Ni	$6.433 \cdot 10^{-4}$	0.989
Pt + 40 µm Ni	$1.500 \cdot 10^{-3}$	0.995

Table 10.1: Parabolic constants calculated according to Monceau's model for the standard Pt-aluminide and for coatings modified with different thickness of the pre-deposited Ni layer.

Understanding the oxidation behavior of these coatings requires consideration of two interrelated factors: (i) the amount and spatial distribution of Pt within the bond coat, and (ii) the availability of Al within the β-phase matrix. When the Ni layer thickness is increased up to 10 µm, Pt becomes more uniformly distributed throughout the coating, and the formation of $PtAl_2$ is considerably reduced. This favors the incorporation of Pt into the NiAl lattice, forming a stable and protective β-(Ni,Pt)Al phase. This phase not only improves selective Al oxidation and the formation of a dense Al_2O_3 scale, but also enhances its adhesion [100,108]. Moreover, uniform Pt distribution avoids the detrimental segregation effects observed in coatings with Pt-rich precipitates, where localized depletion of Ni and Al can promote premature degradation [105].

In contrast, when the Ni layer thickness is increased to 20 µm, the outer region of the coating becomes significantly depleted in Pt, while Pt concentration is highest in the central region of the bond coat. This distribution limits the effectiveness of Pt-related oxidation resistance mechanisms in the most critical area near the surface. As a result, the initial oxide scale formation is less controlled, and long-term performance does not improve further. However, it must also be considered that the high Ni content in the outermost region promotes the formation of an Al-rich β-NiAl phase. This phase

exhibits inherently high oxidation resistance, even in the absence of Pt, due to its ability to maintain a protective Al_2O_3 layer [266,267]. Additionally, the Pt reservoir beneath acts as a diffusion barrier which can limit the inward diffusion of Al, helping retain Al in the outer coating and delaying depletion. These two opposing effects (reduced Pt-assisted oxide stability on one hand, and enhanced intrinsic Al retention on the other) likely balance out, resulting in an overall performance comparable to standard Pt-aluminide coatings. In addition, it is worth considering that the suppression of the fragile $PtAl_2$ phase in the outermost region of the coating with 20 microns Ni is expected to increase mechanical properties [255], which reduce the likelihood of oxide scale cracking and rumpling [268]. Thus, the microstructural modification associated with Ni addition may also contribute indirectly to enhanced oxidation resistance by improving the mechanical stability of the TGO.

Figure 10.14, Figure 10.15 and Figure 10.16 present the microstructural evolution of Ni-modified Pt-aluminide coatings after 100 h, 500 h, and 1000 h of isothermal exposure at 1100 °C, respectively. After 100 h of oxidation (Figure 10.14), early signs of Ni_3Al nucleation, indicated by the light grey regions in BSE contrast, are observed only in the coating modified with 5 µm of Ni (Figure 10.14 (a)). This happens despite the relatively low weight gain of same sample during this initial exposure period, suggesting that Al depletion due to oxide growth, whose scale appears dense and adherent, is not the only factor governing γ′ formation. In contrast, coatings with higher Ni layer thicknesses (10, 20, and 40 µm, in Figure 10.14 (b), (c) and (d), respectively) do not yet show significant Ni_3Al formation, with only a few isolated precipitates forming along grain boundaries. The delayed appearance of Ni_3Al in these coatings suggests that a thicker pre-deposited Ni layer results in a more robust β-NiAl reservoir, which slows Al depletion in the early stages of oxidation by providing a greater capacity for Al storage and controlled diffusion. This aligns with literature findings indicating that thicker β-phase layers can buffer Al depletion during early oxidation stages [238].

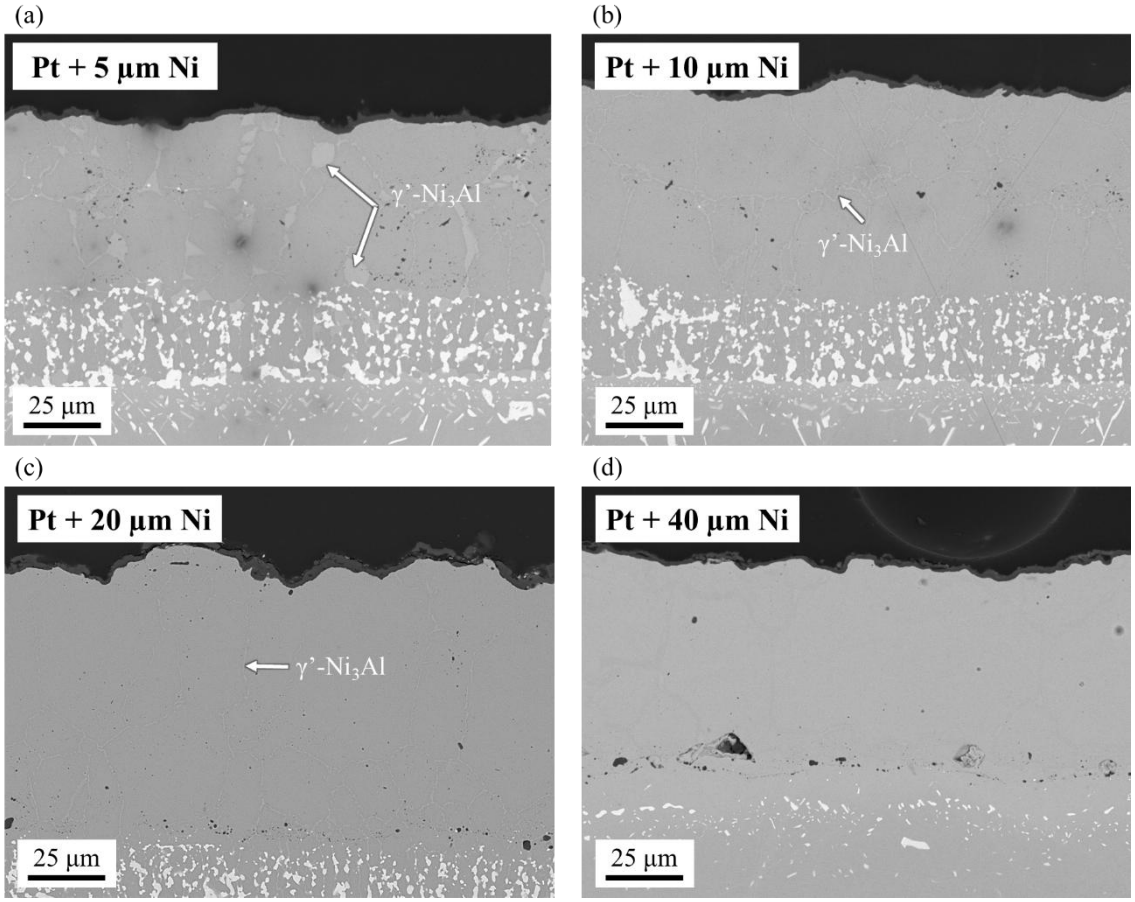

Figure 10.14: Cross-sectional micrographs after 100 hours of exposure at 1100 °C for coatings modified with: (a) 5 µm Ni, (b) 10 µm Ni, (c) 20 µm Ni and (d) 40 µm Ni.

At 500 h (Figure 10.15), the formation of Ni_3Al precipitates becomes more pronounced. Coatings modified with 10 and 20 µm of Ni (Figure 10.15 (b) and (c)) begin to exhibit larger Ni_3Al regions, especially at triple grain junctions, indicating progressive transformation of the β-phase due to continued Al depletion. Nevertheless, the oxide scale remains dense and adherent, which is critical for maintaining oxidation resistance. The delayed β-to-γ′ transformation further supports the stabilizing effect of Pt and Ni on the β-(Ni,Pt)Al phase.

In the 40 µm Ni coating (Figure 10.15 (d)), degradation mechanisms become more pronounced. The significant outward diffusion of Ni and inward diffusion of Al result in Al depletion at the interface, accompanied by the formation of Kirkendall voids and a visible diffusion front. These are classical indicators of long-range interdiffusion and element imbalances, as reported by Pint et al. [105], and they weaken the mechanical integrity of the bond coat. Similar results on void formation were reported by Vialas and Monceau [133] after long terms exposure at 1050°C of Al-defective β-(Ni,Pt)Al coatings.

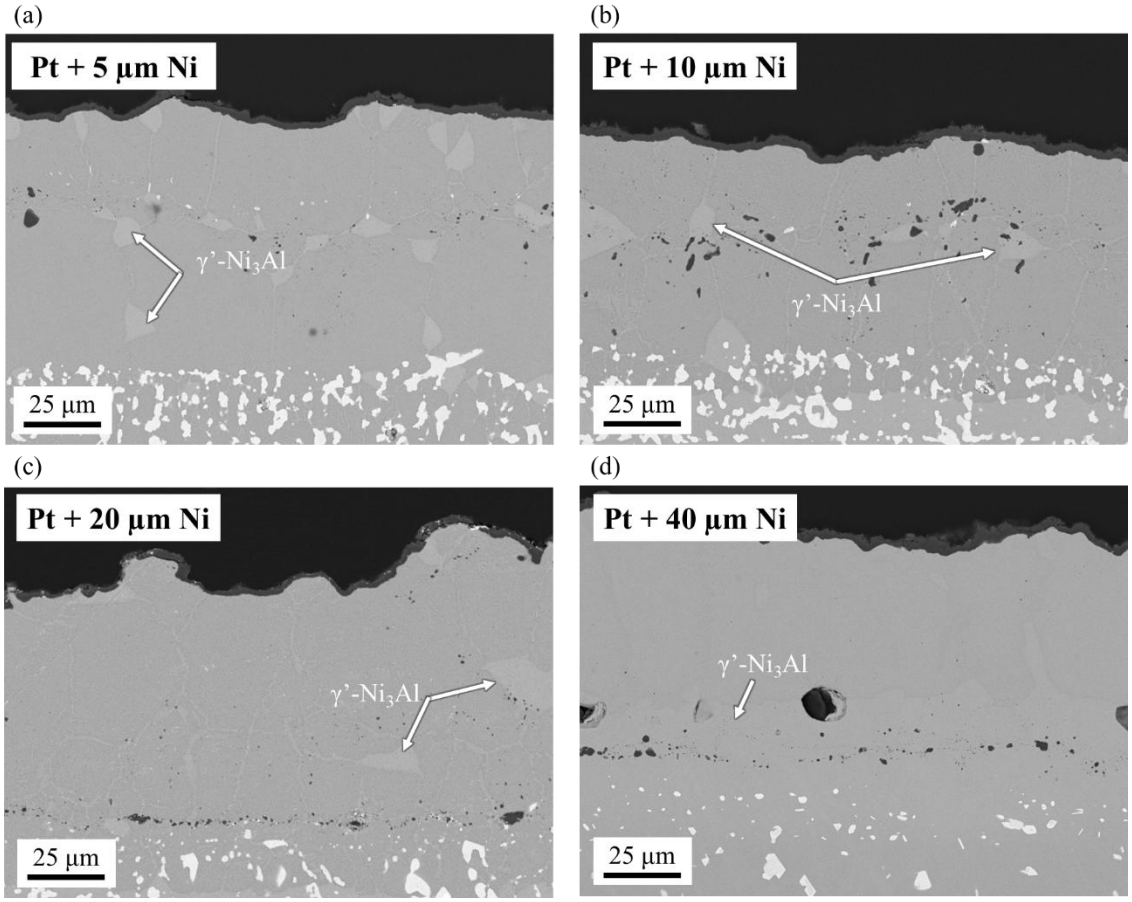

Figure 10.15:. Cross-sectional micrographs after 500 hours of exposure at 1100 °C for coatings modified with: (a) 5 µm Ni, (b) 10 µm Ni, (c) 20 µm Ni and (d) 40 µm Ni.

At 1000 h (Figure 10.16), the all coatings still retain a significant fraction of the β-phase, although the inner regions have partially transformed into the γ′-(Ni_3Al) phase. This transformation is a classic consequence of prolonged Al depletion, where the remaining matrix lacks sufficient Al to stabilize the β-(Ni,Pt)Al phase and instead favors the precipitation of γ′. The degree to which this transformation progresses varies between samples. Notably, the 10 µm Ni coating retains the thickest and most continuous β-phase region, in agreement with its superior oxidation resistance as determined from oxidation kinetics curves (Figure 10.13). The persistence of the β-phase in this coating reflects a balanced Pt and Al distribution, which optimizes both oxidation resistance and structural stability over long-term exposure.

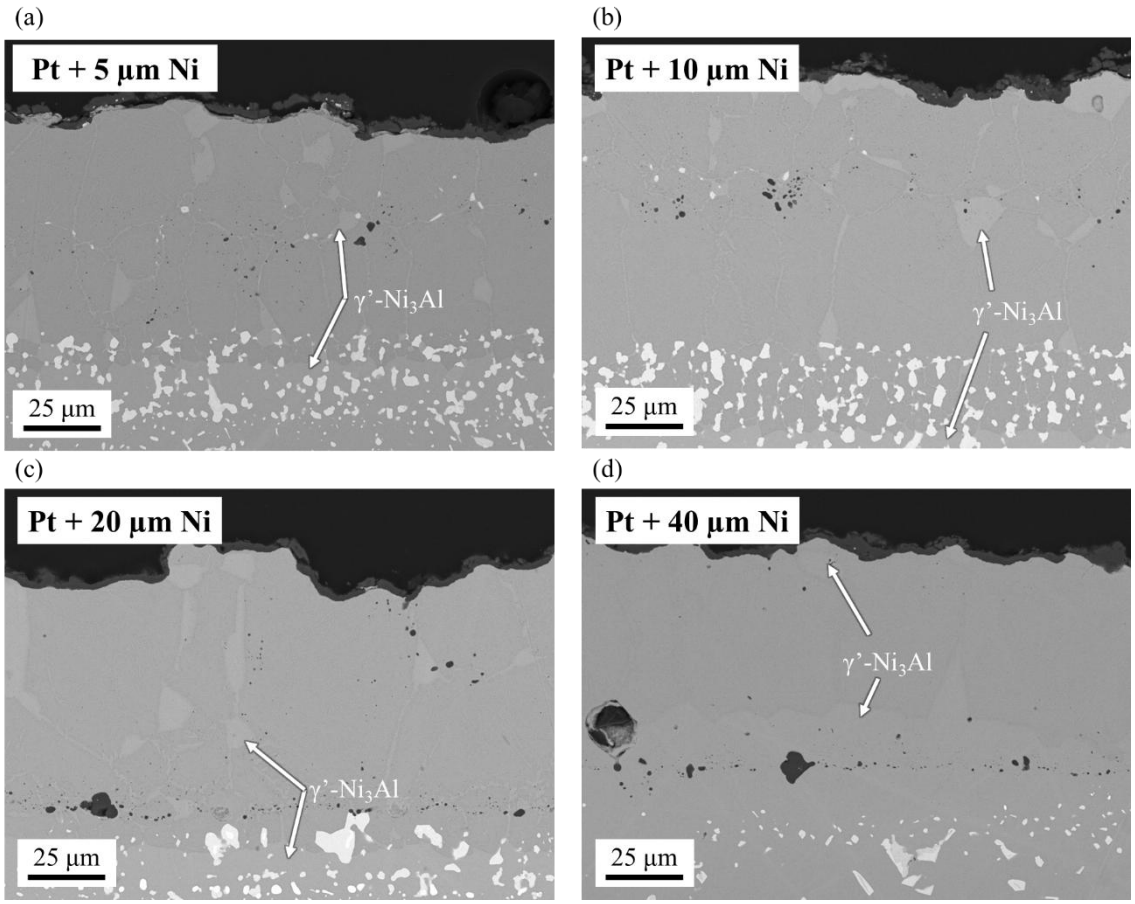

Figure 10.16: Cross-sectional micrographs after 1000 hours of exposure at 1100 °C for coatings modified with: (a) 5 µm Ni, (b) 10 µm Ni, (c) 20 µm Ni and (d) 40 µm Ni.

To fully assess oxidation behavior, Figure 10.17 documents the evolution of the alumina scale across all coatings at 100, 500, and 1000 h. Up to 500 h, a dense, continuous, and adherent α-Al_2O_3 scale is observed in all modified coatings, confirming their protective properties. By 1000 h, the oxide scale has thickened significantly due to ongoing oxidation, yet remains mostly adherent in all cases. Local spallation is observed only in the 5 µm and 10 µm Ni coatings, and even then, only in limited areas. Notably, in these coatings, the presence of bright Ta-rich precipitates within the oxide layer is observed, likely originating from substrate diffusion. The presence of such precipitates is undesirable as they may compromise the integrity of the oxide scale, acting as stress concentrators or promoting micro-crack initiation. Conversely, Ta contamination is absent in the coatings modified with 20 and 40 µm of Ni, suggesting that thicker Ni layers act more effectively as diffusion barriers, limiting the outward migration of refractory from the substrate. This enhances the chemical purity of the oxide scale and helps preserve its protective function.

In the 20 µm Ni coating, the oxide scale at 500 h appears denser and more adherent than at 100 h, indicating that a longer incubation period is needed to form a fully protective oxide layer. This delay is consistent with the reduced Pt concentration in the outer region due to initial dilution by the thick Ni layer. As described earlier, platinum plays a critical role in catalyzing the θ- to α-Al_2O_3

transformation and improving scale adherence. Thus, in the early stages of oxidation, the lower Pt availability in the 20 µm Ni coating slightly delays the development of a mature, slow-growing α-Al_2O_3 scale. However, once formed, the scale remains stable and protective due to the favorable composition of the underlying β-(Ni,Pt)Al layer and the suppression of detrimental element diffusion.

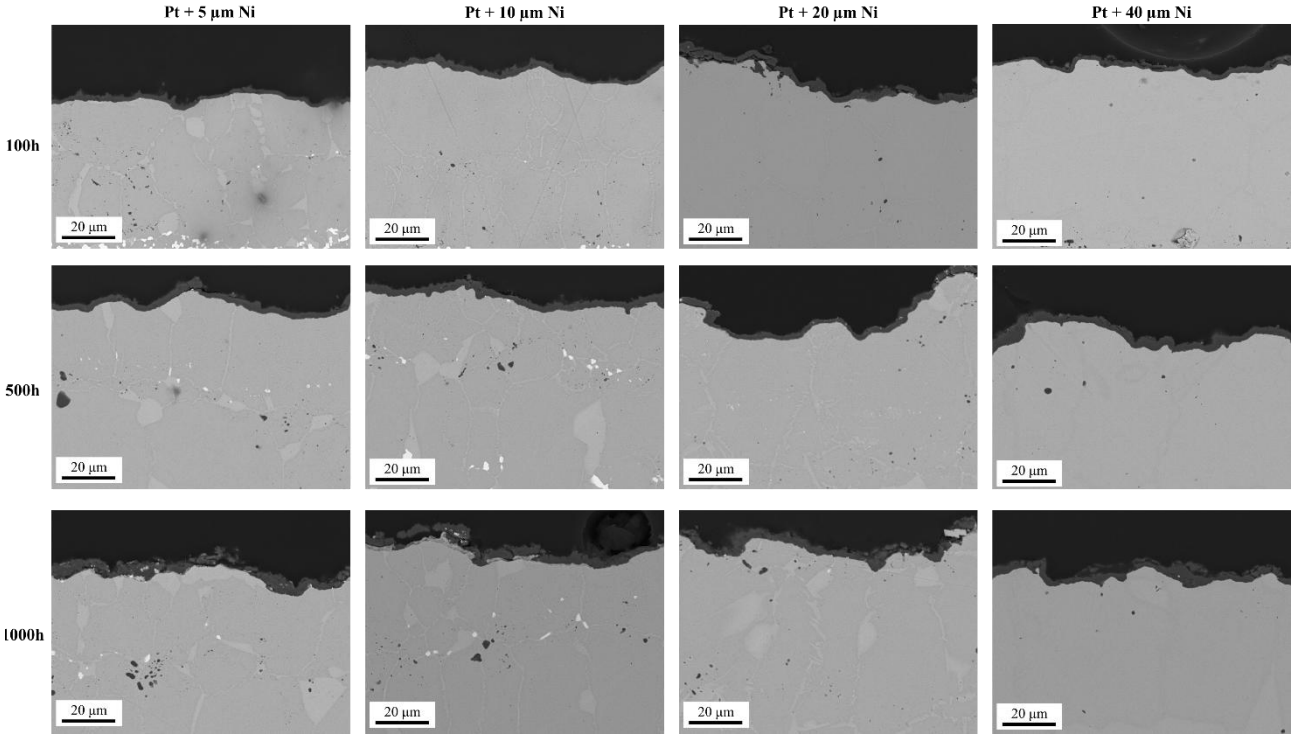

Figure 10.17: Evolution of the alumina scale across all modified coatings at 100, 500, and 1000 h of exposure at 1100°C.

XRD analysis was performed on the surface of Ni-modified Pt-aluminide coatings after 100 h, 500 h, and 1000 h of isothermal exposure at 1100 °C to investigate phase evolution and surface oxidation products, and spectra are reported in Figure 10.18. For all modified coatings, intensity of the β-NiAl peaks show a steady decrease in intensity with increasing exposure time; simultaneously, the intensity of γ′-Ni_3Al peaks increases, reflecting the transformation of β-(Ni,Pt)Al into γ′ due to aluminum depletion. This evolution is consistent with the SEM cross-sectional observations, which show gradual Al depletion and nucleation of Ni_3Al at triple junctions and grain boundaries, particularly after 500 h and 1000 h of exposure.

The relative intensity of the Ni_3Al peaks tends to decrease with increasing initial Ni layer thickness. This trend matches well with the microstructural evidence indicating that thicker Ni layers. are associated with a more stable and thicker β-phase reservoir, capable of sustaining Al supply and delaying transformation into γ′. In the 40 µm Ni coating, only very weak Ni_3Al peaks are detected, even at 1000 h, despite the SEM indicating significant γ′ formation near the substrate. This is attributed to he limited penetration depth of X-rays, which primarily probe the near-surface region.

Since Ni_3Al formation in the 40 µm coating occurs deeper in the coating, it remains largely undetected by XRD scans.

For the 5 µm Ni coating, TiO_2 peaks are already visible after 500 h of oxidation. This early appearance suggests rapid outward diffusion of Ti, likely from the underlying superalloy substrate. The thinner Ni layer and relatively faster Al depletion may accelerate diffusion of reactive elements like Ti toward the surface. In contrast, TiO_2 is only detected after 1000 h in the 10 µm and 20 µm Ni coatings, indicating that thicker Ni layers act as more effective diffusion barriers, delaying Ti migration and incorporation into the oxide scale. A weak $NiAl_2O_4$ spinel peak is identified only in the 20 µm Ni coating after 1000 h, although such oxide was not observed in SEM cross-sectional analysis. Nonetheless, the low intensity of the peak and the absence of structural degradation suggests that its formation is likely very moderate and caused by local Al depletion in the proximity of the oxide scale.

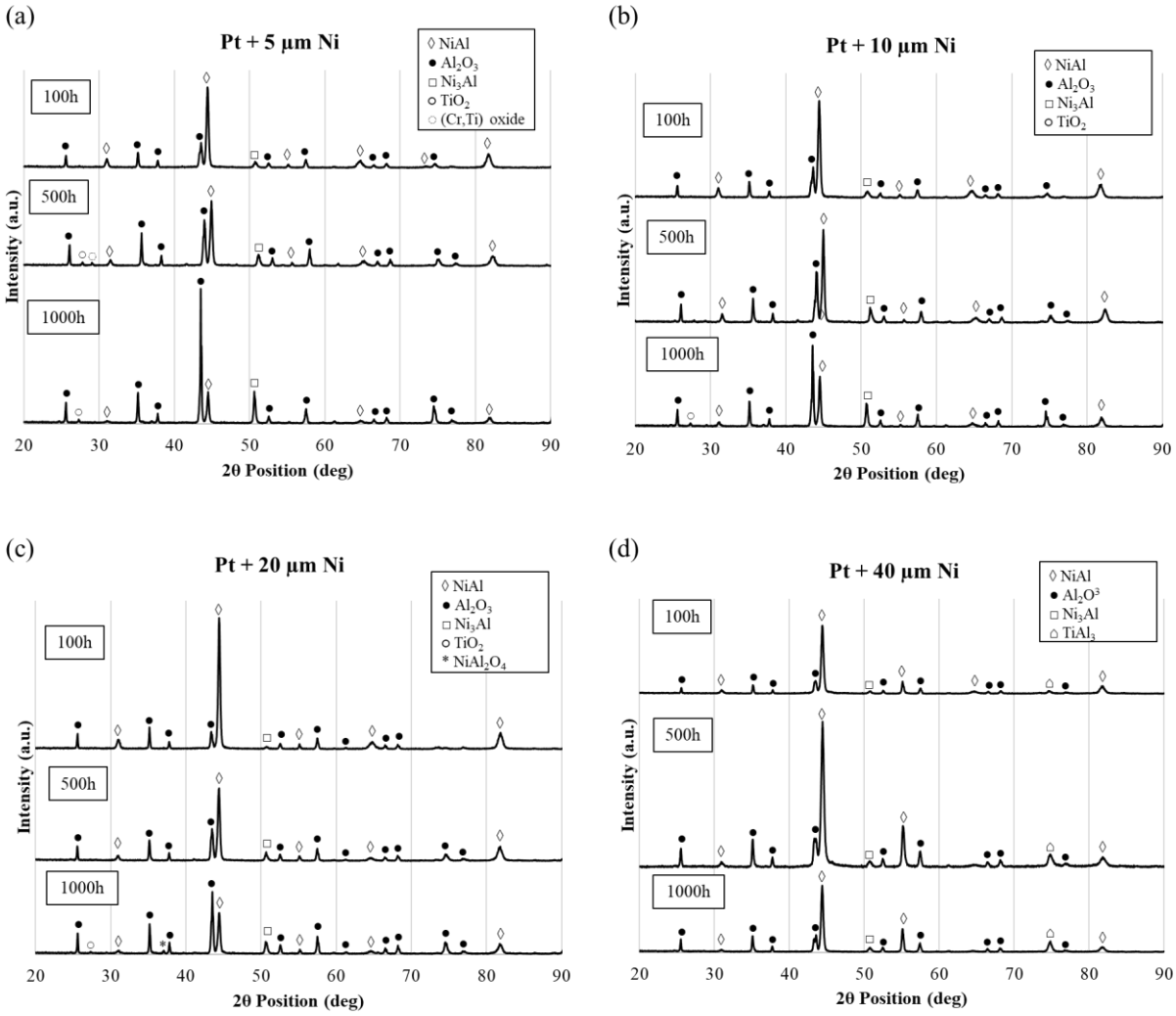

Figure 10.18: XRD spectra of coatings modified with (a) 5 µm Ni, (b) 10 µm Ni, (c) 20 µm Ni and (d) 40 µm Ni after 100, 500, and 1000 h of exposure at 1100°C.

10.4 Influence of Ni thickness od SRZ formation

The effect of the pre-deposited Ni layer on the formation of TCP phases was investigated by evaluating the SRZ thickness after 1000 h of isothermal exposure at 1100 °C, as shown in Figure 10.19 for coatings with 5 µm (a), 10 µm (b), 20 µm (c), and 40 µm (d) of pre-deposited Ni. Clearly SRZ thickness decreases as the Ni layer thickness increases, and is eliminated in the coating with a 40 µm Ni layer. This can be explained considering that introduction of a thicker Ni layer greatly retards interdiffusion processes between the coating and the underlying superalloy substrate. This was already demonstrated in the as-aluminized condition, when it was observed that IDZ becomes progressively thinner as the Ni layer thickness increases and fewer precipitates were present in the inner bond coat layer, indicating reduced outward diffusion of superalloy elements (particularly refractory elements such as Re, W, and Mo) and lower inward flux of Al during coating formation.

During long-term high-temperature exposure, Al diffuses inward, while Ni diffuses outward: this elemental redistribution destabilizes the coherent γ/γ′ microstructure of the substrate, promoting TCP phase precipitation. These phases typically nucleate when solute atoms such as Ta, W, Mo, or Cr become supersaturated due to their limited solubility in the β and γ′ phases compared to the γ matrix, leading to their segregation and eventual precipitation [102,209]

These needle-like or platelet like TCP phases observed in the SRZ are particularly detrimental, as they cause: (i) local depletion of solid-solution strengthening elements, (ii) increased brittleness, especially along grain boundaries and (iii) reduced creep strength and fatigue resistance due to microstructural degradation and crack initiation at phase interfaces.

The introduction of a pre-deposited Ni layer serves as an effective diffusion barrier, performing two key functions:

1. Retards inward Al diffusion from the coating to the substrate;
2. Suppresses Ni depletion from the substrate, thereby maintaining the γ/γ′ balance and limiting the driving force for TCP formation.

With increasing Ni layer thickness, these effects become more pronounced and amount of TCP phases as well as overall thickness of the SRZ are reduced. In the case of the 40 µm Ni layer, diffusion between the coating and substrate is so limited that no IDZ is observed even in the as-aluminized state. Consequently, during service at high temperature, no SRZ develops, and the coherent γ/γ′ microstructure of the substrate remains stable. This stability correlates with the near-complete absence of TCP precipitates in these coatings, as visually confirmed in Figure 10.19(d).

By reducing or preventing the precipitation of brittle TCP phases better creep resistance and ductility are preserved, leading enhanced overall mechanical integrity of the system.

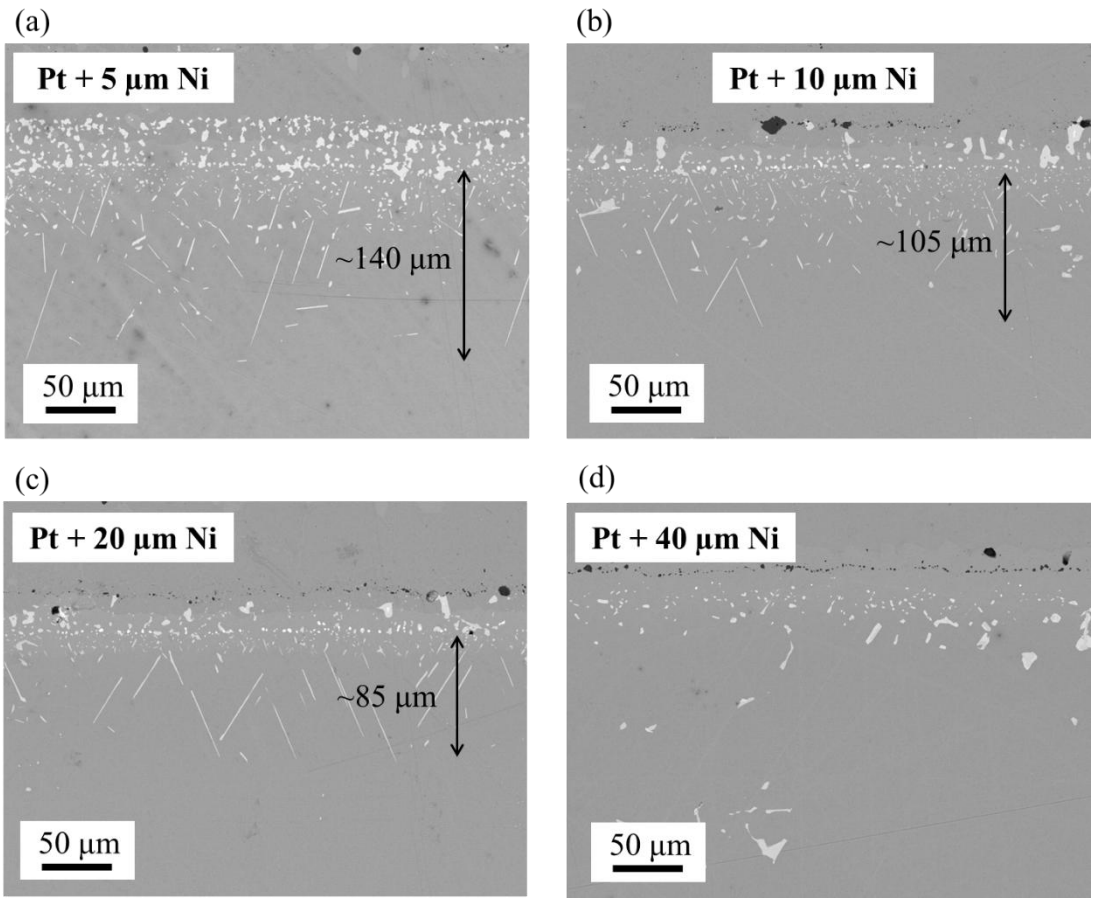

Figure 10.19: SRZ thickness after 1000 h of exposure at 1100°C for coatings modified with 5 µm (a), 10 µm (b), 20 µm (c), and 40 µm (d) of pre-deposited Ni.

10.5 Conclusions

This chapter investigated the modification of Pt-aluminide bond coat architectures by inserting an electroless-deposited Ni interlayer after Pt deposition, prior to diffusion and aluminizing. The addition of a Ni interlayer modifies the concentration gradients during diffusion and aluminizing, enabling effective control over phase formation and distribution.

As the Ni layer thickness increased from 5 µm to 40 µm, the coating evolved from a dual-phase structure (β-(Ni,Pt)Al + ζ-$PtAl_2$) to a nearly single-phase β-(Ni,Pt)Al microstructure. The progressive suppression of the brittle $PtAl_2$ phase represent a substantial improvement in the expected mechanical integrity of the bond coat.

Increasing the Ni interlayer thickness also led to a systematic reduction in IDZ thickness, reflecting its role as an external Ni reservoir during aluminizing. A Ni thickness of 10–20 µm offered the most effective balance: minimizing $PtAl_2$, reducing IDZ thickness and maintaining a favorable β-phase structure without the insurgence of porosity.

Coatings modified with a 10 µm Ni layer demonstrated the lowest weight gain and oxidation rate over 1000 h, confirming the optimal balance between Pt and Al distribution in the β-phase matrix. In contrast, 40 µm Ni coatings showed the worst performance, likely due to lower Al content in the β-

phase and reduced Pt availability at the surface. Early-stage oxidation revealed faster oxide growth in Ni-modified coatings due to delayed Pt-facilitated θ- to α-Al_2O_3 transformation, underscoring Pt's role in early oxide stabilization.

All coatings developed adherent α-Al_2O_3 scales, with thicker Ni layers acting as diffusion barriers, limiting refractory element migration and improving oxide purity. Over time, β-phase transformation to γ′-Ni_3Al occurred due to Al depletion. However, 10 and 20 µm Ni variants best retained a continuous β-phase region, correlating with superior oxidation resistance. Delayed γ′ formation in thicker Ni coatings suggests enhanced Al retention.

Eventually, it was demonstrated that thicker Ni layers significantly reduced SRZ formation after high temperature exposure, limiting the formation of TCP phases by reducing interdiffusion with the substrate.

The 10 µm Ni-modified coating achieved the best compromise between oxidation resistance and microstructural stability, maintaining high Pt activity near the surface for early-stage oxide stabilization and preserved Al availability during prolonged exposure, while minimizing harmful interdiffusion.

In conclusion, the controlled application of a Ni interlayer offers a new and robust tool for the precise engineering of Pt-aluminide bond coats, contributing to the development of thermal barrier systems with enhanced resistance, durability and efficiency.

11. Pt-aluminide nanocomposite coatings

The final stage of this work investigates the preliminary development of nanocomposite Pt-aluminide coatings incorporating Al_2O_3 nanoparticles, with the aim of enhancing oxidation resistance through microstructural refinement and oxide scale stabilization. This approach exploits the inherent advantages of electroless deposition, which, being a deposition from liquid phase, is especially well-suited for the co-deposition of solid inert particles within the metallic layer, enabling a uniform distribution of nanoparticles even on components with complex geometries.

The incorporation of Al_2O_3 nanoparticles into the electroless Pt layer prior to aluminizing is hypothesized to offer multiple benefits. Most notably, these nanoparticles are expected to function as epitaxial nucleation sites for α-Al_2O_3, promoting the early formation of the thermodynamically stable alumina phase during high-temperature oxidation. This is a significant improvement over the typical formation of metastable γ- and θ-alumina, which are associated with faster growth kinetics, inferior adherence, and phase transformation-induced damage such as microcracking and interfacial voids. The α-Al_2O_3 phase, by contrast, exhibits superior scale adherence, better protection against oxygen diffusion and greater structural integrity, thereby enhancing the coating's protective performance. Moreover, a well-dispersed ceramic phase can help to homogenize the differences in thermal expansion coefficients, thereby reducing interfacial stress during thermal cycling, and act as a mechanical barrier to the detrimental diffusion of substrate elements.

This chapter presents an initial exploration into the suspension stability, particle incorporation efficiency and microstructural characteristics of electroless-deposited Pt layers containing Al_2O_3 nanoparticles. The subsequent aluminizing step yields a Pt-aluminide nanocomposite coating in which the distribution and retention of the ceramic phase within the outer regions are critically assessed and. Preliminary oxidation tests at elevated temperatures are employed to evaluate the effect of nanoparticle reinforcement on the kinetics and phase composition of the thermally grown oxide (TGO). The results obtained serve as a proof-of-concept for the feasibility of this nanocomposite design strategy and provide the foundation for future optimization of particle selection, concentration, and coating architecture.

11.1 As deposited Pt-nanocomposite

Pt-based nanocomposite coatings were fabricated on René N4 nickel-based superalloy substrates by electroless plating, in which 10.5 mg/cm² of Pt was deposited as the base metallic matrix. The incorporation of Al_2O_3 nanoparticles was initiated 10 minutes after the onset of pure Pt deposition, with particle concentrations in the plating bath equal to 0.25 g/L, 0.5 g/L, 1.0 g/L, and 1.5 g/L. The

delay in particle introduction was intended to promote nucleation and establishment of a coherent initial metallic layer, enhancing the adhesion and stability of subsequently incorporated particles.

The surface morphology of the reference Pt coating, deposited in the absence of nanoparticles, is recalled in Figure 11.1 (a), while the corresponding nanocomposite coatings produced with increasing concentrations of Al_2O_3 are depicted in Figure 11.1 (b–e). All coatings exhibit the characteristic nodular (cauliflower-like) microstructure commonly associated with electroless plating. This morphology arises from the preferential nucleation of Pt at high-energy catalytic sites, followed by the autocatalytic reduction of metal ions that drives the growth and coalescence of initial nuclei, leading to the formation of the nodular structure [167].

In nanocomposite coatings, clusters of agglomerated Al_2O_3 nanoparticles are visible on the surface, as indicated by red arrows in the micrographs. Regardless of particle concentration, all Al_2O_3-reinforced coatings display a finer nodule size and more refined morphology compared to the standard Pt coating. This can be explained considering two primary mechanisms associated with the presence of nanoparticles: (i) the physical presence of Al_2O_3 within the growing matrix can limit the lateral growth of individual nodules, thereby promoting the formation of nodule with smaller sizes [269,270]; (ii) Al_2O_3 nanoparticles, due to their high surface energy, can act as additional catalytic sites for deposition, increasing the density of nucleation events and yielding a greater number of nodules of smaller dimensions [271,272]. These observations align with numerous reports in the literature where the incorporation of both conductive and inert nanoparticles in electroless coatings results in altered surface topography and morphology [273,274].

Particle incorporation also appears to reduce the extent and severity of on accretion stresses and surface cracking. Indeed, all nanocomposites show a noticeable reduction in surface crack density compared to the standard Pt coating. This behavior may be attributed to the adsorption–desorption dynamics of nanoparticles at the substrate/solution interface, which likely promote the removal of gas bubbles (e.g., H_2, N_2) generated during the oxidation of hydrazine, that would otherwise remain trapped within the growing metallic layer, inducing local stress and microcracking.

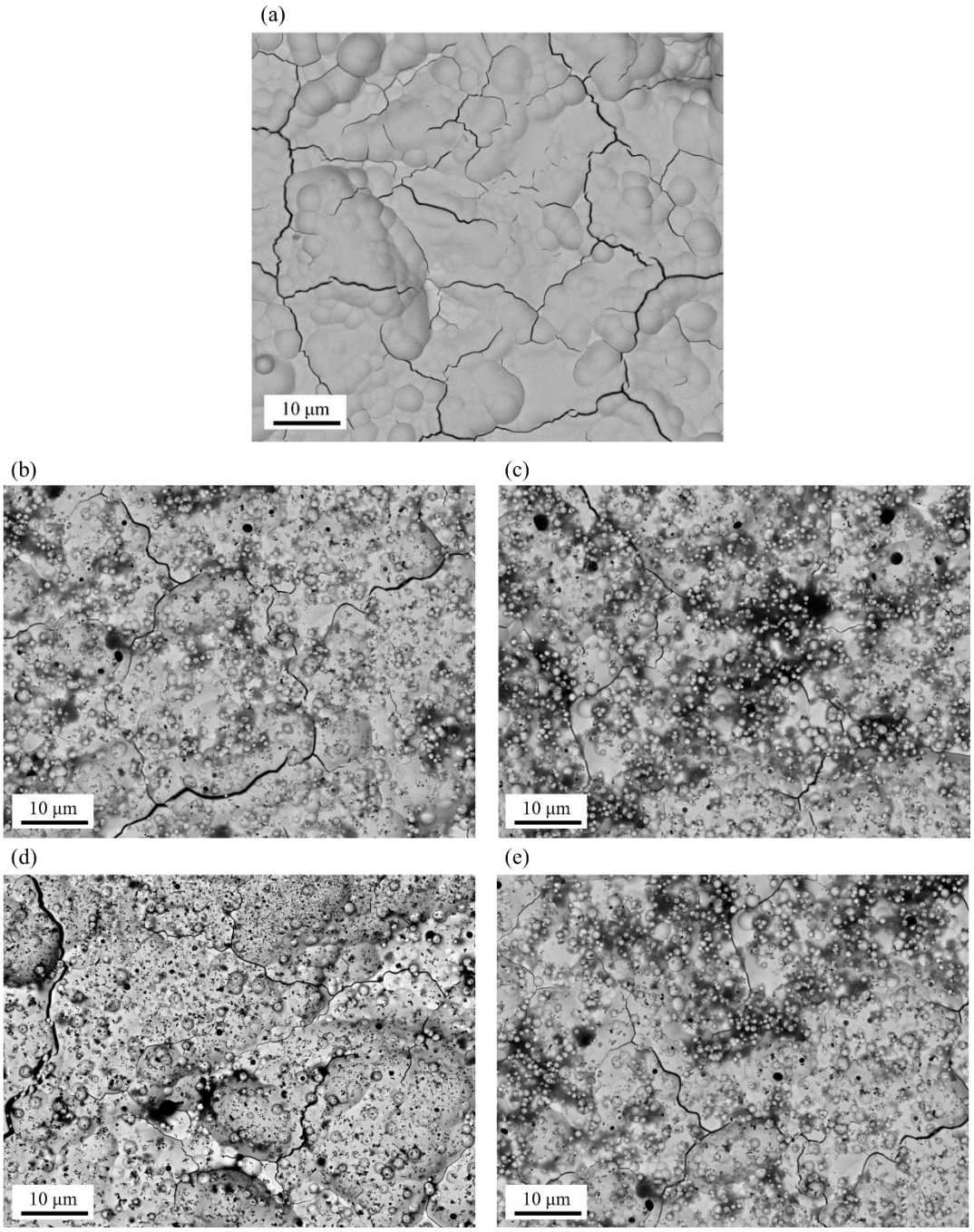

Figure 11.1: Surface morphology of the standard Pt coating (a) and of nanocomposite coatings manufactured with 0.25 g/L (b), 0.50 g/L (c), 1.0 g/L (d) and 1.5 g/L (e) of Al_2O_3.

To provide a more detailed view of nanoparticle incorporation, high-magnification SEM micrographs of the surface of the coating produced with 1.0 g/L of Al_2O_3 are shown in Figure 11.2 (SE image in (a) and BSE image in (b)). The corresponding EDS analysis confirms the successful incorporation of Al_2O_3 into the Pt matrix, with only Pt, Al, and O peaks detected. A minor C peak is also present, which is attributed to some unavoidable organic contamination due to sample handling and preparation.

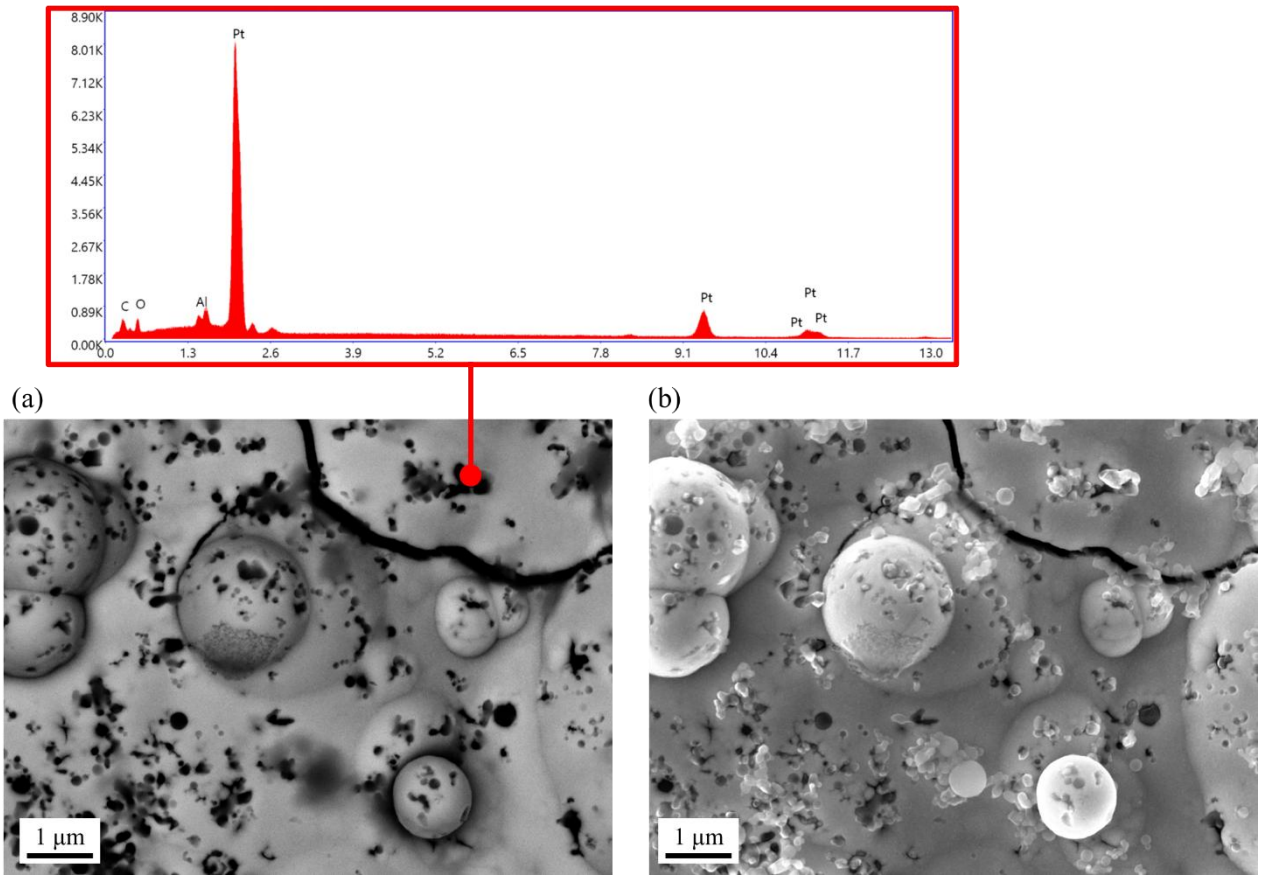

Figure 11.2: High-magnification SEM micrographs of the surface of the coating produced with 1.0 g/L of Al_2O_3 (SE image in (a) and BSE image in (b)) and corresponding EDS spectrum.

XRD spectrum of the nanocomposite coating is presented in Figure 11.3. The diffractogram exhibits intense peaks corresponding to Pt, along with low-intensity diffraction peaks belonging to Al_2O_3, which provides further evidence of the successful embedding of ceramic nanoparticles. The low peak intensity of Al_2O_3 reflects both the small particle size and their relatively low area fraction within the coating matrix.

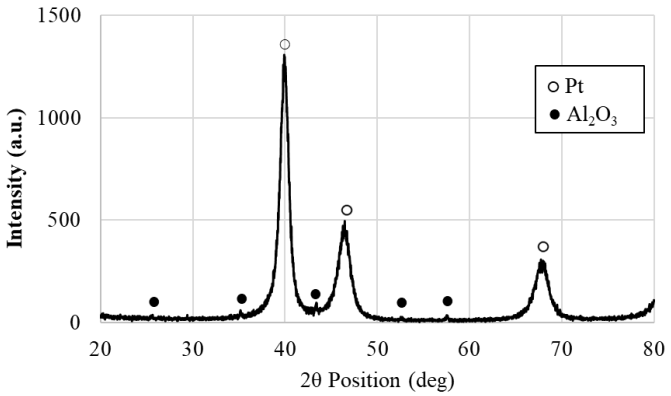

Figure 11.3: XRD spectrum of the Pt-nanoAl_2O_3 nanocomposite coating.

Cross-sectional BSE-SEM micrographs of coatings reinforced with varying Al_2O_3 concentrations are shown in Figure 11.4. A clear dependence of the degree of particle incorporation on the Al_2O_3 concentration in the plating bath is observed. Specifically, coatings fabricated with 0.25 g/L exhibit

the lowest nanoparticle density. The highest degree incorporation is found at 0.5 g/L, whereas a modest reduction in incorporated particle density is observed for 1.0 g/L and 1.5 g/L concentrations, suggesting a non-linear relationship between bath concentration and actual incorporation.

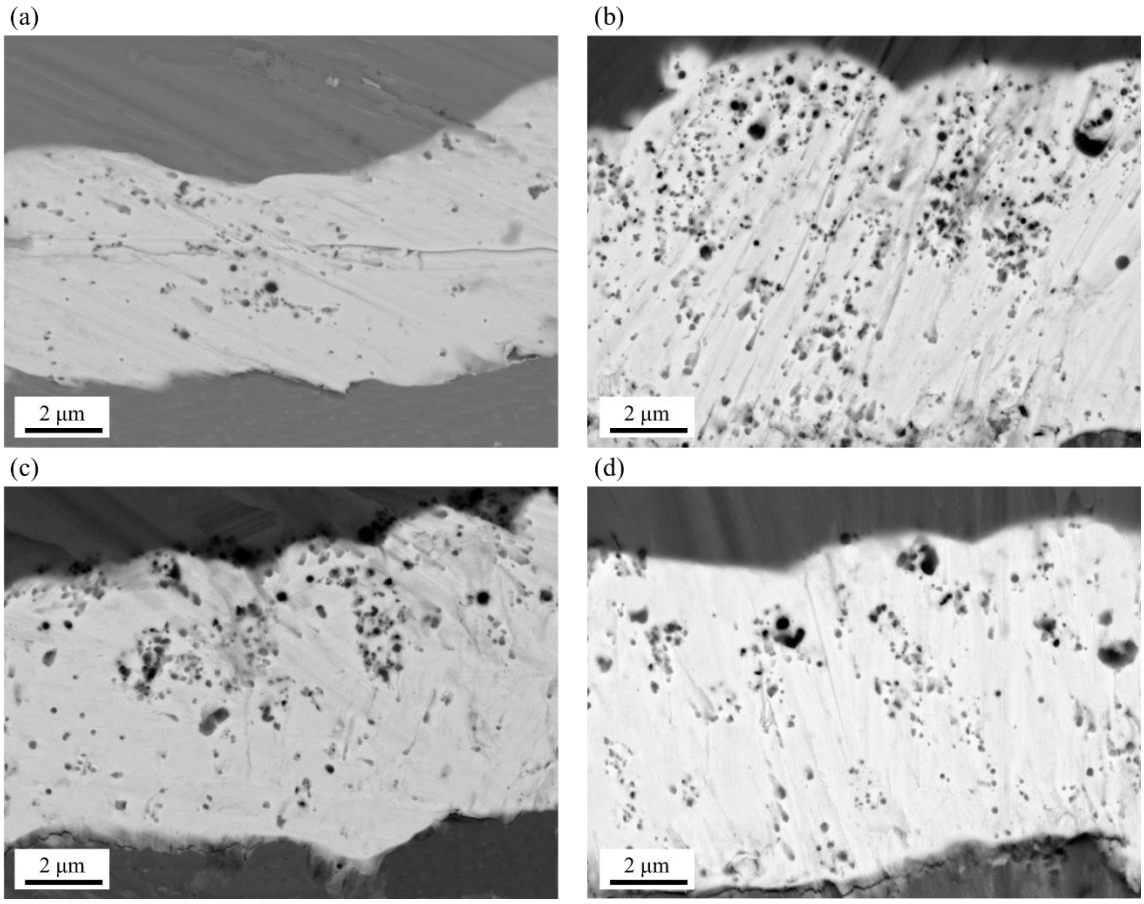

Figure 11.4: Cross-sectional BSE-SEM micrographs of coatings reinforced with 0.25 g/L (a), 0.50 g/L (b), 1.0 g/L (c) and 1.5 g/L (d) of Al_2O_3.

Quantitative analysis of nanoparticle incorporation is presented in Figure 11.5: Figure 11.5 (a) reports the area fraction (A%) of Al_2O_3 nanoparticles within the coating as a function of their concentration in the bath, while Figure 11.5 (b) shows the average number of particles per agglomerate (Na), serving as a metric for in-coating agglomeration. It can be observed that A% increases with increasing particle concentration up to 0.5 g/L. These results are consistent with many literature data [275–279], and can be explained by the classical impingement and settling mechanism of particle incorporation [212,280]. In this model, particles initially undergo reversible physical adsorption on the growing surface, and given sufficient residence time, they are eventually permanently embedded in the growing matrix. Higher nanoparticle concentrations increase the local population density near the deposition interface, enhancing the probability of entrapment.

However, a dramatic decrease in the yield of incorporation is registered when concentration is raised to 1 g/l and 1.5 g/l. This phenomenon is attributed to particle agglomeration in the plating bath, which becomes more prevalent at higher concentrations. Indeed, nanoparticles are surrounded by an ionic

double layer and, due to their high surface energy, are thermodynamically driven to minimize interfacial free energy through clustering [281]. Although mechanical stirring reduces this tendency, it cannot fully prevent agglomeration. These larger clusters are less likely to be stably embedded into the growing metallic matrix due to their size and reduced adhesion, leading to both lower incorporation yield and higher agglomeration in the coating [282–284]. The increase in Na with increasing nanoparticles concentration in the plating solution, shown in Figure 10.5(b), further confirms this interpretation, highlighting that particle–particle interactions dominate the deposition behavior at higher loadings.

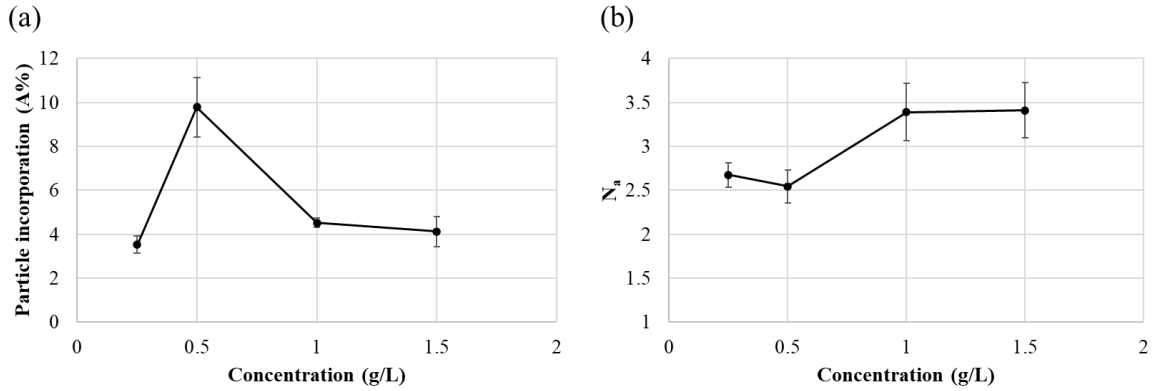

Figure 11.5: Quantitative analysis of nanoparticle incorporation: (a) area fraction (A%) of Al_2O_3 nanoparticles within the coating and (b) average number of particles per agglomerate (Na).

From Figure 11.4 it can also be observed that a modest increase in coating thickness is observed for nanocomposite coatings fabricated with Al_2O_3 concentrations exceeding 0.5 g/L. The increase in thickness can be attributed to the catalytic role played by Al_2O_3 nanoparticles during the electroless deposition process. Due to their nanometric size and high surface-to-volume ratio, these particles provide additional active sites for metal ion reduction, effectively increasing the total available surface area for deposition. Al_2O_3 nanoparticles readily adsorb onto the substrate or onto the growing metallic film, acting as heterogeneous nucleation centers. Their presence lowers the activation energy required for Pt nucleation, thereby accelerating the local deposition kinetics. As a result, for a fixed deposition time, higher coating thicknesses are attained in the presence of nanoparticles, in agreement with previous findings on nanoparticle-enhanced electroless processes [275,285].

Interestingly, no further increase in coating thickness is observed when the particle concentration is raised to 1.0 g/L and 1.5 g/L, indicating the onset of a steady-state regime. This suggests that, beyond a certain threshold, the rate at which nanoparticles approach and interact with the substrate becomes balanced by the rate at which they are co-deposited or desorbed, thus limiting any further increase in catalytic surface area [286,287].

To further confirm the catalytic role of Al_2O_3 nanoparticles, a post-deposition analysis was conducted. At the end of plating experiments performed with 0.5 g/L of Al_2O_3, the plating bath was filtered to

recover residual nanoparticles that were not embedded in the coating. The recovered particles were subsequently examined via SEM and EDS, as shown in Figure 11.6. The EDS spectrum reveals the presence of Pt on the surface of the isolated nanoparticles, indicating that Pt was nucleated and partially deposited on suspended Al_2O_3 particles within the bath. This observation confirms their catalytic functionality, even in the absence of direct substrate interaction, and supports the conclusion that Al_2O_3 particles not only act as passive fillers but actively promote Pt reduction reactions, thereby enhancing the overall deposition kinetics and influencing the final microstructure of the coating.

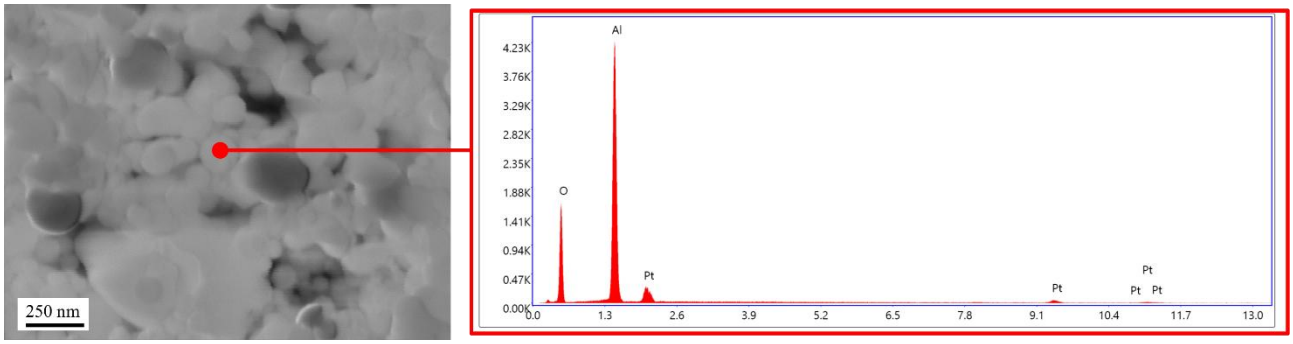

Figure 11.6: SEM-BSE micrograph and EDS analysis of WC nanoparticles after deposition.

11.2 As diffused and as aluminized Pt nanocomposite

Based on the superior yield of incorporation and reduced agglomeration observed in coatings fabricated with 0.5 g/L of Al_2O_3, this concentration was selected for the manufacturing of the Pt nanocomposite layer used to modify the Pt-aluminide system. The selected nanocomposite coatings were subsequently subjected to the diffusion heat treatment at 1100°C for 1h, followed by the slurry aluminizing process.

The top-view SEM micrograph of the nanocomposite coating after the diffusion treatment is presented in Figure 11.7. The surface appears uniform, dense, and free of cracks, with Al_2O_3 nanoparticles visibly and homogeneously distributed across the entire surface. The presence of nanoparticles on the surface suggests that they remain concentrated in the outermost region of the coating, a critical requirement to ensure that, during high-temperature oxidation, they may serve as epitaxial nucleation sites for the growth of the thermodynamically stable α-Al_2O_3 oxide scale.

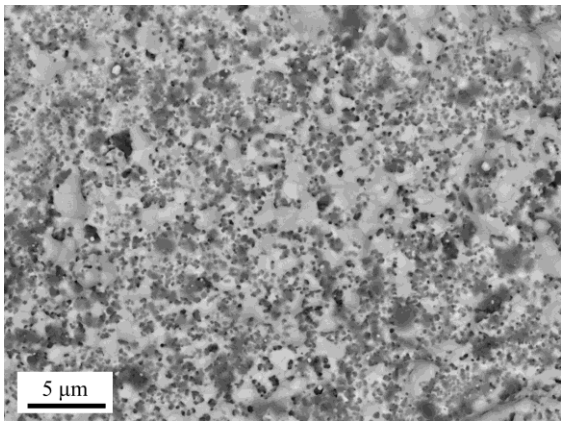

Figure 11.7: Surface morphology of the Pt-nanocomposite coating after the diffusion treatment.

Cross-sectional micrographs of standard and nanocomposite coatings after diffusion are provided in Figure 11.8 (a) and (b), respectively. Both systems exhibit a comparable microstructure, characterized by the conventional dual-layer γ/γ′ configuration. The outer layer is predominantly composed of a Pt-enriched γ phase, while the interdiffusion zone contains a mixture of γ and γ′ phases. The primary diffusion front appears irregular in both cases, and no significant enrichment in refractory elements is detected, despite their high mobility at temperatures above 1000 °C [236].

The Al_2O_3 nanoparticles exhibit limited mobility during the diffusion process, remaining concentrated in the outer region of the coating. Voids are observed at the interface between the interdiffusion zone and the substrate, which also coincides with the Pt diffusion front and the Al-depletion zone. Presence of voids can be explained by the Kirkendall effect, where differential diffusivity between species (in this case, the faster diffusion of Ni relative to Pt), leads to the accumulation of excess vacancies and the formation of voids. This effect on similar systems was first observed by Purvis and Warnes [288], who highlighted the formation of Kirkendall porosity in Pt-plated Ni systems subjected to high-temperature exposure. Void formation in γ/γ′ coatings has been extensively documented in the literature [289–293]. While some studies suggest that electroplating parameters may influence void formation [293], the present work employed electroless Pt deposition, thereby excluding a relation between void formation and Pt deposition method. Instead, the observed voids are most likely caused by the net vacancy flux arising from unbalanced interdiffusion during the heat treatment. Furthermore, it is plausible that the nanometric size of grains in the electroless deposited Pt layer can enhance atomic diffusivity and void formation kinetics.

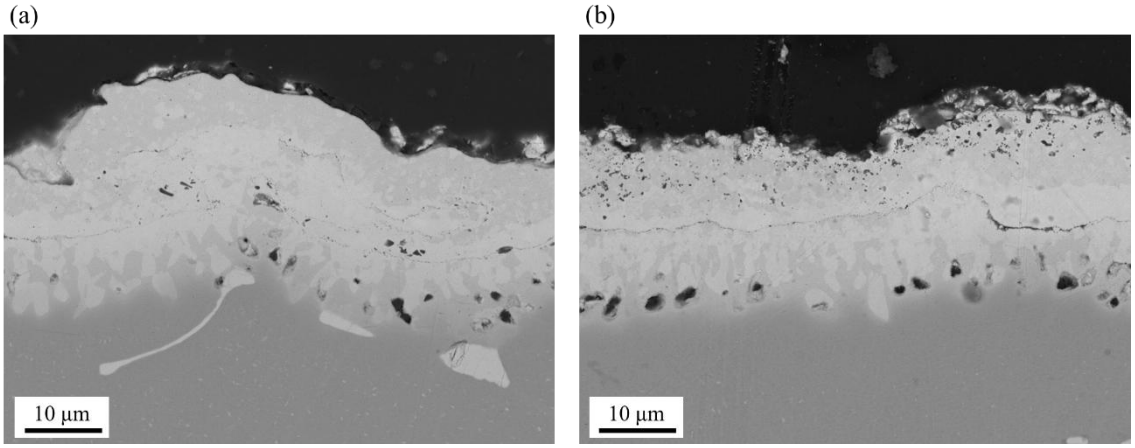

Figure 11.8: Cross-sectional micrographs of standard (a) and nanocomposite (b) coatings after diffusion.

EDS concentration curves of the standard and nanocomposite coatings after diffusion are shown in Figure 11.9. Concentration profiles of Ni, Al and Pt are comparable in both coatings and no obvious differences can be observed; nonetheless, the nanocomposite coating displays a slightly higher Al content in the outermost region, attributable to the presence of Al_2O_3 nanoparticles. Conversely, a slightly higher Pt concentration near the IDZ is observed in the standard coating, possibly suggesting that nanoparticles might act as a diffusion barrier to the inward diffusion of Pt.

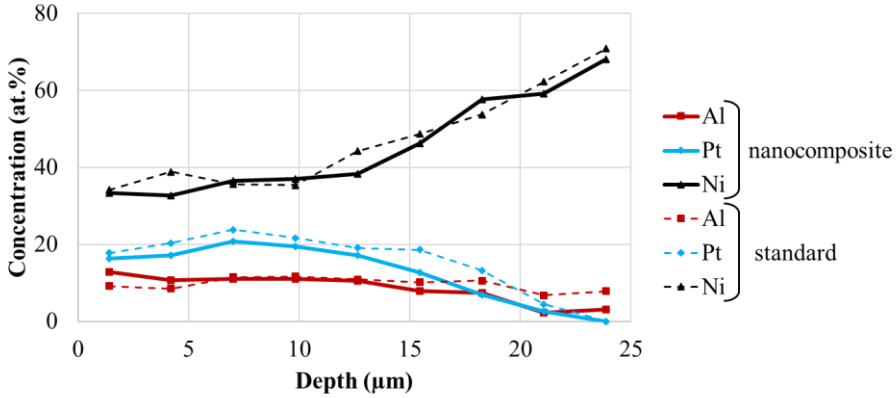

Figure 11.9: EDS concentration curves of the standard and nanocomposite coatings after diffusion.

The XRD analysis of the nanocomposite coating after diffusion is presented in Figure 11.10. The spectrum exclusively exhibits peaks corresponding to γ′-Ni_3Al, with a pronounced shift toward lower diffraction angles, indicative of lattice expansion due to the substitutional incorporation of Pt atoms into the Ni_3Al lattice [254]. No additional phases are detected, and no significant differences are observed between the spectra of nanocomposite and standard coatings (refer to Section 10.1), confirming that the presence of Al_2O_3 nanoparticles does not alter the phase constitution or crystallographic structure of the metallic matrix after diffusion.

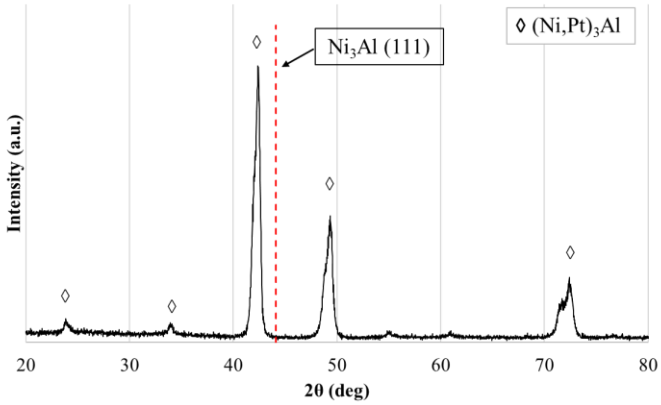

Figure 11.10: XRD spectra of the Pt-nanocomposite coating after diffusion.

Cross-sectional SEM micrographs of standard and nanocomposite Pt-aluminide coatings after the slurry aluminizing process are shown in Figure 11.11. Both coatings exhibit a similar microstructure, composed of an outer dual-phase region consisting of ζ-$PtAl_2$ and β-(Ni,Pt)Al, and an inner single-phase β-(Ni,Pt)Al zone. The microstructure is typical of inward-grown aluminides, characterized by the presence of Cr-, W-, and Ta-rich precipitates, which originate from diffusion of refractory elements from the superalloy substrate, within the single β-phase region. Both standard and nanocomposite coatings are uniform, dense, and free of porosity throughout the entire cross section. The total bond coat thickness is approximately 120 µm, consisting of a ~35 µm outer dual-phase region and a ~20 µm IDZ.

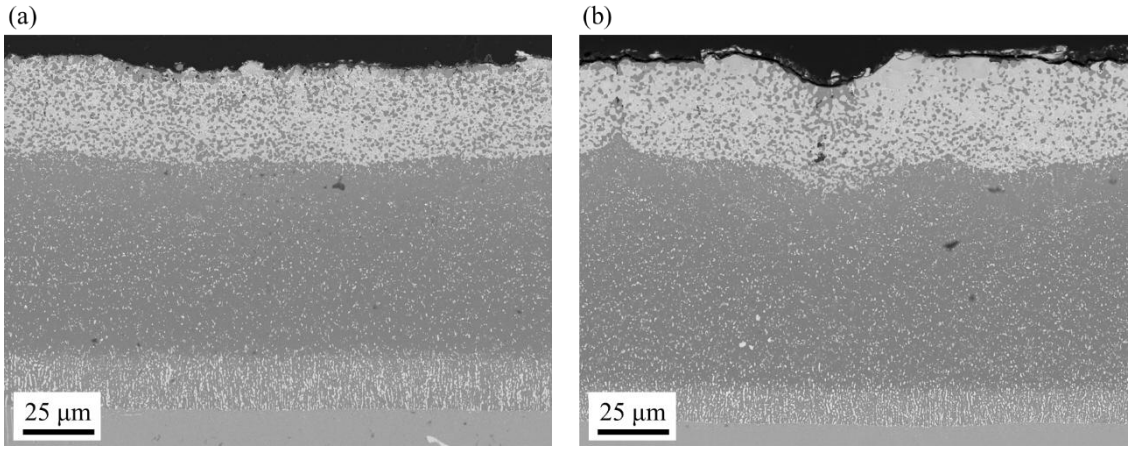

Figure 11.11: Cross-sectional SEM micrographs of nanocomposite (a) and standard (b) Pt-aluminide coatings after the slurry aluminizing process.

Higher magnification SEM micrographs of the outer region of the nanocomposite coating are presented in Figure 11.12. The black spots indicated by red arrows in Figure 11.12 (b) correspond to Al_2O_3 nanoparticles, which originate from the nanoparticles co-deposited in the initial Pt layer. These particles are well-dispersed and uniformly distributed, remaining localized in the outermost region of the coating. This distribution confirms the inward growth direction of the aluminide layer during the slurry process, since nanoparticles act as inert markers. Their positioning near the surface is critical,

as they are expected to act as epitaxial nucleation sites for the growth of the thermodynamically stable α-Al_2O_3 scale during high-temperature oxidation.

It is worth noticing that nanoparticles are predominantly located at grain boundaries, and the grain size of the Pt-aluminide nanocomposite, particularly in the ζ-$PtAl_2$ phase, appears to be slightly reduced compared to the standard aluminide, as detailed in Table 11.1. This grain size refinement can be attributed to the Zener pinning mechanism, by which dispersed nanoparticles inhibit grain boundary motion, thereby refining the grain structure [294]. This is significant because, during high-temperature oxidation, elemental diffusion along grain boundaries is much faster than through the lattice. Therefore, fine-grained structures can enhance the effective diffusivity of species. According to Wagner's theory, the minimum Al concentration required for the formation of an external protective α-Al_2O_3 scale decreases as Al diffusivity increases, which, in turn, improves as grain size is reduced [295]. As such, the refined grain structure of the nanocomposite Pt-aluminide is expected to have a beneficial impact on oxidation resistance. Similar results about grain refinement in aluminide coatings after Al2O3 co-deposition were reported in [147].

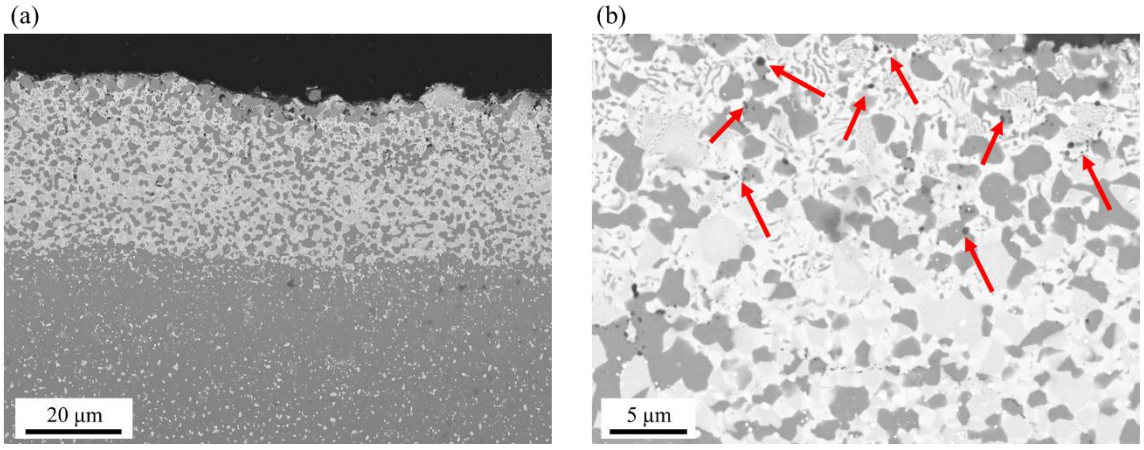

Figure 11.12: High magnification SEM micrographs of the outer region of the nanocomposite coating (a) and detail of the dual-phase region showing nano-Al_2O_3 located at grain boundaries (pointed by red arrows) (b).

	ζ-$PtAl_2$ grain size (µm)	**β-(Ni,Pt)Al grain size (µm)**
Pt-aluminide	2.57 ± 0.25	1.34 ± 0.13
Nanocomposite Pt-aluminide	1.21 ± 0.12	1.11 ± 0.11

Table 11.1: Grain size of ζ-$PtAl_2$ and β-(Ni,Pt)Al phases in the outer region of standard and nanocomposite Pt-aluminides.

EDS compositional curves reported in Figure 11.1 demonstrate nearly identical elemental composition of standard and nanocomposite Pt aluminides, which show relative amounts of Ni and Al that correspond to beta phase throughout coating thickness.

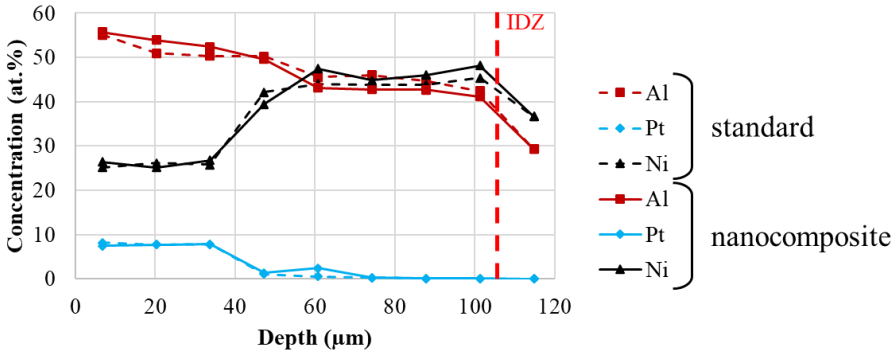

Figure 11.13: EDS compositional curves of Al, Ni and Pt as a function of the distance from the external surface for standard and nanocomposite Pt-aluminides.

Similarly, the XRD spectra of both standard and nanocomposite coatings appear nearly identical. For this reason, only the spectrum of the nanocomposite coating is shown in Figure 11.14 (a) as a representative example. The diffraction pattern confirms the presence of $PtAl_2$ and NiAl phases only, with the addition of a minor Al_5Cr peak, which is attributed to residual slurry material. As already noted in previous chapters, the β-NiAl phase occurs in the form of (Ni,Pt)Al, as evidenced by systematic left-shifts in the diffraction peaks compared to stoichiometric β-NiAl. These shifts reflect lattice distortion resulting from the substitutional incorporation of Pt atoms at Ni lattice sites. Similarly, the $PtAl_2$ peaks also deviate from their nominal positions, which can be explained by the presence of Ni and Cr in solid solution within the $PtAl_2$ structure (Figure 11.14 (b)).

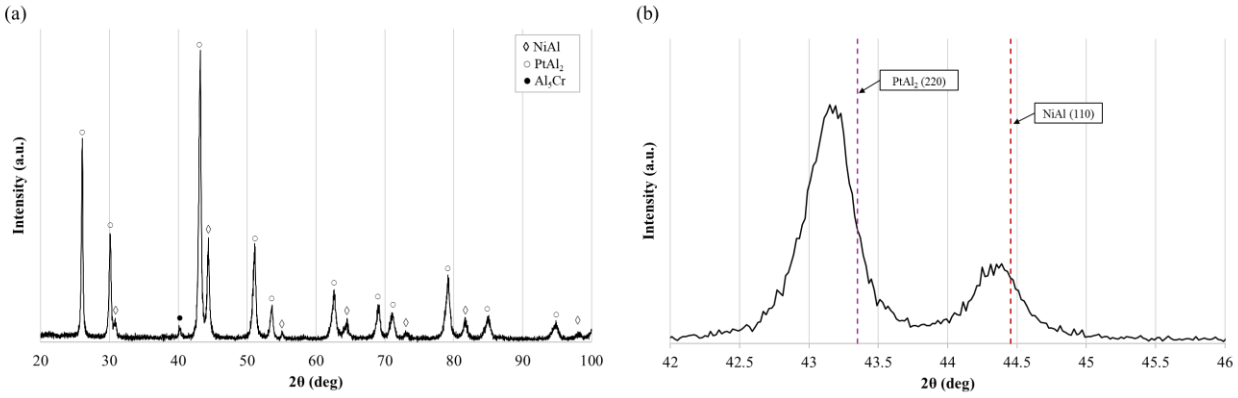

Figure 11.14: XRD spectrum of the nanocomposite Pt-aluminide (a) and detail of the diffractograms highlighting NiAl and $PtAl_2$ peak shifting.

11.3 Oxidation resistance

Preliminary accelerated oxidation tests were carried out at 1100 °C for 500 h. The corresponding weight gain curves are shown in Figure 11.15, where both the standard and nanocomposite coatings exhibit similar overall oxidation kinetics. During the transient stage (first ~30 h), the nanocomposite shows a lower weight gain, after which its oxidation rate converges with that of the standard coating. This behavior suggests a faster transformation from the metastable θ-Al_2O_3 to the stable α-Al_2O_3

phase in the nanocomposite coating. To quantitatively compare oxidation behavior, the experimental data were fitted using the Monceau parabolic model (dashed lines in Figure 11.15) [53], and the corresponding parabolic rate constants (k_p) are summarized in Table 11.2. The results confirm the comparable oxidation kinetics for both coatings, with the nanocomposite displaying a slightly lower k_p, indicating a marginally enhanced oxidation resistance. The high correlation coefficients (R_{corr} > 0.98) confirm the robustness of the model fit.

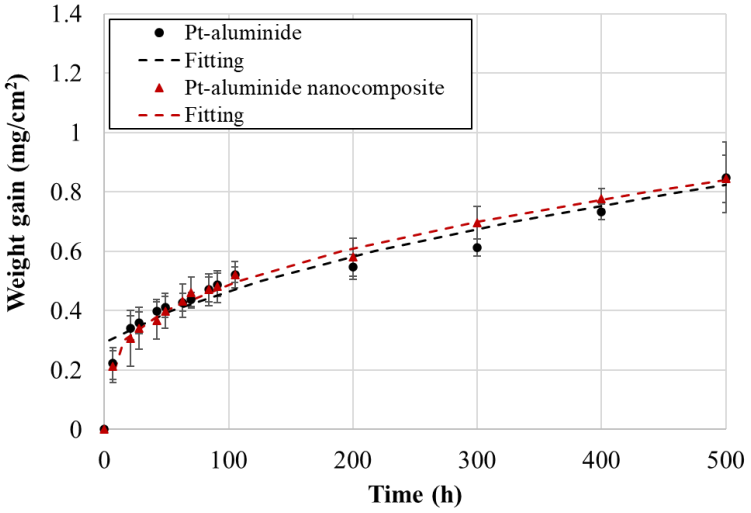

Figure 11.15: Weight gain curves up to 500 h of oxidation at 1100°C for standard Pt-aluminides and Pt-aluminide nanocomposites (curve fitting according to Monceau's model is reported in dashed-lines).

	k_p (mg²/cm⁴/h)	R_{corr}
Pt-aluminide	$9.635 \cdot 10^{-4}$	0.981
Pt-aluminide nanocomposite	$7.728 \cdot 10^{-4}$	0.997

Table 11.2: Parabolic constants calculated according to Monceau's model for Pt-aluminides and Pt-aluminide nanocomposites thickness and correlation coefficient of data fitting.

Two mechanisms can be taken into account to understand the oxidation resistance of the nanocomposite. First, the co-deposited Al_2O_3 nanoparticles retard grain growth in the aluminide during the manufacturing process, resulting in a finer-grained microstructure. Finer grains enhance Al diffusion to the surface, promoting faster formation of the protective α-Al_2O_3 layer and reducing the growth rate of the oxide scale [147]. Second, during the early stages of oxidation, Al_2O_3 transitions through several metastable polymorphs (e.g. θ-Al_2O_3) before forming stable α-Al_2O_3: in the nanocomposite coating, this transformation occurs more rapidly, likely due to epitaxial nucleation promoted by the Al_2O_3 nanoparticles, which act as templates for α-Al_2O_3 crystallization. Analogous behavior has been reported for other oxides such as Cr_2O_3 [296], Fe_2O_3 [297], and La_2O_3 [143], owing to their crystallographic similarity with α-Al_2O_3.

However, it should be noted that the accelerated nature of the test performed at extremely high temperature complicates definitive identification of the nanoparticle-specific mechanisms. Additional

tests at lower temperatures will be required to fully elucidate their role in long-term oxidation resistance.

Figure 11.16 shows SEM micrographs of the oxide-metal interface after 500 h at 1100 °C. In the standard Pt-aluminide (Figure 11.16 (a)), localized γ′-Ni_3Al precipitates form beneath the oxide scale and at grain boundaries, indicating Al depletion due to oxidation. In addition, interfacial voids at the oxide/metal interface can be observed, which are attributed to the Kirkendall effect, where differential diffusion of Ni and Al leads to vacancy accumulation. Despite void formation, no spallation or abrupt weight gain were observed in the weight gain curves. In contrast, the nanocomposite coating (Figure 11.16 (b)), do not show any void formation. Despite some γ′ precipitation at grain boundaries is evident, the oxide scale remains compact and well-adhered, indicating an enhanced oxidation resistance.

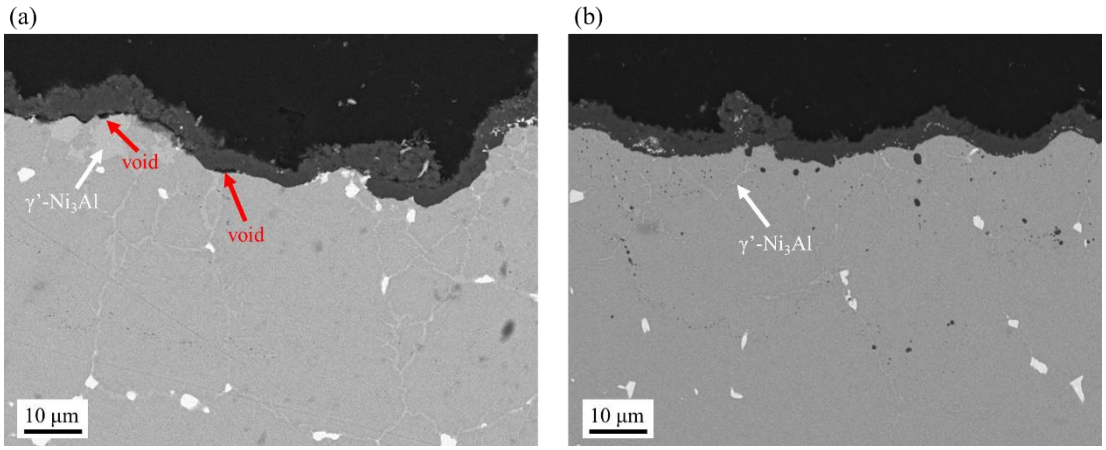

Figure 11.16: Cross-sectional micrographs after 500 hours of exposure at 1100 °C for standard Pt-aluminides (a) and Pt-aluminide nanocomposites (b).

The evolution of phase composition during oxidation was investigated by XRD analysis after 100 h and 500 h, as shown in Figure 11.17. After 100 h, both coatings show dominant β-NiAl peaks with the initial appearance of Al_2O_3 and TiO_2. However, after 500 h, the standard coating exhibits a strong increase in Al_2O_3 peak intensity and the emergence of sharp Ni_3Al peaks, consistent with SEM observations of γ′ phase formation. In contrast, the nanocomposite coating shows lower Ni_3Al peak intensity and β-NiAl remains dominant, indicating that more of the protective β-phase is retained and Al depletion is less severe. This behavior supports the hypothesis that the early and efficient θ-to-α Al_2O_3 transformation in nanocomposite coatings helps minimize Al consumption and delays degradation.

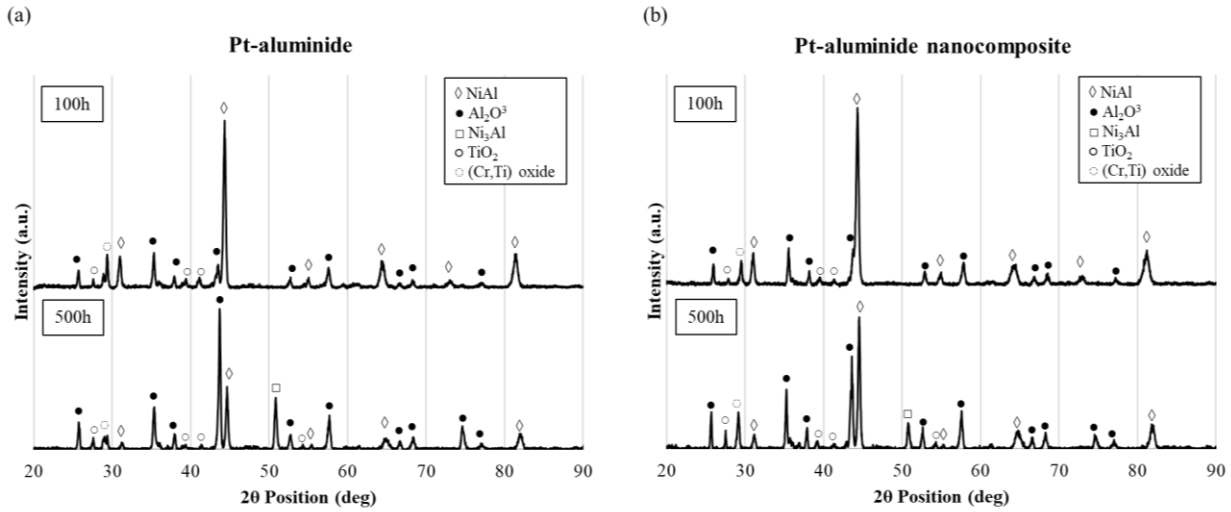

Figure 11.17: XRD spectra of coatings standard Pt-aluminides (a) and Pt-aluminide nanocomposites (b) after 100 h and 500 h of exposure at 1100°C.

These findings indicate that Pt-aluminide nanocomposite coatings exhibit promising oxidation resistance, enabled by nanoparticle-induced grain refinement and accelerated formation of protective α-Al_2O_3, making them a strong candidate for high-temperature protective applications.

11.4 Conclusions

This chapter presented the development and characterization of Pt-aluminide nanocomposite coatings incorporating Al_2O_3 nanoparticles, with the aim of enhancing high-temperature oxidation resistance. The incorporation of nanoparticles into the electroless-plated Pt layer, followed by diffusion and slurry aluminizing treatments, resulted in coatings with uniform structure and consistent phase composition compared to conventional Pt-aluminides. Detailed microstructural analysis demonstrated that Al_2O_3 nanoparticles remain well-dispersed and localized in the outermost regions of the final coating, particularly along grain boundaries, which is critical for their function as epitaxial nucleation sites for α-Al_2O_3. Their presence also led to a refined grain structure, attributed to Zener pinning, particularly within the ζ-$PtAl_2$ phase.

Despite their structural similarity, nanocomposite coatings exhibited small but meaningful advantages in oxidation performance. Accelerated oxidation tests at 1100 °C revealed comparable overall kinetics between standard and nanocomposite coatings, though the latter showed a slightly reduced k_p and evidence of a faster transformation from metastable Al_2O_3 phases to stable α-Al_2O_3. The refined grain size enhanced Al diffusion and likely contributed to the early establishment of a protective oxide scale, while XRD and SEM analyses confirmed lower Al depletion and reduced void formation at the oxide-metal interface in the nanocomposites. These outcomes highlight the beneficial role of nanoparticles in improving both the structural stability and long-term oxidation behavior of Pt-aluminide coatings.

Overall, the results demonstrate that Pt-aluminide nanocomposites represent a promising and scalable advancement in bond coat technology for high-temperature applications, offering enhanced performance without compromising structural integrity. Future work will focus on validating these improvements under more moderate oxidation conditions, to fully establish the reinforcing mechanisms given by Al_2O_3 addition and, in under thermal cycling, to fully assess their long-term reliability and eventually evaluate the possibility of further enhancement of resistance by a reduction in CTE mismatch by the introduction of the ceramic phase.

12. Conclusions

This work presents a comprehensive investigation into the development, characterization, and optimization of platinum-modified aluminide coatings manufactured via electroless deposition routes, with the ultimate aim of enhancing their structural uniformity, functional performance, and high-temperature oxidation resistance. The research also explores innovative strategies to tailor coating architecture, including the use of a pre-deposited Ni interlayer to control diffusion gradients, reduce interdiffusion zone thickness, and influence phase formation. In parallel, the feasibility of introducing Al_2O_3 nanoparticles into the coating via electroless co-deposition is demonstrated, enabling preliminary development of nanocomposite Pt-aluminide systems for future performance enhancement.

The first part of the work established a reliable and industrially applicable electroless Pt deposition process. This method demonstrated several advantages over traditional electrodeposition, including excellent uniformity on complex geometries, the absence of current density issues, and higher reproducibility. The resultant Pt layers showed controlled thickness and high purity, providing a stable foundation for subsequent aluminizing treatments. Notably, the plating process was based on a newly developed, stable electroless bath formulation, which is not available in existing patents or literature. This novel chemistry enabled reproducible deposition and is characterized by several advances compared to commercially available electrolytic solutions and represents a significant contribution to the advancement of electroless platinum technologies.

The second phase evaluated the performance of electroless Pt coatings in comparison with standard electrolytic coatings after aluminizing. Despite equivalent phase compositions and morphological features, electroless coatings exhibited improved homogeneity and slightly slower oxidation kinetics. These findings validate the electroless method as a technically sound alternative for manufacturing Pt-aluminide coatings, particularly in industrial contexts where coating uniformity is critical.

In the third part, a detailed optimization of the slurry aluminizing process was conducted to refine aluminum concentration across coating thickness and improve control over coating composition. By adjusting slurry loading and concentration, coatings with optimal β-NiAl phase content across the entire coating thickness was achieved. The optimized slurry method was validated for the manufacturing of Pt aluminides, and the effect of initial Pt layer thickness was also studied, revealing its influence on ζ-$PtAl_2$ formation and long-term oxidation behavior. These insights enabled the definition of optimized process parameters that balance performance with cost-effectiveness.

Building upon this foundation, the fourth part introduced an electroless-deposited nickel interlayer to further tailor diffusion dynamics. This modification proved effective in minimizing $PtAl_2$ content,

reducing IDZ thickness, and limiting substrate degradation via suppression of TCP phase formation. Among all studied configurations, coatings with a 10 µm Ni interlayer provided the best compromise between oxidation resistance, mechanical stability, and structural uniformity.

The final phase of the thesis focused on a novel nanocomposite approach, incorporating Al_2O_3 nanoparticles into the electroless Pt layer. The co-deposition of these particles was successfully achieved, with optimal distribution and minimal agglomeration at 0.5 g/L concentration. After aluminizing, the nanoparticles remained localized in the outer coating region, which is critical for their role in promoting early transformation of metastable alumina to the protective α-Al_2O_3 phase. The nanocomposite coatings exhibited refined grain structure, reduced interfacial voids, and slightly improved oxidation resistance at 1100 °C.

In summary, the research demonstrates that electroless processing not only enables precise control over Pt distribution, but also opens up new pathways for advanced bond coat architectures. The findings support the feasibility of industrial-scale implementation of electroless Pt-aluminides and lay the groundwork for future enhancements through additional modifications and nanocomposite formation. Further studies, particularly under thermal cycling, are recommended to fully assess the long-term durability and industrial applicability of the approach.

References

[1] M.T. Schobeiri, Turbomachinery Flow Physics and Dynamic Performance, 2012. https://doi.org/10.1007/978-3-642-24675-3.

[2] A.M.Y. Razak, Industrial gas turbines: Performance and operability, 2007. https://doi.org/10.1533/9781845693404.

[3] https://en.wikipedia.org/wiki/World_energy_supply_and_consumption, (2025).

[4] https://www.iata.org/en/programs/sustainability/flynetzero/, (2021).

[5] M.M. Rahman, T.K. Ibrahim, K. Kadirgama, R. Mamat, R.A. Bakar, Influence of Operation Conditions and Ambient Temperature on Performance of Gas Turbine Power Plant, Adv Mat Res 189–193 (2011) 3007–3013. https://doi.org/10.4028/www.scientific.net/AMR.189-193.3007.

[6] J.C. Zhao, J.H. Westbrook, Ultrahigh-temperature materials for jet engines, MRS Bull 28 (2003) 622–627. https://doi.org/10.1557/mrs2003.189.

[7] M. Cervenka, The Rolls-Royce Trent Engine, Rollce- Royce, 2000.

[8] L. Xu, S. Bo, Y. Hongde, W. Lei, Evolution of Rolls-royce Air-cooled Turbine Blades and Feature Analysis, Procedia Eng 99 (2015) 1482–1491. https://doi.org/10.1016/j.proeng.2014.12.689.

[9] M. Rezazadeh Reyhani, M. Alizadeh, A. Fathi, H. Khaledi, Turbine blade temperature calculation and life estimation - a sensitivity analysis, Propulsion and Power Research 2 (2013) 148–161. https://doi.org/10.1016/j.jppr.2013.04.004.

[10] C.H. White, Nickel Base Alloys, in: G.W. Meethan (Ed.), The Development of Gas Turbine Materials, 1981: pp. 89–119.

[11] M.J. Donachie, S.J. Donachie, Superalloys: A Technical Guide, Second Edition, ASM Internationa, 2002.

[12] T.S. Sidhu, S. Prakash, R.D. Agrawal, Hot corrosion and performance of nickel-based coatings, Curr Sci 90 (2006) 41–47.

[13] S. Gialanella, A. Malandruccolo, Topics in Mining, Metallurgy and Materials Engineering: Aerospace Alloys, Springer, 2020.

[14] T. Himo, Y. Yoshioka, K. Nagata, H. Kashiwaya, T. Kobayashi, Y. Koizumi, H. Harada, T. Yamagata, Design of a high Re containing single crystal superalloys for industrial gas turbines, Proc. 6th Liege Conference on Materials for Advanced Power Engineering, COST (1998).

[15] Kobayashi T, Y. Koizumi, H. Harada, T. Yamagata, Design of high Re containing single crystal superalloys with balanced intermediate and high temperature creep strengths, Proc. 4th Int'l Charles Parsons Turbine Conference (1997) 766–773.

[16] A. Sato, H. Harada, A.-C. Yeh, K. Kawagishi, T. Kobayashi, Y. Koizumi, T. Yokokawa, J.-X. Zhang, A 5th generation SC superalloy with balanced high temperature properties and processability , Superalloys (2008) 131–138.

[17] T. Yokokawa, M. Osawa, K. Nishida, T. Kobayashi, Y. Koizumi, H. Harada, Partitioning behavior of platinum group metals on the γ and γ′ phases of Ni-base superalloys at high temperatures, Scr Mater 49 (2003) 1041–1046. https://doi.org/10.1016/S1359-6462(03)00437-8.

[18] I. Aniekan Essienubong, O. Ikechukwu, P.O. Ebunilo, E. Ikpe, Material Selection for High Pressure (HP) Turbine Blade of Conventional Turbojet Engines, American Journal of Mechanical and Industrial Engineering 1 (2016) 1–9.

[19] K.L. Edwards, ASM handbook, volume 11: failure analysis and prevention, Mater Des 25 (2004) 735–736. https://doi.org/10.1016/j.matdes.2004.03.005.

[20] G.E. Dieter, Mechanical Metallurgy, McGraw-Hill, New York, 1076.

[21] American Society for Testing Materials, ASTM E139-11(2018) Standard Test Methods for Conducting Creep, Creep-Rupture, and Stress-Rupture Tests of Metallic Materials, (2018).

[22] H. Altenbach, Introduction to Creep Mechanics, in: Encyclopedia of Continuum Mechanics, 2020: pp. 1337–1343.

[23] R.W. Hertzberg, Deformation and Fracture Mechanics of Engineering Materials, John Wiley & Sons, 1996.

[24] Nabarro F. R. N., H.L. de Villiers, The Physics of Creep: Creep and Creep-Resistant Alloys, CRC Press, n.d.

[25] J.E. Dorn, Creep and Stress Rupture in Metals, McGraw-Hill, 1054.

[26] H.J. Frost, M.F. Ashby, Deformation Mechanism Maps: The Plasticity and Creep of Metals and Ceramics, Pergamon Press, 1982.

[27] M.F. Ashby, R.S. Verrall, Micromechanisms of flow and fracture, and their relevance to the rheology of the upper mantle, Philosophical Transactions of the Royal Society of London. Series A, Mathematical and Physical Sciences 288 (1978) 59–95. https://doi.org/10.1098/rsta.1978.0006.

[28] J.-P. Poirier, Diffusion creep, grain-boundary sliding and superplasticity, in: Creep of Crystals: High-Temperature Deformation Processes in Metals, Ceramics and Minerals, 1985: pp. 194–212.

[29] A.S. Argon, Strengthening mechanisms in crystal plasticity, Oxford University Press, 2008.

[30] C. Herring, Diffusional viscosity of a polycrystalline solid, J Appl Phys 21 (1950) 437–444.

[31] F.R.N. Nabarro, Deformation of crystals by the motion of single ions, Proceedings of the Physical Society 59 (1948) 256–272.

[32] R.L. Coble, A Model for Boundary Diffusion Controlled Creep in Polycrystalline Materials, J Appl Phys 34 (1963) 1679–1682. https://doi.org/10.1063/1.1702656.

[33] U.R. Evans, R.D. Rawlings, The role of diffusion in creep processes, Acta Metallurgica 17 (1969) 143–152.

[34] R. Raj, M.F. Ashby, On grain boundary sliding and diffusional creep, Metallurgical Transactions 2 (1971) 1113–1127.

[35] A. Needleman, J.R. Rice, Plastic creep flow effects in the diffusive cavitation of grain boundaries, Acta Metallurgica 28 (1980) 1315–1332. https://doi.org/10.1016/0001-6160(80)90001-2.

[36] J.P. Hirth, J. Lothe, Theory of dislocations, Krieger Publishing Company, 1982.

[37] T.G. Langdon, Grain boundary sliding revisited: Developments in sliding over four decades, J Mater Sci 41 (2006) 597–609. https://doi.org/10.1007/s10853-006-6476-0.

[38] T.G. Langdon, A unified approach to grain boundary sliding in creep and superplasticity, Acta Metallurgica et Materialia 42 (1994) 2437–2443. https://doi.org/10.1016/0956-7151(94)90322-0.

[39] M.F. Ashby, A first report on deformation-mechanism maps, Acta Metallurgica 20 (1972) 887–897. https://doi.org/10.1016/0001-6160(72)90082-X.

[40] M.R. Notis, Deformation Mechanism Maps — A Review with Applications, in: Deformation of Ceramic Materials, Springer US, Boston, MA, 1975: pp. 1–23. https://doi.org/10.1007/978-1-4613-4431-5_1.

[41] T.M. Pollock, S. Tin, Nickel-Based Superalloys for Advanced Turbine Engines: Chemistry, Microstructure and Properties, J Propuls Power 22 (2006) 361–374. https://doi.org/10.2514/1.18239.

[42] J.X. Zhang, T. Murakumo, Y. Koizumi, T. Kobayashi, H. Harada, Slip geometry of dislocations related to cutting of the γ′ phase in a new generation single-crystal superalloy, Acta Mater 51 (2003) 5073–5081. https://doi.org/10.1016/S1359-6454(03)00355-0.

[43] A.C. Yeh, S. Tin, Effects of Ru and Re additions on the high temperature flow stresses of Ni-base single crystal superalloys, Scr Mater 52 (2005) 519–524. https://doi.org/10.1016/j.scriptamat.2004.10.039.

[44] L.J. Carroll, Q. Feng, T.M. Pollock, Interfacial Dislocation Networks and Creep in Directional Coarsened Ru-Containing Nickel-Base Single-Crystal Superalloys, Metallurgical and Materials Transactions A 39 (2008) 1290–1307. https://doi.org/10.1007/s11661-008-9520-7.

[45] D.J. Young, High Temperature Oxidation and Corrosion of Metals, Second Edition, Elsevier, 2016. https://doi.org/10.1016/C2014-0-00259-6.

[46] B. Gleeson, Thermodynamics and Theory of External and Internal Oxidation of Alloys, in: Shreir's Corrosion, Elsevier, 2010: pp. 180–194. https://doi.org/10.1016/B978-044452787-5.00012-3.

[47] A.S. Ulrich, U. Glatzel, M.C. Galetz, Discontinuities in Oxidation Kinetics: A New Model and its Application to Cr–Si-Base Alloys, Oxidation of Metals 95 (2021) 445–465. https://doi.org/10.1007/s11085-021-10029-8.

[48] D. Chellaganesh, M. Adam Khan, J.T. Winowlin Jappes, S. Sathiyanarayanan, Cyclic Oxidation and Hot Corrosion Behavior of Nickel–Iron-Based Superalloy, High Temperature Materials and Processes 37 (2018) 173–180. https://doi.org/10.1515/htmp-2016-0130.

[49] J. Dai, J. Zhu, C. Chen, F. Weng, High temperature oxidation behavior and research status of modifications on improving high temperature oxidation resistance of titanium alloys and titanium aluminides: A review, J Alloys Compd 685 (2016) 784–798. https://doi.org/10.1016/j.jallcom.2016.06.212.

[50] A.C. Elias, Principles and Presentation of Corrosion, 1996.

[51] V.P. Zhdanov, B. Kasemo, Cabrera–Mott kinetics of oxidation of nm-sized metal particles, Chem Phys Lett 452 (2008) 285–288. https://doi.org/10.1016/j.cplett.2008.01.006.

[52] C. Wagner, Theoretical Analysis of the Diffusion Processes Determining the Oxidation Rate of Alloys, J Electrochem Soc 99 (1952) 369. https://doi.org/10.1149/1.2779605.

[53] D. Monceau, B. Pieraggi, Determination of Parabolic Rate Constants from a Local Analysis of Mass-Gain Curves, Oxidation of Metals 50 (1998) 477–493. https://doi.org/10.1023/A:1018860909826.

[54] N. Birks, G.H. Meier, F.S. Pettit, Hot corrosion, in: Introduction to the High Temperature Oxidation of Metals, Cambridge University Press, 2006.

[55] R.A. Rapp, Y.-S. Zhang, Hot corrosion of materials: Fundamental studies, JOM 46 (1994) 47–55. https://doi.org/10.1007/BF03222665.

[56] S. Pahlavanyali, A. Sabour, M. Hirbod, The hot corrosion behaviour of HVOF sprayed MCrAlX coatings under Na2SO4(+NaCl) salt films, Materials and Corrosion 54 (2003) 687–693. https://doi.org/10.1002/maco.200303681.

[57] P. Zhang, Performance of MCrAlX coatings : Oxidation, Hot corrosion and Interdiffusion, Linköping University Electronic Press, Linköping, 2019. https://doi.org/10.3384/diss.diva-161511.

[58] B. Salehnasab, E. Poursaeidi, S.A. Mortazavi, G.H. Farokhian, Hot corrosion failure in the first stage nozzle of a gas turbine engine, Eng Fail Anal 60 (2016) 316–325. https://doi.org/10.1016/j.engfailanal.2015.11.057.

[59] T.S. Sidhu, S. Prakash, R.D. Agrawal, Hot corrosion and performance of nickel-based coatings, Curr Sci 90 (2006) 41–47.

[60] J.F.G. Condé, E. Erdös, A. Rahmel, Mechanisms of Hot Corrosion, in: High Temperature Alloys for Gas Turbines 1982, Springer Netherlands, Dordrecht, 1982: pp. 99–148. https://doi.org/10.1007/978-94-009-7907-9_4.

[61] N. Birks, G.H. Meier, F.S. Pettit, Erosion–corrosion of metals in oxidizing atmospheres, in: Introduction to the High Temperature Oxidation of Metals, Cambridge University Press, 2006: pp. 253–270. https://doi.org/10.1017/CBO9781139163903.

[62] J.G.A. Bitter, A study of erosion phenomena part I, Wear 6 (1963) 5–21. https://doi.org/10.1016/0043-1648(63)90003-6.

[63] T.M. Pollock, S. Tin, Nickel-Based Superalloys for Advanced Turbine Engines: Chemistry, Microstructure and Properties, J Propuls Power 22 (2006) 361–374. https://doi.org/10.2514/1.18239.

[64] P.K. Wright, A.G. Evans, Mechanisms governing the performance of thermal barrier coatings, Curr Opin Solid State Mater Sci 4 (1999) 255–265. https://doi.org/10.1016/S1359-0286(99)00024-8.

[65] N.P. Padture, M. Gell, E.H. Jordan, Thermal Barrier Coatings for Gas-Turbine Engine Applications, Science (1979) 296 (2002) 280–284. https://doi.org/10.1126/science.1068609.

[66] D.R. Clarke, C.G. Levi, Materials Design for the Next Generation Thermal Barrier Coatings, Annu Rev Mater Res 33 (2003) 383–417. https://doi.org/10.1146/annurev.matsci.33.011403.113718.

[67] U. Schulz, C. Leyens, K. Fritscher, M. Peters, B. Saruhan-Brings, O. Lavigne, J.-M. Dorvaux, M. Poulain, R. Mévrel, M. Caliez, Some recent trends in research and technology of advanced thermal barrier coatings, Aerosp Sci Technol 7 (2003) 73–80. https://doi.org/10.1016/S1270-9638(02)00003-2.

[68] C.U. Hardwicke, Y.-C. Lau, Advances in Thermal Spray Coatings for Gas Turbines and Energy Generation: A Review, Journal of Thermal Spray Technology 22 (2013) 564–576. https://doi.org/10.1007/s11666-013-9904-0.

[69] P.K. Das, P. Acharya, Thermal barrier coatings application and development, International Journal of Research in Engineering and Science 6 (2018) 100–103.

[70] M.J. Pomeroy, Coatings for gas turbine materials and long term stability issues, Mater Des 26 (2005) 223–231. https://doi.org/10.1016/j.matdes.2004.02.005.

[71] B. Cheng, N. Yang, Q. Zhang, M. zhang, Y.-M. Zhang, L. Chen, G.-J. Yang, C.-X. Li, C.-J. Li, Sintering induced the failure behavior of dense vertically crack and lamellar structured TBCs with equivalent thermal insulation performance, Ceram Int 43 (2017) 15459–15465. https://doi.org/10.1016/j.ceramint.2017.08.092.

[72] J.A. Krogstad, S. Krämer, D.M. Lipkin, C.A. Johnson, D.R.G. Mitchell, J.M. Cairney, C.G. Levi, Phase Stability of t′-Zirconia-Based Thermal Barrier Coatings: Mechanistic Insights, Journal of the American Ceramic Society 94 (2011). https://doi.org/10.1111/j.1551-2916.2011.04531.x.

[73] V. Genova, G. Pedrizzetti, L. Paglia, F. Marra, C. Bartuli, G. Pulci, Diffusion aluminide coating modified via electroless nickel plating for Ni-based superalloy protection, Surf Coat Technol 439 (2022) 128452. https://doi.org/10.1016/j.surfcoat.2022.128452.

[74] S. Ajdari, F. Shahriari Nogorani, P. Zamani Moghadam, The effect of the MCrAlY composition and aluminizing cycle upon the microstructure and hot corrosion resistance of the over-aluminized MCrAlY coating on IN738LC alloy substrate, Materials and Corrosion 74 (2023) 846–858. https://doi.org/10.1002/maco.202213496.

[75] J.P. Martins, H. Yu, Y. Chen, G. Brewster, R. McIntyre, P. Xiao, Effect of bond coat topography on the fracture mechanics and lifetime of air-plasma sprayed thermal barrier coatings, Surf Coat Technol 421 (2021) 127447. https://doi.org/10.1016/j.surfcoat.2021.127447.

[76] G. Pulci, J. Tirillò, F. Marra, F. Sarasini, A. Bellucci, T. Valente, C. Bartuli, High Temperature Oxidation and Microstructural Evolution of Modified MCrAlY Coatings, Metallurgical and Materials Transactions A 45 (2014) 1401–1408. https://doi.org/10.1007/s11661-013-2086-z.

[77] X. Hu, Q. Liu, Z. Xie, S. Liu, Q. Wen, J. Guo, W. Zhu, Effect of bond coating surface roughness on high-temperature performance of EB-PVD thermal barrier coatings, Ceram Int 51 (2025) 14307–14318. https://doi.org/10.1016/j.ceramint.2025.01.267.

[78] T. Kepa, F. Pedraza, F. Rouillard, Intermetallic formation of Al-Fe and Al-Ni phases by ultrafast slurry aluminization (flash aluminizing), Surf Coat Technol 397 (2020) 126011. https://doi.org/10.1016/j.surfcoat.2020.126011.

[79] F. Bozza, G. Bolelli, C. Giolli, A. Giorgetti, L. Lusvarghi, P. Sassatelli, A. Scrivani, A. Candeli, M. Thoma, Diffusion mechanisms and microstructure development in pack

aluminizing of Ni-based alloys, Surf Coat Technol 239 (2014) 147–159. https://doi.org/10.1016/j.surfcoat.2013.11.034.

[80] G.W. Goward, D.H. Boone, Mechanisms of formation of diffusion aluminide coatings on nickel-base superalloys, Oxidation of Metals 3 (1971) 475–495. https://doi.org/10.1007/BF00604047.

[81] R. Bianco, R.A. Rapp, Pack cementation diffusion coatings, in: Metallurgical and Ceramic Protective Coatings, Springer Netherlands, Dordrecht, 1996: pp. 236–260. https://doi.org/10.1007/978-94-009-1501-5_9.

[82] Y.Q. Wang, G. Sayre, Factors affecting the microstructure of platinum-modified aluminide coatings during a vapor phase aluminizing process, Surf Coat Technol 203 (2009) 1264–1272. https://doi.org/10.1016/j.surfcoat.2008.10.031.

[83] J. Grüters, M.C. Galetz, Influence of thermodynamic activities of different masteralloys in pack powder mixtures to produce low activity aluminide coatings on TiAl alloys, Intermetallics (Barking) 60 (2015) 19–27. https://doi.org/10.1016/j.intermet.2015.01.001.

[84] J. Benoist, K.F. Badawi, A. Malié, C. Ramade, Microstructure of Pt modified aluminide coatings on Ni-based superalloys without prior Pt diffusion, Surf Coat Technol 194 (2005) 48–57. https://doi.org/10.1016/j.surfcoat.2004.04.094.

[85] N. Voudouris, Ch. Christoglou, G.N. Angelopoulos, Formation of aluminide coatings on nickel by a fluidised bed CVD process, Surf Coat Technol 141 (2001) 275–282. https://doi.org/10.1016/S0257-8972(01)01193-8.

[86] R. Mévrel, C. Duret, R. Pichoir, Pack cementation processes, Materials Science and Technology 2 (1986) 201–206. https://doi.org/10.1179/mst.1986.2.3.201.

[87] N. Birks, G.H. Meier, F.S. Pettit, Protective Coatings , in: Introduction to the High Temperature Oxidation of Metals, 2nd Edition, 2006: pp. 271–277.

[88] D. Martelli, S. Bassini, M. Utili, M. Tarantino, S. Lionetti, E. Zanin, LIFUS II corrosion loop final design and screening of an Al based diffusion coating in stagnant LLE environment, Fusion Engineering and Design 160 (2020) 112034. https://doi.org/10.1016/j.fusengdes.2020.112034.

[89] T. Dudziak, E. Rząd, T. Polczyk, K. Jahns, W. Polkowski, A. Polkowska, M. Wójcicki, Preliminary Studies on Rare Elements Addition and Effect on Oxidation Behaviour of Pack Cementation Coatings Deposited on Variety of Steels at High Temperature, Materials 14 (2021) 6801. https://doi.org/10.3390/ma14226801.

[90] B. Rannou, B. Bouchaud, J. Balmain, G. Bonnet, F. Pedraza, Comparative Isothermal Oxidation Behaviour of New Aluminide Coatings from Slurries Containing Al Particles and

Conventional Out-of-Pack Aluminide Coatings, Oxidation of Metals 81 (2014) 139–149. https://doi.org/10.1007/s11085-013-9427-6.

[91] M.C. Galetz, X. Montero, M. Mollard, M. Günthner, F. Pedraza, M. Schütze, The role of combustion synthesis in the formation of slurry aluminization, Intermetallics (Barking) 44 (2014) 8–17. https://doi.org/10.1016/j.intermet.2013.08.002.

[92] B. Grégoire, G. Bonnet, F. Pedraza, Mechanisms of formation of slurry aluminide coatings from Al and Cr microparticles, Surf Coat Technol 359 (2019) 323–333. https://doi.org/10.1016/j.surfcoat.2018.11.077.

[93] X. Montero, M.C. Galetz, M. Schütze, Low-activity aluminide coatings for superalloys using a slurry process free of halide activators and chromates, Surf Coat Technol 222 (2013) 9–14. https://doi.org/10.1016/j.surfcoat.2013.01.033.

[94] M. Conti, L. Paglia, V. Genova, G. Pedrizzetti, L. Baiamonte, F. Marra, The Effects of Deposition Parameters on the Properties of NiCr Coatings Obtained by Electroless Plating, Chem Eng Trans 100 (2023) 427–432. https://doi.org/10.3303/CET23100072.

[95] Z. Li, C. Wang, X. Ding, X. Li, J. Yu, Q. Li, Y. Qu, Effect of Slurry Thickness on the Quality of Aluminized Coatings, Materials 15 (2022) 6758. https://doi.org/10.3390/ma15196758.

[96] F.H. Stott, The Oxidation of Alumina-Forming Alloys, Materials Science Forum 251–254 (1997) 19–32. https://doi.org/10.4028/www.scientific.net/MSF.251-254.19.

[97] R. Prescott, M.J. Graham, The formation of aluminum oxide scales on high-temperature alloys, Oxidation of Metals 38 (1992) 233–254. https://doi.org/10.1007/BF00666913.

[98] V.K. Tolpygo, D.R. Clarke, The effect of oxidation pre-treatment on the cyclic life of EB-PVD thermal barrier coatings with platinum–aluminide bond coats, Surf Coat Technol 200 (2005) 1276–1281. https://doi.org/10.1016/j.surfcoat.2005.07.088.

[99] V.K. Tolpygo, D.R. Clarke, K.S. Murphy, Oxidation-induced failure of EB-PVD thermal barrier coatings, Surf Coat Technol 146–147 (2001) 124–131. https://doi.org/10.1016/S0257-8972(01)01482-7.

[100] Y. Liu, M. Wu, H. Zhou, J. Zeng, H. Zhang, W. Guo, Y. Pei, S. Li, S. Gong, D. Hu, Enhancing long-term cyclic oxidation performance of a dual-phase PtAl coatings at 1200 ℃ by Ru modification, Corros Sci 222 (2023) 111418. https://doi.org/10.1016/j.corsci.2023.111418.

[101] Z. Bai, D. Li, H. Peng, J. Wang, H. Guo, S. Gong, Suppressing the formation of SRZ in a Ni-based single crystal superalloy by RuNiAl diffusion barrier, Progress in Natural Science: Materials International 22 (2012) 146–152. https://doi.org/10.1016/j.pnsc.2012.03.007.

[102] H. Murakami, T. Sakai, Anisotropy of secondary reaction zone formation in aluminized Ni-based single-crystal superalloys, Scr Mater 59 (2008) 428–431. https://doi.org/10.1016/j.scriptamat.2008.04.025.

[103] M. Zagula-Yavorska, J. Sieniawski, Cyclic oxidation of palladium modified and nonmodified aluminide coatings deposited on nickel base superalloys, Archives of Civil and Mechanical Engineering 18 (2018) 130–139. https://doi.org/10.1016/j.acme.2017.05.004.

[104] Y. Zhang, J.A. Haynes, G. Wright, B.A. Pint, K.M. Cooley, W.Y. Lee, P.K. Liaw, Effects of Pt incorporation on the isothermal oxidation behavior of chemical vapor deposition aluminide coatings, Metallurgical and Materials Transactions A 32 (2001) 1727–1741. https://doi.org/10.1007/s11661-001-0150-6.

[105] B.A. Pint, The role of chemical composition on the oxidation performance of aluminide coatings, Surf Coat Technol 188–189 (2004) 71–78. https://doi.org/10.1016/j.surfcoat.2004.08.007.

[106] F. Pedraza, A.D. Kennedy, J. Kopecek, P. Moretto, Investigation of the microstructure of platinum-modified aluminide coatings, Surf Coat Technol 200 (2006) 4032–4039. https://doi.org/10.1016/j.surfcoat.2004.12.019.

[107] L.C. Zhang, A.H. Heuer, Microstructural evolution of the nickel platinum-aluminide bond coat on electron-beam physical-vapor deposition thermal-barrier coatings during high-temperature service, Metallurgical and Materials Transactions A 36 (2005) 43–53. https://doi.org/10.1007/s11661-005-0137-9.

[108] D.K. Das, Microstructure and high temperature oxidation behavior of Pt-modified aluminide bond coats on Ni-base superalloys, Prog Mater Sci 58 (2013) 151–182. https://doi.org/10.1016/j.pmatsci.2012.08.002.

[109] J. Benoist, K.F. Badawi, A. Malié, C. Ramade, Microstructure of Pt modified aluminide coatings on Ni-based superalloys without prior Pt diffusion, Surf Coat Technol 194 (2005) 48–57. https://doi.org/10.1016/j.surfcoat.2004.04.094.

[110] J. Angenete, K. Stiller, Comparison of inward and outward grown Pt modified aluminide diffusion coatings on a Ni based single crystal superalloy, Surf Coat Technol 150 (2002) 107–118. https://doi.org/10.1016/S0257-8972(01)01544-4.

[111] Y. Li, S. Li, C. Zhang, N. Xu, Z. Bao, Oxidation Behavior and Oxide Transformation of a Pt-Modified Aluminide Coating at Moderate High Temperature, Crystals (Basel) 11 (2021) 972. https://doi.org/10.3390/cryst11080972.

[112] G.R. Krishna, D.K. Das, V. Singh, S. V Joshi, Role of Pt content in the microstructural development and oxidation performance of Pt-aluminide coatings produced using a high-activity aluminizing process, 1998.

[113] A. Littner, F. Pedraza, A.D. Kennedy, P. Moretto, L. Peichl, T. Weber, M. Schuetze, Performance and thermal stability of Pt-modified Al-diffusion coatings for superalloys under cyclic and isothermal conditions, Materials at High Temperatures 22 (2005) 411–420. https://doi.org/10.1179/mht.2005.048.

[114] Y.F. Yang, C.Y. Jiang, Z.B. Bao, S.L. Zhu, F.H. Wang, Effect of aluminisation characteristics on the microstructure of single phase β-(Ni,Pt)Al coating and the isothermal oxidation behaviour, Corros Sci 106 (2016) 43–54. https://doi.org/10.1016/j.corsci.2016.01.024.

[115] M. Zagula-Yavorska, J. Sieniawski, Microstructural Study on Oxidation Resistance of Nonmodified and Platinum Modified Aluminide Coating, J Mater Eng Perform 23 (2014) 918–926. https://doi.org/10.1007/s11665-013-0841-3.

[116] Y.F. Yang, C.Y. Jiang, H.R. Yao, Z.B. Bao, S.L. Zhu, F.H. Wang, Cyclic oxidation and rumpling behaviour of single phase β-(Ni,Pt)Al coatings with different thickness of initial Pt plating, Corros Sci 111 (2016) 162–174. https://doi.org/10.1016/j.corsci.2016.05.011.

[117] Y.F. Yang, C.Y. Jiang, Z.Y. Zhang, Z.B. Bao, M.H. Chen, S.L. Zhu, F.H. Wang, Hot corrosion behaviour of single-phase platinum-modified aluminide coatings: Effect of Pt content and pre-oxidation, Corros Sci 127 (2017) 82–90. https://doi.org/10.1016/j.corsci.2017.08.015.

[118] H. Zhang, Y. Liu, H. Su, W. Qu, H. Zhang, Y. Pei, S. Li, S. Gong, Effects of coating growth mode on the oxidation behavior of a hybrid Pt/Ru-modified aluminide coating at 1200 °C, Corros Sci 225 (2023) 111608. https://doi.org/10.1016/j.corsci.2023.111608.

[119] Z. Zhang, B. Bai, H. Peng, S. Gong, H. Guo, Effect of Ru on interdiffusion dynamics of β-NiAl/DD6 system: A combined experimental and first-principles studies, Mater Des 88 (2015) 667–674. https://doi.org/10.1016/j.matdes.2015.09.041.

[120] H.M. Tawancy, N.M. Abbas, T.N. Rhys-Jones, Role of platinum in aluminide coatings, Surf Coat Technol 49 (1991) 1–7. https://doi.org/10.1016/0257-8972(91)90022-O.

[121] Y. Cadoret, D. Monceau, M.-P. Bacos, P. Josso, V. Maurice, P. Marcus, Effect of Platinum on the Growth Rate of the Oxide Scale Formed on Cast Nickel Aluminide Intermetallic Alloys, Oxidation of Metals 64 (2005) 185–205. https://doi.org/10.1007/s11085-005-6558-4.

[122] Y.F. Yang, S.X. Ren, P. Ren, Q.W. Wang, Z.B. Bao, W. Li, S.L. Zhu, F.H. Wang, Hot corrosion and cyclic oxidation performance of a PtAl2-dispersed (Ni,Pt)Al coating prepared by low-activity high-temperature aluminizing, J Alloys Compd 911 (2022) 164978. https://doi.org/10.1016/j.jallcom.2022.164978.

[123] J. Peng, T. Huang, P. Song, W. Huang, Y. He, T. Ma, B. Yang, Y. Liang, M. Wu, R. Chen, Effect of platinum and pre-oxidation on the hot corrosion behavior of aluminide coating with NaCl at 1050 °C, Mater Res Express 7 (2020) 116402. https://doi.org/10.1088/2053-1591/abc4b2.

[124] Y.F. Yang, Z.L. Liu, P. Ren, Q.W. Wang, Z.B. Bao, S.L. Zhu, W. Li, Hot corrosion behavior of Pt+Hf co-modified NiAl coating in the mixed salt of Na2SO4-NaCl at 900 °C, Corros Sci 167 (2020) 108527. https://doi.org/10.1016/j.corsci.2020.108527.

[125] K. Shirvani, A. Rashidghamat, Evolution of Oxide Scale on Aluminide and Pt-Aluminide Coatings Exposed to Type I (870 °C) Hot Corrosion, Oxidation of Metals 85 (2016) 75–85. https://doi.org/10.1007/s11085-015-9580-1.

[126] L. Ye, H. Chen, B. Liu, G. Yang, H. Luo, Y. Gao, Effect of Pt content on initial TGO formation and available Al reserve of Pt-Al coatings during thermal cycling, Surf Coat Technol 337 (2018) 82–89. https://doi.org/10.1016/j.surfcoat.2018.01.002.

[127] J. Li, L. Wei, J. He, H. Chen, H. Guo, The role of Re in improving the oxidation-resistance of a Re modified PtAl coating on Mo-rich single crystal superalloy, J Mater Sci Technol 58 (2020) 63–72. https://doi.org/10.1016/j.jmst.2020.03.054.

[128] H. Liu, S. Li, C.-Y. Jiang, C.-T. Yu, Z.-B. Bao, S.-L. Zhu, F.-H. Wang, Oxidation Performance and Interdiffusion Behavior of a Pt-Modified Aluminide Coating with Pre-deposition of Ni, Acta Metallurgica Sinica (English Letters) 32 (2019) 1490–1500. https://doi.org/10.1007/s40195-019-00918-y.

[129] Z. Xie, Q. Liu, X. Hu, J. Guo, W. Zhu, On the Thermal Shock Resistance and Failure Mechanism of the Pt-Modified Aluminide Bond Coating, Coatings 14 (2024) 326. https://doi.org/10.3390/coatings14030326.

[130] Md. Zafir Alam, N. Hazari, V.K. Varma, D.K. Das, Effect of Cyclic Oxidation Exposure on Tensile Properties of a Pt-Aluminide Bond-Coated Ni-Base Superalloy, Metallurgical and Materials Transactions A 42 (2011) 4064–4074. https://doi.org/10.1007/s11661-011-0803-z.

[131] C. Oskay, M.C. Galetz, H. Murakami, Mechanical behaviour of conventional, Pt- and Pt/Ir-modified NiAl diffusion coatings after thermocyclic exposure at 1100°C, Materials at High Temperatures 36 (2019) 404–416. https://doi.org/10.1080/09603409.2019.1591064.

[132] X. Tao, K. Tan, X. Wang, J. Liang, Y. Zhou, J. Li, X. Sun, Cyclic oxidation-induced deleterious effects of Ru on the surface rumpling of a Pt-modified aluminide coating, Surf Coat Technol 478 (2024) 130416. https://doi.org/10.1016/j.surfcoat.2024.130416.

[133] N. Vialas, D. Monceau, Effect of Pt and Al content on the long-term, high temperature oxidation behavior and interdiffusion of a Pt-modified aluminide coating deposited on Ni-base

superalloys, Surf Coat Technol 201 (2006) 3846–3851. https://doi.org/10.1016/j.surfcoat.2006.07.246.

[134] V.K. Tolpygo, D.R. Clarke, On the rumpling mechanism in nickel-aluminide coatings, Acta Mater 52 (2004) 5115–5127. https://doi.org/10.1016/j.actamat.2004.07.019.

[135] Q. Fan, H. Yu, T.-G. Wang, Z. Wu, Y. Liu, Preparation and Isothermal Oxidation Behavior of Zr-Doped, Pt-Modified Aluminide Coating Prepared by a Hybrid Process, Coatings 8 (2017) 1. https://doi.org/10.3390/coatings8010001.

[136] R. Filip, M. Góral, M. Zawadzki, A. Nowotnik, M. Pytel, The Influence of Long-Term Heat Treatment on Microstructure of Zr-Modified Aluminide Coating Deposited by CVD Method on MAR M200+Hf Nickel Superalloy, Key Eng Mater 592–593 (2013) 469–472. https://doi.org/10.4028/www.scientific.net/KEM.592-593.469.

[137] S.J. Hong, G.H. Hwang, W.K. Han, S.G. Kang, Cyclic oxidation of Pt/Pd-modified aluminide coating on a nickel-based superalloy at 1150°C, Intermetallics (Barking) 17 (2009) 381–386. https://doi.org/10.1016/j.intermet.2008.08.014.

[138] D. Wang, H. Peng, S. Gong, H. Guo, NiAlHf/Ru: Promising bond coat materials in thermal barrier coatings for advanced single crystal superalloys, Corros Sci 78 (2014) 304–312. https://doi.org/10.1016/j.corsci.2013.10.013.

[139] Y. Matsuoka, K. Chikugo, T. Suzuki, Y. Matsunaga, S. Taniguchi, Isothermal Oxidation Behavior of Ru Modified Aluminide Coating on a Fourth Generation Single Crystal Superalloy, Materials Science Forum 512 (2006) 111–116. https://doi.org/10.4028/www.scientific.net/MSF.512.111.

[140] Y. Huang, X. Peng, The promoted formation of an α-Al2O3 scale on a nickel aluminide with surface Cr2O3 particles, Corros Sci 112 (2016) 226–232. https://doi.org/10.1016/j.corsci.2016.07.029.

[141] W. Zhao, Z. Li, B. Gleeson, A New Kinetics-Based Approach to Quantifying the Extent of Metastable → Stable Phase Transformation in Thermally-Grown Al2O3 Scales, Oxidation of Metals 79 (2013) 361–381. https://doi.org/10.1007/s11085-013-9365-3.

[142] D.M. Lipkin, D.R. Clarke, M. Hollatz, M. Bobeth, W. Pompe, Stress development in alumina scales formed upon oxidation of (111) NiAl single crystals, Corros Sci 39 (1997) 231–242. https://doi.org/10.1016/S0010-938X(97)83344-6.

[143] X. Peng, T. Li, W.P. Pan, Oxidation of a La2O3-modified aluminide coating, Scr Mater 44 (2001) 1033–1038. https://doi.org/10.1016/S1359-6462(01)00666-2.

[144] M. Bai, B. Song, L. Reddy, T. Hussain, Preparation of MCrAlY–Al2O3 Composite Coatings with Enhanced Oxidation Resistance through a Novel Powder Manufacturing Process, Journal

of Thermal Spray Technology 28 (2019) 433–443. https://doi.org/10.1007/s11666-019-00830-y.

[145] A. Khan, Y. Huang, Z. Dong, X. Peng, Effect of Cr2O3 nanoparticle dispersions on oxidation kinetics and phase transformation of thermally grown alumina on a nickel aluminide coating, Corros Sci 150 (2019) 91–99. https://doi.org/10.1016/j.corsci.2019.01.032.

[146] A. Khan, A. Rauf, S. Ullah, H.U. Jan, T. Aziz, S.H. Zhang, G.S. Song, ZrO2-nanoparticle assisted phase transformation and oxidation kinetics of thermally grown alumina on nickel aluminide coatings, Surf Coat Technol 470 (2023) 129852. https://doi.org/10.1016/j.surfcoat.2023.129852.

[147] Y.B. Zhou, H.J. Zhang, Preparation and oxidation of an Al2O3-modified aluminide coating, Vacuum 86 (2012) 1353–1357. https://doi.org/10.1016/j.vacuum.2011.12.024.

[148] M. Zagula-Yavorska, J. Morgiel, J. Romanowska, J. Sieniawski, Nanoparticles in zirconium-doped aluminide coatings, Mater Lett 139 (2015) 50–54. https://doi.org/10.1016/j.matlet.2014.09.128.

[149] J. Romanowska, J. Morgiel, M. Zagula-Yavorska, J. Sieniawski, Nanoparticles in hafnium-doped aluminide coatings, Mater Lett 145 (2015) 162–166. https://doi.org/10.1016/j.matlet.2015.01.089.

[150] L. Qian, F. Xu, K.T. Voisey, V. Nekouie, Z. Zhou, V. V. Silberschmidt, X. Hou, Incorporation and evolution of ZrO2 nano-particles in Pt-modified aluminide coating for high temperature applications, Surf Coat Technol 311 (2017) 238–247. https://doi.org/10.1016/j.surfcoat.2016.12.106.

[151] X. Peng, Y. Guan, Z. Dong, C. Xu, F. Wang, A fundamental aspect of the growth process of alumina scale on a metal with dispersion of CeO2 nanoparticles, Corros Sci 53 (2011) 1954–1959. https://doi.org/10.1016/j.corsci.2011.02.014.

[152] X. Tan, X. Peng, F. Wang, The mechanism for self-formation of a CeO2 diffusion barrier layer in an aluminide coating at high temperature, Surf Coat Technol 224 (2013) 62–70. https://doi.org/10.1016/j.surfcoat.2013.03.003.

[153] X. Zhao, C. Zhou, Effect of Y2O3 content in the pack on microstructure and hot corrosion resistance of Y–Co-modified aluminide coating, Corros Sci 86 (2014) 223–230. https://doi.org/10.1016/j.corsci.2014.05.018.

[154] C. Choux, A.J. Kulińska, S. Chevalier, High temperature reactivity of nickel aluminide diffusion coatings, Intermetallics (Barking) 16 (2008) 1–9. https://doi.org/10.1016/j.intermet.2007.07.014.

[155] C. Rao, D. Trivedi, Chemical and electrochemical depositions of platinum group metals and their applications, Coord Chem Rev 249 (2005) 613–631. https://doi.org/10.1016/j.ccr.2004.08.015.

[156] Y.D. Gamburg, Zangari G, Theory and Practice of Metal Electrodeposition, Springer, 2011.

[157] C.-D. Gu, T.-Y. Zhang, Electroplating, in: Q.J. Wang, C Y W (Eds.), Encyclopedia of Tribology, Springer, 2013: pp. 946–951.

[158] M.E. Baumgärtner, J. Raub, The Electrodeposition of Platinum and Platinum Alloys, Platin Met Rev 32 (1988) 188–197. https://doi.org/10.1595/003214088X324188197.

[159] R. Le Penven, W. Levason, D. Pletcher, Studies of platinum electroplating baths Part I: The chemistry of a platinum tetrammine bath, J Appl Electrochem 22 (1992) 415–420. https://doi.org/10.1007/BF01077542.

[160] S.J. Hemsley, W. Zhou, Platinum plating for turbine blades: technology development and process improvement, Transactions of the IMF 88 (2010) 11–16. https://doi.org/10.1179/174591909X12614816487692.

[161] Johnson Matthey Materials Technology, European Patent 358 375, 1989.

[162] W.J. Basirun, D. Pletcher, A. Saraby-Reintjes, Studies of platinum electroplating baths Part IV: Deposits on copper from Q bath, J Appl Electrochem 26 (1996) 873–880. https://doi.org/10.1007/BF00683750.

[163] W.J. Basirun, D. Pletcher, Studies of platinum electroplating baths Part VI: Influence of some experimental parameters on deposit quality, J Appl Electrochem 28 (1997) 167–172. https://doi.org/10.1023/A:1003278608576.

[164] A. Brenner, G.E. Riddel, Nickel Plating on Steel by Chemical Reduction, Journal of Research of Natural Bureau Standards 37 (1946) 31–34.

[165] C.R. Shipley, Historical Highlights of Electroless Plating, Plating and Surface Finishing 71 (1984) 92–99.

[166] G.O. Mallory, J.B. Hajdu, Electroless Plating: Fundamentals And Applications, American Electroplaters and Surface Finishers Society, 1990.

[167] J. Sudagar, J. Lian, W. Sha, Electroless nickel, alloy, composite and nano coatings - A critical review, J Alloys Compd 571 (2013) 183–204. https://doi.org/10.1016/j.jallcom.2013.03.107.

[168] E.J. O'Sullivan, Fundamental and Practical Aspects of the Electroless Deposition Reaction, in: R.C. Alkire, D.M. Kolb (Eds.), Advances in Electrochemical Science and Engineering, Wiley-VCH, 2002: pp. 225–270.

[169] L. Das, D.-T. Chin, Effect of Bath Stabilizers On Electroless Nickel Deposition on Ferrous Substrates, Plating and Surface Finishing 83 (1996) 55–61.

[170] H. Keping, J.L. Fang, Stabilization effect of electroless nickel plating by thiourea, Metal Finishing 95 (1997) 73–75. https://doi.org/10.1016/S0026-0576(97)81818-1.

[171] V. Genova, L. Paglia, G. Pulci, G. Pedrizzetti, A. Pranzetti, M. Romanelli, F. Marra, Medium and High Phosphorous Ni-P Coatings Obtained via an Electroless Approach: Optimization of Solution Formulation and Characterization of Coatings, Coatings 13 (2023). https://doi.org/10.3390/coatings13091490.

[172] N. V. Sotskaya, The Role of Organic Additives in the Electroless Nickel Plating Bath, Protection of Metals 39 (2003) 245–249. https://doi.org/10.1023/A:1023915103849.

[173] M. Paunovic, M. Schleisinger, Electroless Deposition, in: Fundamentals of Electrochemical Deposition, 2nd ed., John Wiley & Sons, 2006: pp. 139–165.

[174] I. Ohno, Electrochemistry of electroless plating, Materials Science and Engineering: A 146 (1991) 33–49. https://doi.org/10.1016/0921-5093(91)90266-P.

[175] A. Brenner, G.E. Riddel, Deposition of Nickel and Cobalt by Chemical Reduction, Journal of Research of Natural Bureau Standards 39 (1947) 385–395.

[176] G. Gutzeit, Industrial Nickel Coating by Chemical Catalytic Reduction, Transactions of the IMF 33 (1955) 383–423. https://doi.org/10.1080/00202967.1955.11869708.

[177] R.M. Lukes, The chemistry of the autocatalytic reduction of copper by alkaline formaldehyde, Plating 5 (1964).

[178] G. Salvago, P.L. Cavallotti, Characteristics of the chemical reduction of Ni alloys with hypophosphite, Plating 59 (1972).

[179] J.-P. Rondin, H.E. Hintermann, A Calorimetric Study of the Electroless Deposition of Nickel, J Electrochem Soc 117 (1970) 160. https://doi.org/10.1149/1.2408405.

[180] J.E.A.M. Van Den Meerakker, On the mechanism of electroless plating. II. One mechanism for different reductants, J Appl Electrochem 11 (1981) 395–400. https://doi.org/10.1007/BF00613960.

[181] N.K. Kim, S.M. Kang, T. Kim, S. Kim, G.H. Kim, Electroless Plating on Polymer Surfaces: Comprehensive Review of Mechanism, Process, Analysis, and Future Applications, Adv Mater Interfaces (2025). https://doi.org/10.1002/admi.202400931.

[182] R. Saxena, M. De, Enhanced performance of supported Pd-Pt bimetallic catalysts prepared by modified electroless deposition for butane dehydrogenation, Appl Catal A Gen 610 (2021) 117933. https://doi.org/10.1016/j.apcata.2020.117933.

[183] P. Bindra, A. Hazra, Electroless deposition of Pd/Pt nanoparticles on electrochemically grown TiO_2 nanotubes for ppb level sensing of ethanol at room temperature, Analyst 146 (2021) 1880–1891. https://doi.org/10.1039/D0AN01757D.

[184] G. Zhu, C. Zhang, C. Zhang, Y. Yi, Electroless deposition of platinum on graphdiyne for electrochemical sensing, Chemical Engineering Journal 497 (2024) 154512. https://doi.org/10.1016/j.cej.2024.154512.

[185] Q. Cheng, C. Hu, G. Wang, Z. Zou, H. Yang, L. Dai, Carbon-Defect-Driven Electroless Deposition of Pt Atomic Clusters for Highly Efficient Hydrogen Evolution, J Am Chem Soc 142 (2020) 5594–5601. https://doi.org/10.1021/jacs.9b11524.

[186] J.S. Park, J.M. Kinsella, D.D. Jandial, S.B. Howell, M.J. Sailor, Cisplatin-Loaded Porous Si Microparticles Capped by Electroless Deposition of Platinum, Small 7 (2011) 2061–2069. https://doi.org/10.1002/smll.201100438.

[187] R.N. Rhoda, R.F. Vines, Bath and process for platinum and platinum alloys, US Patent 3,486,928, 1969.

[188] P. Steinmetz, S. Alperine, A. Friant-Costantini, P. Josso, Electroless deposition of pure nickel, palladium and platinum, Surf Coat Technol 43–44 (1990) 500–510. https://doi.org/10.1016/0257-8972(90)90101-H.

[189] F.H. Leaman, Method and composition of platinum plating, US Patent 3,698,939, 1972.

[190] B. Kong, V. Ivanov, Z.-W. Sun, J. Tong, Electroless deposition of platinum on copper, US 2013/0340648 A1, 2013.

[191] C.W. Walter, F.H. Leaman, Method and composition for platinum plating and articles plated therewith, US Patent 3,562,911, 1971.

[192] C.R.K. Rao, M. Pushpavanam, Electroless deposition of platinum on titanium substrates, Mater Chem Phys 68 (2001) 62–65. https://doi.org/10.1016/S0254-0584(00)00268-6.

[193] R.K. Paul, H.-D. Jang, B.-T. Lee, Fabrication of platinum coating on continuous porous SiC–Si3N4 composites by the electroless deposition process, J Mater Process Technol 209 (2009) 2958–2962. https://doi.org/10.1016/j.jmatprotec.2008.07.002.

[194] J. Strejcek, Ger. Offen. DE 2607988, 1977.

[195] A.S. Koslov, T. Palanisamy, D. Narasimhan, Electroless autocatalytic platinum plating, US Patent 6,391,477 B1, 2002.

[196] T. Kato, Watanabe H, Electroless Platinum Plating Solution, EP 3 363 928 A1, 2018.

[197] T. Sasamura, K. Tanabe, H. Okubo, T. Someya, E. Furuya, Electroless Platinum Plating Bath, US Patent 2019/0309423 A1, 2019.

[198] S.S. Alarfaji, S. Hussain, M. Arshed, S.H. Talib, T.U. Rahman, A. Rauf, I.U. Khan, Electroless platinum and palladium deposition over alumina coated stainless steel plates and their catalytic activity for hydrogen mitigation in severe nuclear accidents, Int J Hydrogen Energy 47 (2022) 36843–36849. https://doi.org/10.1016/j.ijhydene.2022.08.260.

[199] K. Shibata, U. Kamimura, Electroless Platinum Plating Solution and Platinum Film Obtained Using Same, US 2020/0157686 A1, 2020.

[200] L. Tamasauskaite-Tamasiunaite, Y. Dordi, E. Norkus, I. Stankeviciene, A. Jagminiene, A. Naujokaitis, L. Tumonis, V. Buzas, L. Maciulis, Electroless Platinum Deposition Using Co3+/Co2+ Redox Couple as a Reducing Agent, Materials 14 (2021) 1893. https://doi.org/10.3390/ma14081893.

[201] E.W. Ross, K.S. O'Hara, René N4: a first generation single crystal turbine airfoil alloy with improved oxidation resistance, low angle grain boundary strength and superior long time rupture strength, Superalloys (1996).

[202] J. Wang, X. Bai, X. Shen, X. Liu, B. Wang, Effect of micro-texture on substrate surface on adhesion performance of electroless Ni–P coating, J Manuf Process 74 (2022) 296–307. https://doi.org/10.1016/j.jmapro.2021.12.025.

[203] G. Pedrizzetti, Electroless deposition of metals for high temperature applications, Sapienza University of Rome, 2020.

[204] G. Saji, "Long-Cell Action" Corrosion: A Basic Mechanism Hidden Behind Components Degradation Issues in Nuclear Power Plants, in: Volume 1: Plant Operations, Maintenance and Life Cycle; Component Reliability and Materials Issues; Codes, Standards, Licensing and Regulatory Issues; Fuel Cycle and High Level Waste Management, ASMEDC, 2006: pp. 495–511. https://doi.org/10.1115/ICONE14-89350.

[205] Thermo Scientific Chemicals, "Ethylenediaminetetraacetic acid disodium salt dihydrate" - Product Information, n.d.

[206] J. Liu, K. Li, H. Wang, M. Zhu, H. Xu, H. Yan, Self-assembly of hydroxyapatite nanostructures by microwave irradiation, Nanotechnology 16 (2005) 82–87. https://doi.org/10.1088/0957-4484/16/1/017.

[207] D.H. Busch, J.C. Bailar, The Stereochemistry of Complex Inorganic Compounds. XX. The Tetradentate and Bidentate Complexes of Ethylenediaminetetraacetic Acid, J Am Chem Soc 78 (1956) 716–719.

[208] K. Kakehi, F.H. Latief, T. Sato, Influence of primary and secondary orientations on creep rupture behavior of aluminized single crystal Ni-based superalloy, Materials Science and Engineering A 604 (2014) 148–155. https://doi.org/10.1016/j.msea.2014.02.079.

[209] C.M.F. Rae, M.S. Hook, R.C. Reed, The effect of TCP morphology on the development of aluminide coated superalloys, Materials Science and Engineering A 396 (2005) 231–239. https://doi.org/10.1016/j.msea.2005.01.005.

[210] V. Genova, L. Paglia, F. Marra, C. Bartuli, G. Pulci, Pure thick nickel coating obtained by electroless plating: Surface characterization and wetting properties, Surf Coat Technol 357 (2019) 595–603. https://doi.org/10.1016/j.surfcoat.2018.10.049.

[211] S. Novak, M. Kalin, The effect of pH on the wear of water-lubricated alumina and zirconia ceramics, Tribol Lett 17 (2004) 727–732. https://doi.org/10.1007/s11249-004-8080-2.

[212] M.-D. Ger, B.J. Hwang, Effect of surfactants on codeposition of PTFE particles with electroless Ni-P coating, Mater Chem Phys 76 (2002) 38–45. https://doi.org/10.1016/S0254-0584(01)00513-2.

[213] G. Pedrizzetti, L. Paglia, V. Genova, S. Cinotti, M. Bellacci, F. Marra, G. Pulci, Microstructural, mechanical and corrosion characterization of electroless Ni-P composite coatings modified with ZrO2 reinforcing nanoparticles, Surf Coat Technol 473 (2023). https://doi.org/10.1016/j.surfcoat.2023.129981.

[214] D.L. Sahagian, A.A. Proussevitch, 3D particle size distributions from 2D observations: stereology for natural applications, Journal of Volcanology and Geothermal Research 84 (1998) 173–196. https://doi.org/10.1016/S0377-0273(98)00043-2.

[215] Y.D. He, H.F. Fu, X.G. Li, W. Gao, Microstructure and properties of mechanical attrition enhanced electroless Ni–P plating on magnesium alloy, Scr Mater 58 (2008) 504–507. https://doi.org/10.1016/j.scriptamat.2007.10.051.

[216] K. Pawar, P. Dixit, A critical review of copper electroless deposition on glass substrates for microsystems packaging applications, Surface Engineering 38 (2022) 576–617. https://doi.org/10.1080/02670844.2022.2142002.

[217] G.R. Stafford, S. Ambrozik, U. Bertocci, Y. Liu, M.C. Lafouresse, T.P. Moffat, In Situ stress Measurements during Strained-Layer Electrodeposition, ECS Meeting Abstracts MA2018-02 (2018) 800–800. https://doi.org/10.1149/MA2018-02/22/800.

[218] N. Pangarov, R. Pangarova, Stress in electrodeposited metals general thermodynamic theory, J Electroanal Chem Interfacial Electrochem 91 (1978) 173–188. https://doi.org/10.1016/S0022-0728(78)80098-9.

[219] Y. Jin, H. Yu, D. Yu, D. Sun, Effects of complexing agents on acidic electroless nickel deposition, Rare Metals 29 (2010) 401–406. https://doi.org/10.1007/s12598-010-0138-8.

[220] Y.S. Huang, F.Z. Cui, Effect of complexing agent on the morphology and microstructure of electroless deposited Ni-P alloy, Surf Coat Technol 201 (2007) 5416–5418. https://doi.org/10.1016/j.surfcoat.2006.07.189.

[221] H. Honma, T. Kobayashi, Electroless Copper Deposition Process Using Glyoxylic Acid as a Reducing Agent, J Electrochem Soc 141 (1994) 730–733. https://doi.org/10.1149/1.2054800.

[222] A. Salicio-Paz, I. Ugarte, J. Sort, E. Pellicer, E. García-Lecina, Full optimization of an electroless nickel solution: Boosting the performance of low-phosphorous coatings, Materials 14 (2021). https://doi.org/10.3390/ma14061501.

[223] S. Karthikeyan, B. Ramamoorthy, Effect of reducing agent and nano Al2O3 particles on the properties of electroless Ni-P coating, Appl Surf Sci 307 (2014) 654–660. https://doi.org/10.1016/j.apsusc.2014.04.092.

[224] S.S. Djokić, Electroless Deposition of Cobalt Using Hydrazine as a Reducing Agent, J Electrochem Soc 144 (1997) 2358–2363. https://doi.org/10.1149/1.1837818.

[225] M. Anik, E. Körpe, E. Şen, Effect of coating bath composition on the properties of electroless nickel–boron films, Surf Coat Technol 202 (2008) 1718–1727. https://doi.org/10.1016/j.surfcoat.2007.07.031.

[226] A.Y. Gerard, E.J. Kautz, D.K. Schreiber, J. Han, S. McDonnell, K. Ogle, P. Lu, J.E. Saal, G.S. Frankel, J.R. Scully, The role of chromium content in aqueous passivation of a non-equiatomic Ni38Fe20CrxMn21-0.5xCo21-0.5x multi-principal element alloy (x = 22, 14, 10, 6 at%) in acidic chloride solution, Acta Mater 245 (2023) 118607. https://doi.org/10.1016/j.actamat.2022.118607.

[227] H. Mu, J. Seok, R.Y. Lin, Nickel Thin Film Coatings on Steels with Electroless Plating and Sputter Deposition, J Electrochem Soc 150 (2003) C67. https://doi.org/10.1149/1.1534711.

[228] P. Moretto, J. Bressers, D.J. Arrell, Evolution of a PtAl2 coating on the nickel-base alloy CMSX-6 subjected to thermo-mechanical fatigue, Materials Science and Engineering: A 272 (1999) 310–320. https://doi.org/10.1016/S0921-5093(99)00506-7.

[229] M. Watanabe, D.R. Mumm, S. Chiras, A.G. Evans, Measurement of the residual stress in a Pt–aluminide bond coat, Scr Mater 46 (2002) 67–70. https://doi.org/10.1016/S1359-6462(01)01198-8.

[230] P.T. Moseley, K.R. Hyde, B.A. Bellamy, G. Tappin, The microstructure of the scale formed during the high temperature oxidation of a fecralloy steel, Corros Sci 24 (1984) 547–565. https://doi.org/10.1016/0010-938X(84)90036-2.

[231] J. Angenete, K. Stiller, V. Langer, Oxidation of Simple and Pt-Modified Aluminide Diffusion Coatings on Ni-Base Superalloys—I. Oxide Scale Microstructure, Oxidation of Metals 60 (2003) 47–82. https://doi.org/10.1023/A:1024665229656.

[232] D. Serafin, W.J. Nowak, B. Wierzba, The calculation of the diffusion coefficients in ternary multiphase Ti-NiAl system, Comput Mater Sci 165 (2019) 1–6. https://doi.org/10.1016/j.commatsci.2019.04.019.

[233] S. Mazumder, M. V. Pantawane, N.B. Dahotre, Influence of high heating rates on evolution of oxides on directed laser energy additively fabricated IN718, Npj Mater Degrad 5 (2021) 45. https://doi.org/10.1038/s41529-021-00193-2.

[234] V. Genova, L. Paglia, G. Pulci, C. Bartuli, F. Marra, Diffusion aluminide coatings for hot corrosion and oxidation protection of nickel-based superalloys: Effect of fluoride-based activator salts, Coatings 11 (2021). https://doi.org/10.3390/coatings11040412.

[235] B. Bouchaud, B. Rannou, F. Pedraza, Slurry aluminizing mechanisms of Ni-based superalloys incorporating an electrosynthesized ceria diffusion barrier, Mater Chem Phys 143 (2013) 416–424. https://doi.org/10.1016/j.matchemphys.2013.09.022.

[236] M.S.A. Karunaratne, R.C. Reed, Interdiffusion of the platinum-group metals in nickel at elevated temperatures, Acta Mater 51 (2003) 2905–2919. https://doi.org/10.1016/S1359-6454(03)00105-8.

[237] A. Chien, D. Gan, P. Shen, Microstructures of two-stage aluminized coatings on Inconel 600, Materials Science and Engineering: A 206 (1996) 215–224. https://doi.org/10.1016/0921-5093(95)09899-2.

[238] J. Benoist, T. Girardeau, P. Goudeau, K.F. Badawi, A. Traverse, Study by complementary X-ray techniques of in-depth microstructure in Ni-based superalloys after Pt diffusion treatment, Surf Coat Technol 161 (2002) 200–209. https://doi.org/10.1016/S0257-8972(02)00559-5.

[239] J. Angenete, K. Stiller, A comparative study of two inward grown Pt modified Al diffusion coatings on a single crystal Ni base superalloy, Materials Science and Engineering: A 316 (2001) 182–194. https://doi.org/10.1016/S0921-5093(01)01236-9.

[240] S.P. Garg, G.B. Kale, R.V. Patil, T. Kundu, Thermodynamic interdiffusion coefficient in binary systems with intermediate phases, Intermetallics (Barking) 7 (1999) 901–908. https://doi.org/10.1016/S0966-9795(98)00139-3.

[241] M. Bai, Fabrication and characterization of thermal barrier coatings, 2015.

[242] E. Pauletti, A.S.C.M. d'Oliveira, Influence of Pt concentration on structure of aluminized coatings on a Ni base superalloy, Surf Coat Technol 332 (2017) 57–63. https://doi.org/10.1016/j.surfcoat.2017.10.052.

[243] F. Lang, T. Narita, Improvement in oxidation resistance of a Ni3Al-based superalloy IC6 by rhenium-based diffusion barrier coatings, Intermetallics (Barking) 15 (2007) 599–606. https://doi.org/10.1016/j.intermet.2006.10.042.

[244] Y. Wu, X.W. Li, G.M. Song, Y.M. Wang, T. Narita, Improvement of the Oxidation Resistance of the Single-Crystal Ni-Based TMS-82+ Superalloy by Ni–Al Coatings with/without the

Diffusion Barrier, Oxidation of Metals 74 (2010) 287–303. https://doi.org/10.1007/s11085-010-9211-9.

[245] Y. Wang, H. Guo, H. Peng, L. Peng, S. Gong, Diffusion barrier behaviors of (Ru,Ni)Al/NiAl coatings on Ni-based superalloy substrate, Intermetallics (Barking) 19 (2011) 191–195. https://doi.org/10.1016/j.intermet.2010.08.016.

[246] L. Zhu, S. Zhu, F. Wang, Preparation and oxidation behaviour of nanocrystalline Ni+CrAlYSiN composite coating with AlN diffusion barrier on Ni-based superalloy K417, Corros Sci 60 (2012) 265–274. https://doi.org/10.1016/j.corsci.2012.03.027.

[247] J. Müller, M. Schierling, E. Zimmermann, D. Neuschütz, Chemical vapor deposition of smooth α-Al2O3 films on nickel base superalloys as diffusion barriers, Surf Coat Technol 120–121 (1999) 16–21. https://doi.org/10.1016/S0257-8972(99)00333-3.

[248] Y. Qiao, T. Chen, X. Guo, Diffusion barrier effect of Al2O3 layer at the interface between Mo-Si-B- coating and Nb-Si based alloy, Corrosion Communications (2022). https://doi.org/10.1016/j.corcom.2021.10.003.

[249] M. Masoumi Balashadehi, P. Nourpour, A. Sabour Rouh Aghdam, M.H. Allahyarzadeh, A. Heydarzadeh, M. Hamdi, The formation, microstructure and hot corrosion behaviour of slurry aluminide coating modified by Ni/Ni-Co electrodeposited layer on Ni-base superalloy, Surf Coat Technol 402 (2020). https://doi.org/10.1016/j.surfcoat.2020.126283.

[250] A. Zakeri, M.R. Masoumi Balashadehi, A. Sabour Rouh Aghdam, Development of hybrid electrodeposition/slurry diffusion aluminide coatings on Ni-based superalloy with enhanced hot corrosion resistance, Journal of Composites and Compounds 2 (2021) 1–8. https://doi.org/10.52547/jcc.3.1.1.

[251] D.H. Boone, P. Deb, L.I. Purvis, D. V. Rigney, Surface morphology of platinum modified aluminide coatings, Journal of Vacuum Science & Technology A: Vacuum, Surfaces, and Films 3 (1985) 2557–2563. https://doi.org/10.1116/1.572833.

[252] P. Audigié, A. Rouaix-Vande Put, A. Malié, D. Monceau, High-temperature cyclic oxidation behaviour of Pt-rich γ-γ' coatings. Part I: Oxidation kinetics of coated AM1 systems after very long-term exposure at 1100 °C, Corros Sci 144 (2018) 127–135. https://doi.org/10.1016/j.corsci.2018.08.050.

[253] P. Audigié, A. Vande Put, B. Malard, A. Malié, D. Monceau, Analysis of void formation in Pt-rich γ-γ' bond-coatings for TBC system application, Corros Sci 249 (2025) 112785. https://doi.org/10.1016/j.corsci.2025.112785.

[254] P. Audigié, A. Rouaix-Vande Put, A. Malié, P. Bilhé, S. Hamadi, D. Monceau, Observation and modeling of α-NiPtAl and Kirkendall void formations during interdiffusion of a Pt coating

with a γ-(Ni-13Al) alloy at high temperature, Surf Coat Technol 260 (2014) 9–16. https://doi.org/10.1016/j.surfcoat.2014.08.083.

[255] D. Texier, D. Monceau, S. Selezneff, A. Longuet, E. Andrieu, High Temperature Micromechanical Behavior of a Pt-Modified Nickel Aluminide Bond-Coating and of Its Interdiffusion Zone with the Superalloy Substrate, Metallurgical and Materials Transactions A 51 (2020) 1475–1480. https://doi.org/10.1007/s11661-020-05634-2.

[256] M. Taylor, H. Evans, E. Busso, Z. Qian, Creep properties of a Pt–aluminide coating, Acta Mater 54 (2006) 3241–3252. https://doi.org/10.1016/j.actamat.2006.03.010.

[257] O. Franke, K. Durst, M. Göken, Microstructure and local mechanical properties of Pt-modified nickel aluminides on nickel-base superalloys after thermo-mechanical fatigue, Materials Science and Engineering: A 467 (2007) 15–23. https://doi.org/10.1016/j.msea.2007.02.069.

[258] F. Grube, E. Affeldt, H. Mughrabi, Thermomechanical Fatigue Behavior of an Aluminide-Coated Monocrystalline Ni-Base Superalloy, in: Thermomechanical Fatigue Behavior of Materials: 4th Volume, ASTM International100 Barr Harbor Drive, PO Box C700, West Conshohocken, PA 19428-2959, 2003: pp. 164–179. https://doi.org/10.1520/STP11433S.

[259] X. Montero, M.C. Galetz, M. Schütze, Slurry coated Ni-plated Fe-base alloys: Investigation of the influence of powder and substrate composition on interdiffusional and structural degradation of aluminides, Surf Coat Technol 236 (2013) 465–475. https://doi.org/10.1016/j.surfcoat.2013.10.038.

[260] S. Sarraf, S. Rastegari, M. Soltanieh, Deposition of a low-activity type cobalt-modified aluminide coating by slurry aluminizing of a pre-Co-electroplated Ni-based superalloy (IN738LC), Journal of Materials Research and Technology 30 (2024) 1183–1193. https://doi.org/10.1016/j.jmrt.2024.03.132.

[261] J.M. Brossard, B. Panicaud, J. Balmain, G. Bonnet, Modelling of aluminized coating growth on nickel, Acta Mater 55 (2007) 6586–6595. https://doi.org/10.1016/j.actamat.2007.08.025.

[262] B. Rannou, M. Mollard, B. Bouchaud, J. Balmain, G. Bonnet, V. Kolarik, F. Pedraza-Diaz, On the Influence of a Heat Treat for an Aluminizing Progress Based on Al Microparticles Slurry for Model Ni and Ni20Cr. Experimental and Theoretical Approaches., Defect and Diffusion Forum 323–325 (2012) 373–379. https://doi.org/10.4028/www.scientific.net/DDF.323-325.373.

[263] S. Frank, S.V. Divinski, U. Södervall, C. Herzig, Ni tracer diffusion in the B2-compound NiAl: influence of temperature and composition, Acta Mater 49 (2001) 1399–1411. https://doi.org/10.1016/S1359-6454(01)00037-4.

[264] S. V. Divinski, C. Herzig, Ni Tracer Self-Diffusion, Interdiffusion and Diffusion Mechanisms in NiAl, Defect and Diffusion Forum 203–205 (2002) 177–192. https://doi.org/10.4028/www.scientific.net/DDF.203-205.177.

[265] A. Paul, A.A. Kodentsov, F.J.J. Van Loo, On diffusion in the β-NiAl phase, J Alloys Compd 403 (2005) 147–153. https://doi.org/10.1016/j.jallcom.2005.04.194.

[266] B.A. Pint, P.F. Tortorelli, I.G. Wright, The Oxidation behavior of ODS iron aluminides, Materials and Corrosion 47 (1996) 663–674. https://doi.org/10.1002/maco.19960471202.

[267] V.K. Tolpygo, D.R. Clarke, Surface rumpling of a (Ni, Pt)Al bond coat induced by cyclic oxidation, Acta Mater 48 (2000) 3283–3293. https://doi.org/10.1016/S1359-6454(00)00156-7.

[268] V.K. Tolpygo, D.R. Clarke, Rumpling of CVD (Ni,Pt)Al diffusion coatings under intermediate temperature cycling, Surf Coat Technol 203 (2009) 3278–3285. https://doi.org/10.1016/j.surfcoat.2009.04.016.

[269] M. Islam, M.R. Azhar, N. Fredj, T.D. Burleigh, O.R. Oloyede, A.A. Almajid, S. Ismat Shah, Influence of SiO2 nanoparticles on hardness and corrosion resistance of electroless Ni-P coatings, Surf Coat Technol 261 (2015) 141–148. https://doi.org/10.1016/j.surfcoat.2014.11.044.

[270] S.M.A. Shibli, K.S. Chinchu, M.A. Sha, Development of Nano-tetragonal Zirconia-Incorporated Ni–P Coatings for High Corrosion Resistance, Acta Metallurgica Sinica (English Letters) 32 (2019) 481–494. https://doi.org/10.1007/s40195-018-0823-4.

[271] M. Khodaei, A.M. Gholizadeh, SiC nanoparticles incorporation in electroless NiP-Graphene oxide nanocomposite coatings, Ceram Int 47 (2021) 25287–25295. https://doi.org/10.1016/j.ceramint.2021.05.250.

[272] S.S. Djokić, N.S. Djokić, Electroless Deposition of Metallic Powders, J Electrochem Soc 158 (2011) D204. https://doi.org/10.1149/1.3548097.

[273] M.H. Sliem, K. Shahzad, V.N. Sivaprasad, R.A. Shakoor, A.M. Abdullah, O. Fayyaz, R. Kahraman, M.A. Umer, Enhanced mechanical and corrosion protection properties of pulse electrodeposited NiP-ZrO2 nanocomposite coatings, Surf Coat Technol 403 (2020). https://doi.org/10.1016/j.surfcoat.2020.126340.

[274] M. Sarret, C. Müller, A. Amell, Electroless NiP micro- and nano-composite coatings, Surf Coat Technol 201 (2006) 389–395. https://doi.org/10.1016/j.surfcoat.2005.11.127.

[275] C. Zhao, Y. Yao, Preparation and mechanical properties of electroless nickel-phosphorus-tungsten carbide nanocomposite coatings, J Mater Eng Perform 23 (2014) 193–197. https://doi.org/10.1007/s11665-013-0753-2.

[276] K. Czapczyk, P. Zawadzki, N. Wierzbicka, R. Talar, Microstructure and properties of electroless ni-p/si3n4 nanocomposite coatings deposited on the aw-7075 aluminum alloy, Materials 14 (2021). https://doi.org/10.3390/ma14164487.

[277] S.A.Abde. l Gawad, A.M. Baraka, M.S. Morsi, M.S.A. Eltoum, Development of Electroless Ni-P-Al2O3 and Ni-P-TiO2 Composite Coatings from Alkaline Hypophosphite Gluconate Baths and their Properties, Int J Electrochem Sci 8 (2013) 1722–1734. https://doi.org/10.1016/S1452-3981(23)14260-X.

[278] Y. He, S. Zhang, Y. He, R. Song, Z. Zhang, B. Liu, H. Li, J. Shangguan, Effects of yttrium-stabilized zirconia (different yttrium content) doping on the structure, corrosion resistance and wear resistance of Ni-P electroless coating, Colloids Surf A Physicochem Eng Asp 654 (2022). https://doi.org/10.1016/j.colsurfa.2022.130059.

[279] E.M. Fayyad, M.K. Hassan, K. Rasool, K.A. Mahmoud, A.M.A. Mohamed, G. Jarjoura, Z. Farhat, A.M. Abdullah, Novel electroless deposited corrosion — resistant and anti-bacterial NiP–TiNi nanocomposite coatings, Surf Coat Technol 369 (2019) 323–333. https://doi.org/10.1016/j.surfcoat.2019.04.064.

[280] A. Grosjean, M. Rezrazi, P. Bercot, M. Tachez, Adaptation of a mathematical model to the incorporation of silicon carbide particles in an electroless nickel deposit, Metal Finishing 96 (1998) 14–17. https://doi.org/10.1016/S0026-0576(97)86615-9.

[281] W. Chen, W. Gao, Microstructures and properties of sol-enhanced nanostructured metal-oxide composite coatings, Progress in Natural Science: Materials International 21 (2011) 355–362. https://doi.org/10.1016/S1002-0071(12)60069-0.

[282] K.H. Hou, M.D. Ger, L.M. Wang, S.T. Ke, The wear behaviour of electro-codeposited Ni–SiC composites, Wear 253 (2002) 994–1003. https://doi.org/10.1016/S0043-1648(02)00222-3.

[283] M. Der Ger, Electrochemical deposition of nickel/SiC composites in the presence of surfactants, Mater Chem Phys 87 (2004) 67–74. https://doi.org/10.1016/j.matchemphys.2004.04.022.

[284] D. Ahmadkhaniha, C. Zanella, The effects of additives, particles load and current density on codeposition of SiC particles in NiP nanocomposite coatings, Coatings 9 (2019). https://doi.org/10.3390/coatings9090554.

[285] M. Sheng, Y. Wang, Q. Zhong, H. Wu, Q. Zhou, H. Lin, The effects of nano-SiO2 additive on the zinc phosphating of carbon steel, Surf Coat Technol 205 (2011) 3455–3460. https://doi.org/10.1016/j.surfcoat.2010.12.011.

[286] Z.A. Hamid, S.A. El Badry, A.A. Aal, Electroless deposition and characterization of Ni-P-WC composite alloys, Surf Coat Technol 201 (2007) 5948–5953. https://doi.org/10.1016/j.surfcoat.2006.11.001.

[287] V. Medelien, The influence of B4C and SiC additions on the morphological, physical, chemical and corrosion properties of Ni coatings, Surf Coat Technol 154 (2002) 104–111. https://doi.org/10.1016/S0257-8972(01)01703-0.

[288] A.L. Purvis, B.M. Warnes, A study of the diffusional response of refractory and other elements in superalloy systems during diffusion coating, Surf Coat Technol 133–134 (2000) 23–27. https://doi.org/10.1016/S0257-8972(00)00890-2.

[289] J.A. Haynes, B.A. Pint, Y. Zhang, I.G. Wright, Comparison of the cyclic oxidation behavior of β-NiAl, β-NiPtAl and γ–γ′ NiPtAl coatings on various superalloys, Surf Coat Technol 202 (2007) 730–734. https://doi.org/10.1016/j.surfcoat.2007.06.039.

[290] T. Izumi, N. Mu, L. Zhang, B. Gleeson, Effects of targeted γ-Ni+γ′-Ni3Al-based coating compositions on oxidation behavior, Surf Coat Technol 202 (2007) 628–631. https://doi.org/10.1016/j.surfcoat.2007.08.014.

[291] Y. Zhang, J.P. Stacy, B.A. Pint, J.A. Haynes, B.T. Hazel, B.A. Nagaraj, Interdiffusion behavior of Pt-diffused γ+γ′ coatings on Ni-based superalloys, Surf Coat Technol 203 (2008) 417–421. https://doi.org/10.1016/j.surfcoat.2008.08.053.

[292] Y. Zhang, D.A. Ballard, J.P. Stacy, B.A. Pint, J.A. Haynes, Synthesis and oxidation behavior of platinum-enriched γ+γ′ bond coatings on Ni-based superalloys, Surf Coat Technol 201 (2006) 3857–3861. https://doi.org/10.1016/j.surfcoat.2006.07.245.

[293] J.P. Stacy, Y. Zhang, B.A. Pint, J.A. Haynes, B.T. Hazel, B.A. Nagaraj, Synthesis and oxidation performance of Al-enriched γ+γ′ coatings on Ni-based superalloys via secondary aluminizing, Surf Coat Technol 202 (2007) 632–636. https://doi.org/10.1016/j.surfcoat.2007.06.053.

[294] S. Manna, H. Chan, A. Ghosh, T. Chakrabarti, S.K. Sankaranarayanan, Understanding and control of Zener pinning via phase field and ensemble learning, Comput Mater Sci 229 (2023) 112384. https://doi.org/10.1016/j.commatsci.2023.112384.

[295] Z. Liu, W. Gao, K. Dahm, F. Wang, The effect of coating grain size on the selective oxidation behaviour of Ni-Cr-Al alloy, Scr Mater 37 (1997) 1551–1558. https://doi.org/10.1016/S1359-6462(97)00291-1.

[296] M.W. Brumm, H.J. Grabke, The oxidation behaviour of NiAl-I. Phase transformations in the alumina scale during oxidation of NiAl and NiAl-Cr alloys, Corros Sci 33 (1992) 1677–1690. https://doi.org/10.1016/0010-938X(92)90002-K.

[297] Y. Kitajima, S. Hayashi, T. Nishimoto, T. Narita, S. Ukai, Rapid Formation of α-Al2O3 Scale on an Fe–Al Alloy by Pure-Metal Coatings at 900 °C, Oxidation of Metals 73 (2010) 375–388. https://doi.org/10.1007/s11085-009-9184-8.